

Diss. ETH No. 19993

**Composition and reactivity analysis of diesel soot
with advanced FTIR spectroscopy and a new TG-FTIR system at
the example of the oxidation with O₂, NO₂ and H₂SO₄
and the SCR reaction with NO_x and NH₃**

A dissertation submitted to

ETH ZURICH

for the degree of

Doctor of Sciences

presented by

MAX MEHRING

Dipl. Ing. in Chemistry, Technical University of Darmstadt

born October 11, 1980

citizen of Germany

accepted on the recommendation of

Prof. Dr. A. Wokaun, examiner

Prof. Dr. J. van Bokhoven, co-examiner

Dr. O. Kröcher, co-examiner

2011

Meinen Eltern,
die mir die Freiheit und den Halt gaben
die Welt auf eigenen Füßen entdecken zu können.

Acknowledgements

I would like to extend my thanks to Prof. Dr. Alexander Wokaun for giving me the opportunity to do research at Paul Scherrer Institute, for the very helpful and inspiring discussions as well as for his motivating interest in my work.

Also, I would like to express my gratitude to Dr. Oliver Kröcher for support, guidance and confidence throughout my time at Paul Scherrer Institute. Thanks for the help during the preparation of publications and talks - I admire how he is able to formulate difficult subjects in brief words.

I would like to thank Prof. Dr. Jeroen van Bokhoven for taking the task as co-examiner.

My sincerest thanks goes to Martin Elsener, who is the core of the laboratories on the 4th floor in the OLGA building. Thanks for fighting with me against the adversities during the setup of the TG-FTIR instrument and the help with the experiments. But, I also thank him for unforgettable snowshoe tours, dinners in Klingnau and just for being a friend.

Thanks to Lukas Bächli for starting up the TG-FTIR system every day and the installation of several meters of gas tubes. My thanks also goes to the other current and former members of the Catalysis for Energy group: Dr. Maria Casapu, Daniel Peitz, Andreas Bernhard and all not mentioned members, as well as our intern Deborah Studer.

Furthermore, I would like to thank Dr. Sandro Brandenberger, who was also a member of the Catalysis for Energy group, but is first and foremost my friend, who helped me feeling home in Switzerland.

I would like to thank the Swiss National Fond (project # 200021_125257) as well as the "Forschungsvereinigung Verbrennungsforschung e.V." (project 1006) for financial support.

My thank goes to Marcel Hottiger and to the members of the LOG workshops.

At this point, I would like to address my thanks to those who provided the soot samples for the composition and reactivity analysis: Dr. R. von Borstel (VW), Dr. Dieter Rothe (MAN), Prof. Dr. Stefan Pischinger (RWTH Aachen), Michael Fiebig (RWTH Aachen), Prof. Dr. Reinhard Niessner (TU München) and Johannes Schmid (TU München).

Furthermore, I want thank Urs Jörimann and Dr. Markus Schubnell from Mettler-Toledo for giving me the opportunity to join a training for Mettler-Toledo technicians. Also thanks to Dominik Hohler, Dr. Hans-Hermann Belz and Dr. Alfred Möps from Thermo Scientific.

Thanks to Dr. Robert Büchel (ETHZ) and Dr. Eberhard Jacob (Emissionskonzepte Krailing) for their support and helpful discussions.

Last but not least my special thanks goes to my parents, my sister, grandparents and my friends for everything they did for me in the past and present. And of course thanks to Hemma Zöhrer, I am so glad that you ran out of nitric acid.

Table of contents

Summary	11
Kurzfassung.....	15
1. Introduction	19
1.1. Diesel engine emissions and their legal regulation	19
1.2. Diesel particulate matter.....	21
1.2.1. Diesel particulate matter formation.....	21
1.2.2. Diesel particulate matter composition.....	23
1.2.3. Diesel particulate filter.....	24
1.2.4. Oxidation of particulate matter	26
1.2.5. Statutory diesel particulate matter analysis – methods and problems	31
1.3. Reduction of NO _x in the exhaust gas of diesel engines.....	35
1.3.1. Selective catalytic reduction of NO _x over inorganic catalysts.....	35
1.3.2. Selective catalytic reduction of NO _x on soot.....	39
1.4. Scope of the thesis.....	45
2. Methods and experimental equipment	47
2.1. Analysis of PM composition and surface reactions.....	47
2.1.1. Thermogravimetry coupled with FTIR spectroscopy	47
2.1.2. Hydrocarbon analysis	48
2.1.3. Tubular quartz reactor for the investigation of the SCR effect over diesel soot and the influence of H ₂ SO ₄ on the soot oxidation with NO ₂	49
2.1.4. Wet chemical analysis for the estimation of the SO ₃ /H ₂ SO ₄ and SO ₂ content	54
2.2. Investigated PM samples.....	58
2.2.1. PM samples on cordierite	59
2.3. Additional characterization techniques	61

2.3.1.	BET measurements	61
2.3.2.	ICP-OES measurements.....	61
2.3.3.	Transmission electron microscopy.....	62
2.3.4.	DRIFTS measurements	62
2.4.	Data Evaluation	63
2.4.1.	Carbon oxidation rate	63
2.4.2.	NO _x reduction	64
2.4.3.	NO ₂ and NH ₃ conversion.....	64
2.4.4.	Stoichiometric ratio	64
2.4.5.	Mass flow calculated from the gravimetric and gas phase analysis....	65
2.4.6.	Gas hourly space velocity.....	66
2.4.7.	Estimation of the onset temperature of a PM mass loss in TG-FTIR experiments	66
3.	Development of the TG-FTIR instrument.....	68
3.1.	Introduction.....	68
3.2.	Changes of the thermogravimetric analyzer	69
3.3.	Changes of the FTIR spectrometer	75
3.4.	Gas mixing unit.....	78
3.5.	Hydrocarbon analysis by flame ionization detector	79
3.6.	Final setup of the TG-FTIR system.....	81
3.7.	Performance test of the TG-FTIR system	82
3.8.	Conclusions	86
4.	Composition analysis of soot with the TG-FTIR system.....	87
4.1.	Introduction.....	87
4.2.	Experimental	87
4.2.1.	TPD/O measurements	87
4.2.2.	TPO measurements	89
4.2.3.	Types of PM samples	90

4.3. Results and discussion of the composition analysis.....	92
4.3.1. Method development based on the VW Samples 1-4	92
4.3.2. Graphite and GfG soot.....	96
4.3.3. Printex U, Euro 0, Euro V and the mixed soot sample.....	98
4.3.4. PM samples on metal filters	99
4.3.5. Error analysis of the composition analysis	102
4.4. Results of the reactivity analysis	104
4.4.1. VW Sample 2	104
4.4.2. Printex U, Euro 0, Euro V and the mixed soot sample.....	110
4.4.3. Graphite and GfG soot.....	113
4.4.4. PM samples on metal filters	115
4.5. Discussion of the reactivity analysis	117
4.5.1. Trends of the C-oxidation rates	117
4.5.2. Influence of water on the oxidation and the CO ₂ /CO ratios	120
4.5.3. Reaction network and mechanistic details of PM oxidation.....	122
4.6. Conclusions	133
5. Influence of H₂SO₄ on the soot oxidation with NO₂.....	135
5.1. Introduction.....	135
5.2. Experimental	136
5.3. Results	137
5.3.1. Introductory example for the impact of H ₂ SO ₄ on the soot oxidation	137
5.3.2. NO ₂ conversion and C-oxidation rates.....	140
5.3.3. HNO ₃ evolution	145
5.4. Discussion.....	147
5.5. Conclusions	153
6. Selective catalytic reduction of NO_x with NH₃ on soot.....	154
6.1. Introduction.....	154
6.2. Experimental	156

6.2.1.	Samples and their characterization.....	156
6.2.2.	Activity measurements in the tubular quartz reactor.....	159
6.2.3.	Activity measurements in the TG-FTIR system.....	162
6.2.4.	DRIFTS investigations of Printex U.....	163
6.3.	Results and Discussion.....	164
6.3.1.	SCR reaction of Printex U in the presence of NO and NH ₃	164
6.3.2.	SCR reaction over Printex U in the presence of NO ₂ , NO and NH ₃ ...	166
6.3.3.	C-oxidation rates of Printex U in the presence of NO ₂ , NO and NH ₃	171
6.3.4.	Byproducts generated in the presence of NO ₂ , NO and NH ₃ over Printex U.....	175
6.3.5.	Influence of the space velocity on the SCR reaction over Printex U..	182
6.3.6.	SCR reaction over diesel soot in comparison to Printex U.....	186
6.3.7.	SCR effect over diesel soot in the presence of H ₂ SO ₄	195
6.3.8.	Investigation of the SCR effect over diesel soot in the TG-FTIR system	197
6.3.9.	DRIFTS measurements with Printex U.....	198
6.4.	Mechanism.....	205
6.5.	Conclusions.....	209
7.	Summary and Outlook.....	212
8.	Bibliography.....	214
	List of publications.....	227
	Curriculum vitae.....	230

Summary

In the last two decades nitrogen oxides (NO_x) and particulate matter (also denoted as PM or soot) in the exhaust gas of diesel engines had to be drastically reduced due to the stepwise introduction of emission limitations. At the beginning the reductions were reached by improvements of the combustion process and the engine management. However, as the limits were tightened, additional exhaust gas aftertreatment techniques had to be applied.

The research in this field is so far divided into two parts: On the one side, the NO_x reduction, which is mainly reached by the selective catalytic reduction (SCR) with ammonia (NH_3) and on the other side the PM reduction by the diesel particulate filter (DPF). This makes sense as long as the current emission limits can be reached by applying either a SCR system or a DPF and adapt the engine settings accordingly. However, the stricter future emission limits necessitate the application of both aftertreatment techniques in series. According to this necessity, a combination of DPF and SCR system would be conceivable. Then, the reducing agent for the SCR has to be also dosed upstream of the DPF. However, the parallel presence of NO_x , NH_3 and PM will lead most probably to the superposition of physical and chemical processes, as these compounds may all react with each other. Furthermore, it is likely that the composition of PM will change.

Due to this development, this work was focused on the investigation of surface reactions of PM with compounds contained in the exhaust gas of diesel engines and the composition of PM. For that purpose a TG-FTIR (TG: thermogravimetry, FTIR: Fourier-Transform infrared spectroscopy) system for investigations with corrosive and condensable reactive gases was developed in the first phase of the project. The standard gas inlet and outlet of the thermogravimetric analyzer were changed to avoid condensation. The gas

measuring cell of the FTIR spectrometer was designed such that an optimum compromise between the small flow rates through the thermogravimetric analyzer and a short residence time of the gases in the gas measuring cell could be achieved.

In the second phase, a TPD/O (temperature-programmed desorption followed by oxidation) method was developed for the total composition analysis of PM samples down to 300 μg with the TG-FTIR system. The EC (elemental carbon) and OC (organic carbon) content was quantified precisely, whereby the contributions of thermally unstable surface functional groups and adsorbed hydrocarbons (HC) to the OC could be discriminated. Additionally, the oxygen, hydrogen, water and ash content of the samples were measured as well as the amount of sulfuric acid (H_2SO_4) adsorbed on the PM.

After the composition analysis the reactivity of the PM samples was investigated by TPO (temperature-programmed oxidation) experiments with different feed gases containing O_2 , H_2O and NO_2 in the TG-FTIR system. By adding NO_2 , the soot oxidation started at lower temperatures and the addition of H_2O led to a shift of the maxima of the carbon oxidation rates to lower temperatures. The experimental results showed that beside the composition analysis, the investigation of PM reactivities with wet and corrosive gases is one of the main strengths of the TG-FTIR system in comparison to other instruments, because conditions similar to those in the DPF can be simulated.

In the third phase of the project the influence of H_2SO_4 traces on the soot oxidation with NO_2 was investigated. These experiments were performed in a tubular quartz reactor coupled with FTIR spectroscopy for the gas analysis in the temperature range between 100°C and 700°C . The feed gas contained also O_2 and H_2O beside NO_2 and the H_2SO_4 traces. When there was NO_2 in the feed, the addition of H_2SO_4 traces enhanced the soot oxidation over the whole

Summary

temperature range. Without NO_2 only a slight increase of the soot oxidation was observed above 480°C . In addition, it was found that in the presence of H_2SO_4 the HNO_3 concentration increased.

From these results a mechanism was developed, where H_2SO_4 can accelerate the soot oxidation at two points of the reaction network. On the one hand H_2SO_4 enhanced the formation of nitronium ions (NO_2^+) from HNO_3 , which are the active species during the nitration of the aromatic carbon structures. And as the nitration of the aromatic soot structures is one of the major process steps during soot oxidation with NO_2 , an enhanced concentration of NO_2^+ explains the increased oxidation rates. On the other hand, H_2SO_4 also catalyzed the disproportionation of two NO_2 molecules into HNO_2 and HNO_3 by protonation of the intermediate N_2O_4 . This resulted in an increased HNO_3 concentration, which further enhanced the NO_2^+ concentration.

In the final step of the project, a detailed investigation of the NO_x reduction activity of PM samples was performed, as a SCR reaction of NH_3 and NO_x on PM samples was actually observed, which occurs most probably also in combined DPF-SCR systems.

The NO_x reduction activity of the samples was investigated also in the tubular quartz reactor in dependence of the NO_2 , NO and NH_3 concentration in the temperature range between 200°C and 350°C . The highest NO_x reduction of up to 25% was measured in the presence of both NO_2 and NO at a GHSV of $35,000\text{ h}^{-1}$. Decreasing space velocities resulted in an increase of the SCR activity. In the absence of NO_2 , NO_x reduction was not observed. Carbon oxidation and SCR reaction, which occurred in parallel due to the presence of NO_2 and O_2 , hardly influenced each other. Together with the fact that the SCR process on PM is a rather slow process in comparison to the SCR reaction over inorganic catalysts, this led to the assumption that in the NO_x reduction on PM

most probably physisorbed species were involved. The observed stoichiometric ratios indicated the action of the *fast SCR* reaction in the presence of NO and the *NO₂ SCR* reaction in the absence of NO, while the observed gas phase and surface species indicated that the reaction steps were similar to those on classical SCR catalyst. In the presence of H₂SO₄ a significant increase of the NO_x reduction activity was observed. This observation was due to the acceleration of the decomposition of N₂O₄ formed in the NO₂ disproportionation similar to the influence of H₂SO₄ on the soot oxidation, because this disproportionation was the first reaction step in the SCR process, too.

Kurzfassung

In den letzten zwanzig Jahren wurden die Stickoxide (NO_x) und Particulate Matter (im Folgenden auch als PM oder Russ bezeichnet) im Abgas von Dieselmotoren durch die schrittweise Einführung von gesetzlichen Grenzwerten drastisch reduziert. Zu Beginn konnten die Grenzwerte noch durch Verbesserungen des Verbrennungsprozesses und des Motormanagements eingehalten werden, aber im Zuge weiterer Grenzwertverschärfungen mussten auch Abgasnachbehandlungstechniken eingesetzt werden.

Die Forschung im Bereich der Abgasnachbehandlung ist bisher in zwei Teile unterteilt: Auf der einen Seite die NO_x -Reduktion, die hauptsächlich über das Verfahren der selektiven katalytischen Reduktion (SCR) mit Ammoniak (NH_3) erreicht wird und auf der anderen Seite die PM-Reduktion mittels Dieselpartikelfilter (DPF). Diese Unterteilung war bisher möglich, da es zum Erreichen der bisherigen Grenzwerte ausreichte, entweder ein SCR System oder ein DPF bei entsprechender Anpassung der Motoreneinstellung einzusetzen. In Zukunft müssen allerdings beide Techniken zum Einsatz kommen, um die weiter sinkenden Grenzwerte einzuhalten. Dementsprechend wäre es vorstellbar Filter- und SCR-Technologie zu einem System zu kombinieren, bei dem das Reduktionsmittel für die SCR vor dem DPF eingespeist würde. Allerdings führt die gleichzeitige Anwesenheit von NO_x , NH_3 und PM aber zu einer Überlagerung chemischer und physikalischer Prozesse, da alle vorhandenen Komponenten miteinander reagieren können, und auch eine Veränderung der PM-Zusammensetzung zu erwarten ist.

Aufgrund der beschriebenen Entwicklungen bestand der Fokus dieser Arbeit in der Untersuchung von Oberflächenreaktionen von PM mit

Dieselabgasbestandteilen und der Zusammensetzung von PM. Zu diesem Zweck wurde ein TG-FTIR- (TG: Thermogravimetrie, FTIR: Fourier-Transform Infrarot Spektroskopie) System für Untersuchungen mit kondensierbaren und korrosiven Gasen im ersten Teil dieses Projekts entwickelt. Dazu wurden der Standardgasein- und -auslass der Thermowaage so verändert, um Kondensation zu vermeiden. Zusätzlich wurde die Gasmesszelle des FTIR-Spektrometers so verändert, dass sie einen Kompromiss zwischen den kleinen Gasflüssen im System und möglichst kurzen Verweilzeiten darstellt.

In der zweiten Phase, wurde eine TPD/O- (Temperature-programmierte Desorption gefolgt von Oxidation) Methode für das TG-FTIR-System entwickelt, die eine Analyse der Zusammensetzung von Proben bis 300 µg ermöglicht. Der EC- (Elemental Carbon) und OC- (Organic Carbon) Gehalt konnten präzise bestimmt werden, wobei es sogar möglich war, die Beiträge der thermisch instabilen Oberflächengruppen und der adsorbierten Kohlenwasserstoffe (HC) zum OC zu unterscheiden. Zusätzlich wurden der Sauerstoff-, Wasserstoff-, Wasser- und Ascheanteil der Proben ebenso wie der Anteil an adsorbierter Schwefelsäure (H₂SO₄) bestimmt.

Nach der Zusammensetzungsanalyse wurde die Reaktivität der Proben mit TPO- (Temperature-programmierte Oxidation) Experimenten mit unterschiedlichen Gasgemischen, die O₂, H₂O und NO₂ enthielten im TG-FTIR-System untersucht. Das Zufügen von NO₂ zum Reaktivgas führte zu einer Absenkung der Starttemperatur der Oxidation und das Zufügen von H₂O führte zu einer Verschiebung der Maxima der Kohlenstoffoxidationsraten zu niedrigeren Temperaturen. Die erhaltenen Resultate zeigten, dass neben den Zusammensetzungsanalysen die Reaktivitätsuntersuchungen mit

kondensierbaren und korrosiven Gasen eine grosse Stärke des Systems sind, da ähnliche Bedingungen wie in einem DPF simulierte werden können.

Im dritten Teil der Arbeit, wurde der Einfluss von Spuren von H_2SO_4 auf die Russoxidation mit NO_2 untersucht. Diese Experimente wurden in einem Temperaturbereich von $100\text{-}700^\circ\text{C}$ in einem Rohrreaktor aus Quarzglas mit anschliessendem FTIR-Spektrometer für die Gasanalyse durchgeführt. Die dosierten Gasmische enthielten neben NO_2 und Spuren von H_2SO_4 auch O_2 und H_2O . In Anwesenheit von NO_2 führte das Zufügen von wenigen ppm H_2SO_4 zu einer deutlichen Steigerung der Russoxidation im gesamten Temperaturbereich. Ohne NO_2 konnte nur eine geringe Steigerung der PM-Oxidation oberhalb von 480°C beobachtet werden. Zusätzlich konnte in Anwesenheit von H_2SO_4 eine erhöhte HNO_3 Konzentration gemessen werden.

Basierend auf diesen Resultaten wurde ein Reaktionsmechanismus entwickelt, bei dem H_2SO_4 die Russoxidation an zwei Stellen des Reaktionsnetzwerks beschleunigen kann. Auf der einen Seite steigert H_2SO_4 nämlich die Bildung von Nitroniumionen (NO_2^+) aus HNO_3 , die die aktiven Spezies bei der Nitrierung von Aromaten sind. Und da die Nitrierung der aromatischen Russstrukturen einer der Hauptschritte der Russoxidation mit NO_2 ist, erklärt eine erhöhte NO_2^+ -Konzentration die erhöhten Oxidationraten. Auf der anderen Seite katalysiert H_2SO_4 die Disproportionierung von zwei NO_2 Molekülen in HNO_2 und HNO_3 über die Protonierung des Intermediats N_2O_4 . Dies führt zu einer erhöhten HNO_3 Konzentration und damit auch einer weiteren Erhöhung der NO_2^+ Konzentration.

Im letzten Abschnitt des Projekts wurde eine detaillierte Untersuchung der NO_x -Reduktion von Russproben durchgeführt, da tatsächlich eine SCR-Reaktion von NO_x mit NH_3 über Russproben beobachtet wurde, die

höchstwahrscheinlich auch in einem kombinierten System auf DPF und SCR-Katalysator ablaufen würde.

Die Aktivitätsuntersuchungen der Russproben bezüglich der NO_x -Reduktion wurden ebenfalls in einem Rohrreaktor in Abhängigkeit der NO_2 , NO und NH_3 Konzentration im Temperaturbereich zwischen 200°C und 350°C durchgeführt. Die höchste NO_x -Reduktion von bis zu 25% wurde in Anwesenheit von NO_2 und NO bei einer GHSV von $35,000\text{ h}^{-1}$ gemessen. Niedrigere Raumgeschwindigkeiten führten zu einem Anstieg der SCR-Aktivität. In Abwesenheit von NO_2 konnte keine NO_x -Reduktion beobachtet werden. Russoxidation und SCR-Reaktion, die aufgrund der Anwesenheit von NO_2 und O_2 parallel ablaufen, beeinflussten sich gegenseitig kaum. Daraus wurde zusammen mit der Tatsache, dass der SCR-Prozess über PM ein eher langsamer Prozess im Vergleich zur SCR-Reaktion über anorganischen Katalysatoren ist, geschlossen, dass bei der NO_x -Reduktion physisorbierte Spezies beteiligt sind. Die gemessenen stöchiometrischen Verhältnisse deuten auf eine *fast* SCR-Reaktion in Anwesenheit von NO hin und dessen Abwesenheit auf eine NO_2 SCR-Reaktion, wobei die detektierten Gasphasen- und Oberflächenspezies darauf hindeuten, dass die Reaktionsschritte denen auf anorganischen Katalysatoren ähneln.

In Anwesenheit von H_2SO_4 wurde ein deutlicher Anstieg der NO_x -Reduktion beobachtet, der auf der Katalyse der Zersetzung von N_2O_4 beruht, wie es bereits beim Einfluss von H_2SO_4 auf die Russoxidation beschrieben wurde, das die Disproportionierung auch der erste Schritt der SCR-Reaktion ist.

1. Introduction

1.1. Diesel engine emissions and their legal regulation

During the combustion of carbon based fuels carbon monoxide (CO), nitrogen oxides (NO_x = sum of nitrogen dioxide (NO_2) and nitric oxide (NO)), hydrocarbons (HC) and particulate matter (PM; also denoted as soot in this thesis) are emitted, which are known to have adverse effects on human health and the environment [1-4]. Since traffic is a major source of these pollutants, the emissions of cars and heavy duty vehicles have been limited stepwise by law in industrial countries like the US, Japan and the European Union (EU) [5], as shown exemplarily for heavy duty diesel engines and diesel passenger cars in the EU in Table 1 and Table 2.

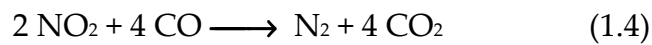
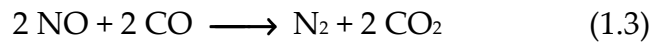
Table 1: Development of the European emission limits for diesel passenger cars. Shown limits have to be reached during the NEDC (New European Driving Cycle) [5].

	Euro 1	Euro 2	Euro 3	Euro 4	Euro 5	Euro 6
effective date	1992/93	1995/96	2000/01	2005/06	2008/09	2012/13
CO [g/km]	3.16	1	0.64	0.5	0.5	0.5
(HC + NO_x) [g/km]	1.13	0.9	0.56	0.3	0.23	0.17
NO_x [g/km]	-	-	0.5	0.25	0.18	0.08
PM [g/km]	0.18	0.1	0.05	0.025	0.005	0.005

Table 2: Development of the European emission limits of heavy duty vehicles above 3.5 t. Shown limits have to be reached during the ESC (European Steady State Cycle) [5].

	Euro I	Euro II	Euro III	Euro IV	Euro V	Euro VI
effective date	1992/93	1995/96	2000/01	2005/06	2008/09	2012/13
CO [g/kWh]	4.5	4	2.1	1.5	1.5	1.5
HC [g/kWh]	1.1	1.1	0.66	0.46	0.46	0.13
NO_x [g/kWh]	8	7	5	3.5	2	0.4
PM [g/kWh]	0.61	0.25	0.13	0.02	0.02	0.01

Otto engine emissions were limited comparatively easy by the introduction of the precious metal based three-way-catalyst, which was already introduced in 1973. The catalyst allows the parallel removal of NO_x , CO and HC as shown in eq. (1.1)-(1.4) [6]:



This is possible due to the premixing of air and fuel and the control of λ , which is defined as the ratio of the actually added amount of air and the theoretical amount of air necessary for the total combustion of the injected fuel to CO_2 . By this measure excess oxygen in the exhaust gas is avoided, which would limit the amount of CO necessary for the reduction of NO.

In diesel engines on the other hand the fuel is added directly to the compressed air without premixing, leading to a partial oxygen-diffusion-controlled combustion and excess oxygen in the exhaust gas. As a consequence, the CO concentrations are too low to remove the nitrogen oxides as shown in reactions (1.3) and (1.4) and the three-way catalyst cannot be applied.

Therefore, other techniques had to be found to limit the pollutants in the exhaust gases of diesel engines: For the removal of HC and CO still precious metal based diesel oxidation catalysts (DOC) were used, which oxidize HC and CO to H_2O and CO_2 . For the NO_x and PM reduction engine internal measures (e.g. exhaust gas recirculation (EGR), improved coordination of the fuel injection, intercooling and supercharging [7]) were sufficient to reach the first

emission limits. However, as the possibilities for engine internal measures were exhausted to reach the tightened limitations for NO_x and PM, aftertreatment techniques for their reduction had to be introduced.

For the further reduction of PM, the diesel particulate filter (DPF) (see section 1.2.3) became the accepted technology, while for NO_x removal NO_x storage catalysts and the selective catalytic reduction (SCR) with ammonia (NH₃) (see section 1.3.1) were introduced into the market.

1.2. Diesel particulate matter

1.2.1. Diesel particulate matter formation

During combustion, soot is formed under locally oxygen-deficient regions of the combustion chamber at temperatures of 1100-1200°C [8]. The processes during soot formation are not completely clarified. However, it seems that soot formation can be described as follows: In the oxygen deficient spots the large HC molecules are pyrolyzed and stepwise cracked forming acetylene under dehydrogenation [9-11]. After that, the acetylene molecules rearrange and form sheets of polyaromatic molecules (PAH = polyaromatic hydrocarbons) [9-11], which are curved due to five-membered rings. Several of these curved graphene layers aggregate forming spherical particulates with a diameter of 2-10 nm and a graphitic character. They grow further up to an average diameter of 50-100 nm leading to the “primary soot particulates” [12]. In the last step of the soot formation process, the primary particulates agglomerate and form larger secondary soot particles.

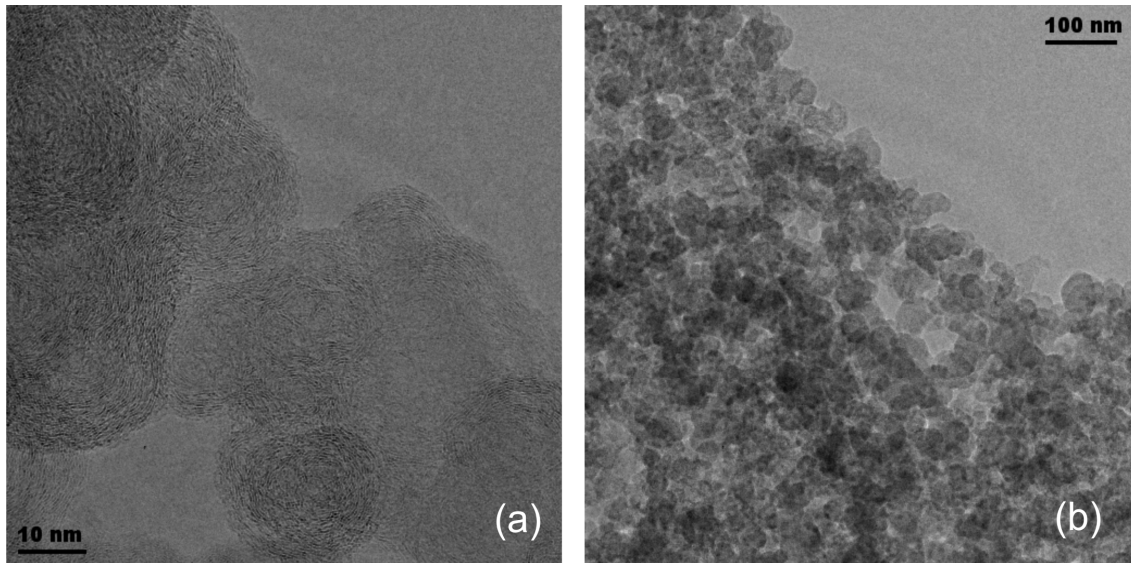


Figure 1 a and b: TEM pictures of an Euro V diesel soot. The left picture shows primary soot particulates, where the polyaromatic graphene layers can be seen. The right picture shows a cutout of a secondary soot particulate with the agglomeration of primary soot particles.

For clarification Figure 1 a and b illustrate the structures of primary and secondary particulates of an Euro V soot. In Figure 1 a, the structure of the primary soot particulates with layers of accreted PAH is shown, which is also called turbostratic [13] and Figure 1 b shows the agglomeration of primary soot particulates forming secondary soot particulates.

Although, the described general process of soot formation is valid for all PM samples, they can differ significantly in composition, particulate size, structure, amount and reactivity, whereupon the arrangement and the length of the polyaromatic graphene layers seem to have a large influence [14]. The reasons for these differences are manifold as they are dependent on engine type [15, 16], engine load [17-19], fuel [20], injection pressure [21] and residence time in the combustion chamber [18] to name at least a few.

1.2.2. Diesel particulate matter composition

Diesel particulate matter (PM) is the generic term for solid particulates emitted during combustion processes. PM mainly consists of carbon, however, it also contains oxygen, hydrogen, sulfur and nitrogen compounds as well as metal oxides and salts [22] in dependence on the applied fuel and the operation conditions of the engine [23].

In the average about 5-35 wt% of a particulate consist of a fraction, which is soluble in an organic solvent (SOF); the other 65-95 wt% are insoluble (INSOF) [22, 24]. The SOF fraction consists of adsorbed paraffinic or aromatic HC, which can be partially oxidized and may contain heteroatoms like O, S and N [25, 26]. The origin of SOF are unburned fuel and lubrication oil HC [27], which adsorb on the particulate surface in the gas cooling phase [28]. As shown by Clague et al. and Stanmore et al., the INSOF can consist of 84-98 wt% carbon, but also contains 3-15 wt% oxygen, 1-2 wt% hydrogen, 0.1-0.6 wt% sulfur and 0.2-0.4 wt% nitrogen [22, 24]. In addition, INSOF analyses showed that this fraction can include an inorganic fraction of up to 25% sulfate and oxide ashes [29]. This inorganic fraction results from the combustion of fuel and lubrication additives as well as engine wear.

Beside these classifications, the carbon content of PM is divided into the organic carbon (OC) content, which is similar to the SOF, and the elemental carbon (EC) content, which is the carbon part of the INSOF. The OC content can be desorbed by thermal treatment of the PM sample under inert conditions, while the EC content can only be gasified in the presence of an oxidant.

1.2.3. Diesel particulate filter

As aftertreatment device for the further reduction of particle emissions from passenger cars and heavy duty vehicles, DPFs have become generally accepted. Most frequently wall-flow filters made from porous ceramics or sintered metals as shown in Figure 2 are used [30]. In these systems, the exhaust gases enter the DPF and have to pass the porous walls, where PM is retained.

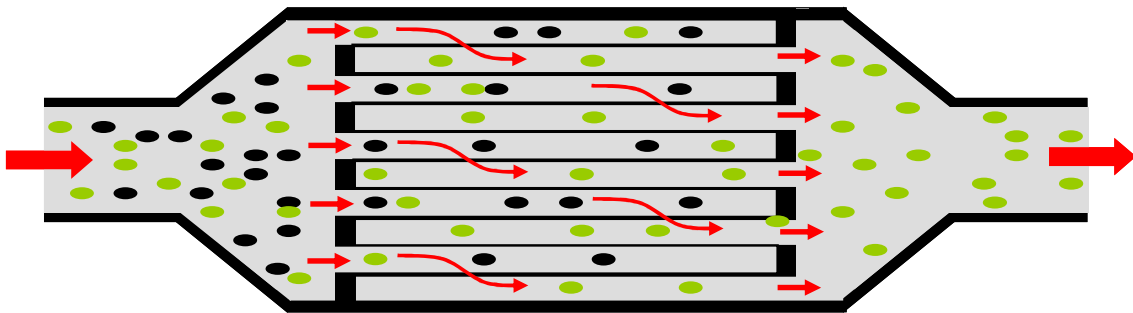


Figure 2: Diesel particulate filter in wall-flow design adapted from [7]. The exhaust gases enter the filter from the left side and have to pass the system walls, where PM is collected. Black spots: PM; green spots: gaseous exhaust components.

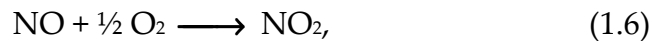
Beside the wall-flow filters also “open” designs of particle filters exist, which are not based on the filtration of the exhaust gas stream, but on the adhesion of the soot particles on the filter walls [31, 32]. These systems consist of metal honeycombs, which are corrugated and broken. This leads to a turbulent exhaust gas stream contributing considerably to the high adhesion rates of the filters.

Due to the constant deposition of the PM in the filter, the pressure drop over the filter system rises with time. Therefore the filter must be regenerated continuously or intermittent by oxidation of the soot to CO_2 . For the

intermittent regeneration, the differential pressure is measured over the filter and at a certain threshold value the regeneration with oxygen is started:



The temperatures for the regeneration need to be at least 500-550°C. However, the exhaust gas temperature of the diesel engine in city traffic mode is usually not higher than 200°C. Therefore, it has to be increased by active measures such as additional fuel burning or electrical heating [33]. For the continuous passive regeneration of DPFs nitrogen dioxide (NO₂) is used as oxidant [34-43]:



This procedure is called passive, since it can run continuously during normal driving conditions. Due to the higher reactivity of NO₂ lower temperatures are needed in comparison to the intermittent regeneration with oxygen. NO₂ is generated from nitrogen monoxide (NO) contained in the exhaust gas in the DOC upstream of the particulate filter [33].

Another possibility to improve the regeneration of the DPF is the coating of the filter with catalytic active material [30, 33]. By the introduction of such a coating the soot oxidation temperature with O₂ can be lowered up to 300 K [44, 45]. The catalytic active materials mostly consist of transition metals (Fe, V, Ce, Cu, Mn, Pt, Pd, etc.), which contain promoters like KCl and SrCl₂ [43, 45]. However, this work was mainly focused on the uncatalyzed PM reactivity and reactions on

the carbon surface. Thus, a closer look will only be taken on the mechanism of uncatalyzed PM oxidation, in the next section.

1.2.4. Oxidation of particulate matter

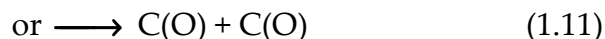
The oxidation of the soot collected in the DPF with oxygen and NO₂ can be described by the reactions (1.5)-(1.7). However, these equations describe only the overall process and therefore the question remains how the oxidation proceeds in detail?

Soot oxidation is a very old process, which is however still the subject of many investigations, since the involved reactions are complex. Not only chemical kinetics and heat transport have to be considered, but also the mass transport of the species. Independently of the oxidant, diesel soot oxidation can be generally described by three steps, which are common to all mechanisms. First, an oxidant molecule adsorbs on the carbon surface. Second, an oxygen atom is transferred from the oxidant to the surface, while an oxygen-carbon complex is formed. In the last step this complex decomposes under formation of CO₂ or CO, which desorbs from the surface.

For the uncatalyzed oxidation with oxygen, Marsh and Kuo proposed the following formal mechanism [46], where C* is an active carbon site, C(O₂) a localized oxygen molecule, C(O₂)_m mobile molecular oxygen, C(O) a localized oxygen atom and C(O)_m a mobile oxygen atom:

Adsorption (step 1) and formation of oxygen-carbon complexes (step 2):



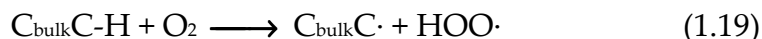


Decomposition of oxygen-carbon complexes (step 3):

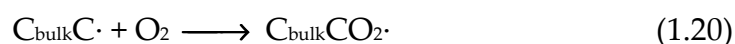


Similar to Marsh and Kuo most of the authors reporting about soot oxidation presume an active carbon site labeled as C^* or simple as C [35, 40, 43, 47-49]. However, only little is said about the nature of this site or how it is formed. Most probably the sites do not reach their active status already during soot formation since they are too reactive to survive under the soot formation conditions. It is reasonable to assume that these sites, which are placed at edges of the carbon surfaces, are saturated with hydrogen or partially oxidized surface functional groups when the soot is collected in the DPF, which is supported by the findings of Schuster et al. [15]. This means, that the active carbon sites have to be formed prior or at least during the formation of the carbon oxygen complexes. The mechanism is most probably similar to the

radical oxidation of other organic compounds starting with hydrogen abstraction [50]:



$C_{\text{bulk}}C\cdot$ is similar to the active carbon site C^* , which is attacked by another O_2 molecule in a second step forming either a peroxide radical as in eq. (1.8):



or the oxygen molecule adsorbs dissociatively as in eq. (1.9)-(1.11):



Beside $HOO\cdot$ also $HO\cdot$ is formed, which both undergo further reactions with the carbon surface [50]. If the precursor of the active site is a partially oxidized surface functional group the reaction mechanism also starts with radical hydrogen abstraction similar to the autoxidation of oxidized organic compounds [51].

It was previously mentioned that NO_2 exhibits a substantially higher reactivity for soot oxidation than oxygen at low temperatures, which is a clear advantage for its use as oxidizing agent in the DPF. However, for the clarification of the NO_2 -based soot oxidation mechanism it has to be considered that oxygen is always present beside NO_2 and that both oxidants can influence each other. In general, three different ways of interaction were proposed in the literature,

which occur most probably in parallel. But their contribution to the overall soot oxidation rate depends on the soot origin and structure:

First, a parallel non-interfering mechanism of O₂ and NO₂ with active sites on the soot surface was proposed leading to the formation of oxygen surface functional groups [39]. The increased soot oxidation was explained with the higher reactivity of NO₂ towards carbon.

Second, Setibudi et al. and Jaquot et al. presented a co-operative mechanism, where NO₂ reacts first with active carbon sites forming oxygen containing-surface functional groups and evolving NO. In a subsequent step, these functional groups further react with O₂ or NO₂ evolving CO₂, CO and in the case of NO₂ also NO [36, 40]. The active carbon sites were assumed to be unreactive to O₂ before the NO₂ attack, but after the first oxidative step the complexes were activated towards the reaction with O₂.

And third, a co-operative mechanism was proposed by Jeguirim et al., where O₂ adsorbs on the soot surface and forms carbon-oxygen complexes, which are attacked faster by NO₂ than O₂ evolving NO, CO and CO₂ [52].

The active sites proposed for the NO₂ attack are formed similar to those in eq. (1.20). However, in the first and second proposed reaction pathway the hydrogen is most probably abstracted by NO₂, which has been confirmed by HONO measurements (eq. 1.22), as shown by Stadler and Rossi [42] and as it is known for light alkanes [50]:



The alkyl nitrite species (C-ONO) in eq. (1.23) were confirmed by DRIFTS measurements of Azambre et al. [53]. The bond cleavage in eq. (1.24) results in radicals similar to those formed in the presence of oxygen only. Furthermore, active sites also can be formed directly at the carbon backbone by aromatic nitration followed by homolytic C-N bond cleavage [54] or by nitro-nitrite rearrangement [54-58].

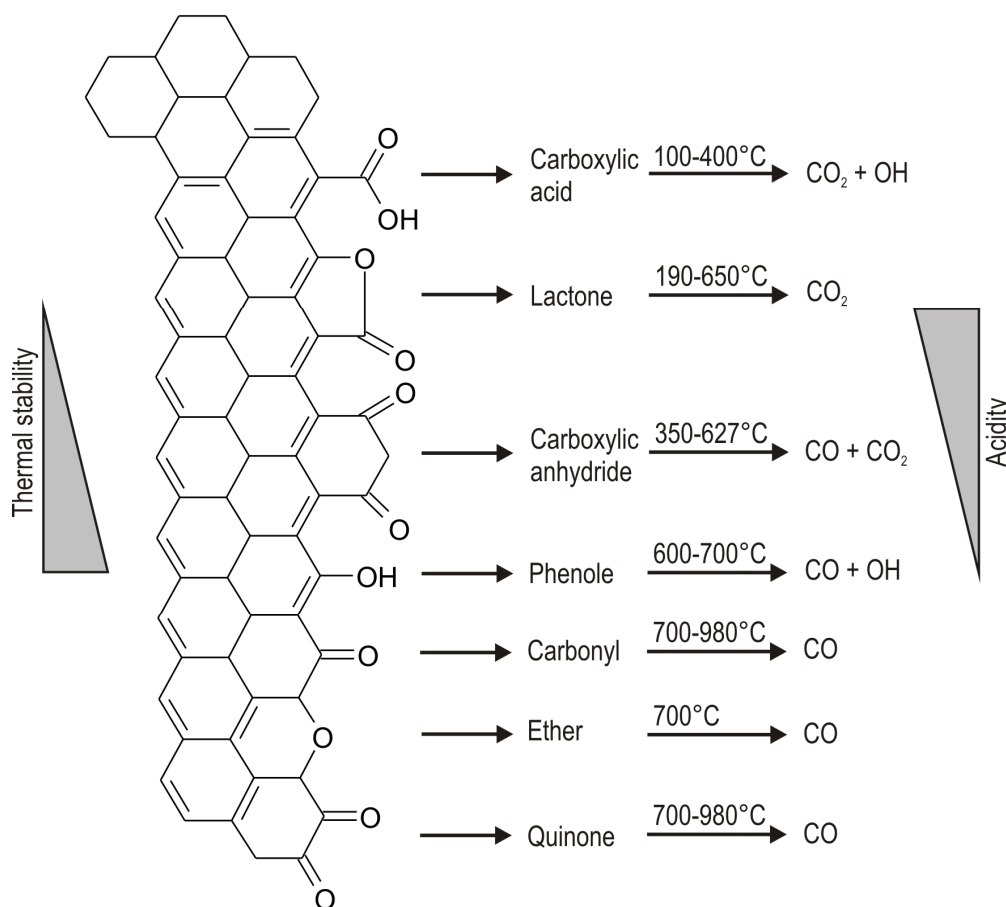


Figure 3: Oxygen surface functional groups formed on the carbon surface taken from [59]. The thermal stability decreases with increasing acidity.

The radicalic groups ($C_{\text{bulk}}C\cdot$ and $C_{\text{bulk}}CO\cdot$) formed in the initial steps of soot oxidation can react again with O_2 , NO_2 or $HOO\cdot$ and $HO\cdot$, which are still

present on the soot surface. This leads to the formation of acylnitrites [59], alkylnitrites [53, 60, 61], alkylnitrates [41, 53], carboxylates, carbonyls, lactones, ethers, etc. [61, 62], which decompose under release of CO₂ and CO as well as NO in the case of nitrites and nitrates.

Muckenhuber et al. reported that in the presence of NO₂ the formation of acidic surface functional groups increased [59]. This also explains the higher reactivity of NO₂ towards soot, since the more acidic a functional group is the lower is the decomposition temperature as listed in Figure 3.

1.2.5. Statutory diesel particulate matter analysis – methods and problems

Since 1982, engine emissions are collected for analysis using the standardized constant volume sampling (CVS) dilution method [7]. For that purpose, standardized transient test cycles are carried out, which simulate real engine operating conditions. All exhaust gases emitted during the test cycles are first fully diluted with air in a dilution tunnel to avoid condensation of gas components on the system walls. Then, a small quantity of the diluted exhaust gas is extracted and collected in a bag for later analysis of the average gas concentrations.

PM, which is also present in the diluted exhaust gas, is trapped by passing a partial stream of the diluted exhaust gas over a metal or quartz fiber filter for gravimetric quantification. This procedure of PM quantification is also the mandatory technique to prove the compliance of the legal PM emission limits. However, the gravimetric determination of the particle mass collected in the dilution tunnel has reached its detection limits due to the reduction in raw

emissions through internal engine refinements and the introduction of diesel particulate filters. Furthermore, the composition of PM has changed as the reduction of the total amount was mainly due to a reduction of the carbon fraction. The absolute amounts of other components like organic nitrogen and oxygen compounds, engine wear, ash, water and sulfur oxides (SO_x) and sulfates from the combustion of lubrication oil additives and sulfur-containing fuels remained nearly constant as illustrated in Figure 4. Therefore, their relative influence on the oxidation behavior in the DPF and also on the environmental impact of the particulates increased. Due to this development, new techniques are needed for the analysis of PM emissions, which have lower detection limits for the measurement of the total carbon amount on the one hand, but also address the necessity of a detailed chemical PM analysis.

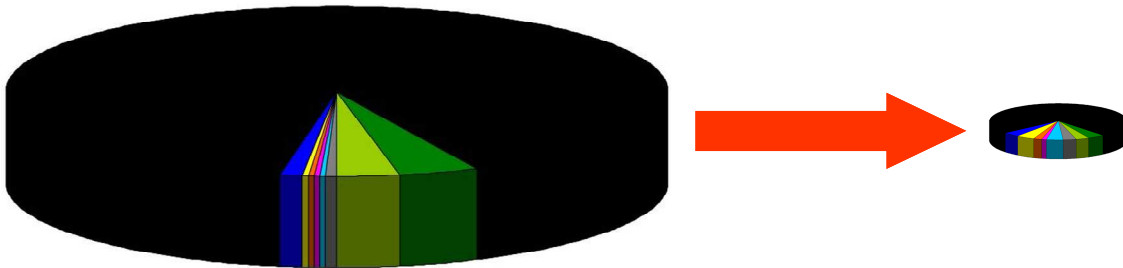


Figure 4: PM composition of an old diesel engine on the left side in comparison to the PM composition of a modern diesel engine. The total amount of PM was reduced by 80%, however, the absolute amount of the non-carbon remained nearly constant and therefore gained in importance.

There are many methods for PM composition analysis as shown in Table 3 taken from the review of Maricq [63]. However, most of these methods address only one PM component. There are other analysis methods like BET analysis [64, 65], Raman spectroscopy [15, 66, 67], EELS (electron energy loss

spectroscopy) [68], TEM (transmission electron microscopy) [14] TEM-EELS (transmission electron microscopy-EELS) [69], XPS (X-ray photoelectron spectroscopy) [70], NEXAFS (near-edge X-ray absorption fine structure spectroscopy) [68] and DRIFTS (diffusive reflectance infrared Fourier-transform spectroscopy [62, 71], but some of these methods are highly sophisticated and hardly applicable for quantification. However, for the routine PM analysis methods are needed, which are robust and fast, providing as much information as possible.

Table 3: Methods for chemical analysis of PM composition taken from the review of Maricq [63].

Species	Analysis method
total mass	gravimetric
size selective cyclones for PM ₁₀ and PM _{2.5}	gravimetric
soluble organic fraction	weight loss after extraction with dichloromethane and drying
Elemental/organic carbon	thermal/optical reflectance (TOR)
metals and elements Al, Si, P, S, Cl, K, Ca, Ti, V, Cr, Mn, Fe, Co, Ni, Cu, Zn, Ga, As, Se, Br, Rb, Sr, Y, Zr, Mo, Pd,...	coupled plasma mass spectrometry, X-ray fluorescence
inorganic ions and acids NO ₂ ⁻ , NO ₃ ⁻ , SO ₄ ²⁻ , PO ₄ ³⁻ , NH ₄ ⁺ , HNO ₂ , HNO ₃ , H ₂ SO ₄	water extraction and ion chromatography
semivolatile organic compounds, heavy hydrocarbons, PAH, hopanes/steranes	extraction, HPLC separation, high resolution GC-MS
Nitro-PAH	extraction, HPLC separation, negative ion chemical ionization GC-MS
polar organic compounds	extraction, conversion to silyl or methyl ester derivatives, GC-MS
dioxins/furans	extraction, high resolution GC-MS

Israël et al. [72] suggested the use of thermolysis in a quartz furnace with subsequent gas analysis by non-dispersive infrared spectroscopy (NDIR) as an alternative to gravimetric PM analysis. They were able to estimate the organic carbon (OC) content by heating a PM sample in inert atmosphere detecting the CO₂ after the evolved gases passed an oxidation catalyst. By subsequent oxidation in O₂ the EC (elemental carbon) content was also estimated from the CO₂ measured after the oxidation catalyst. Following these results, the standardized thermal analysis methods BGI 505-44 [73], VDI 2465 Bl.1 [74, 75] and NIOSH 5040 [76] were investigated for OC and EC analysis, and high resolution and good agreement for the EC and OC masses were obtained [77].

The thermolysis of PM seems to be a very promising technique for a detailed PM analysis, especially when it is performed in a thermogravimetric (TG) analyzer coupled with a Fourier-transform Infrared (FTIR) spectrometer or a mass spectrometer (MS). The coupling with a gas analyzer allows not only the carbon detection as CO₂, but also a measurement of CO and water as well as other compounds. In addition, these methods are robust, fast and easy to handle, which are prerequisites for the use as routine analysis techniques.

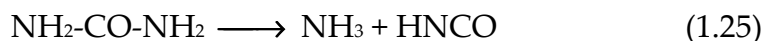
Thermogravimetry was applied for PM investigations by different researchers [28, 78, 79] and also the coupling with and FTIR spectrometer [80, 81] or an MS [82, 83] was already performed, however, it was not tried to use these techniques for a total analysis of PM considering also oxygen, nitrogen, hydrogen, sulfur and the content of residuals.

1.3. Reduction of NO_x in the exhaust gas of diesel engines

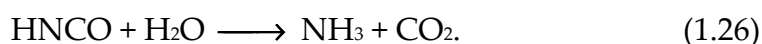
1.3.1. Selective catalytic reduction of NO_x over inorganic catalysts

Beside the reduction of PM emissions in the DPF also aftertreatment techniques for the reduction of NO_x emissions have been developed. The selective catalytic reduction (SCR) of the nitrogen oxides with ammonia (NH₃-SCR) as reducing agent has become the state-of-the-art technology for heavy-duty diesel engines and also for passenger cars [84-87]. The currently applied catalysts for the NH₃-SCR process are either metal oxide catalysts (mostly V₂O₅/WO₃-TiO₂) or metal-exchanged zeolites (metals: Fe, Cu) [87].

The toxic and corrosive NH₃, which is required in this process, is stored in form of an aqueous solution of the harmless NH₃ precursor compound urea in an extra tank in the vehicle. In dependence on the actual amount of NO_x in the exhaust gas the urea solution is injected into the exhaust stream, where it decomposes thermally to NH₃ and isocyanic acid (HNCO):

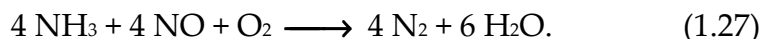


Isocyanic acid is then hydrolyzed into NH₃ and CO₂, leading to two molecules of NH₃ per molecule of urea:

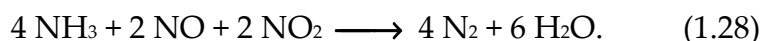


Three SCR pathways with ammonia, which are relevant for the exhaust gas aftertreatment of diesel engine, are known and described in overall reactions. Their occurrence depends on the composition of the exhaust gas. The reaction

of NH_3 with NO and oxygen, which are both available in excess in the exhaust gas, is termed as *standard SCR* reaction [88, 89]:



When NO_2 and NO are present in parallel in the exhaust gas stream, the so-called *fast SCR* reaction also takes place over the catalyst, which is substantially faster in comparison to the *standard SCR* reaction [88, 89]:



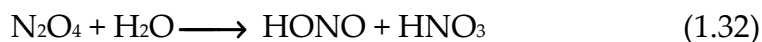
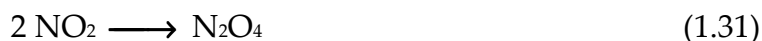
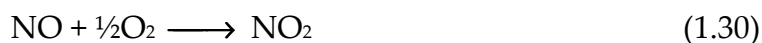
Beside *fast SCR* and *standard SCR* reaction the NO_2 SCR reaction occurs as the third pathway, when NO_2 is present in excess compared to NO [90]:



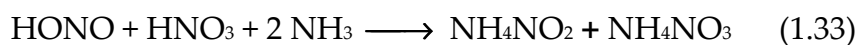
The mechanisms leading to the SCR overall reactions (1.27)-(1.29) are different for V/Ti-based SCR catalysts and metal-exchanged zeolites. In the V/Ti-based catalytic systems the active species were found to be $\text{V}^{5+}=\text{O}$ and $\text{V}^{4+}-\text{OH}$ [91, 92]. Based on these V-species Koebel et al. proposed a mechanism for *fast SCR* reaction [91], where the $\text{V}^{5+}=\text{O}$ is first attacked by NH_3 leading to $\text{HO}-\text{V}^{4+}-\text{N}\cdot\text{H}_2$, which reacts with NO forming $\text{HO}-\text{V}^{4+}-\text{NH}_2-\text{NO}$. The latter decomposes into $\text{V}^{4+}-\text{OH} + \text{N}_2 + \text{H}_2\text{O}$. In the last step of the turnover, the $\text{V}^{4+}-\text{OH}$ is reoxidized to $\text{V}^{5+}=\text{O}$ by NO_2 . This *fast SCR* mechanism is similar to the *standard SCR* mechanism suggested by Ramis et al. except for the reoxidation step, where oxygen instead of NO_2 is the oxidant [92].

The active species in the NO_2 SCR reaction on V/Ti-based catalysts were suggested to be $\text{V}^{5+}=\text{O}$ and $[\text{V}^{5+}-\text{OH}]^-$ [93]. However, as it is slower in comparison to the standard SCR reaction [86] it plays a minor role for the practical application and therefore, it will not be discussed here in more detail.

The SCR mechanisms occurring on metal-exchanged zeolites can be summarized based on the review of Kröcher [87] as follows: Independently of the reaction pathway, the initial step of the SCR is the formation (ep. (1.31)) and subsequent disproportionation (ep. (1.32)) of N_2O_4 leading to nitrous acid (HNO_2) and nitric acid (HNO_3). N_2O_4 is formed from NO_2 , which is either present in the exhaust gas or formed from the oxidation of NO (eq. (1.30)):



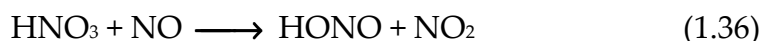
HNO_2 and HNO_3 react with NH_3 forming NH_4NO_2 and NH_4NO_3 , respectively:



NH_4NO_2 decomposes immediately, forming N_2 and water:



Up to that point the reaction pathways are similar for the *fast SCR*, *standard SCR* and the NO_2 SCR reaction, but for the reduction of the NH_4NO_3 different pathways occur. In the case of the *fast SCR* and *standard SCR* NH_4NO_3 decomposes into HNO_3 and NH_3 (eq. 1.35)). HNO_3 is then reduced by NO forming HNO_2 (eq. (1.36)), which reacts with NH_3 to NH_4NO_2 decomposing as shown in (eq. 1.34) [94]:

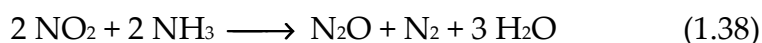


In the NO_2 SCR mechanism NO is missing as reducing agent and NH_3 has to take the role as the reducing agent. After the decomposition of NH_4NO_3 according to reaction (1.35), HNO_3 is reduced by NH_3 , leading to HNO_2 and N_2 [95]:

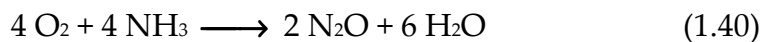


In a further reaction of HNO_2 with NH_3 again NH_4NO_2 is formed, which decomposes into N_2 and H_2O according to reaction (1.34).

At temperatures above 200°C also the formation of N_2O from the oxidation of NH_3 has to be considered, which is an important side reaction under SCR conditions [86]:



At temperatures above 380°C N₂O can also result from the reaction of NH₃ with O₂ [96]:



1.3.2. Selective catalytic reduction of NO_x on soot

The selective catalytic reduction of NO_x in the presence of NH₃ had already been used for the exhaust gas cleaning of stationary combustion and industrial processes over several decades before it was introduced to mobile applications [97-99]. However, since the used catalysts were mainly V/Ti-based catalysts the exhaust gases had to be reheated above 300°C for an effective NO_x removal [100]. In order to evade the reheating, it was searched for new catalytic materials, which allow the parallel removal of NO_x at temperatures of 100-150°C.

For that purpose, *Takeda Chemical Industries* and the *Bergbau-Forschung* developed activated carbon catalysts for the NO_x removal around 150°C in the 1970s and 80s [100-116]. Beside the lower temperatures, these catalysts had the additional advantage that SO_x, which is most often present beside NO_x, could be removed in parallel.

The *Bergbau-Forschung* used the activated carbon catalysts in two-stage fluidized bed processes [106]. In the first stage, a large part of the SO_x is removed from the exhaust gases on the carbon catalyst by adsorption. In the second stage, NH₃ is added to the exhaust gases for the SCR of NO_x over the carbon catalyst, which is also used for the removal of residual SO_x. A deactivation in the second stage due to small amounts of adsorbed SO_x was not

observed [107]. The fluidized catalyst beds are connected and the flow direction of the bed is opposite to the exhaust gases, in order to transport the catalyst, which was used for the SCR reaction, to the SO_x removal stage as adsorber material. After the SO_x removal step, the carbon catalyst is transferred to a regeneration stage, where SO_x is removed.

The base carbon materials, which were used as precursors for the NO_x reduction catalysts were mainly based on coal [100]. However, other precursor materials were investigated: Szymánski et al. [117], Singoredjo et al. [118], Martin-Martínez et al. [119] and Ahmed et al. [120] for example used commercially available activated carbons. But also carbon fibers of different origin [121-123] and cellophane were tested [124, 125]. Most often, the precursor carbons were first calcined at temperatures between 850°C and 1100°C under inert conditions and then activated with oxygen [100, 125], CO₂ [119, 126], steam, nitric acid (HNO₃) [117] and sulfuric acid (H₂SO₄) [120, 127].

The activity of these modified activated carbons was investigated only with NO in the feed gas. NO₂ in the feed gas was not considered, as NO/NO₂ ratios in exhaust gases of stationary combustion processes are 90:10 to 95:5 [106, 128]. The relevant temperature range was 100-400°C [100, 121]. The gas hourly space velocities (GHSV) were most often below 2000 h⁻¹ [100, 103, 127, 129], which is about a 15-20 times less than for mobile application. Ahmed et al. showed that the NO conversion is strongly dependent on the type of activated carbon catalyst and temperature (Figure 5) [130]. With the catalysts used in the process of the *Bergbau-Forschung* even 80% NO conversion were reached at 100-150°C [107].

The reasons for the different NO conversion rates are manifold and comparison is difficult, as the applied materials differ significantly. However, the main

findings can be summarized as follows: first, the NO conversion strongly depends on the amount of acidic surface functional groups on the carbon surface as they are important for the adsorption of NH_3 [117-120, 129, 131]. Furthermore, it was shown that nitrogen embedded in the carbon structure could increase the activity [100, 121, 132]. The role of the surface area is rather unclear, as some authors observed a dependency of the surface area on the NO conversion rates [110, 129, 133], but others did not [100, 120, 127, 130]. Ahmed et al. could also show that the presence of alkali metals leads to a decreased NO reduction activity [130]. They explained this observation with the increased basicity of the catalyst introduced by the metals that decreased the NH_3 adsorption rate.

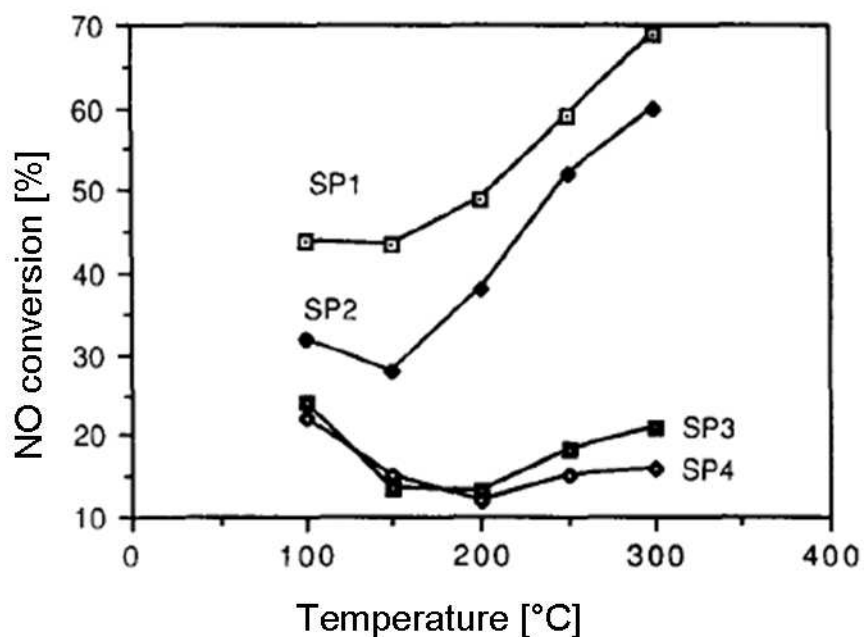


Figure 5: NO conversion rates of four different commercially available activated carbons plotted over temperature taken from [130].

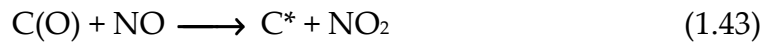
Jüntgen et al., Muníz et al. and Shirahama et al. assumed that the oxidation of NO is a prerequisite step for the SCR reaction on soot in presence of NO [121, 134, 135]:



This assumption is supported by experiments with varying oxygen concentrations, as the SCR activity increases with increasing oxygen concentration [118, 125, 130, 136]. Muníz et al. proposed that the NO oxidation takes place at an oxygen-containing surface functional group consisting of an active carbon C* carrying chemisorbed oxygen (O) [121]:

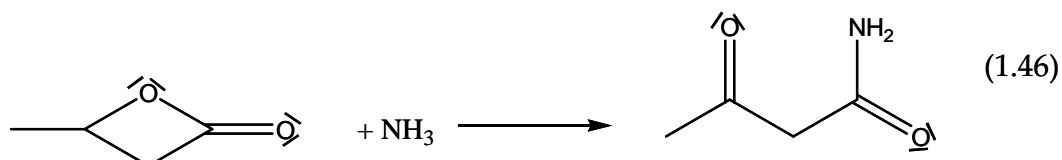
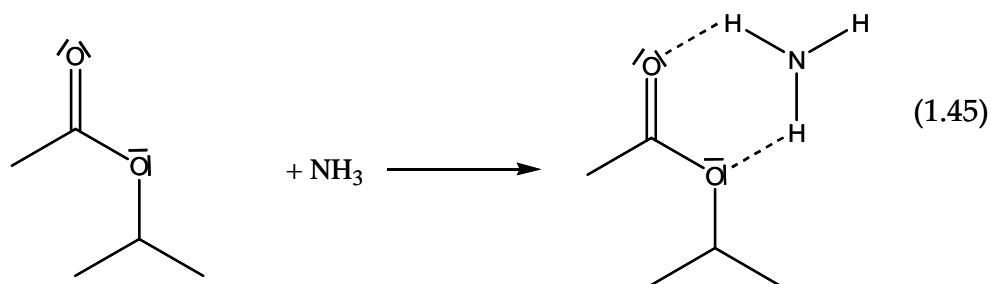


NO adsorbs well on these complexes leading to the formation of NO₂; without oxygen in the feed gas no NO adsorption was observed below 100°C [121]:

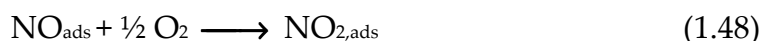


For the adsorption of NH₃ three types of interaction are proposed by Chughtai et al. [137]: first, acid-base interaction (eq. (1.44)), second hydrogen bonds (eq. (1.45)) and third reactive adsorption (eq. (1.46)):

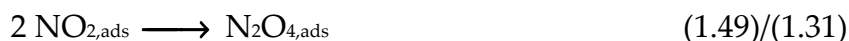




Based on experimental findings, Jüntgen et al. and Richter et al. proposed the following reaction scheme for the NO conversion in the presence of NH_3 below and above 100°C [103, 115]. First, NO adsorbs on the carbon surface, where it is oxidized to NO_2 , which remains on the surface (all species, which remain adsorbed on the surface are labeled ads):

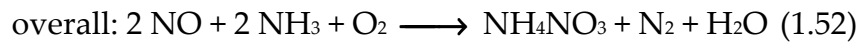


At temperatures between 50°C to 100°C the authors assumed NO_2 to dimerize forming N_2O_4 , as already shown for the SCR reaction on inorganic catalysts (eq. (1.31)):

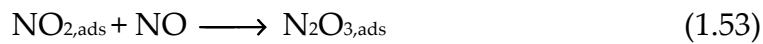


Jüntgen and Richter proposed that N_2O_4 reacts with NH_3 and water, forming NH_4NO_3 and NH_4NO_2 (eq. (1.48)) in that temperature range. The nitrite was

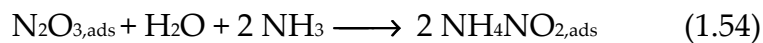
suggested to decompose according to reaction (1.34) into nitrogen and water, while the nitrate remained on the surface as the analysis of the used carbon catalysts by Richter et al. showed [115]. This leads to the formulation of the overall reaction eq. (1.50) for *standard SCR* on carbon catalysts:



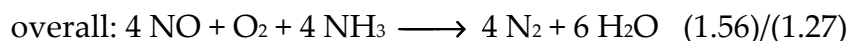
Above 100°C the mechanism was assumed to change since the NO oxidation rate decreases. The authors supposed that only the nitrite and no nitrate was formed because the analysis of the carbon catalyst did not show nitrate [103, 115]. Therefore, a reaction of NO₂ and NO to N₂O₃, the anhydride of nitric acid was assumed, to explain the NO_x removal activity:



N₂O₃ reacts with NH₃ and water to the nitrite, which decomposes as in reaction (1.51)/(1.34) into nitrogen and water:



Based on their results, the authors formulated an overall reaction equation, which is similar to reaction (1.27), showing the 1:1 NO/NH₃ ratio of the *standard SCR* reaction



1.4. Scope of the thesis

For the effective operation of diesel particulate filters exact knowledge of the PM reactivity under realistic conditions and the composition, which has changes significantly due to the reduction of the carbon content, are indispensable. However, the established methods for PM composition analysis have reached their detection limits due to the reduced PM emissions. And the methods for reactivity investigations often do not allow dosing feed gas components like NO₂, H₂O, SO₂ and O₂ due to their corrosivity and condensability. But for realistic reactivity measurements the ability to dose these compounds is important because diesel exhaust gases also contain these components and they are known to influence the activity of PM significantly. The reactivity situation becomes even more complicated as DPF and SCR system have to be applied in series to meet the stricter future emission limits and ideas are forwarded to combine both functions in one aftertreatment device. This will result in the parallel presence of NO_x, NH₃ and PM in one single compartment, where all three compounds would be able to interact with one another. Actually, a reduction of NO_x in the presence of NH₃ in parallel to the soot oxidation was observed over diesel soot in preliminary experiments in our research group at the Paul Scherrer Institute.

In order to investigate the reactivity of diesel soot in more detail and to eliminate the lack of analytical instruments for the composition analysis, a TG-FTIR system for investigations with condensable and corrosive gases should be developed as first part of the thesis. The basis for the system was formed by a standard thermogravimetric analyzer (TGA/DSC 1, Mettler-Toledo) and a FTIR spectrometer (Antaris IGS, Thermo Scientific). Both instruments had to be coupled and adapted to allow for the small flow rates through the system and to avoid condensation on the system walls.

After finishing the TG-FTIR system should be used for the detailed chemical analysis of the composition of different PM samples and moreover detailed reactivity investigations should be performed. The reactivity experiments should consider not only classical model diesel exhaust gases containing O_2 , H_2O and NO_2 , but special attention should be turned on the NO_x reduction activity of diesel in the presence of NH_3 . Therefore, it was intended to identify the occurring reactions and the dependencies of soot origin, temperature, space velocity and feed gas composition. As the final stage of this thesis, the influence of H_2SO_4 on the soot oxidation with NO_2 should be investigated because H_2SO_4 might play an important role during the DPF regeneration in application with fuel containing large amounts of sulfur.

2. Methods and experimental equipment

2.1. Analysis of PM composition and surface reactions

2.1.1. Thermogravimetry coupled with FTIR spectroscopy

For the composition and the reactivity analysis of PM samples and the investigation of the SCR effect over diesel soot thermogravimetry coupled with Fourier-Transform-Infrared spectroscopy (TG-FTIR) was used.

Since these investigations included the use of corrosive and condensable gases a standard TG-FTIR system based on a Mettler-Toledo TGA/DSC 1 thermogravimetric analyzer (TGA) and a Thermo Scientific Antaris IGS FTIR spectrometer was redesigned in order to avoid condensation and damage of the system. The thermogravimetric analyzer was equipped with a furnace/balance combination for investigations of samples up to 5 g with a resolution of 0.1 μg in the temperature range between 25-1100°C. The standard FTIR spectrometer had a gas measuring cell with a path length of 2 m at a volume of 240 mL. The calibration was done with the Quant Pad software provided by Thermo Scientific. The classical least square (CLS) algorithm, which is used in the software, allows the consideration of non-linearities and the interference of different gas compounds. In section 3 a detailed description of the changes and the improvements of the system are given since the setup and development of this system was a main part of this work.

In general, for TG-FTIR analyses the samples were placed on a precise balance. Then they were heated up with a controlled heating ramp or kept at a constant temperature in a flow of inert or reactive gas. A mass loss due to desorption of sample compounds or a mass increase due to adsorption of gas molecules on the surface was followed by recording the balance signal. For the correction of

lift effects due to heating, a blank curve had to be collected, which was subtracted from the measuring curve. The inert or reactive gas flow transferred the gasified sample compounds to the spectrometer, where they were quantified.

2.1.2. Hydrocarbon analysis

The HC concentration of PM samples was selectively estimated during their composition analysis in the TG-FTIR using a flame ionization detector (FID), which was installed downstream of FTIR spectrometer.

By the temperature increase during the thermolysis the HC desorbed into the gas phase and were transferred to the FID. In the FID the HC were totally oxidized over several steps in a small hydrogen flame burning in air. During one of the oxidation steps the carbon-hydrogen bonds were cleaved, while carbon cations are formed. By applying a small electric field to the flame, these cations produced an ion current, which was proportional to the amount of carbon atoms in the analyzed compounds. The proportionality was quantified by a calibration, which had to be done before and after each measurement to keep the precision of the system.

The analytical device allowed the estimation of the carbon content of every gaseous substance, which contains carbon-hydrogen bonds or weaker carbon bonds (related to the bonds strength). Although the FID is most probably the most precise HC gas phase analysis tool it has the disadvantage that only the total amount of carbon in the HC compounds is quantified, but a qualitative analysis is impossible.

2.1.3. Tubular quartz reactor for the investigation of the SCR effect over diesel soot and the influence of H_2SO_4 on the soot oxidation with NO_2

The investigation of the oxidation behavior of soot (Printex U) in the presence of NO_2 and $\text{SO}_3/\text{H}_2\text{SO}_4$ and the SCR tests over diesel soot were performed in a heated tubular quartz reactor. The flow charts of the experimental setups for these investigations are shown in Figure 6 (H_2SO_4 influence) and Figure 7 (SCR over diesel soot).

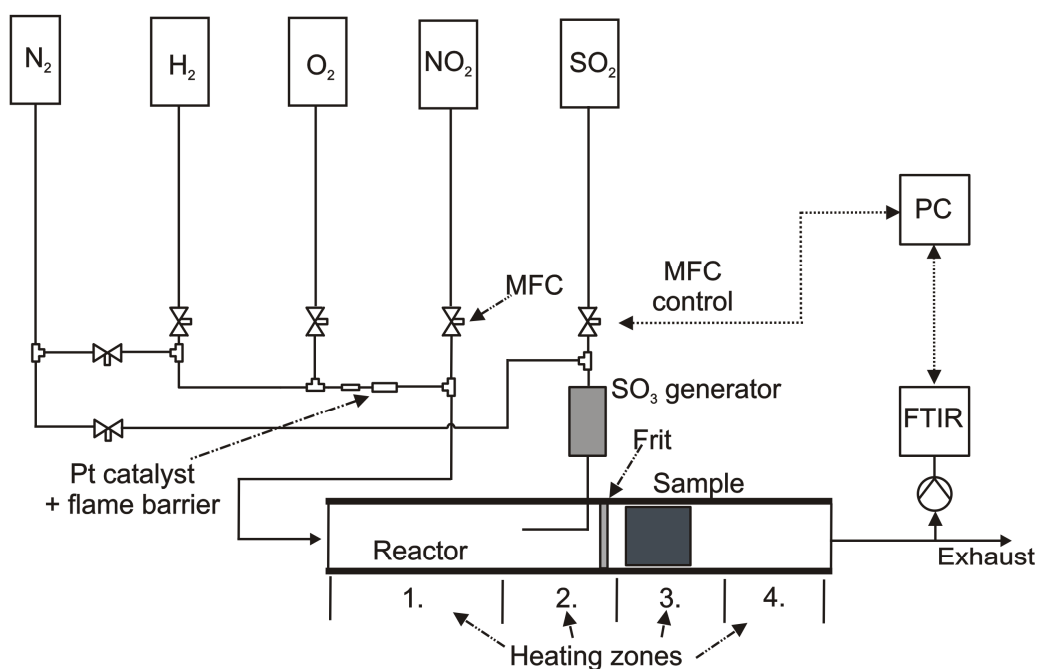


Figure 6: Flow chart of the experimental setup for the investigation of the influence of H_2SO_4 on the soot oxidation with NO_2 . The dotted lines symbolize the communication connections of the FTIR spectrometer and the MFCs with the PC.

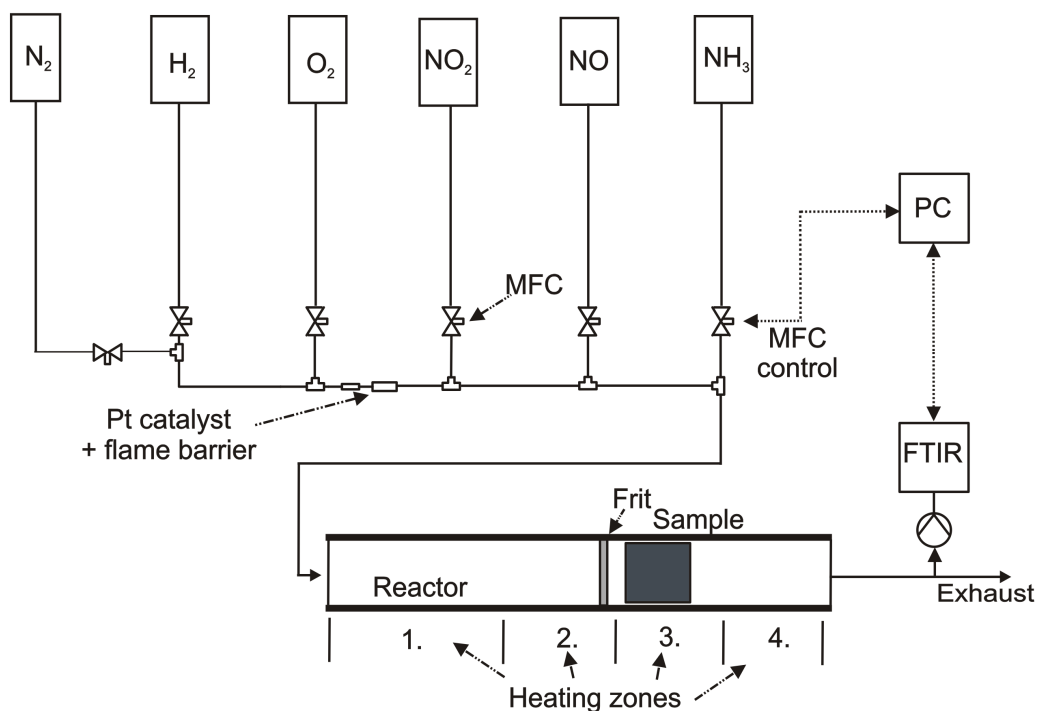


Figure 7: Flow chart of the experimental setup for the investigation of the SCR effect on diesel soot. The dotted lines symbolize the communication connections of the FTIR spectrometer and the MFCs with the PC.

For both experiments the same reactor, which had a length of 650 mm and an inner diameter of 49 mm, was used. After the gases entered the reactor, they were temperature-controlled in the pre-heating zone (1. heating zone), which was filled with ceramic beads. Then the gases reached the second heating zone, which was also filled with ceramic beads for effective heat transfer. This zone controlled the region around the inlet of the SO_3 generator, which was used for the investigation of the oxidation behavior of soot in the presence H_2SO_4 . For the measurements of the SCR effect over diesel soot the SO_3 generator was removed and the SO_3 inlet was closed with a blind plug. After passing the frit, the gases entered the reaction zone, where the sample holder was placed. The last heating zone controlled the reactor outlet downstream of the sample, where a part of the product gas flow was extracted continuously for gas analysis.

The soot samples were brought into the tubular quartz reactor coated on cordierite monoliths (400 cpsi) (for preparation see section 2.2.1). The loaded monoliths were placed in a sample holder that allowed the reproducible positioning of the samples in the reactor. The gap between the sample holder and the reactor walls was sealed with a ceramic fiber mat to avoid any bypass.

The gases were provided by a gas mixing unit consisting of five mass flow controllers (Brooks 5850S) for the investigation of the influence of H_2SO_4 on the soot oxidation in the presence of NO_2 and six mass flow controllers for the investigation of the SCR effect over diesel soot. Water was generated by controlled hydrogen oxidation over a Pt catalyst (2% Pt on SiO_2).

SO_3 , which was needed for the H_2SO_4 experiments, was generated by oxidation of SO_2 over a second Pt catalyst (2% Pt on SiO_2) in a bypass stream of 15% of the total flow (Figure 6). Since the SO_2 conversion rates on the catalyst did not exceed 60-70%, SO_2 always had to be dosed in excess. After entering the main gas stream, which contained water, H_2SO_4 was formed in equilibrium with SO_3 in dependence on water partial pressure and temperature.

The base feed gas, which was used for all experiments, consisted of 10% oxygen and 5% water with nitrogen as balance. The total flow was 550 L/h at STP for the investigation of soot oxidation in the presence of H_2SO_4 and NO_2 . The flow through the SO_3 generator was 90 L/h at STP of the total flow. For the investigation of the SCR effect over diesel soot the total flows were 550 L/h or 275 L/h at STP, respectively, depending on the desired space velocity.

The gas tubes downstream of the tubular reactor were prepared from quartz glass to avoid sulfur poisoning. All tubes downstream of the gas mixing unit as well as the FTIR gas measuring cell were heated to 180°C to avoid condensation by trace heating.

The gas composition was analyzed quantitatively downstream of the quartz reactor using a Nicolet Nexus 600 FTIR spectrometer with a nitrogen-cooled MCT detector and a gas measuring cell of 2 m path length and ZnSe windows. Each spectrum was the average of 8 scans at a resolution of 0.5 cm⁻¹.

The spectrometer was already calibrated for the gas components listed in Table 4, except for HONO, SO₂ and H₂SO₄. HONO was not calibrated before the investigation of the SCR on diesel soot in Chapter 6; therefore it was not available for the investigation of the H₂SO₄ influence on soot oxidation with NO₂.

Table 4: Calibrated components and their detection limits of the Nicolet Nexus FTIR spectrometer. The detections limits of HNO₃ and HNO₂ in this table are only valid in the absence of NH₃. HNO₂ was calibrated for the investigation of the SCR reaction over diesel soot, but was not available for the investigation of the H₂SO₄ influence on soot oxidation with NO₂.

Component		Detection limits [ppm]
Carbon dioxide	CO ₂	0.5
Carbon monoxide	CO	0.2
Nitric oxide	NO	1
Nitrogen dioxide	NO ₂	1
Ammonia	NH ₃	0.2
Nitrous oxide	N ₂ O	0.1
Hydrogen cyanide	HCN	0.2
Isocyanic acid	HNCO	0.2
Formic acid	HCOOH	0.2
Nitric acid	HNO ₃	0.5
Nitrous acid	HONO	0.5
Formaldehyde	H ₂ CO	1
Sulfur dioxide	SO ₂	1
Sulfuric acid	H ₂ SO ₄	1

For the data analysis it has to be taken into account that HNO₃ and even more pronounced HONO showed cross-sensitivities to NH₃, which could not be removed by the software. Therefore, the results for HNO₃ had to be analyzed

carefully and in the case of HONO it was only possible to analyze spectra in the absence of NH_3 since the HONO signal showed a baseline shift in addition.

SO_2 was calibrated in a standard procedure by using a calibration gas from a gas bottle. The calibration of H_2SO_4 was more difficult, because first a qualitative reference spectrum of H_2SO_4 had to be collected and in a second step the quantification method of the spectrometer had to be calibrated with a nitrogen-based model gas containing 10% O_2 + 5% H_2O + 2, 6 and 10 ppm H_2SO_4 .

For recording the reference spectrum of H_2SO_4 a dry nitrogen flow was saturated in a temperature-controlled wash-bottle containing conc. H_2SO_4 solution. As the spectrum showed absorption bands of both, SO_3 and H_2SO_4 , the region between 1200-1260 cm^{-1} showing only specific bands of H_2SO_4 [138] was used as reference for the further calibration.

The quantification of the reference spectrum was performed in the presence of O_2 and H_2O by dosing different SO_2 concentrations over a Pt catalyst. The generated amounts of H_2SO_4 were analyzed with a modified wet chemical analysis method described in the VDI guide line 2462 [139-141] (wet chemical analysis procedure: see section 2.1.4). As the $\text{H}_2\text{SO}_4/\text{SO}_3$ equilibrium is completely on the side of H_2SO_4 in the presence of 5% H_2O at 180°C in the gas measuring cell, a calibration of SO_3 was unnecessary. Contrary, under reaction conditions H_2SO_4 and SO_3 may be present in equilibrium, which should be kept in mind. However, in the following only H_2SO_4 will be used instead of $\text{SO}_3/\text{H}_2\text{SO}_4$.

2.1.4. Wet chemical analysis for the estimation of the SO₃/H₂SO₄ and SO₂ content

The wet chemical analysis based on the VDI guide line 2462 was developed for the parallel quantification of SO₂ and SO₃/H₂SO₄ in the exhaust gases of combustion processes. Since SO₃ and H₂SO₄ form a temperature and water partial pressure dependent equilibrium, which moves to H₂SO₄ with decreasing temperature and increasing water partial pressure, it was not possible to distinguish between these two species.

The gas sampling was performed with a glass probe, in which an aqueous absorption solution is pumped. The hot gases were quenched, while SO₃ reacted with water also to H₂SO₄. After the probe the gas/liquid mixture was cooled to 50°C in a water cooled Teflon capillary. Then IPA was added and the mixture is pumped in a frit apparatus, where H₂SO₄ was edulcorated with high efficiency. The IPA, which is a light reductant, avoided oxidation of SO₂ to H₂SO₄. The absorption solution was collected in a flask downstream of the frits. SO₂ hardly absorbed in the solution and was collected in an additional wash bottle containing hydrogen peroxide, where it is oxidized to H₂SO₄. The feed gas was pumped into a gas meter via an empty wash bottle in order to estimate the sampling volume. The method worked discontinuously meaning that a defined gas volume was extracted over a certain time (usually 30 L at STP) and the SO₂ and SO₃ were collected in the absorption solutions.

At the end of a collection period the glass probe is purged with 2 mL water and the frit apparatus with 25 mL IPA. H₂SO₄ in the IPA solution is titrated with a 0.01 M BaCl₂ solution with thordin as indicator. Subsequent to the SO₃/H₂SO₄ estimation, the traces of absorbed SO₂ in the IPA solution are estimated by oxidation with a small amount of hydrogen peroxide and titrated again with BaCl₂. The detection limit for SO₃/H₂SO₄ was 0.3 ppm.

SO₂ in the wash bottle was first oxidized to H₂SO₄ with hydrogen peroxide and titrated with 0.1 M NaOH with bromophenol blue as indicator if the concentrations were >100 ppm. For smaller concentrations the hydrogen peroxide solution was diluted to 50 ml. Then 20 mL of this solution were further diluted with 80 mL of IPA and titrated with 0.01 M BaCl₂ solution with thorin as indicator. The detection limit for SO₂ was 2 ppm.

After the calibration procedure, the agreement of the FTIR measurements with the wet chemical analysis and the conversion rates of the Pt catalyst were estimated. Moreover, the stability of the SO₂ dosage was checked.

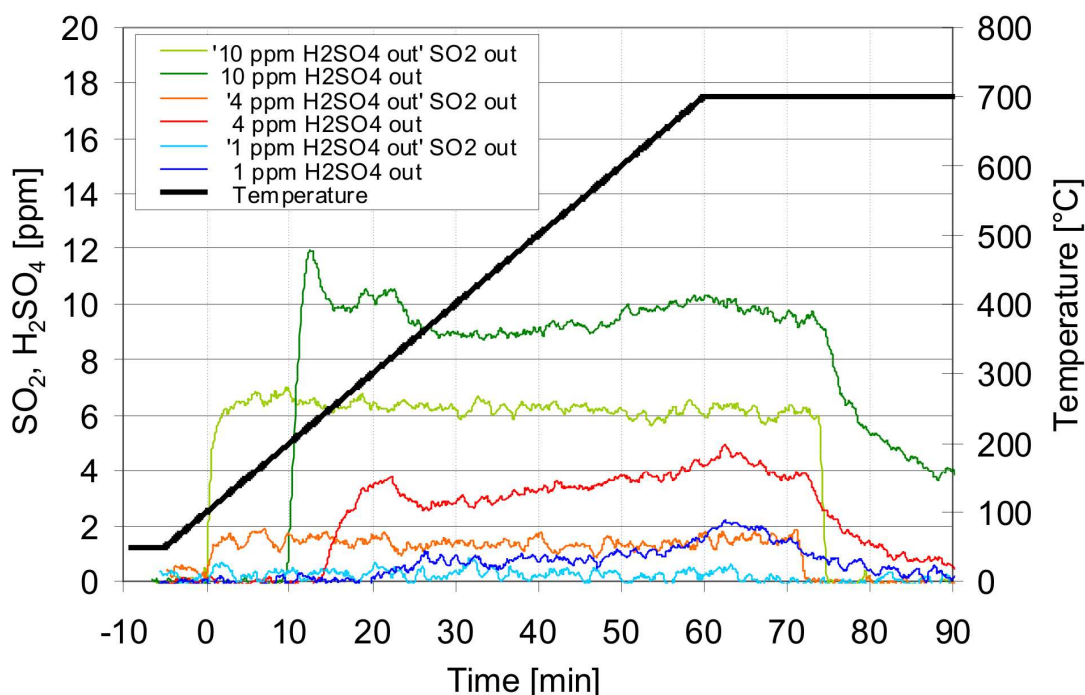


Figure 8: Outlet concentrations of SO₂ and H₂SO₄ in blank experiments without monolith between 50°C and 700°C measured with the FTIR spectrometer. Due to the SO₂ conversion of only 60-70% on the Pt catalyst it had to be added in excess. The time was set to zero, when the SO₂ addition started.

Figure 8 shows the outlet concentrations of SO₂ and H₂SO₄ during blank experiments, in which 1.5, 6 and 18 ppm SO₂ were dosed over 68 min measured

with the FTIR spectrometer. From these measurements the conversion rates of the Pt catalyst were estimated and the long-term stability of the SO₂ dosage was confirmed. Due to the smaller adsorption probability of SO₂ its concentration was slightly more stable than that of H₂SO₄.

After the start of the SO₂ dosage at 100°C the SO₂ concentration rose immediately for the SO₂ inlet concentrations of 6 and 18 ppm, but in the case 1.5 ppm SO₂ inlet concentration hardly any SO₂ was measured over the whole experiment. The mean SO₂ outlet concentrations were ca. 6 ppm at 18 ppm SO₂ inlet concentration and ca. 1.8 ppm at 6 ppm SO₂ inlet concentration.

The break-through of H₂SO₄ was delayed in dependence on the SO₂ inlet concentration due to the adsorption of H₂SO₄ on the Pt catalyst and the walls of the quartz reactor. The H₂SO₄ increased slightly with temperature due to desorption of H₂SO₄, which adsorbed on the walls at lower temperatures. The mean H₂SO₄ outlet concentrations were ca. 10 ppm at 18 ppm SO₂ inlet concentration, ca. 4 ppm at 6 ppm SO₂ inlet concentration and less than 1 ppm for 1.5 ppm SO₂ inlet concentration.

Based on these results, the conversion rates were estimated to 60-70%. The experiments showed that the SO₂ dosage and conversion were stable enough to allow reproducible measurements over the whole temperature range.

After that, the agreement of the FTIR spectrometer results and the results of the wet chemical analysis were examined with three experiments, in which 1, 4 and 10 ppm H₂SO₄ were dosed over Printex U (correspondingly, SO₂ had to be dosed in excess). Figure 9 shows the results of these measurements. The H₂SO₄ concentration measured by FTIR spectrometer and the discontinuous titration between 50°C and 700°C are plotted over the reaction time and referred to the temperature. In difference to the rest of the experiments during this study, the

soot was loaded on ceramic fiber mats, which were stacked with corrugated metal sheets as distance holder. This preparation method was used at the beginning of the study before the soot loading on monoliths was developed. Due to the complex titration procedure this experiment was not repeated with soot loaded on monoliths.

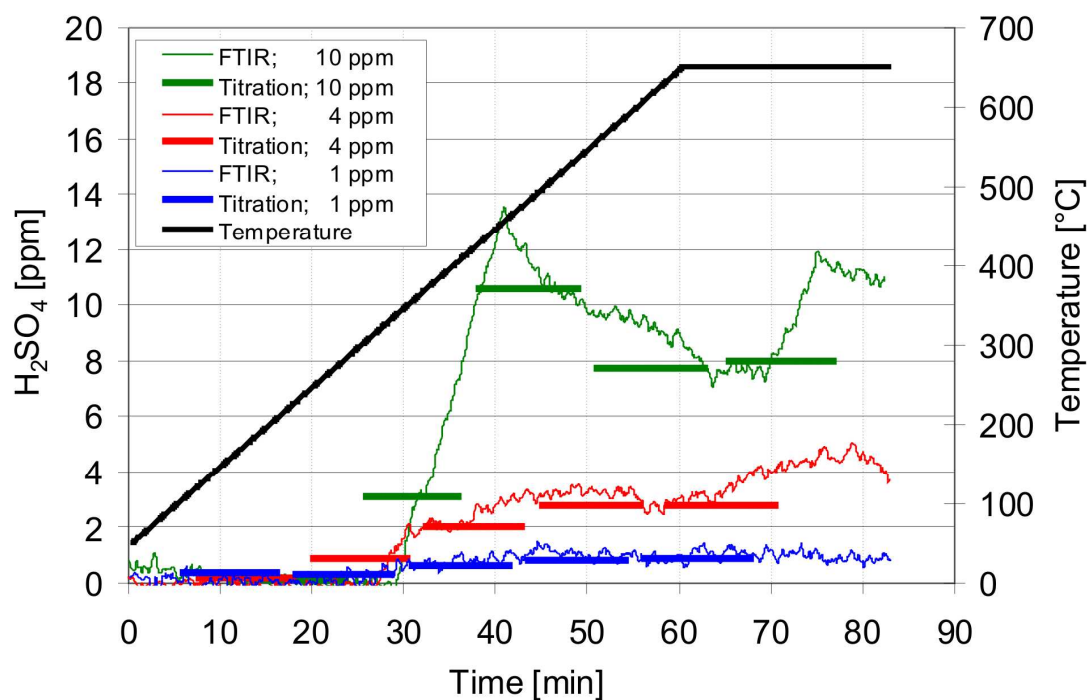


Figure 9: Comparison of the H_2SO_4 analysis by FTIR spectroscopy and titration during a soot oxidation experiment with Printex U. Reactive gas composition: 200 ppm NO_2 + 10% O_2 + 5% H_2O + 2, 10 and 18 ppm SO_2 . In comparison to the other measurements the soot was loaded on ceramic fiber mats in loose contact.

The agreement between both analysis methods was very good for all experiments. In comparison to the measurements shown in Figure 8 the break-through of H_2SO_4 was delayed and independent of the SO_2 inlet concentration due to adsorption on the soot. At 480°C the H_2SO_4 concentration dropped due to direct oxidation of soot and the formation of SO_2 . The decrease was very pronounced for 10 ppm H_2SO_4 , less pronounced for 6 ppm and undetectable for 1 ppm H_2SO_4 .

2.2. Investigated PM samples

In this work real diesel PM samples collected from engine test benches, commercially available synthetic PM samples and samples produced individually in the laboratory were analyzed. The real PM samples were either provided as powders or collected on metal and quartz fiber filters. They were donated by Volkswagen (VW), MAN, Daimler and the RWTH Aachen (Lehrstuhl für Verbrennungskraftmaschinen VKA) and are listed in Table 5. The commercially available PM samples were powders and provided by Evonik and the TU München (Institute of Water Chemistry and Chemical Balneology). The individually generated GfG soot sample was a powder and generated by the Institute of Water Chemistry and Chemical Balneology at the TU München in a soot generator (GfG 1000, Palas GmbH, Karlsruhe) by spark-discharging. The use of the spark-discharger allows the production of large amounts of soot in reproducible quality, which was already used in several studies [16, 67].

From the large number of samples investigated during this work 16 representative samples shown in Table 5 were selected for presenting the results. The samples summarized in Table 5 were used for the composition and reactivity analysis in the TG-FTIR system as well as for the investigation of the influence of H_2SO_4 on the soot oxidation with NO_2 and the SCR effect on soot in the tubular reactor.

A large part of the SCR on soot experiments and of the investigation of the H_2SO_4 influence on the soot oxidation with NO_2 was performed with Printex U since it was available in sufficient amounts, with a reproducible composition and was well characterized in many studies as model substance for diesel soot [40, 62, 142]. The diesel soot samples were available only in small amounts and, therefore, only a limited number of experiments could be performed.

Table 5: Soot samples for the composition and reactivity measurements in the TG-FTIR system, the investigation of the influence of H₂SO₄ on the soot oxidation with NO₂ and the SCR effect on soot in the tubular reactor. In the “project” column the type of investigation is listed, for which the samples were used. 1: composition analysis; 2: reactivity analysis; 3: SCR over diesel soot; 4: influence of H₂SO₄ on the soot oxidation with NO₂.

Sample name	Type	Origin	Provider	Project
VW Sample 1	powder	classic car	VW	1
VW Sample 2	powder	modern car	VW	1, 2
VW Sample 3	powder	classic heavy duty vehicle	VW	1
VW Sample 4	powder	modern heavy duty vehicle	VW	1
Printex U	powder	synthetic gas soot	Evonik; comm. avail.	1, 2, 3, 4
Euro 0	powder	Euro 0 diesel engine	MAN	1, 2, 4
Euro V	powder	EuroV diesel engine	MAN	1, 2, 4
mixed soot	powder	test bench separator	MAN	1, 2, 4
GfG	powder	graphite spark generator	TU München	1, 2
graphite	powder	synthetic	TU München / Fluka	1, 2
A1	metal filter	modern diesel engine	RWTH Aachen	1, 2
A2	metal filter	modern diesel engine	RWTH Aachen	1, 2
B1	metal filter	modern diesel engine	RWTH Aachen	1, 2
B2	metal filter	modern diesel engine	RWTH Aachen	1, 2
C1	metal filter	modern diesel engine	RWTH Aachen	1, 2
C2	metal filter	modern diesel engine	RWTH Aachen	1, 2

2.2.1. PM samples on cordierite

The PM samples for the investigations in the tubular quartz reactor were loaded with soot by dip coating into a dispersion of soot and isopropyl alcohol (IPA). Subsequently to the dipping, the solvent was removed first with an airblower for 2 min and after that dried at 85°C for 4 h in a cabinet dryer.

For the investigations of the influence of H₂SO₄ on the soot oxidation and the SCR effect over diesel soot a part of the loaded monoliths was impregnated with 1 (±10%), 2 (±10%), 5 (±10%) and 10 (±10%) mg H₂SO₄. The impregnation was performed by dipping the monoliths one time into H₂SO₄ solutions of different concentrations and subsequent drying at RT. The demanded concentrations of these solutions were calculated from the water absorption

capacity of a monolith during one-time dipping. For the monoliths used in this work, the maximum water absorption capacity was 1.7 mL leading to the H_2SO_4 concentrations shown in Table 6.

Table 6: H_2SO_4 concentration of the H_2SO_4 solutions used for the impregnation of the soot-loaded monoliths.

H_2SO_4 concentration in precursor solution	H_2SO_4 on monolith
[mol/L]	[mg]
0.060	10
0.030	5
0.010	2
0.006	1

Monoliths of different sizes were prepared in order to vary the space velocities independently on the variation of the total flow, which could be set to 275 L/h or 550 L/h at STP. By variation of both, the total flow and the monoliths size, gas hourly space velocities (GHSV) of 3000 h^{-1} , 9000 h^{-1} , 17000 h^{-1} , 35000 h^{-1} and 70000 h^{-1} were realized. Since 35000 h^{-1} is a realistic space velocity for mobile application it was defined as the standard GHSV for the studies and used for the presented experiments if not mentioned differently.

As already mentioned, the loaded monoliths were placed in a sample holder that allowed the reproducible positioning of the samples in the reactor. Since the diameter of the monolith for the investigation of 3000 h^{-1} was too large in volume it was placed without the sample holder in the reactor. In any case the gap between the samples and the reactor wall was sealed with a ceramic fiber tape to avoid a bypass. Table 7 shows the monolith dimensions, the total flows and the mean soot loading of the cordierites for different space velocities.

Table 7: Monolith dimensions, total gas flows and mean loading for different space velocities. The monoliths were cuboids except the one for 3000 h⁻¹, which had a cylindrical shape.

	GHSV [h⁻¹]	Length [mm]	Height [mm]	Width [mm]	Mean soot loading [mg]	Total flow [L/h] at STP
1	3000	56	45 (Ø)		330	275
2	9000	44	26.5	26.5	120	275
3	17,000	22	26.5	26.5	60	275
4	17,000	44	26.5	26.5	120	550
5	35,000	22	26.5	26.5	60	550
6	70,000	11	26.5	26.5	30	550

2.3. Additional characterization techniques

2.3.1. BET measurements

The surface areas of the PM samples, which were used for the analysis of the SCR effect on diesel soot were, measured by BET analysis in order to clarify if the surface area influences the NO_x reduction. The nitrogen adsorption isotherms of Printex U, the Euro 0 sample, the Euro V sample and the mixed soot sample were analyzed with a Quantachrome Autosorb 1-c. The samples were outgassed over night at 300°C. The BET plot between 0.05 and 0.3 p/p₀ was used to estimate the surface areas.

2.3.2. ICP-OES measurements

The metal contents of Printex U, the Euro 0 sample, the Euro V sample and the mixed soot were analyzed by ICP-OES (Inductively Coupled Plasma – Atomic Emission Spectroscopy).

Since the metals have to be dissolved in a liquid for these measurements the PM samples had to be digested. For that purpose, 7-17 mg of the samples were first

dispersed in 4 mL conc. nitric acid (HNO_3) and 1 mL H_2O_2 . Then they were heated up to 130-160°C over 50 min in a microwave furnace (Multiwave 3000, Anton Paar) with 300 W. The maximum pressure was set to 50 bar. This first treatment was applied to remove the carbon framework. In a second step, 10 mL conc. hydrochloric acid (HCl) were added. The solution was then treated again in the same way as in the first step. This time the metal compounds were dissolved completely. A direct treatment with aqua regia failed to dissolve the metals most probably due to a passivation of the surfaces.

2.3.3. Transmission electron microscopy

The structures of Printex U and the Euro V soot sample were investigated with a transmission electron microscope. The measurements were performed to proof the structural similarity of Printex U as model soot and the Euro V sample as a real diesel PM sample.

2.3.4. DRIFTS measurements

The formation of surface functional groups due to the adsorption of NO_2 and NH_3 in the presence of water and oxygen on Printex U was examined with Diffuse Reflectance Infrared Fourier-transform Spectroscopy (DRIFTS). During DRIFTS measurements the infrared (IR) beam is directed on the powder sample. There, it penetrates the sample and is diffusively reflected at the powder particles. While the IR radiation is reflected in the sample it interacts with surface functional groups leading to absorption of radiation. The diffusive reflected beam contains information about vibration and rotation states similar

to those generated during gas phase measurements, however, with a significantly reduced intensity.

The measurements were performed with a Thermo Scientific Nexus 600 FTIR spectrometer in a Thermo Scientific DRIFTS cell. The cell is heatable and equipped with ZnSe windows.

2.4. Data Evaluation

2.4.1. Carbon oxidation rate

The carbon oxidation rate (C-oxidation rate) was used to quantify the amount of carbon, which desorbs from a soot sample by decomposition of surface functional groups formed at the time t .

It is defined as the ratio of the carbon amount in the gas phase at time t ($C_{gas,t}$) in [μg] calculated from the CO, CO₂, HNCO and HCN concentration in the gas phase detected in the FTIR spectrum at time t , and the carbon amount at the time t ($C_{solid,t}$) in [mg] remaining in the solid phase referred to the period of time needed for the collection of a FTIR spectrum $t_{collect}$ in [s]:

$$C\text{-oxidation rate} \left[\frac{\mu\text{g}}{\text{mg} \cdot \text{s}} \right] = \frac{C_{gas,t}}{C_{solid,t}} \cdot \frac{1}{t_{collect}} \quad (2.1)$$

$C_{solid,t}$ was calculated from the total carbon amount at the beginning of the measurements $C_{solid,0}$ minus the sum of carbon desorbed up to time t . This way of calculating the C-oxidation rate is similar to a normalization of the data, which allows comparing the results of different reactive gases and samples of different size.

2.4.2. NO_x reduction

The NO_x reduction describes the activity of the soot samples to reduce NO_x in the feed gas during the SCR reaction:

$$NO_x \text{reduction} [\%] = \frac{NO_{x,in} - NO_{x,out}}{NO_{x,in}} \cdot 100 \quad (2.2)$$

$NO_{x,in}$ represents the NO_x inlet concentration in the feed gas in [ppm] and $NO_{x,out}$ represents the measured NO_x outlet concentration in [ppm].

2.4.3. NO₂ and NH₃ conversion

The NO₂ conversion measured over a soot samples is the sum of NO₂ converted during the SCR reaction (to N₂) and during the soot oxidation (to NO):

$$NO_2 \text{conversion} [\%] = 100 - \frac{NO_{2,out}}{NO_{2,in}} \cdot 100 \quad (2.3)$$

The NH₃ conversion U_{NH_3} measured over a soot samples describes the amount of NH₃ converted during the SCR reaction:

$$U_{NH_3} [\%] = 100 - \frac{NH_{3,out}}{NH_{3,in}} \cdot 100 \quad (2.4)$$

2.4.4. Stoichiometric ratio

During the SCR reaction NH₃ and NO_x react with each other. Based on the converted amounts of NH₃ and NO_x estimated from their concentration

differences in the feed gas inlet and outlet an experimental stoichiometric ratio A of the SCR reaction can be calculated:

$$A = \frac{NH_{3,in} - NH_{3,out}}{NO_{x,in} - NO_{x,out}}, \quad (2.5)$$

$NH_{3,in}$ represented the NH_3 inlet concentration in the feed gas in [ppm] and $NH_{3,out}$ is the sum of the measured NH_3 , HCN and HNCO outlet concentrations, as HCN and HNCO were formed almost exclusively from the reaction of NH_3 with soot. From the comparison of the experimental stoichiometry with the stoichiometry of the SCR reaction equations (1.27)-(1.29), conclusions on the proceeding reactions can be drawn.

2.4.5. Mass flow calculated from the gravimetric and gas phase analysis

From the mass loss curve of the TG apparatus the mass flow in [ng/s] can be calculated, which is a measure of the mass desorbing from the sample into the gas phase:

$$\text{mass flow TGA} \left[\frac{ng}{s} \right] = \frac{m_{solid,t} - m_{solid,t+t_{collect}}}{t_{collect}} \cdot 10^6 \quad (2.6)$$

Here, $m_{solid,t}$ is the mass remaining in the TG furnace at the time t in [mg] and $m_{solid,t+1}$ is the mass remaining in the TG furnace at the time $t + t_{collect}$ in [mg], again referred to the period of time needed for the collection of a FTIR spectrum $t_{collect}$ in [s]. The mass flow can also be calculated from the FTIR data:

$$\text{mass flow FTIR} \left[\frac{\text{ng}}{\text{s}} \right] = \frac{m_{\text{gas},\text{total},t}}{t_{\text{collect}}} \cdot 10^6 \quad (2.7)$$

Here, $m_{\text{gas},\text{total},t}$ is the sum of the masses of the gas components, which were detected in one FTIR spectrum at the time t in [mg], referred to the t_{collect} .

2.4.6. Gas hourly space velocity

The gas hourly space velocity (GHSV) is a measure for the amount of gas, which passes the catalyst per unit of time. It is defined as the ratio gas volume per unit of time \dot{V}_{gas} in [mL/min] or [L/h] and the volume of the catalyst V_{catalyst} in [ml] or [L]:

$$\text{GHSV} \left[\text{h}^{-1} \right] = \frac{\dot{V}_{\text{gas}}}{V_{\text{catalyst}}} \quad (2.8)$$

2.4.7. Estimation of the onset temperature of a PM mass loss in TG-FTIR experiments

The start temperature of a mass loss due to desorption or oxidation of PM components is named “onset temperature”. The onset temperature is estimated from the mass loss curve plotted over temperature of the thermogravimetric experiment by placing two tangents to the curve as shown in Figure 10. The temperature at the intersection of the tangents is the onset temperature.

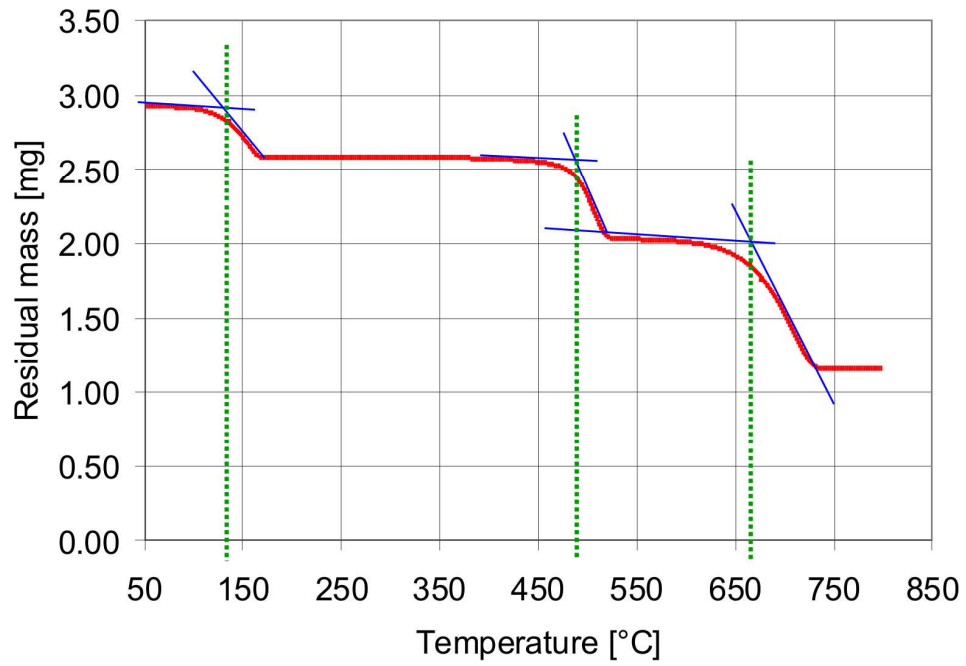


Figure 10: Placing the tangents to the mass loss curve for the estimation of the onset temperature.

3. Development of the TG-FTIR instrument

3.1. Introduction

As part of this thesis, a TG-FTIR system was built for the deeper investigation of composition, reactivity and other surface reactions of PM with wet and corrosive gases under realistic conditions.

Thermogravimetry (TG) is an established technique for the characterization of materials and substances by monitoring the mass change of samples in a flow of inert gas or due to adsorption, desorption and reaction in reactive gases. In standard TG systems, however, the choice of the reactive gas is restricted because balance and furnace housing are temperature controlled to 22-25°C to keep the precision and stability of the mass signal. Gas mixtures or components with dew points around RT cannot be used since they may condensate on the walls of the system and cause corrosion. Therefore, several parts of the standard TG apparatus had to be redesigned and all gas tubes had to be heated.

As already mentioned in the chapter 1, the full potential of thermogravimetry with reactive gases can only be tapped, when the evolved gases are analyzed besides the monitoring of the mass change. For the gas analysis downstream of a TG apparatus, either a MS [143-146] or a FTIR spectrometer [146-152] could be used. The advantage of a MS is the possibility to detect infrared-inactive components like O₂ and N₂ as well as characteristic fragments of larger molecules. However, the signal stability is relatively low and therefore the calibration has to be checked and repeated very often in order to obtain meaningful results. In comparison, FTIR spectroscopy excels by an outstanding long-term stability of the analysis signal and additionally a more robust hardware.

Although, O₂ and N₂ are infrared-inactive, FTIR spectroscopy was preferred for this work, since signal stability and robustness were the most important selection criteria. For the measurements the standard gas measuring cell of the FTIR spectrometer had to be exchanged because of the small flow rates through the system in order to increase the gas exchange rates and to prevent peak broadening.

3.2. Changes of the thermogravimetric analyzer

As the basis for the TG-FTIR system the thermogravimetric analyzer TGA/DSC1 from Mettler-Toledo was chosen. The dew points of the reactive gases used in this standard apparatus have to be significantly below RT since the gas enters and leaves the TGA through flanges which are in contact with the temperature-controlled balance and furnace housing at 25°C. Therefore, mixtures of H₂O, NH₃ and NO₂ for PM investigation under realistic conditions could not be dosed. In order to overcome this problem, the inlet and outlet flanges, where the gases enter and leave the furnace, were replaced by redesigned flanges with trace-heated gas tubes. In Figure 11 a mechanical drawing of the TG shows a cut through the systems, where the changes of the system are marked in red.

The main parts of the TG analyzer are the furnace **1** and the balance **2**. The new reactive gas inlet flange was made from stainless steel and consists of four parts: the back part of the flange **3**, a purge gas inlet **4**, the resistance wire-heated gas tube **5** (stainless steel; $\varnothing = 2 \times 1.5$ mm) and the front part of the inlet flange **6**. (A detailed description of the flange setup will be given in the next section.) The inlet tube for the reactive gases is heated up to the ceramic disk **8**. The disk minimizes the back flow of reactive gas to the front side of the inlet flange, where it might condensate. **7** is the furnace flange, which connects the

balance and the inlet flange. For placing a sample on the sample holder 9 the furnace 2 is moved electrically to the right.

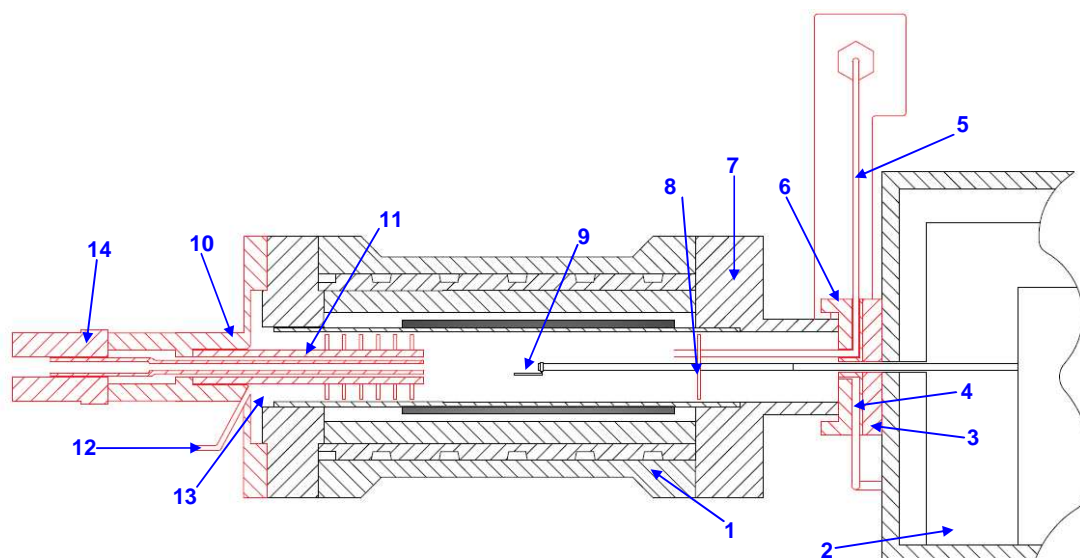


Figure 11: Cut through the redesigned TGA. The changed parts are marked in red. Black indicates original parts.

1: TGA furnace; 2: balance; 3: back part of the new inlet flange; 4: purge gas inlet for prevention of condensation at the front wall of the inlet flange; 5: resistance wire-heated gas tube 6: front part of the new inlet flange; 7: right furnace flange; 8: ceramic disk to avoid backflow of reactive gas; 9: sample holder; 10: left furnace flange; 11: heated quartz glass gas outlet in ceramic tube with disk to avoid backflow and condensation; 12: purge gas inlet for the prevention of condensation in the gas outlet and the left furnace flange; 13: cavity; 14: connection to the transfer line between TGA and FTIR spectrometer.

The gases, which desorb from the sample leave the furnace through the left furnace flange **10**. In a ceramic tube a resistance-heated quartz glass capillary **11** was placed and additionally the purge gas inlet **12** for the dosage of 5 mL/min nitrogen at STP with a mass flow controller (MFC) (Brooks 5850S) was installed. By these measures and the ceramic disk on the ceramic tube any condensation in the design-caused cavity **13** was avoided. The resistance wires (Block) for the heating of the in- and outlet tubes have a diameter of 0.3 mm and a resistance of 6.93 Ω /m. Although, the wire surface is oxidized for electrical isolation an

additional Teflon tube was put over the wires in order to avoid an electrical flashover due to a damaged oxide layer. The electric supply is assured by a linear power supply (Votcraft VLP 2403).

The feed through for the electric connections to the heating wire were sealed with silicone glue. The TGA outlet was connected to the gas transfer line of the FTIR spectrometer by a glass-to-metal connection **14** (Swagelok).

Figure 12 gives a detailed description of the inlet flange. The heatable gas inlet tube **5** was placed in a duct in front part **6** and fixed with the O-ring **15** and the drilled-through screw **16**. After that, the back part **3** was screwed on the front part **6** in order to fix the gas tube with the fixing-plate **17**. Since the flange had to be gas-tight, the contact surfaces between **3** and **6** were sealed with an O-ring **18**. The heatable gas tube **5** was connected to the tube ($\varnothing=3 \times 2$ mm) coming from the gas supply via a 3 mm to 2 mm Swagelok adapter **19**.

Additional to the reactive gas inlet a purge gas inlet **4** for the dosage of 5 mL/min nitrogen at STP with a MFC (Brooks 5850S) was installed at the bottom of the inlet flange. After entering the flange the purge gas flows into a horseshoe-shaped slot, which is indicated at position **20**. Through six holes ($\varnothing=1.6$ mm), which were placed in the notch **22**, the flow leaves the flange and enters the TGA furnace. This gas flow was installed, since the standard protection gas flow (30 mL/min at STP added by a Vögtlin red-y gas flow regulator) through the balance entering the furnace via the duct **21**, was not enough distributed to avoid condensation on the flange. Figure 13 shows a picture of the furnace in open position.

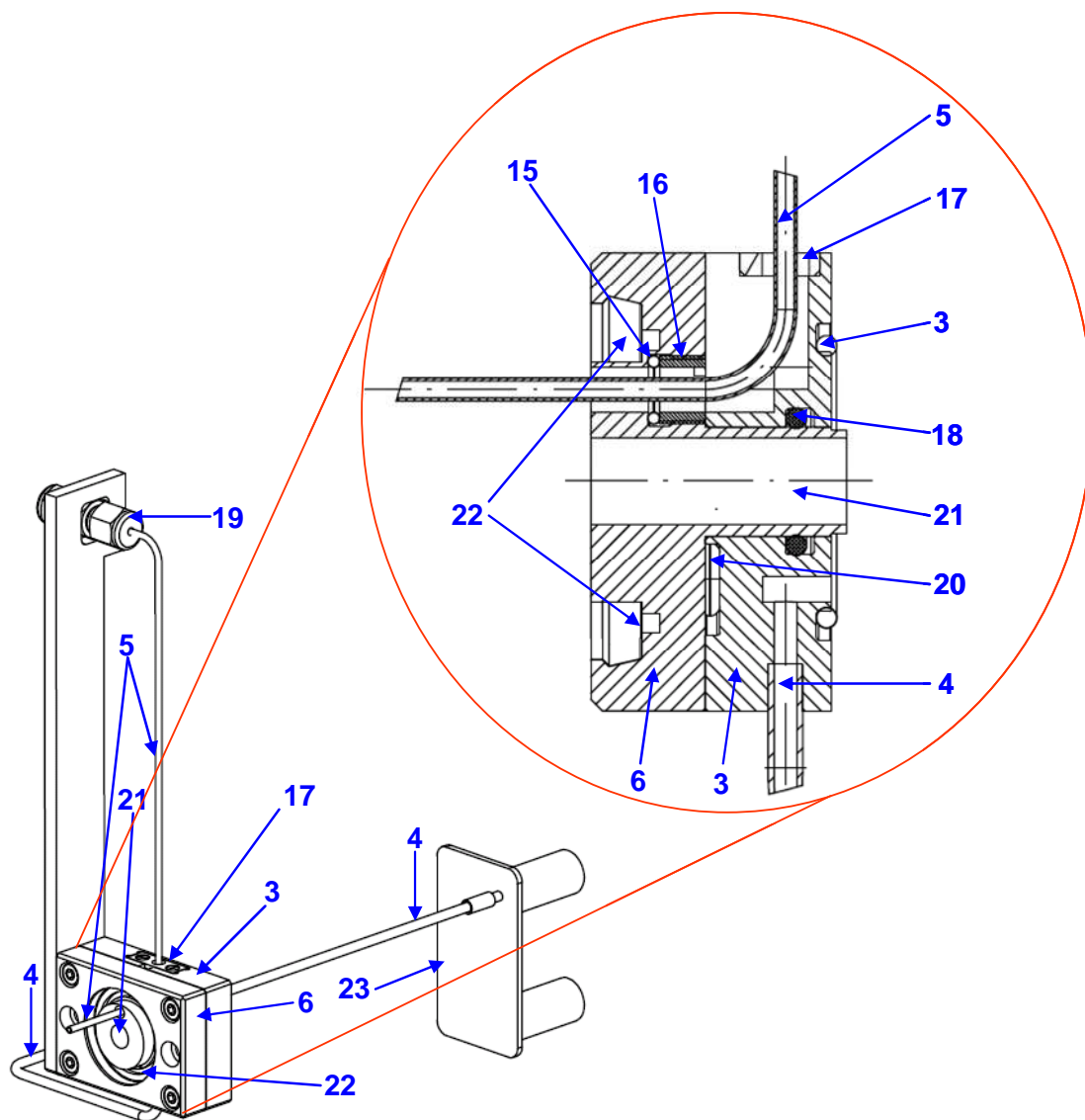


Figure 12: Detailed mechanical drawing of the inlet flange with 90°turned cut out.

3: back part of the new inlet flange; 4: purge gas inlet for prevention of condensation at the front wall of the inlet flange; 5: resistance wire-heated gas tube 6: front part of the new inlet flange; 15: O-ring; 16: screw for fixing the heated gas inlet; 17: fixing plate; 18: O-ring for sealing the contact area between the flange parts; 19: connecting between the 2 mm gas inlet tube and the 3 mm tube from the gas supply; 20: distributor ring for the protection purge gas; 21: channel for the sample holder; 22: notch with purge gas distributor holes; 23: plate for fixing the purge gas tube on the TGA.

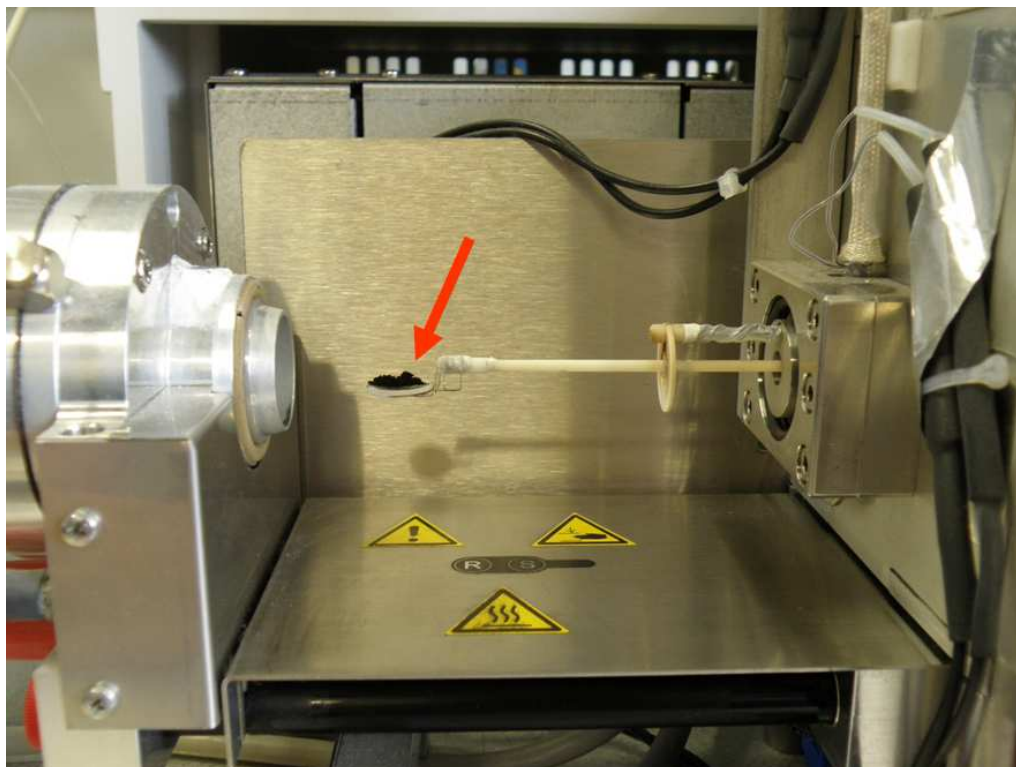


Figure 13: Furnace of the TG system in open position with new inlet flange and the soot-loaded quartz glass disk (red arrow).

Both, the inlet gas tube *5* and the outlet capillary *11* were wound with heating wires in order to heat them up to at least 170°C. Figure 14 shows the temperature profiles measured over the length of the gas inlet and outlet. The profile of the inlet was very stable and varied only little over the tube. The profile of the outlet was more unstable on the first view, but the zone between 0 and 2 cm is additionally heated during operation by the trace heating of the transfer line to the spectrometer (as shown in section 0) and the region around 8 cm is close to the sample, where it is heated by the furnace atmosphere during operation.

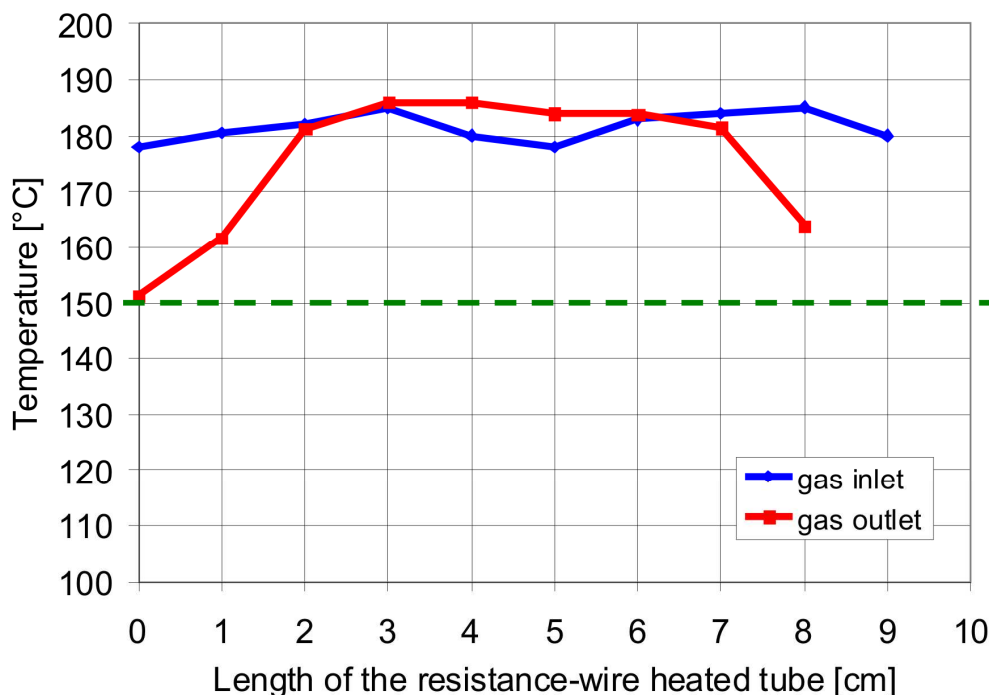


Figure 14: Temperature profiles of the resistance-wire heated gas in- and outlet (5 and 11). Doted line: minimum temperature for condensation prevention - the goal was to reach a mean value of 170°C at least. The temperature drop between 0 and 2 cm is due to the end of the resistance-wire heated zone. During system operation this part was heated by the trace heating of the transfer line to the spectrometer. The drop at 8 cm shows the end of the heating wire in the furnace close to the sample holder.

Typically, for investigations in TG systems, the samples are placed in crucibles. This works without any problem as long as desorption of sample components is examined. However, if reactive gases are dosed mass transport limitations for reaction with the sample have to be taken into account [153, 154]. Therefore, the samples were either placed on a quartz glass disk as shown in Figure 13 or coated on cordierites to limit these transport limitations.

3.3. Changes of the FTIR spectrometer

The FTIR spectrometer (Antaris IGS, Thermo Scientific; see section 2.1.1) for the gas analysis was connected to the TGA via a corrugated tube (DN 4) as transfer line, which was heated up to 180°C by trace heating. The standard gas measuring cell of the spectrometer had a volume of 240 mL and a path length of 2 m. However, the gas flow of only 100-150 mL/min at STP through the TG resulted in low gas exchange rates in the measuring cell, which affected the time resolution. Therefore, the size and shape of the spectrometer gas cell had to be optimized with the objective to find a compromise between small flow rates, which were necessary to get sufficiently high gas concentrations for the detection of even small concentration changes, and a short residence time, which was needed to prevent peak-broadening.

These goals were reached by a newly designed measuring cell from Thermo Scientific with a path length of 178 mm with ZnSe windows and without optics for the reflexion of the IR beam. By this measure the time for IR absorption of the evolved gas becomes smaller, but peak broadening was avoided at the same time. Additionally, the cell volume was reduced to further improve the transfer rates. The typical cylindrical shape of the cell was constricted in the middle, which complies with the shape of the uncollimated beam. The measuring cell had the shape of two cones lying with their tips in opposite to each other as shown in Figure 15, which was the reason to call it double-cone cell. Now, the IR beam “filled” the cell completely and any dead volume was avoided. On the first view, the reduction of the path length by a factor of 10 should degrade the detection limits as well by a factor of 10, but since the IR beam in the new cell does not lose energy due to reflexions, the detection limits were only 2.5-3 times more adverse than those of the standard cell depending on the gas component.

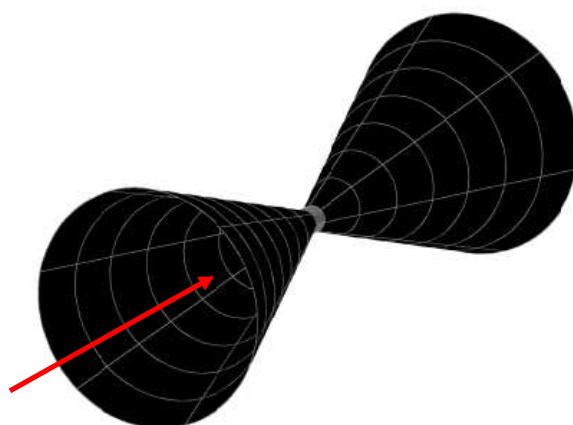


Figure 15: Scheme of the inner shape of the gas measuring cell with a path length of 178 mm. The shape of the uncollimated IR beam was similar and therefore filled the gas cell completely. By this measure any dead volume was avoided and the detection limits of the 2 m standard gas cell were nearly reached.

The housings of the optical bench and the gas measuring cell were purged with 80 and 50 L/h nitrogen at STP, respectively, in order to assure a stable CO₂ and H₂O signal in the background.

The FTIR spectrometer was calibrated for CO₂, CO, NO, NO₂, NH₃, H₂O, SO₂, N₂O, HNO₃, HONO, HCN, HNCO, formic acid and formaldehyde, which are typical exhaust gas components of vehicles equipped with aftertreatment devices. The resolution of the spectra was set to 0.5 cm⁻¹. The carrier gas was nitrogen. CO₂, CO, NO, NO₂ and NH₃ were calibrated in the range of 10-1000 ppm with dilution series based on high purity calibration gases (Airliquide, class: saphire, precision: ±0.5%). SO₂ was calibrated up to 100 ppm with a one-point-calibration since the trend of the calibration curve is linear in this concentration range. H₂O could not be calibrated with a calibration gas; therefore, it was calibrated by dosing H₂ and O₂ over a Pt catalyst. The calibration was based only on the readout of the MFCs and the assumption of a

conversion rate close to 100%. Due to this procedure, the H₂O measurement was expected to be somewhat less precise than for CO₂, CO, NO, NO₂ and NH₃. The calibration spectra of HCN, HNCO, HNO₃, HONO, N₂O, formic acid and formaldehyde were taken from a Nexus 600 (Thermo Scientific) spectrometer, which has a 2 m gas measuring cell similar to the replaced cell of the Antaris IGS. This was possible, since the optical bench including the IR source and the detector of the Nexus 600 spectrometer is identical to the used Antaris IGS and the calibration software Quant pad allows the recalculation of calibration spectra collected at different optical path lengths. Based on the Omnic software a multi-component gas analysis method was developed, which also allows the compensation of cross-sensitivities. In Table 8 the detection limits of the components calibrated in the new double-cone cell are shown in comparison to the detection limits of the components calibrated in the Nexus 600 spectrometer with the 2 m gas cell.

Table 8: Detection limits of the double-cone gas measuring cell and the 2 m cell.

Component	Detection limits of the 2 m cell [ppm]	Detection limits of the double-cone cell [ppm]
CO ₂	0.5	0.7
CO	0.2	1
NO	1	3
NO ₂	1	1.5
NH ₃	0.2	0.8
N ₂ O	0.1	0.5
HCN	0.2	3
HNCO	0.2	0.5
HCOOH	0.2	0.5
HNO ₃	0.5	1.5
HONO	1	3
H ₂ CO	1	2
-C-	not calib.	10
SO ₂	1	2

3.4. Gas mixing unit

In addition to the purge and protection gas MFCs the TG-FTIR system was equipped with a gas mixing unit consisting of 8 MFCs (dosing ranges: 1 MFC for 0-100 mL/min at STP of nitrogen as carrier gas, 1 MFC for 0-25 mL/min oxygen at STP, 1 MFC for 0-10 mL/min H₂ at STP, 5 MFCs for 0-10 mL/min at STP of different feed gas components, i.e. NO₂, NO, NH₃, CO₂, CO, etc.).

Water was generated by controlled hydrogen oxidation in order to dose gaseous water without pulsation to avoid interruption of the balance. A mixture of nitrogen as carrier gas, the right amount of hydrogen to produce the desired amount of water and oxygen in excess was dosed over a platinum catalyst heated to 400°C, where hydrogen was oxidized under controlled conditions. A flashback of the hydrogen flame was avoided by a sinter metal flame barrier after the mixing-point of oxygen and hydrogen. So far the water generator was tested for concentrations between a few hundred ppm and 20%, but higher concentrations should be possible. Nitrogen could be dosed by a MFC in the range from 0 to 100 mL/min at STP, oxygen with a MFC between 0 and 25 mL/min at STP, and hydrogen with a MFC from 0 to 10 mL/min at STP.

Downstream of the water generator up to 5 other gas components can be dosed by MFCs in the range 0-10 mL/min at STP, which were NO, NO₂, NH₃, CO₂ and CO in the experiments for this work. Since the target concentrations of the additional components were most often only in the ppm range, they were dosed as mixtures in nitrogen ranging from 4000 ppm to 5%. Nitrogen, oxygen and hydrogen were taken undiluted from gas cylinders. The total flow for standard experiments with the new system was 100-150 mL/min at STP.

The gas-mixing unit was controlled by a self-programmed LabView application. In this software all flows were adapted automatically to new concentration set-points under consideration of purge and protection gas flows

in order to keep a constant total gas flow. For safety reasons the hydrogen dosage range was restricted in the software. The gas flows can either be manipulated by hand or automatically controlled by the readout of a .txt-file.

All tubes downstream of the water generator were heated to 180°C to reliably avoid condensation of reactants and products on the walls of the system.

3.5. Hydrocarbon analysis by flame ionization detector

Downstream of the FTIR spectrometer a flame ionization detector (FID) was installed for the quantitative analysis of hydrocarbons (HC), which are adsorbed on PM. At first an attempt was made to analyze the HC with the FTIR spectrometer, but the number of different HC adsorbed on PM was too high to calibrate all of them. The calibration of the -CH₂-group signal, which is similar for all HC, was not possible since this group has different adsorption coefficients at different wave lengths for different HC. This is exemplarily shown in Figure 16 by the absorbance spectra of n-oktane, hexane and isopropane from 2500-3300 cm⁻¹. Based on these measurements, the decision was made to use the FID in addition, because it allows a reliable analysis of the HC amounts, which is an important part of PM analysis. Table 9 gives an overview of the FID response factors for different HCs given by the manufacturer and confirmed in our labs.

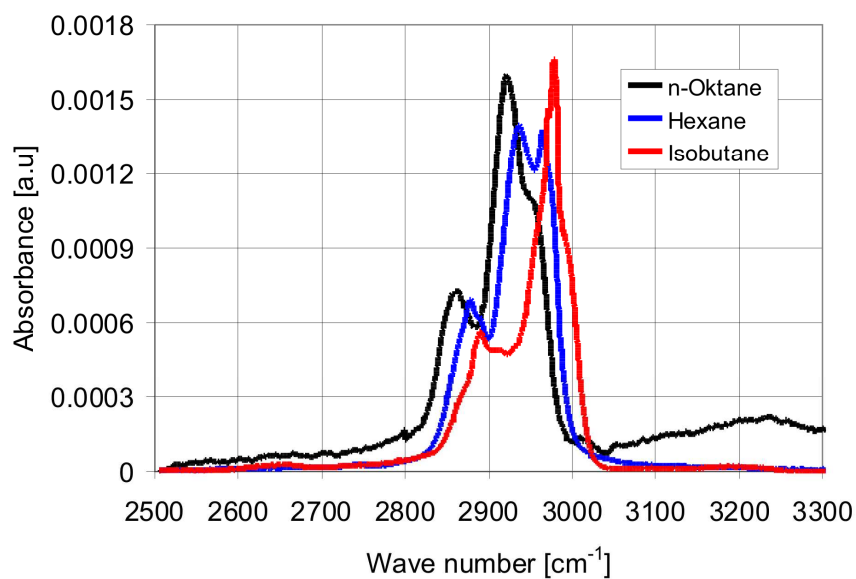


Figure 16: Absorbance spectra of n-octane, hexane and isobutane from 2500-3300 cm^{-1} .

Table 9: Response factors of the FID given by the manufacturer and confirmed by measurements in our lab.

Component	Response factor
Benzene C_6H_6	1.07
Methane CH_4	1.07
Cyclohexane C_6H_{12}	1.02
Ethane C_2H_6	1.01
Propane C_3H_8	1.00
Butane C_4H_{10}	0.98
Toluene C_7H_8	0.96
Ethine C_2H_2	0.95
n-Heptane C_7H_{16}	0.94
Ethylbenzene C_8H_{10}	0.89
p-Xylene C_8H_{10}	0.89
Isopropanol $\text{C}_3\text{H}_8\text{O}$	0.74
Ethylacetate $\text{C}_4\text{H}_8\text{O}_2$	0.72
Acetone $\text{C}_3\text{H}_6\text{O}$	0.71

3.6. Final setup of the TG-FTIR system

In Figure 17 the setup of the TG-FTIR system is summarized in a flow chart.

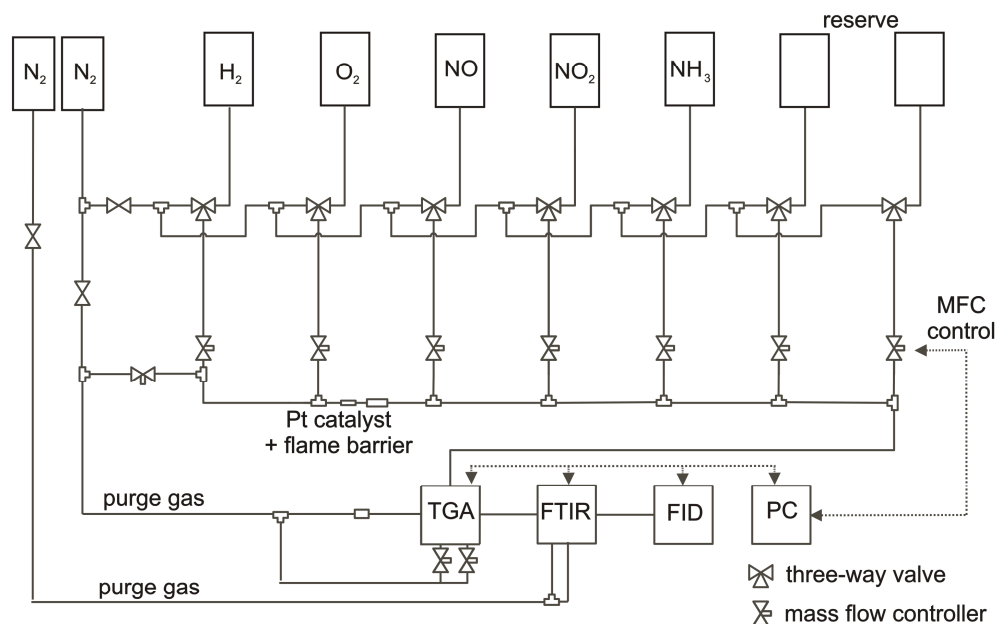


Figure 17: Flow chart of the TG-FTIR system. The dotted lines symbolize communication lines between the PC and the FT-FTIR system and the mass flow controllers. The three-way valves downstream of the gas bottles are used for MFC purging.

Figure 18 shows a picture of the TG-FTIR system in its final version. The system is set up as follows: starting on the right, there is the gas mixing unit *A* and the water generator *B*, where the feed gases are mixed. Downstream of that point all tubes are heated to avoid condensation, visible by the white glass fiber tape insulation of the tubes. Then the gases reach the TG apparatus *C*, where the reactions between reactive gas and sample take place. The TG apparatus is placed on the balance table *D* to absorb vibrations. Since the balance table alone could not absorb all vibrations, which are transmitted via the gas tubes, they were bended to coils, which decoupled the TG apparatus almost completely from any perturbation. *E* is the linear power supply for the in- and outlet

heating. After the TG apparatus, the gases are passed to the FTIR spectrometer *F* for the main gas analysis. When the gases have passed the gas measuring cell, they reach the FID *G* for HC analysis at the end of the TG-FTIR system.

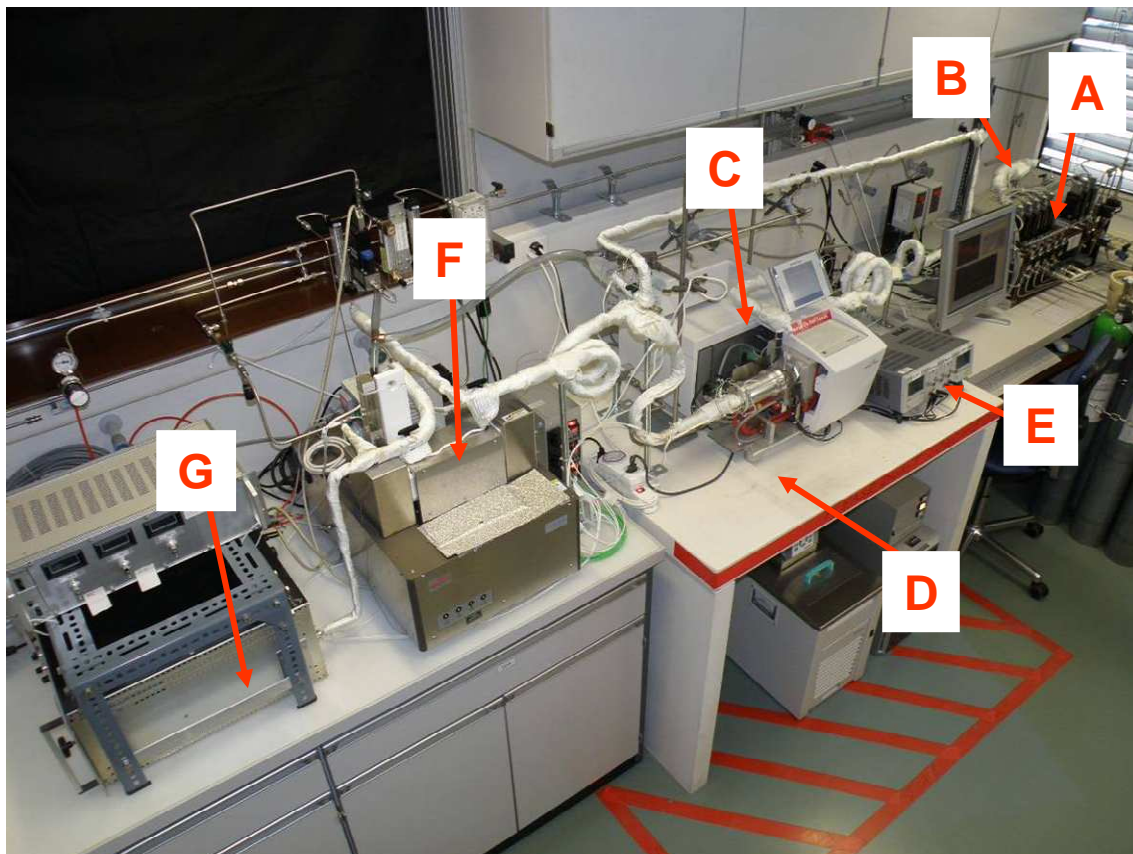


Figure 18: Overview over the TG-FTIR system. A: LabView-controlled gas mixing unit; B: water generator; C: redesigned TGA/DSC1 from Mettler-Toledo; D: balance table; E: power supply for the heating wires; F: FTIR spectrometer Antaris IGS from Thermo Fisher Scientific with the double-cone gas measuring cell; G: FID.

3.7. Performance test of the TG-FTIR system

After finishing the TG-FTIR setup a first performance test was made to check the quality of the spectrometer calibration and the agreement with the TGA data collection. As test compound calcium oxalate monohydrate ($\text{CaC}_2\text{O}_4 \cdot \text{H}_2\text{O}$,

Aldrich) was chosen, since it is an accepted working standard for TGA due to its well-defined decomposition [155]:



First, the water of crystallization is removed around 100°C and anhydrous calcium oxalate (CaC₂O₄) remains. In a second step, the anhydrous oxalate decomposes under CO release forming calcium carbonate (CaCO₃). At temperatures above 550°C the carbonate decomposes into calcium oxide (CaO) under CO₂ release. The decomposition temperatures for each step depend on the heating rate and the sample mass [156], therefore only temperature ranges are indicated here.

For the test of the TG-FTIR system a temperature-programmed desorption (TPD) experiment was performed between 50°C and 800°C with a heating rate of 10 K/min under inert nitrogen conditions. The total flow rate was 100 mL/min at STP. The initial weight was 2.926 mg and with a purity of 98.6% (estimated by a manganometric titration), the absolute amount of pure CaC₂O₄·H₂O was 0.0197 mmol. The sample was placed in an alumina crucible with a volume of 70 µl.

Figure 19 shows the CO, CO₂ and H₂O concentrations measured with the spectrometer and the mass loss curve recorded with the TG apparatus of the TPD. Table 10 gives the amounts of each evolved gas component and a quantitative comparison with the mass loss.

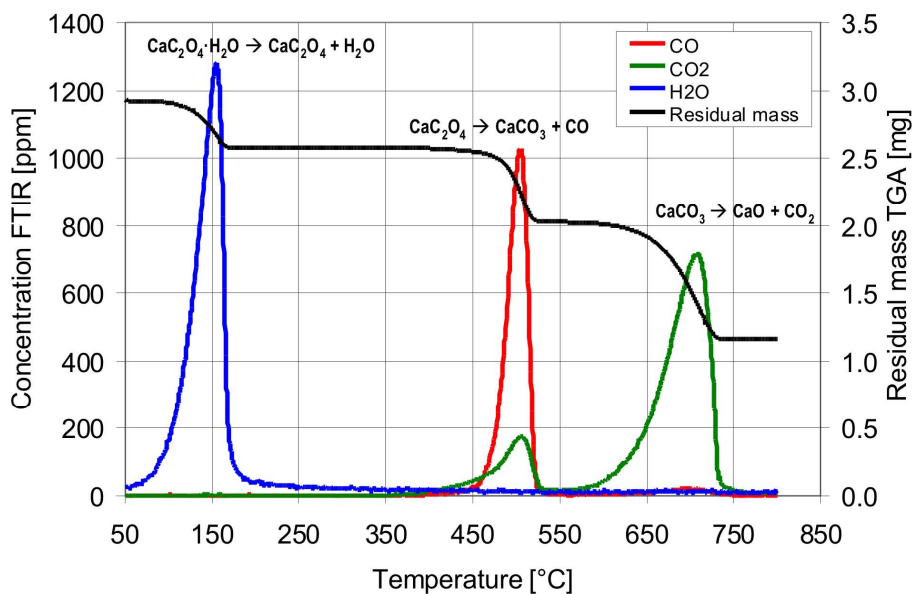


Figure 19: TPD of calcium oxalate monohydrate. The concentrations of CO, CO₂, H₂O and the mass loss curve are plotted over temperature.

Table 10: Summary of the CaC₂O₄·H₂O decomposition results. The purity was 98.6%, which corresponds to an absolute amount of 0.0197 mmol CaC₂O₄·H₂O.

step		mass	amount of substance
		[mg]	[mmol]
start	initial weight	2.926	0.0200 (98.6% purity)
1.step	theo. mass loss as H ₂ O	0.360	0.0197
	actual mass loss	0.345	0.0192
	H ₂ O, FTIR	0.377	0.0209
	CaC ₂ O ₄	2.581	0.0201
2.step	theo. mass loss as CO	0.561	0.0197
	actual mass loss	0.551	0.0197
	CO, FTIR	0.386	0.0138
	CO ₂ , FTIR	0.207	0.0047
	CO _x , FTIR	0.593	0.0185
	CaCO ₃	2.030	0.0203
3.step	theo. mass loss as CO ₂	0.867	0.0197
	actual mass loss	0.871	0.0198
	CO ₂ , FTIR	0.854	0.0194
	CaO	1.159	0.0207
total	theo. mass loss	1.788	-
	actual mass loss, TGA	1.766	-
	actual mass loss, FTIR	1.824	-

In the first step between 50°C and 200°C the water of crystallization was evolved. 2.581 mg CaC_2O_4 remained in the crucible corresponding to a theoretical amount of 0.0201 mmol pure CaC_2O_4 . Based on the FTIR data 0.0209 mmol (0.376 mg) water were calculated.

In the second decomposition step CaCO_3 was formed. The mass of the remaining substance was 2.030 mg (0.0203 mmol - under the assumption of 100% purity). 0.0138 mmol (0.386 mg) CO + 0.0047 mmol (0.207 mg) CO_2 were calculated from the FTIR data. This led to a total carbon amount of 0.0185 mmol for this step. The unexpectedly released CO_2 could not be explained by impurities of calcium bicarbonate, since 1.4% of the initial weight of this substance (as calculated from the purity of 98.6%) would be not enough to generate the measured amount of CO_2 . Most probably the CO_2 was due to oxidation of small parts of CO by residual oxygen in the system.

In the last decomposition step 1.159 mg remaining substance was estimated from the mass loss curve. Assuming of 100% purity this would have been 0.0207 mmol calcium oxide. The emitted CO_2 was calculated to 0.0194 mmol (0.854 mg).

The comparison of the TGA, FTIR and theoretical data of this experiment showed that the spectrometer calibration and the TGA mass loss agreed well. Especially the CO_2 calibration seemed to be very precise as the comparison of the CO_2 evolution and the observed mass loss in the third decomposition step showed. The evaluation of the CO results was a bit more difficult, since first, part of the CO was most probably oxidized and furthermore, it is possible, that impurities falsified the results. However, the calibration of CO still had the demanded precision. The agreement of the water results measured by the

spectrometer and the TGA was good, especially under consideration of the fact, that water could not be calibrated with a calibration gas.

The overall balance was also very good, since the difference between the TGA mass loss and the sum of the gas phase components was only 3.3%.

3.8. Conclusions

Based on the standard TGA/DSC1 system from Mettler-Toledo and the FTIR spectrometer Anataris IGS from Thermo Scientific a TG-FTIR system for PM investigations with condensable and corrosive reactive gases was developed. First, the inlet and outlet parts of the TGA were reconstructed to prevent condensation and corrosion. Moreover, a special FTIR gas measuring cell was designed with a path length of 178 mm and a volume of less than 40 mL, which showed a high signal-to-noise ratio and a short residence time even for small flow rates through the system. For the gas supply a LabView-controlled gas mixing unit was built. A FID was installed for the HC analysis, since the quantitative analysis was not possible with FTIR spectroscopy.

A first performance test with calcium oxalate dehydrate gave promising results. In the next step, the method for the composition and reactivity analysis of PM had to be developed.

4. Composition analysis of soot with the TG-FTIR system

4.1. Introduction

As mentioned in section 1.2.5, thermolysis of PM with subsequent gas analysis is an attractive alternative to the gravimetric PM analysis [72]. Besides the lowering of the detection limits the application of thermoanalysis techniques would also address the changed composition of PM and allows a deeper chemical analysis.

Thus, an analytical method based on the TG-FTIR system presented in chapter 3, was developed that allows qualitative and quantitative determination of the individual PM components. Furthermore, a method for the investigation of PM reactivities under realistic conditions was elaborated. The project was financed and supported by the “Forschungsvereinigung Verbrennungskraftmaschinen e.V.” (FVV) („Dieselruss II – Differenzierte Mikroanalytik von Particulate Matter“ No. 1006).

4.2. Experimental

4.2.1. TPD/O measurements

The composition of the PM samples were investigated in TPD/O experiments (temperature-programmed desorption followed by oxidation) in the TG-FTIR system. As shown in Figure 20 the samples were first heated in a nitrogen gas flow to 700°C at 20 K/min and then cooled to 300°C. This first stage provided information about the OC, oxygen, sulphuric acid and water contents as well as volatile nitrogen compounds, which can be detected as NO, NO₂, N₂O, HCN, HNCO and NH₃. The term OC summarizes all volatile HC as well as carbon-

containing surface functional groups (such as carbonyls and carboxyls) that decompose thermally to CO and CO₂. The oxygen content is calculated from the oxygen in the released CO and CO₂. The heating rate of 20 K/min was chosen from experiments with different heating rates. It was a compromise between acceptable resolution and the time requirement as the method should be applied for routine diesel PM analysis. The FTIR spectra were the sum of 8 scans, which was also adapted after tests with different numbers of scans.

Since it was not possible to maintain the inert gas completely oxygen-free a constant amount of EC was oxidized. This amount was quantified in a second, identical ramped heating stage and subtracted from the OC content measured in the first stage. In a third ramped heating stage (300-750°C at 20 K/min) and an isothermal section of 15 min at 750°C with 10% oxygen in the reactive gas, the thermally stable EC was oxidized and quantified. Beside EC also sulfur and nitrogen, which were embedded in the carbon structures, could be detected as SO₂, NO and NO₂. Oxygen embedded in the carbon structures could not be detected, since oxygen was dosed for the carbon oxidation and a distinction between added and embedded oxygen was not possible.

Since HC analysis was not possible with the FTIR spectrometer the FID was used (section 3.5). In order to assure the precision of the FID measurement, it had to be calibrated prior and after each experiment. By this measure calibration shifts could be compensated.

The total flow during the whole experiment was 100 ml/min at STP (30 ml/min balance protection gas, 5 ml/min inlet purge gas, 5 ml/min outlet purge gas, 70 ml/min reactive gas).

Total analysis was possible for sample sizes larger than 300 µg; samples in the range of 50-300 µg permitted the estimation of EC and OC contents, whereas samples of less than 50 µg could only be analyzed for the total carbon content.

In order to minimize the residual oxygen and other contamination of the TGA, the gas flows of the system were kept up even when the system was unattended. Furthermore, the system was heated up to 800°C before each measurement series (e.g. in the morning, when the system was not used over night) to remove oxygen and organic contamination, which might influence the OC and EC estimation.

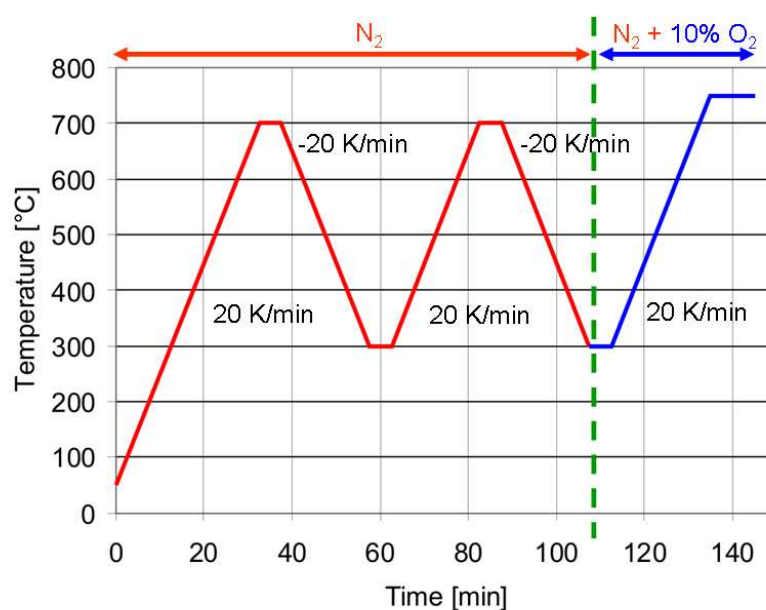


Figure 20: Temperature profile of the TPD/O experiment for the composition analysis of diesel PM. At the end temperature of a heating or cooling ramp temperature was hold for 5 min for equilibration of the system. At the end of the measurement the hold time was 15 min in order to guarantee total oxidation of the PM sample.

4.2.2. TPO measurements

Beside these TPD/O experiments, the TG-FTIR system is also suitable for reactivity tests, in which diesel PM samples are exposed to different feed gas mixtures to mimic the behavior of samples under real-world conditions in the

DPF. The measurements were performed as temperature-programmed oxidation (TPO) experiments.

In the TPO experiments the samples were usually heated from 50-750°C at 10 K/min with an isothermal section of 15 min at 750°C to assure total oxidation of the PM sample. The total flow was 150 mL/min at STP. Table 11 shows the different reactive gas compositions, which were applied for the reactivity measurements. Oxygen and water were already added at 50°C, but NO₂ was not added below 120°C in order to avoid condensation in the cold furnace of TG system. This allowed comparing the influence of different reactive gas components on the oxidation behavior of the PM samples. The optimum sample size was above or equal 300 µg to obtain the full set of information from the TG and the spectrometer. The ratio of CO₂ and CO in the product gas and the comparison of the mass loss signal with the concentrations of formed gas components, give important hints on the different reactions, which occur during the regeneration of a DPF.

Table 11: Composition of the gas mixtures used for the TPO investigations.

mixture	N₂ [%]	O₂ [%]	NO₂ [%]	H₂O [%]
1	85	10	0	0
2	85	10	0	5
3	89.9	10	0.1	0
4	84.9	10	0.1	5

4.2.3. Types of PM samples

The investigated samples were either powders or collected on quartz fiber and metal filters. The filter-carried samples were punched out as a circular part (Ø = 14 mm) of the original filter (Ø = 45 mm).

The gravimetric signal could be analyzed for the powder PM samples in conjunction with gas phase analysis, allowing the observation of adsorption and desorption processes on the surface, e.g. the mass increase due to the partial oxidation of carbon in an oxidizing atmosphere [157] as well as the estimation of the ash content. The ash content of PM samples on cut-outs from larger filters could not be estimated because the tare weight could not be estimated with satisfactory precision due to inhomogeneities in the filters. Furthermore, the oxidation rate could only be determined from the gas phase analysis because the balance must be tared prior to precise collection of a blank curve, which is necessary to correct for lift effects. Thus, the mechanically unstable quartz filters would have to be removed from the balance and inserted again, which might cause mass losses. This part of the procedure increased the measurement uncertainty up to 10-20 μg . Conversely, the metal filters were sufficiently stable but oxidized easily in the presence of oxygen with increases in mass that resulted in a large measurement error. Tests with unloaded passivated metal filters showed no mass increase. Thus, they would allow recording a precise blank curve after testing the loaded filter with the same filter cut-out, in order to study absorption and desorption effects at least.

During this work a large number of PM samples were investigated in terms of composition and reactivity. They were either collected from diesel engine test benches, produced individually in the laboratory or purchased commercially. Here, a representative part of these samples was selected to present the obtained results in this report. Their type, origin and the provider are shown in Table 5. The 4 powder PM samples provided by Volkswagen (VW) were used to develop the TPD/O and TPO methods.

4.3. Results and discussion of the composition analysis

4.3.1. Method development based on the VW Samples 1-4

The samples, referred to as VW Samples 1-4, were externally analyzed, which was a prerequisite for a method validation.

The FTIR and TGA data of the TPD/O experiments are illustrated in Figure 21 and Figure 22 by means of VW Sample 2 as example. In Figure 21 the trends of the CO₂, CO and H₂O concentration during the TPD/O analysis are shown.

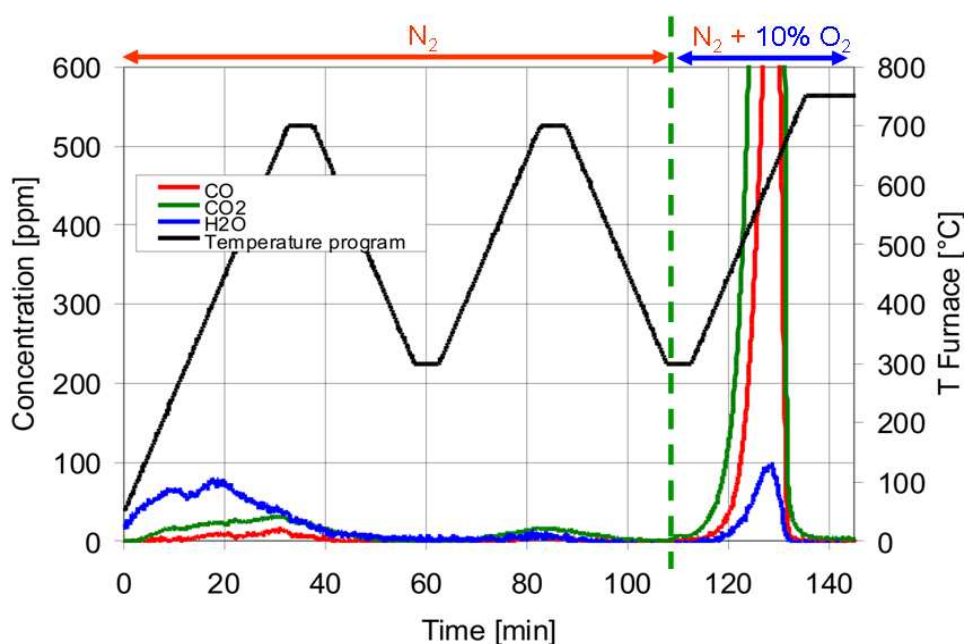


Figure 21: Trend of the CO₂, CO and H₂O concentrations measured with the FTIR spectrometer during a TPD/O analysis of VW Sample 2. The scale of the left y-axis was reduced in order to show the trends in the inert segments. The maximum in the last heating stage was 4010 ppm CO₂ and 850 ppm for CO.

In the first inert stage, the OC desorbed as CO₂ and CO and also adsorbed water was transferred to the gas phase. In the second inert stage only a small evolution of CO₂ and CO, was observed, which was due to EC oxidation with the residual oxygen in the system. In the third segment, the sample is totally oxidized. The maximum concentration for CO₂ was 4010 ppm and 850 ppm for

CO. The other components detected by FTIR spectroscopy were not included in the figure, since their amounts were too small to be visible.

Figure 22 shows the corresponding mass loss curve measured with the TGA. In the first inert segment the mass loss was due to the desorption of OC, H₂O and other unstable components. The mass loss as a result of EC oxidation with residual oxygen in the second inert stage is hardly visible from the balance data. The resolution of the FTIR spectrometer at this point is much higher. In the last heating stage a significant mass loss was observed, which was due to the total oxidation of the sample. 2.4% of the sample remained as ash in the TGA furnace, which was composed of oxides and sulfates of different metals.

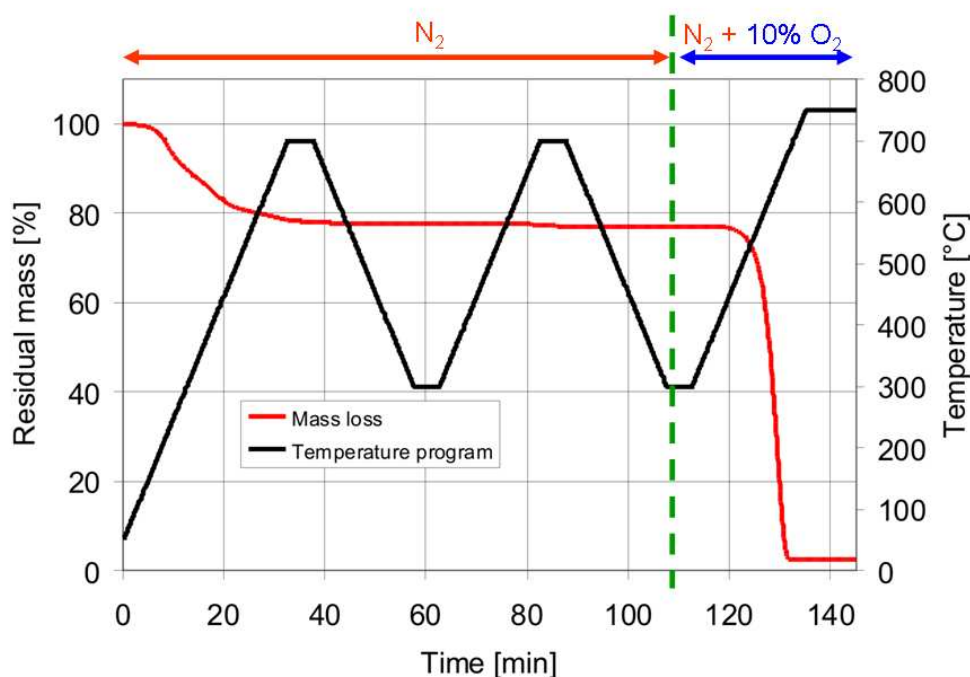


Figure 22: TGA mass loss curve of VW Sample 2 in percent of the initial weight.

An overview of the TPD/O results for VW Samples 1-4 obtained with the TG-FTIR system is given in Figure 23 in comparison to the external analyses. Good agreement is observed between the component concentrations determined by

the different methods. Small differences were found in the fractions of OC and EC, which are likely to be a result of the different definitions for OC and EC.

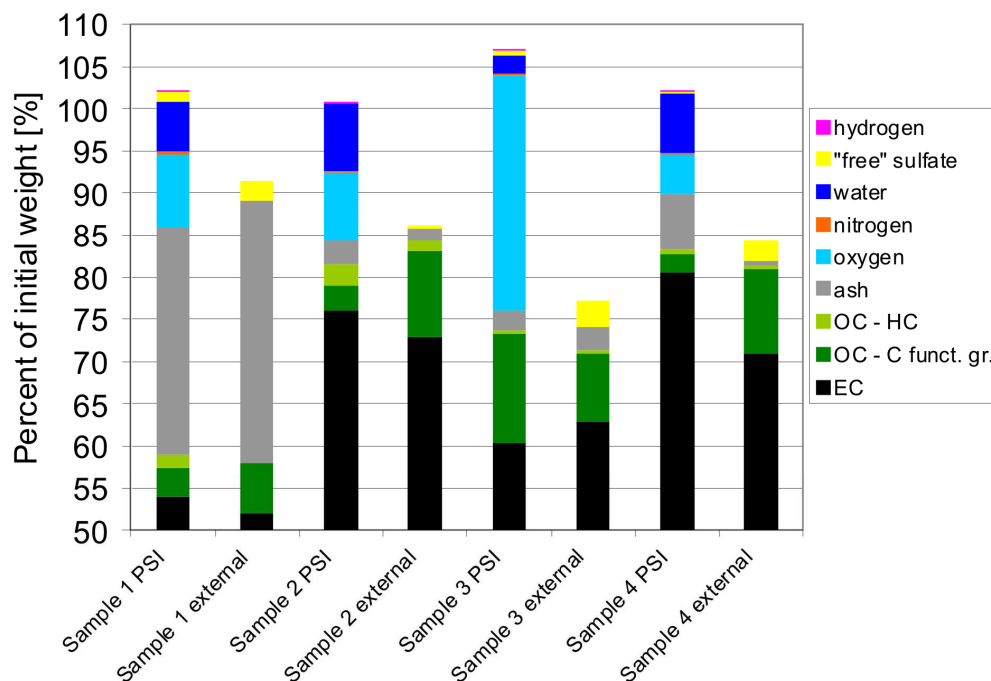


Figure 23: Results for the TPD/O analysis of the powder VW Samples 1-4. The concentration of each component is referred to the initial weight. The range from 0-50% consists of EC.

A comparison of the results for sulfate is difficult because the external analysis method for sulfate was unknown. With the TG-FTIR system only adsorbed H_2SO_4 and sulfur embedded in the carbon structure could be detected as SO_2 . The sulfate content in the ash could not be detected quantitatively. This was confirmed by TPD/O experiments with model substances similar to those performed for the PM analysis shown in Figure 24. First, a mixture of Printex U and 10% calcium sulfate (CaSO_4) was investigated and only 10% of the sulfur were detected in the spectrometer. When pure CaSO_4 was used no SO_2 was detected, since the decomposition of CaSO_4 starts not until 800°C .

In addition, a mixture of Printex U and 5% H₂SO₄ was investigated. The sulfur recovery rate for this experiment was 90%. These results indicated that adsorbed sulfur components and sulfur embedded in the carbon structure, which are released during total oxidation, could be analyzed in opposite to sulfates in the ash.

The ash contents determined for the sample using both methods agreed well, except for Sample 4, which exhibited a large difference between the methods probably due to inhomogeneities in the sample.

The sum of the components of the externally analyzed samples did not reach 100%, since H₂O, hydrogen, oxygen and nitrogen could not be measured there.

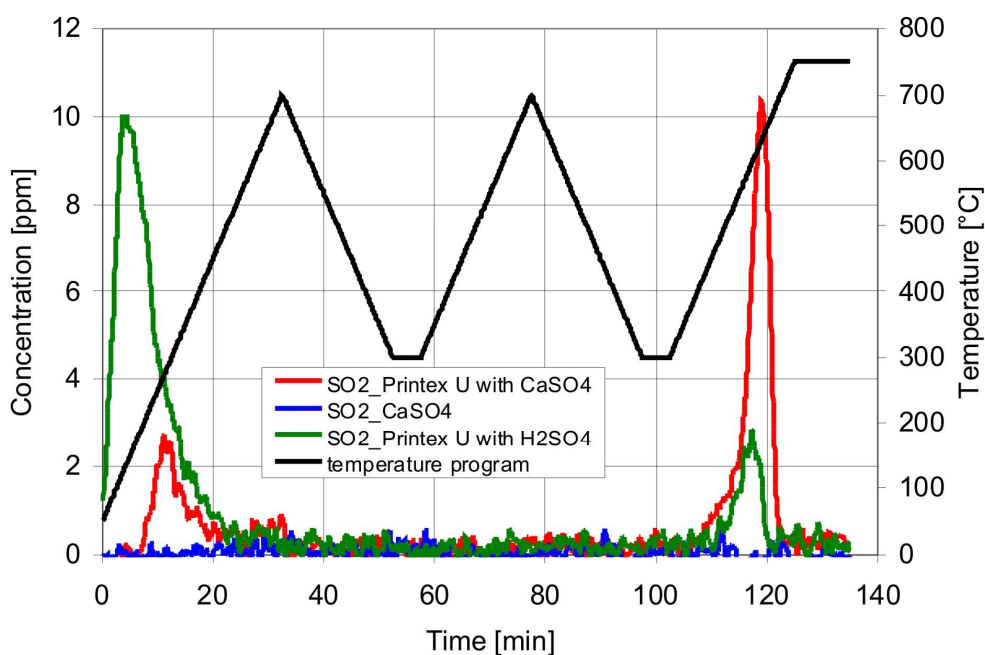


Figure 24: SO₂ released during a TPD/O experiment with a mixture of Printex U and 10% CaSO₄, pure CaSO₄ and a mixture of Printex U and 5% H₂SO₄. 12% sulfur were recovered from the mixture of soot and CaSO₄, hardly SO₂ was detected from the pure sulfate and about 90% of the sulfur were recovered from the mixture of Printex U and H₂SO₄. The feed gas consisted of 100% nitrogen until the sample was cooled down to 300°C the second time, after that 10% O₂ were added.

4.3.2. Graphite and GfG soot

In a second step, a graphite sample and the GfG soot sample both provided by the Institute of Water Chemistry and Chemical Balneology at the TU Munich were tested. It is known, that graphite is rather unreactive in comparison to other carbon materials, and that on the other side GfG soot is known to have a very high reactivity [16, 67]. Therefore, these samples were of special interest because they span the reactivity range, between which the reactivities of PM samples from diesel engines could be ranked. The compositions of both samples are shown in Figure 25.

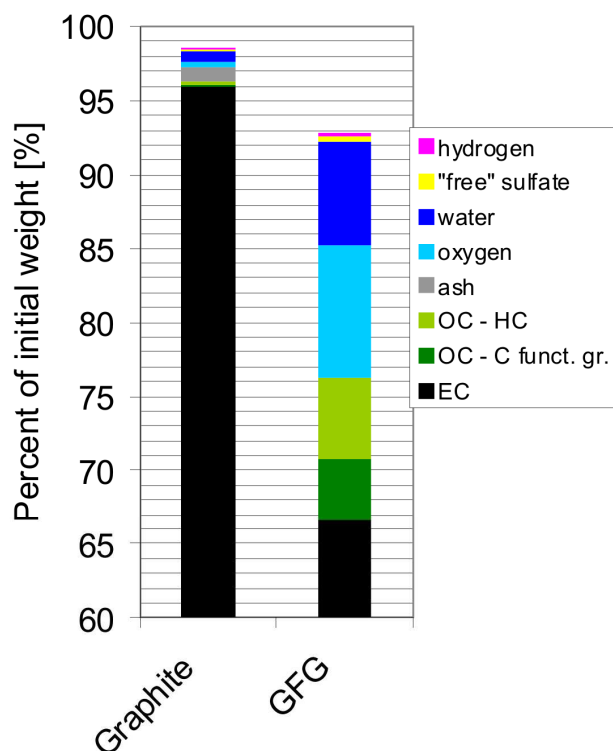


Figure 25: Results of the TPD/O analysis of the graphite and GfG soot. The concentration of each component is referred to the initial weight. The range from 0-60% consists of EC.

In the inert part of the experiment, GfG soot showed a significant mass loss of 35%. The amounts of OC (consisting of 57% HC and 43% thermally unstable

surface groups), oxygen and water were significantly higher than those found in the graphite sample (Figure 26). After introducing oxygen in the third heating ramp, a mass increase of 0.065 mg due to oxygen adsorption and the formation of surface oxygen functional groups was detected (Figure 27) [157]. The graphite sample consisted of 95% EC, small amounts of OC, water and oxygen and a small quantity of ash. The addition of O₂ to the graphite sample did not lead to the formation of surface oxygen functional groups (Figure 27).

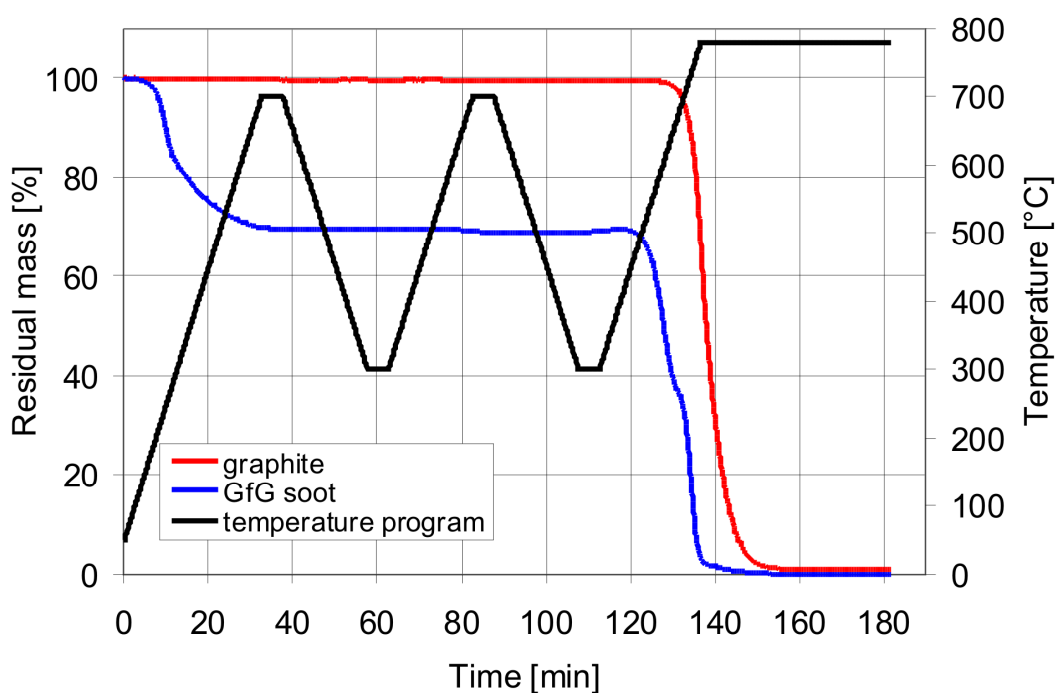


Figure 26: TGA mass loss curves of graphite and the GfG soot sample. Here the temperature in the last heating ramp for the oxidation of the EC had to be increased to 780°C, since the graphite sample was not totally oxidized at temperatures below 760°C. The isothermal section was also increased from 15 min to 45 min. The feed gas consisted of 100% nitrogen until the sample was cooled down to 300°C the second time, after that 10% O₂ were added.

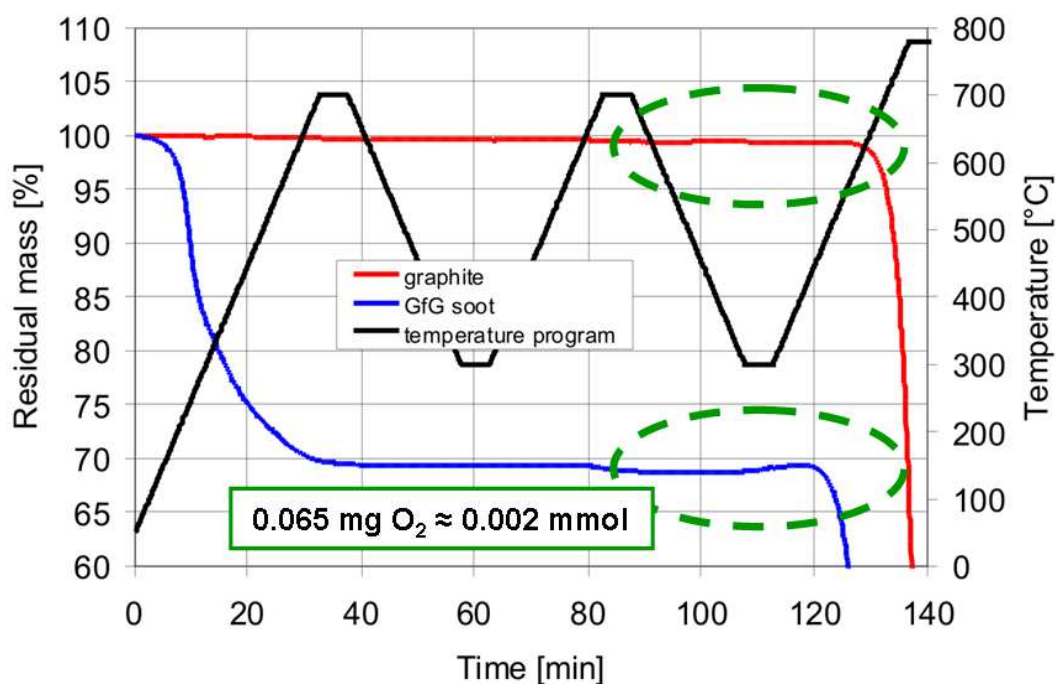


Figure 27: Cutout of the TGA mass loss curves of graphite and the GfG soot sample shown in Figure 26. After the addition of 10% O₂ to the reactive gas the mass of the GfG soot increases about 0.065 mg. This was due to adsorption and reaction of oxygen with the carbon surface. For graphite no mass increase could be observed.

4.3.3. Printex U, Euro 0, Euro V and the mixed soot sample

The composition analyses of the powder samples were completed with the investigation of Printex U, the Euro V, the Euro 0 and the mixed soot sample. The 4 samples were investigated in one series, since they were used for the investigation of the SCR effect on soot (see chapter 6). The results of the composition analysis are shown in Figure 28. Printex U had the largest EC content and the smallest oxygen, hydrogen and water contents in the series. The EC content decreased from Euro V over Euro 0 to the mixed soot sample. The Euro 0 sample showed the largest ash and OC content. In contrast to Printex U the three diesel soot samples contained a fraction of nitrogen, which was

evolved mainly as NH_3 in the case of the mixed soot sample and as NO from the Euro V and Euro 0 samples. The water contents of the samples were rather low except for the mixed soot. Printex U and the mixed soot sample contained a fraction of H_2SO_4 , which was detected as SO_2 . Printex U showed a significant mass increase after the addition of oxygen, but not the real samples Euro V, Euro 0 and the mixed soot sample.

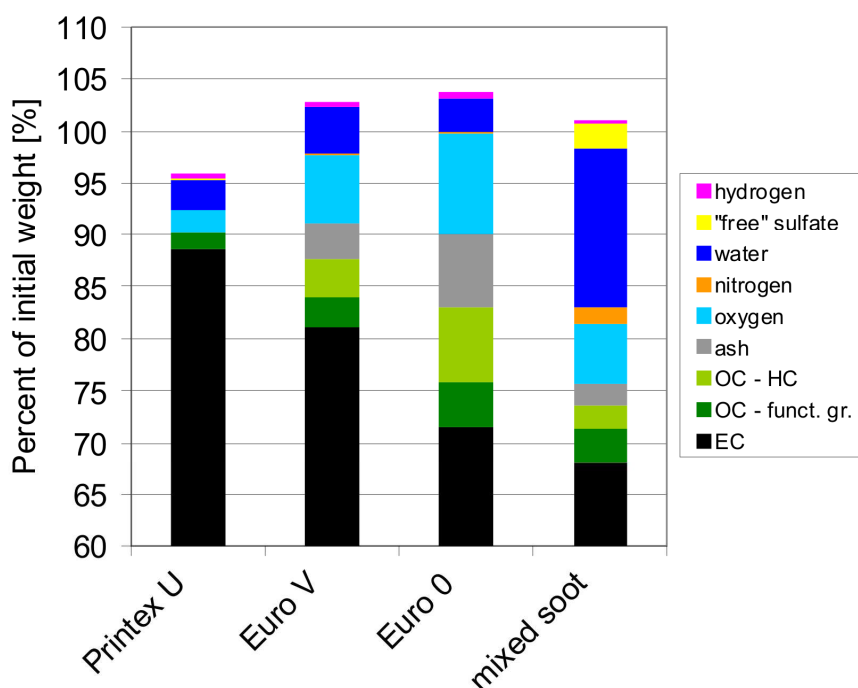


Figure 28: Results for the TPD/O analysis of Printex U, the Euro V sample, the Euro 0 sample and the mixed soot sample. The concentration of each component is referred to the initial weight. The range from 0-60% consists of EC.

4.3.4. PM samples on metal filters

In addition to the powder samples, PM samples collected on filters were also investigated. As an example, samples from a diesel car collected under three different sets of operating conditions (two samples per set of operating conditions), which were provided by the Lehrstuhl für

Verbrennungskraftmaschinen VKA of the RWTH Aachen [158], are presented here. The samples were collected in the main exhaust stream on non-passivated metal filters without a DOC upstream of the filter. The engine conditions during sample collection are shown in Table 12. The effective mean pressure is a measure for the retrieved engine torque. 2 bar effective pressure correspond to ca. 34 Nm and 5 bar to ca. 85.5 Nm. λ is the ratio between the actually added amount of air and the theoretical amount of air necessary for the stoichiometric fuel combustion. The collection time was 5 min for each sample.

Table 12: Details of the PM samples collected on metal filters. Sampling time: 5 min.

Sample	Filter loading [mg]	Engine conditions during sample collection			
		Engine speed [min^{-1}]	Effective mean pressure [bar]	T [$^{\circ}\text{C}$]	λ
A1	4.496	1500	2	465	<1
A2	4.559	1500	2	465	<1
B1	2.303	1500	2	175	>1
B2	2.323	1500	2	175	>1
C1	12.280	2000	5	400	>1
C2	12.121	2000	5	400	>1

The compositions of the samples exhibit good agreement between components of the corresponding pairs, as shown in Figure 29. The C1 and C2 samples had the highest EC content and also the highest total carbon amount because they were generated at the highest engine load of the series. The amount of soot collected of samples B1 and B2 on the other hand, was the smallest due to the lean conditions and the lower engine load in comparison to samples C. Samples B showed the highest amounts of water and OC referred to the sum of the components measured in the infrared gas phase analysis. This was due to the adsorption of water and HC during the cooling phase, since the samples were collected at the lowest temperature in the series. The large oxygen content of samples B suggests a highly reactive structure within the sample.

Samples A were collected under fuel rich conditions, but collected at a rather high temperature of 465°C. Therefore, the amount of adsorbed OC and water was smaller as in the case of samples B, although fuel rich conditions lead to an increase of the HC amount. Based on the effective mean pressure and the engine speed, the sample pair of A and B exhibited a more heterogeneous composition than pair C.

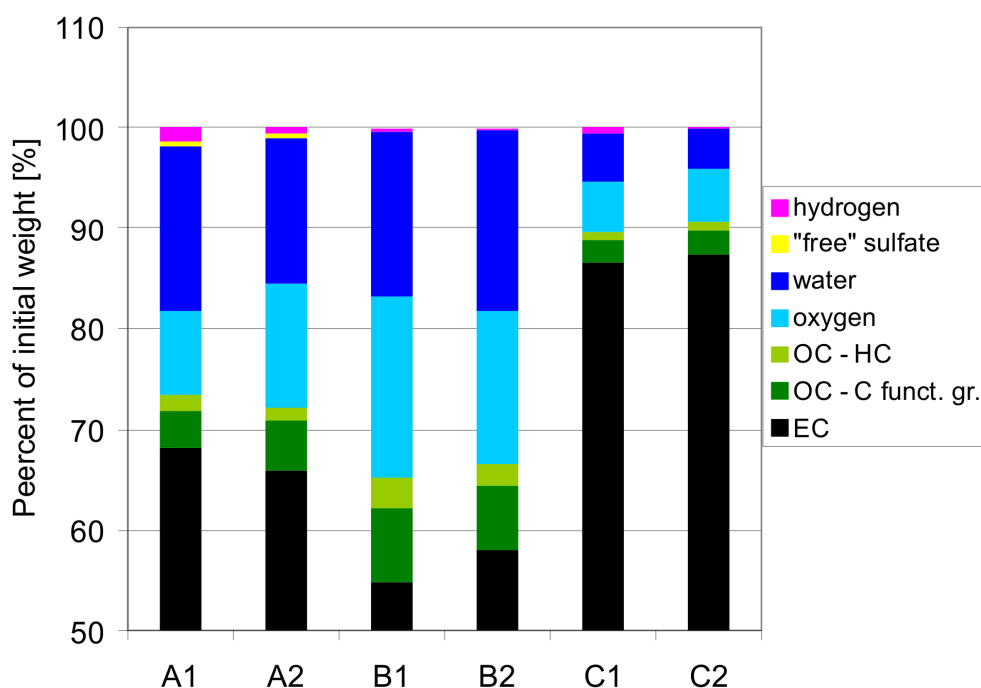


Figure 29: Compositions of samples A1, A2, B1, B2, C1 and C2. The sum of the gas phase components was set to 100%, since the initial weight could not be recorded prior to the experiment. The range from 0-50% consists of EC.

At the end of this section a short remark should be made on the analysis of NH_4NO_3 , urea and cyanuric acid adsorbed on the PM surfaces in the TG-FTIR system, as it may occur on PM samples from SCR-coated DPFs. In order to check if these compounds can also be analyzed quantitatively the pure substances and mixtures with Printex U were investigated. These experiments showed clearly, that a quantitative analysis was not possible, since only a part

decomposed into detectable components like NH₃, NO, NO₂, HCN and N₂O and HNCO. The remaining compounds formed aerosols and could not be detected in the spectrometer. The recovery rates were only between 25-50%.

4.3.5. Error analysis of the composition analysis

Printex U was also used for the estimation of the measurement error of the composition analysis of soot. Therefore, the composition of Printex U was investigated by an elemental analysis in an external laboratory (AQura GmbH, Hanau, Germany) and the TPD/O measurement in the TG-FTIR system was repeated several times.

Table 13 shows a comparison of the elemental C, H, N, S, O analysis results and the mean values for these components measured by the TPD/O method. For the elemental analysis 2x 20 mg and for the TPD/O analysis 1.0-1.5 mg were used. The agreement between the amounts of carbon and hydrogen were good, but for oxygen and sulfur larger differences were detected.

Table 13: Comparison of the results of the TPD/O analysis of Printex U at PSI (initial weight: 1.438 mg) and the external elemental analysis (initial weight: 2x 20 mg). The agreement comparison is also shown.

	elemental analysis [%]	PSI [%]	% of elemental analysis
C	94	90.6	96
H	0.8	0.9	111
N	0.34	0.00	26
S	0.25	0.01	4
O	3.8	2.6	69
Sum	99.1	97.5	98

Under consideration of the fact, that the error of the elemental analysis was reported by the external laboratory to have a mean value of 0.5% for all

components, one might conclude that the error of the TG-FTIR analysis is large in comparison. However, it has to be taken into account that the error estimation of the elemental analysis was performed with pure substances and not with mixtures, e.g. pure graphite was used for the carbon calibration. PM samples on the other hand contain all compounds in parallel, which are in addition imbedded in different structures. This might lead to cross-sensitivities, which could not be considered by the calibration with pure substances [159]. Therefore, only a repeated elemental analysis of Printex U would give the correct error of the elemental analysis, which was not possible due to budget reasons [159].

Table 14 shows the relative error of the measurement of each PM component determined by repeated TPD/O analyses in the TG-FTIR system.

Table 14: Relative measurement errors for each PM component estimated from Printex U in the TG-FTIR system. The error for nitrogen had to be evaluated from measurements of other PM samples, since the nitrogen content of Printex U was too small for meaningful analysis.

component	relative measurement error [%]
EC	1
OC - funct. gr.	3.5
"free" sulfate	10
nitrogen	4.8
oxygen	5.1
hydrogen	17.3
water	16.9
ash	0.6
initial weight	0.6

Nitrogen had to be estimated from measurements of other PM samples since its amount in Printex U was too small to give meaningful results. The relative error of ash was estimated to be the same as the relative error of the initial weight, which was estimated from the repeated insertion of one sample in the TG

furnace. The errors for EC, OC, oxygen, nitrogen and ash are in a very low range. For sulfate and especially for water and hydrogen the error is larger, but still acceptable.

4.4. Results of the reactivity analysis

4.4.1. VW Sample 2

Most of the samples presented in the previous chapter were also investigated in terms of reactivity with different reactive gases.

First, the functionality of the TG-FTIR system was validated by means of the reactivity analysis of Sample 2, obtained from VW with the four different reactive gas compositions shown in Table 11. Figure 30 shows the mass loss of the samples in percent of the initial mass plotted over temperature. In the temperature range up to 300°C, no significant difference between the curves can be observed and therefore OC desorption is supposed to be responsible for the mass loss. At 300°C, the mass decreases significantly for the experiments with NO₂ in the feed gas due to NO₂-oxidation of the carbon. Additionally, a small difference between the experiments with dry and humid feed gas is discernible, whereby the influence of water was even stronger when co-fed with NO₂. The onset-temperature of soot oxidation by oxygen was 540°C and the mass decreased fast at higher temperatures. In the presence of both oxygen and NO₂, there is a transition between both oxidation regimes, which makes the start of the soot oxidation by oxygen less clearly defined compared to an experiment with a feed containing only 10% O₂. The curve intercept at 600°C shows the growing influence of water in this temperature region and the decreasing influence of NO₂. With NO₂ and water in the feed, the soot was completely oxidized at 620°C, while 627°C was required, when only water was added. The

oxidation reaction was completed at 637°C for the experiment with NO₂ and at 647°C, when only the base feed was dosed.

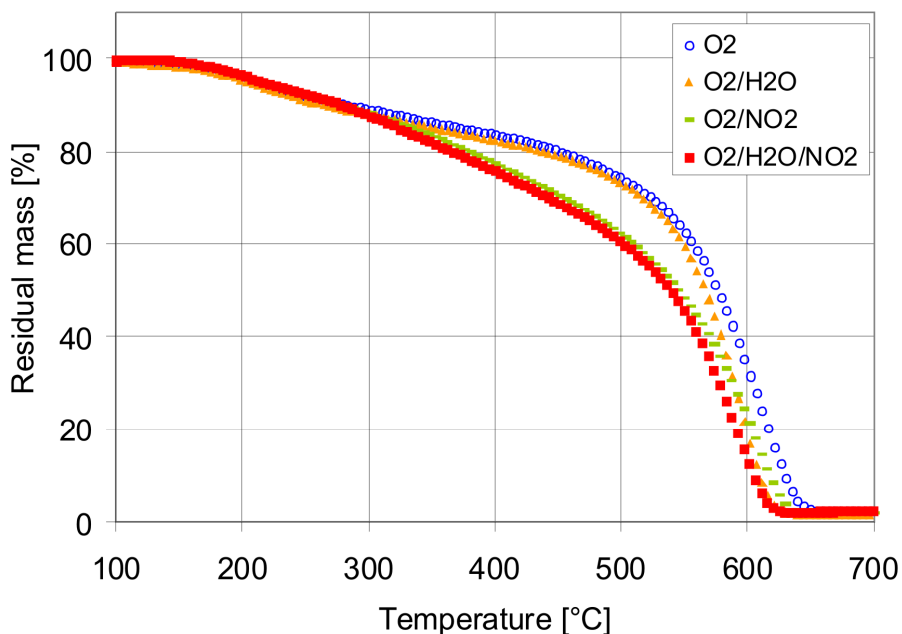


Figure 30: Mass loss curves during the TPO of VW Sample 2 with four different gas compositions.

Figure 31 a and b show the concentrations of CO and CO₂ for all tests, measured with FTIR spectroscopy. In general, the observations from Figure 30 are confirmed by the graphs in Figure 31, but due to the much higher sensitivity of the FTIR signal compared to the mass signal, the features are much more pronounced and the differences are more clearly visible. Already at temperatures less than 200°C, a small difference in the released CO₂ between the experiments with and without NO₂ can be noticed. At higher temperatures the influence of water became visible by the shift of the peak maxima of CO and CO₂ to lower temperatures for the experiments with humid feed gas. The amounts of CO₂ were significantly higher than those of CO, but the amounts differed in dependence of the reactive gas composition. Therefore, the ratio

CO₂/CO was calculated for each CO₂-CO pair in the data sets. In Figure 32 this ratio is plotted over temperature. The CO₂/CO ratios reveal important information about the reaction mechanism and the formed surface functional groups. Below 300°C, the data did not show distinct trends, but at higher temperatures, the ratios in presence of H₂O were significantly higher than those without H₂O. In the presence of NO₂ and H₂O the highest ratios were observed. The ratios in the presence of NO₂ and O₂ were higher than those without NO₂, up to 400°C, but decreased below the latter between 400-580°C. Above 650°C the present carbon amounts were too small to analyze the trends.

The C-oxidation rates of the reactivity experiments of VW Sample 2 are plotted in Figure 33. The data were calculated from the FTIR data of CO₂ and CO. In the NO₂-free experiments (gas mixture 1 and 2 in Table 11), the carbon oxidation rates (C-oxidation rates) up to 400°C were primarily determined by desorption of CO_x, which resulted from the decomposition of surface functional groups. The rate increase above 400°C was due to oxidation by oxygen.

In the presence of NO₂ (gas mixture 3 and 4 in Table 11), increased oxidation rates were observed at temperatures below 200°C due to the increased formation of reactive O- and N-functional groups on the soot [40, 52]. These oxidation rates were further increased by the addition of water. Due to the diffusion limitation of NO₂, the oxidation rates level out between 350°C and 500°C. Above 500°C, the oxidation rates increased significantly for all of the reactive gas compositions and the influence of water on the oxidation behavior became more pronounced. In the experiments with humid reactive gas, the C-oxidation rate maxima were shifted to lower temperatures, which can be observed from the crossing curves for gas mixtures 2 and 3.

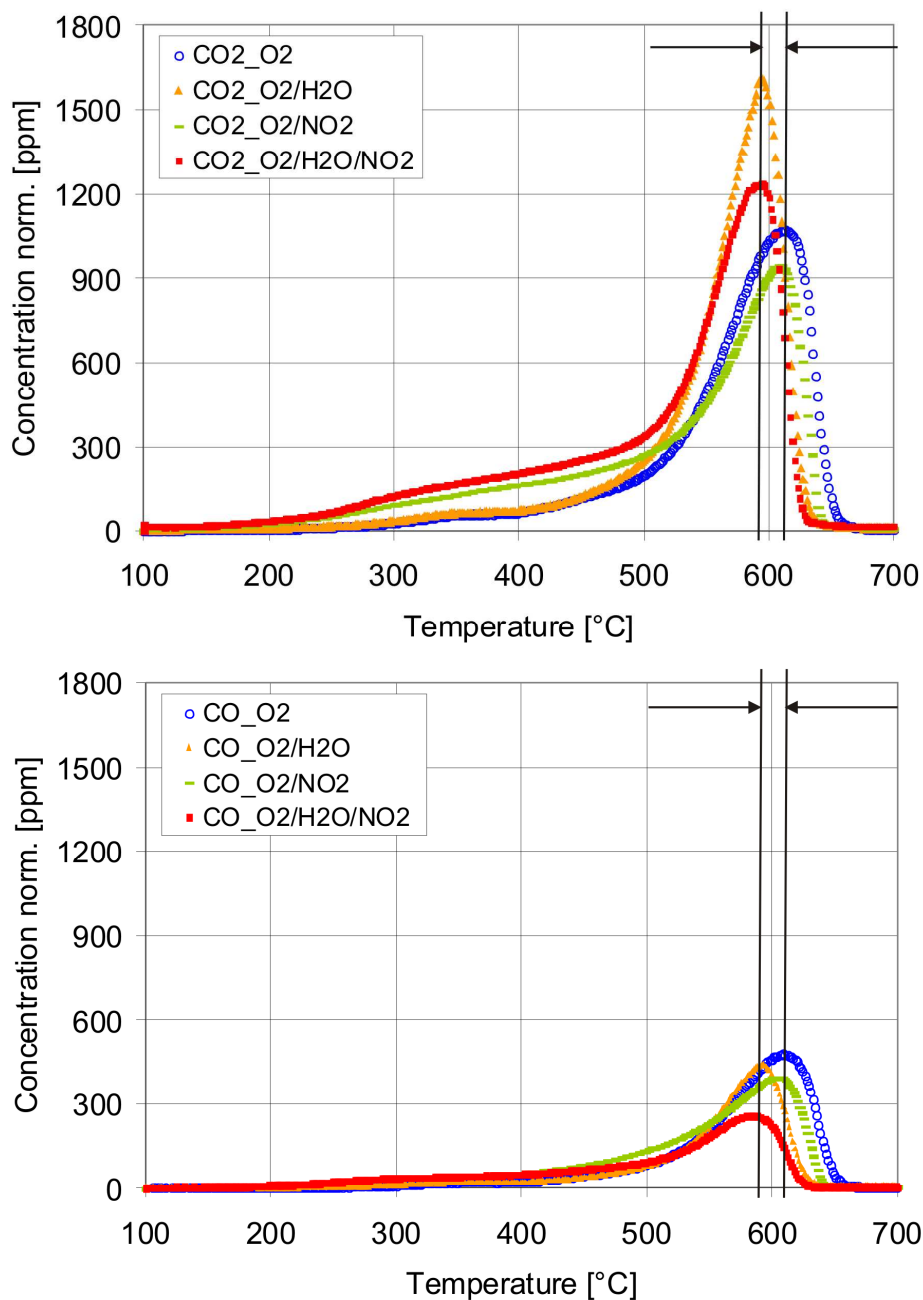


Figure 31: FTIR signals of CO₂ (upper graph) and CO (lower graph) during the TPO analysis of VW Sample 2 with four different gas compositions. The arrows indicate the temperature shift due to water dosage. The detected amounts of CO₂ and CO were normalized to the initial weight of the samples in order to simplify the comparison.

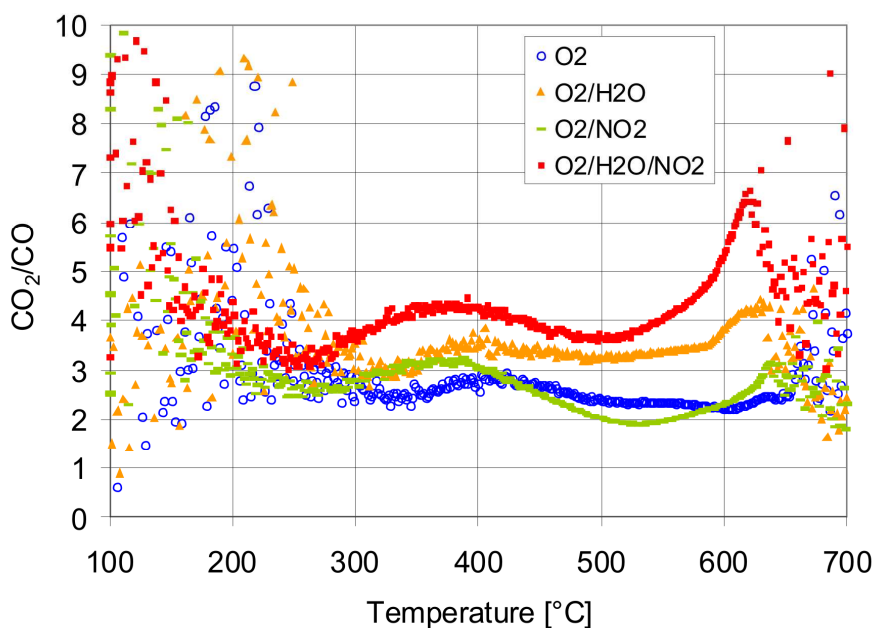


Figure 32: CO₂/CO ratios versus temperature of VW Sample 2 calculated from the FTIR data measured for the different gas compositions.

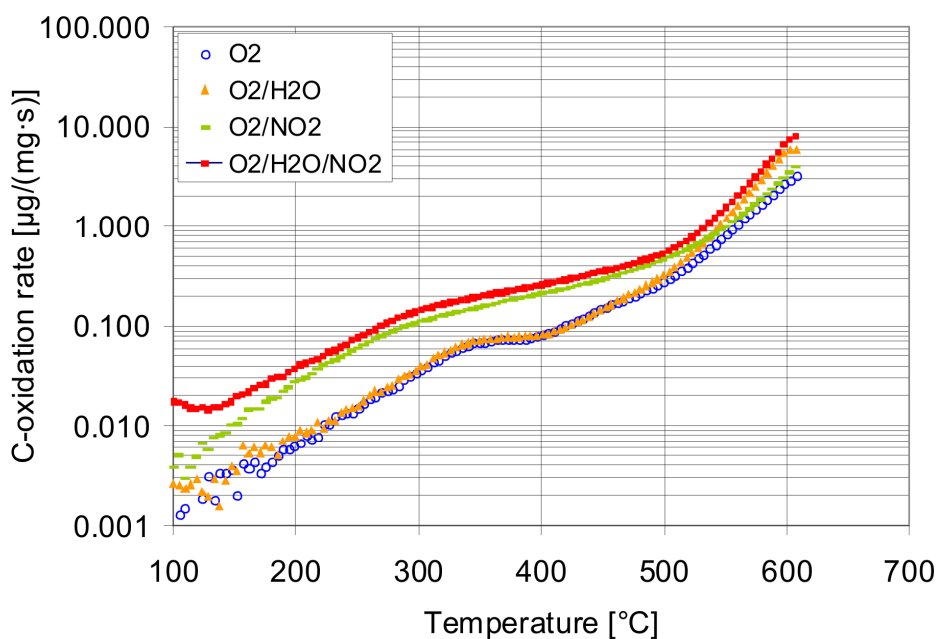


Figure 33: C-oxidation rates during the TPO of VW Sample 2 with four different gas compositions, calculated from the amounts of CO₂ and CO for the different gas compositions. The data are plotted up to 99% carbon conversion.

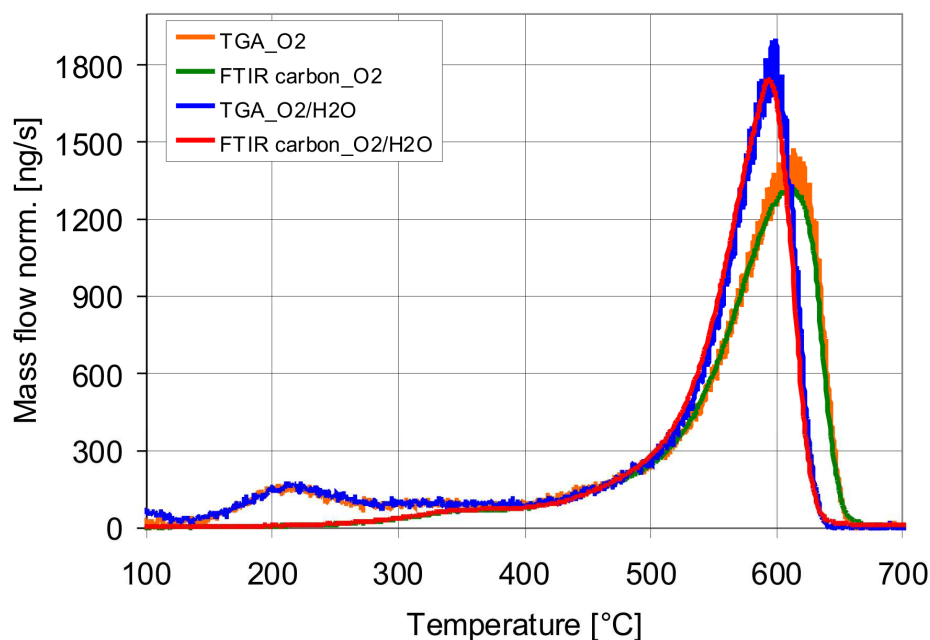


Figure 34: Comparison of the mass flows calculated from the TGA mass loss curves and from the carbon amounts detected as CO₂ and CO in the FTIR spectrometer for the experiments with 10% O₂ and 10% O₂ + 5% H₂O in the feed gas.

The reactivity experiments of VW sample 2 were also used to check and compare the fluctuation of the data generated by the FTIR spectrometer and the TGA. Therefore, the mass flows of the TGA and the FTIR spectrometer were calculated in [ng/s]. For the calculation of the TGA mass flow the mass loss signal was used and the spectrometer mass flow was calculated from the amount of carbon released by CO₂ and CO. Figure 34 shows the comparison of the mass flow curves. The small increase of the TGA mass flows in comparison to the spectrometer mass flow at the beginning of the measurement was due to the release of non-carbon components, which were not considered in the calculation of the spectrometer mass flow. It is obvious that the fluctuations of the FTIR data were significantly smaller than those of the TGA. The small fluctuations were also the reason that changes of the carbon oxidation could be

seen from the FTIR results in Figure 31 around 200°C, while the TGA did not detect any changes in the temperature range (Figure 30).

4.4.2. Printex U, Euro 0, Euro V and the mixed soot sample

After the first experiments with VW Sample 2, the reactivities of Printex U, the Euro V sample, the Euro 0 sample and the mixed soot were investigated. As reactive gases mixtures 10% O₂, 10% O₂ + 5% H₂O and 10% O₂ + 5% H₂O + 1000 ppm NO₂ (mixtures 1, 2 and 4 in Table 11) were used. Figure 35 - Figure 37 show the C-oxidation rates of the Euro V sample, the Euro 0 sample and the mixed soot plotted over temperature. In each figure the C-oxidation rates of Printex U were added in order to facilitate the comparison between the results.

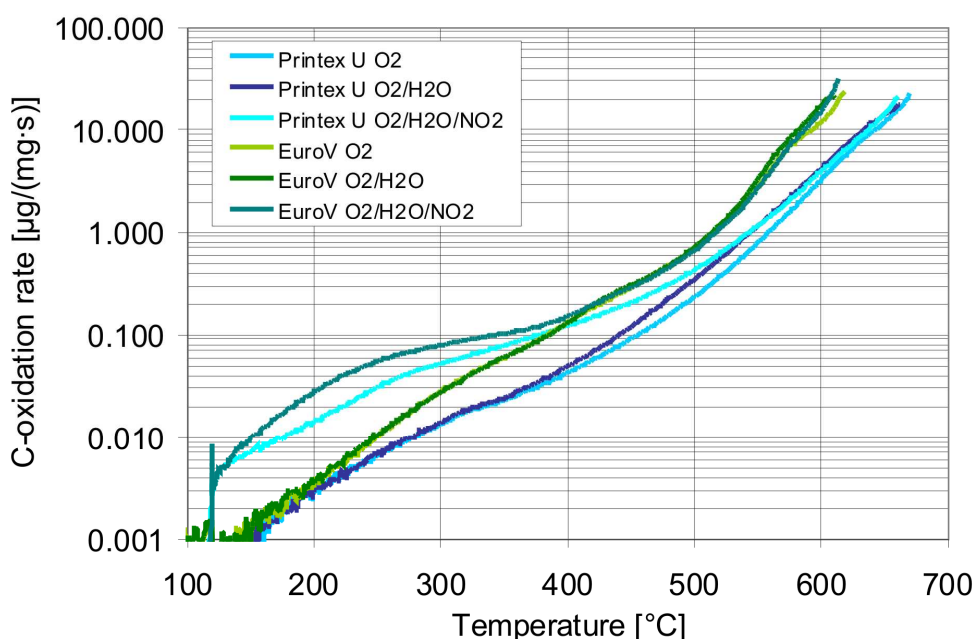


Figure 35: C-oxidation rates calculated from the amounts of CO₂ and CO of Printex U and the Euro V soot by TG-FTIR measurements with three different reactive gas mixtures (10% O₂, 10% O₂ + 5% H₂O, 10% O₂ + 5% H₂O + 1000 ppm NO₂). The data are plotted up to 99% carbon conversion.

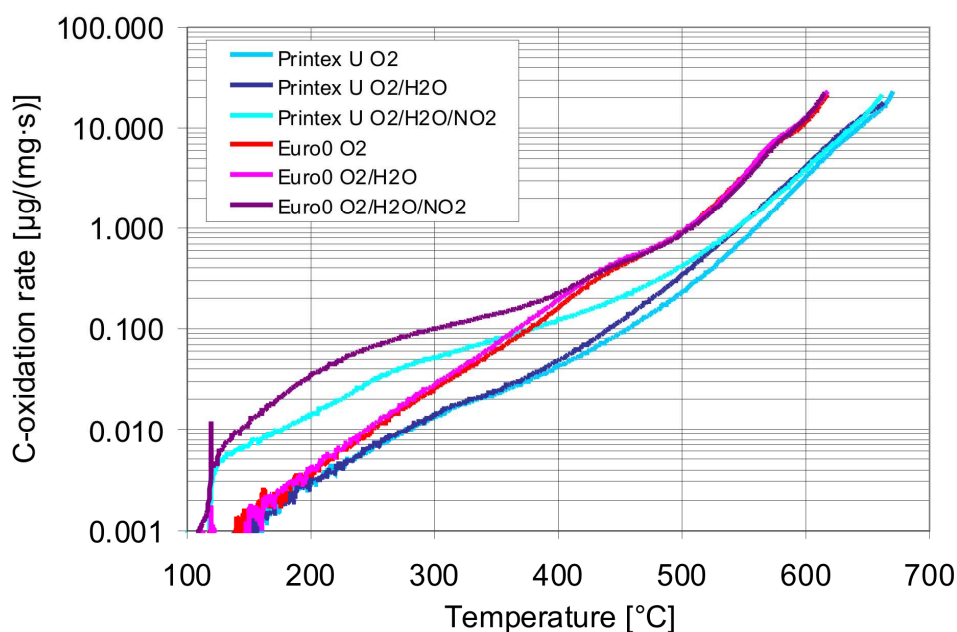


Figure 36: C-oxidation rates calculated from the amounts of CO₂ and CO of Printex U and the Euro 0 soot by TG-FTIR measurements with three different reactive gas mixtures (10% O₂, 10% O₂ + 5% H₂O, 10% O₂ + 5% H₂O + 1000 ppm NO₂). The data are plotted up to 99% carbon conversion.

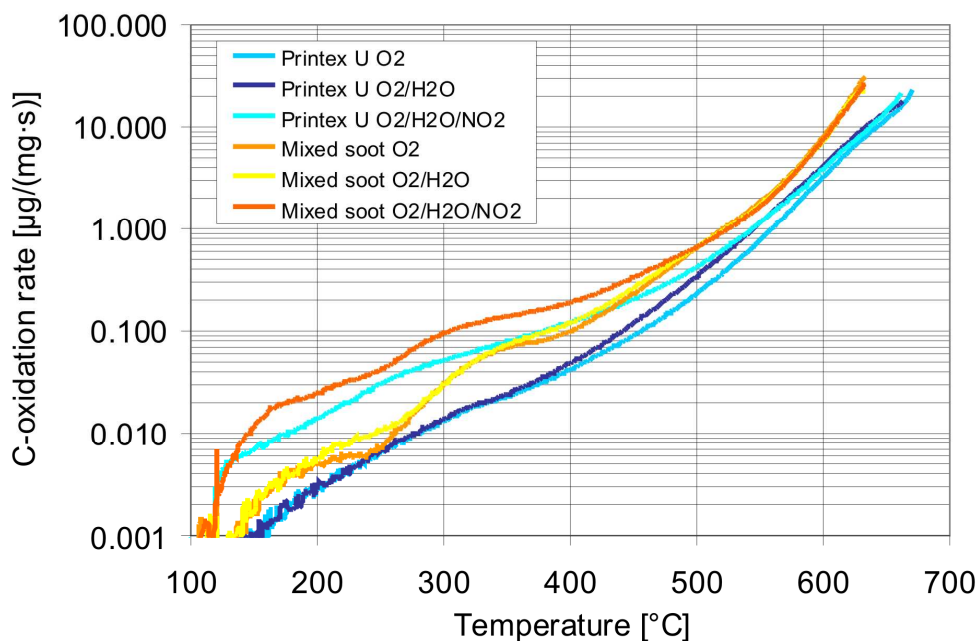


Figure 37: C-oxidation rates calculated from the amounts of CO₂ and CO of Printex U and mixed soot sample by TG-FTIR measurements with three different reactive gas mixtures (10% O₂, 10% O₂ + 5% H₂O, 10% O₂ + 5% H₂O + 1000 ppm NO₂). The data are plotted up to 99% carbon conversion.

The C-oxidation rates of the Euro V and Euro 0 sample showed hardly any difference in the temperature range between 100°C and 350°C in the presence of O₂ and also in the presence of O₂ + H₂O. Between 100°C and 200°C the rates were also similar to those of Printex U, but above 200°C they became higher in comparison to Printex U. Between 350°C and 540°C the Euro 0 sample became more reactive than the Euro V sample, but still only slight gas-dependent differences between the two gas mixtures could be observed for both samples.

The mixed soot showed larger C-oxidation rates between 100°C and 200°C than the other three samples in the presence of O₂ and O₂ + H₂O. Between 200°C and 270°C it was more reactive in the presence of O₂ + H₂O than in the presence of O₂. In the presence of O₂ the C-oxidation rates were even smaller than those of the Euro V and Euro 0 sample in that temperature range. Above 270°C the C-oxidation rates of the mixed soot samples increased again in the presence of O₂. After that the reactivities in the presence of O₂ and O₂ + H₂O of the mixed soot were again higher than those of the other samples up to 385°C. With increasing temperature the C-oxidation rates fell below those of the Euro V and Euro 0 sample, but still remained higher than those of Printex U.

When NO₂ was added to the reactive gas at 120°C the oxidation rates increased significantly for all samples in the range between 120°C and 350°C. Again Printex U was the most unreactive sample of the series, while the Euro 0 sample was again the most reactive. The mixed soot showed a similar behavior as in the presence of O₂ and O₂ + H₂O as its reactivity did not show a constant increase with temperature. Between 300°C and 400°C the C-oxidation rates flatten out for all samples. Around 400°C the oxidation rates of the three diesel soot samples approached each other independent of the reactive gas composition. Only Printex U with O₂ and O₂ + H₂O did not follow this trend and remained below the curves of the other samples. The oxidation rates became completely

independent of the reactive gas composition above 500°C and were determined only by the carbon structure. Printex U was the sample with the lowest reactivity and the Euro V and 0 soot showed the highest reactivity in that temperature range.

4.4.3. Graphite and GfG soot

The reactivity analysis of the powder samples was closed with the investigation of the graphite sample and the GfG soot. In Figure 38 the C-oxidation rates of these investigations in the presence of 10% O₂ and 10% O₂ + 5% H₂O are shown. The rates were much higher for the GfG soot indicating its higher reactivity in comparison to graphite. The C-oxidation rates for graphite are only shown up to 50% conversion because the largest part of the sample was gasified in the isothermal segment at 780°C. Below 440°C, hardly any oxidation was observed for graphite. Water exerted only minor influence on the oxidation behavior of both samples, although for different reasons in each case. The surface of the GfG soot was very reactive and could not be further activated by the addition of water. However, graphite has an inert surface that cannot be attacked by water in the selected temperature range. For the GfG soot, the C-oxidation rates showed several peaks likely due to the presence of carbon structures with different reactivities as will be discussed later. The C-oxidation rates of graphite did not show any peak - only a steep ascent above 440°C. This behavior could also be observed by comparing the mass loss curves of graphite, GfG soot and VW-Sample 2 in Figure 39. The GfG soot showed a higher reactivity than the real diesel PM sample at temperatures up to 600°C. Above that temperature VW Sample 2 became more reactive.

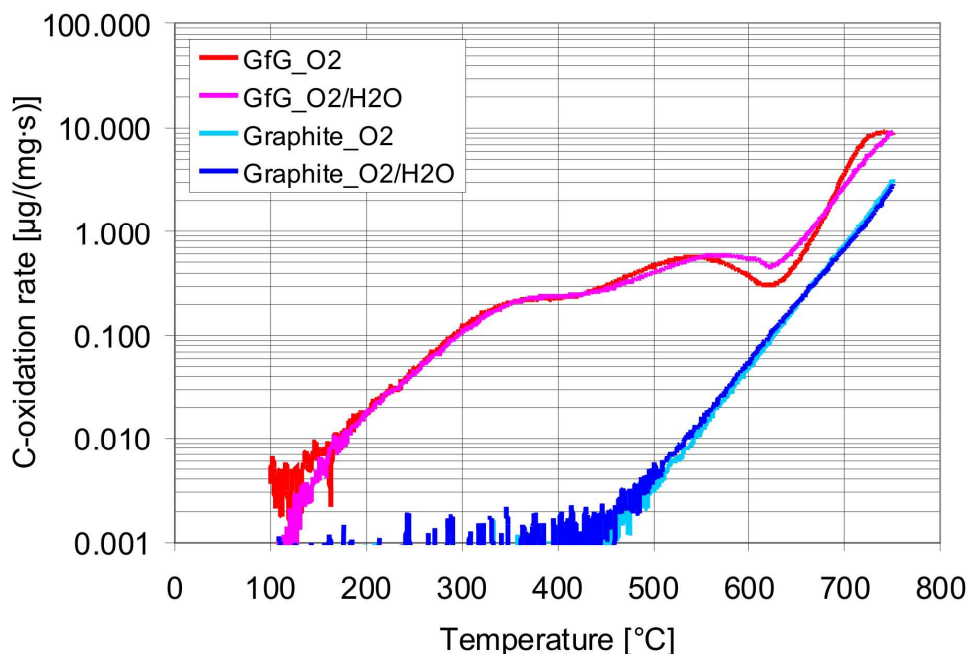


Figure 38: C-oxidation rates calculated from the amounts of CO_2 and CO of the GfG soot and graphite sample by TG-FTIR measurements with two different reactive gas mixtures (10% O_2 , 10% O_2 + 5% H_2O). The data are plotted up to 99% carbon conversion for the GfG soot and only up to 50% for graphite.

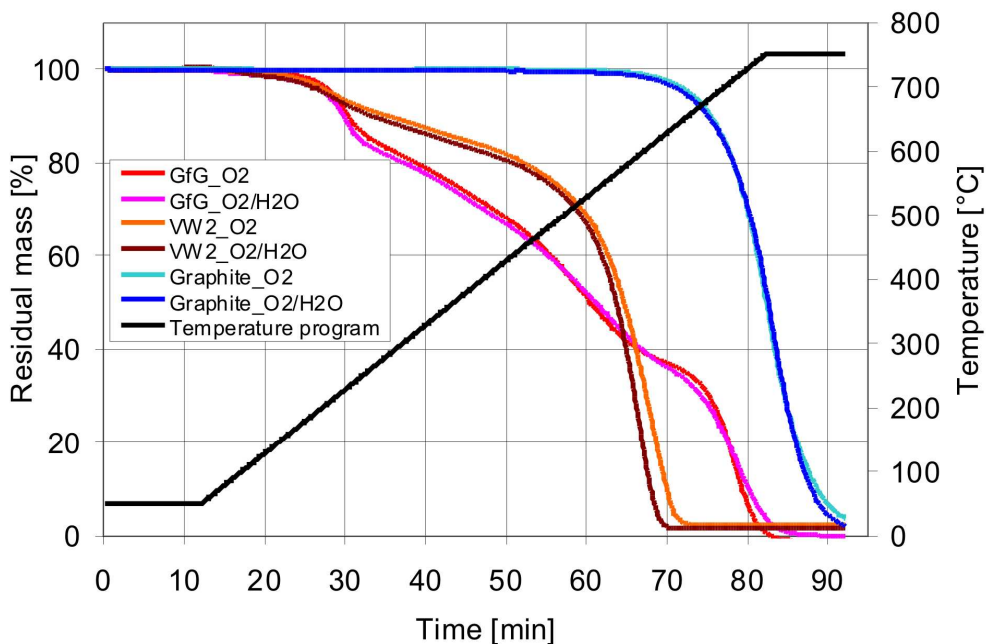


Figure 39: Mass loss during the TPO experiments with GfG soot and VW Sample 2 plotted over the experimental period.

Graphite and GfG soot were also investigated at the Institute of Water Chemistry and Chemical Balneology at the TU Munich in TPO investigations using a heating ramp of 5°C/min. The mass conversion was 12% for graphite at the TU Munich and 15% at Paul Scherrer Institute at temperatures up to 700°C; the mass conversion was 98% for a fresh sample of the GfG soot at the TU Munich and 82% for a sample aged in air at PSI at temperatures up to 700°C. Considering that the heating ramp was two times higher during this work, the agreement of these results is satisfactory.

4.4.4. PM samples on metal filters

The reactivities of the six samples from the RWTH on metal filters were also examined. The results using dry and humid reactive gas (10% O₂ and 10% O₂ + 5% H₂O) are compared in Figure 40. The deviations within the given pairs A, B, C were small in comparison to the deviations between the different samples and the different reactive mixtures in the according regions. In comparison to the powder samples the C-oxidation rates of the samples on metal filters showed large fluctuations up to 200°C, so that the data could not be analyzed between 100°C and 200°C.

The data show clearly, that the operation conditions during soot generation and the collection temperature influenced the oxidation behavior. Between 200°C and 380°C the reactivity order was B1/B2 > A1/A2 > C1/C2 independent of the reactive gas composition. Above 380°C the order changed and samples A were most reactive: A1/A2 > B1/B2 > C1/C2 – also independent of the reactive gas composition. These reactivity orders derived from the C-oxidation rates, agreed well with the results from the RWTH Aachen (Figure 41) [158].

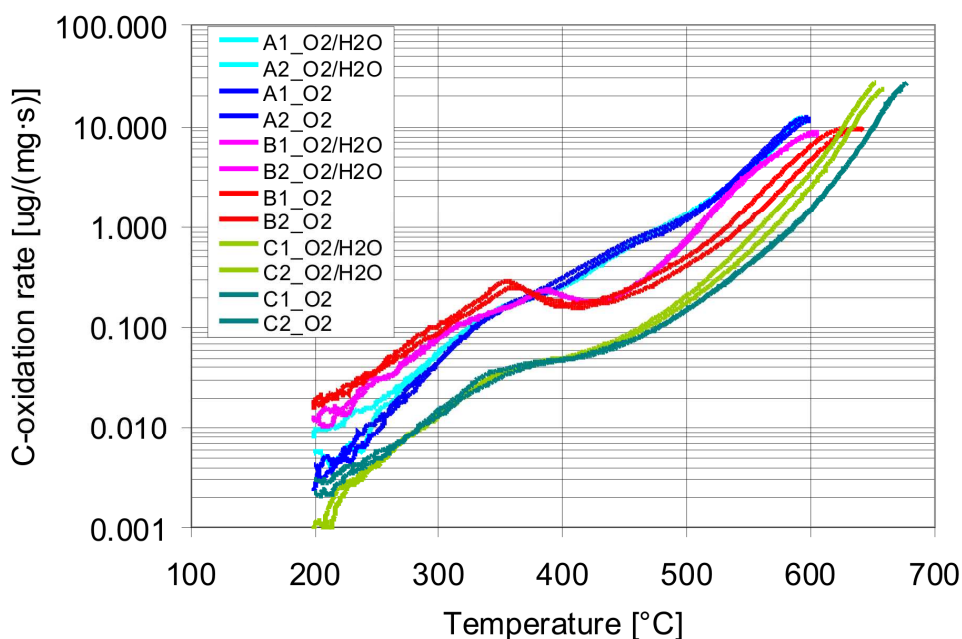


Figure 40: C-oxidation rates calculated from the amounts of CO₂ and CO for samples A1, A2, B1, B2, C1 and C2 with 10% O₂ and 10% O₂ + 5% H₂O in the reactive gas. The data are plotted up to 99% carbon conversion. As the signals fluctuated strongly the data below 200°C could not be analyzed.

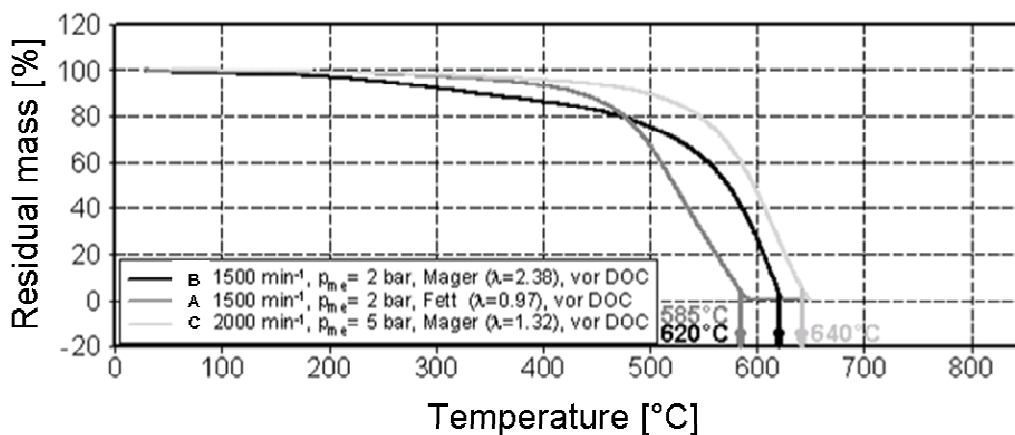


Figure 41: Mass loss curves of the samples A, B and C received from thermogravimetric experiments at the RWTH Aachen [158].

Sample pair B was most reactive below 380°C as it was collected at the lowest temperatures. Therefore, the C-oxidation rate consisted of both thermal OC desorption and EC oxidation in parallel leading to a broad peak around 350°C. Above 380°C samples A became most reactive, as they were collected under

fuel rich conditions. The combustion under fuel rich conditions led to incomplete fuel combustion in comparison to lean conditions, leading to the formation of less dense carbon structures.

Samples C1 and C2 exhibited the highest oxidation temperatures in the series because they were collected at higher engine loads. This led to the formation of large EC amounts (Figure 29), which are probably rather graphitic and so less reactive than the structures formed under the other operational conditions in the series.

The addition of water yielded no increase in the reactivity for samples A, but for samples B and C. Below 400°C, the oxidation of samples B was slightly inhibited in the presence of water, but above 480°C water enhanced the oxidation rates. The oxidation of samples C was not influenced by water below 450°C, but above this temperature an enhancement was observed.

The influence of water in the reactive gas was also reflected by an increase in the CO₂/CO ratio for all samples.

4.5. Discussion of the reactivity analysis

4.5.1. Trends of the C-oxidation rates

The results obtained for the oxidation of VW Sample 2, which was used as base for the development of the reactivity analysis method with different reactive gas compositions, were in agreement with the general reactivity order reported by Stanmore et al. [22]: O₂ < O₂/H₂O ≈ O₂/NO₂ < O₂/H₂O/NO₂. Also Printex U, the Euro V and Euro 0 samples, the mixed soot sample as well as sample B and C of the RWTH Aachen followed these trends. Samples A on metal filters, the graphite sample and the GfG soot, however, did not follow this trend as their reactivity was not enhanced by the addition of water.

The C-oxidation rates of VW Sample 2 for different reactive gases show the typical trends of PM oxidation. In the presence of O_2 and $O_2 + H_2O$ an ascent up to $200^\circ C$ and $250^\circ C$ was observed, which is mainly driven by desorption and oxidation of OC. The oxidation of EC started not until $200^\circ C$ since O_2 did not form surface functional groups, which decompose below that temperature range [37, 59]. In the presence of NO_2 the oxidation of EC started already at $120^\circ C$ in parallel to the OC desorption, as the direct increase of the C-oxidation rates after the beginning of the NO_2 dosage indicated. Between $300^\circ C$ and $400^\circ C$ the C-oxidation rates flattened out due to the total removal of OC, the limited reactivity of O_2 to form unstable surface groups in that temperature range and in the experiments with NO_2 in the feed gas, also due to NO_2 diffusion limitation. With increasing temperature the C-oxidation rates increased again because O_2 started to form surface functional groups, which decomposed quickly. The relative influence of NO_2 decreased more and more as the amount of NO_2 dosed was limited, but the influence of water increased leading to the intersection of the $O_2 + NO_2$ and $O_2 + H_2O$ curves.

However, there were also samples like the GfG soot, the mixed soot and samples B on the metal filters, which show one or two peaks in the C-oxidation rates. From the course of these curves it was concluded, that these samples contain structures of different reactivity occur. Concerning the GfG soot, this was already shown by Su et al. [16], whose samples were also generated on a Palas soot generator by spark-discharging. In thermogravimetric and TEM investigations the authors found that the GfG soot consists of two kinds of structures: first, small primary particles consisting of strongly curved graphene layers with defective surfaces, which can be easily oxidized, and structures of larger primary particles, which are less defective and curved showing a less reactive behavior.

From the results obtained for graphite and GfG soot it can be furthermore concluded that the unreactive structure in the GfG soot is most probably similar to that of graphite as the slope and the onset temperature of the increase above 630°C for both samples were similar. The VW Sample 2 on the other hand did most probably not contain graphitic structures, as it was more reactive than the GfG soot above 600°.

As already mentioned, the mixed soot sample and samples B on the metal filter showed a similar behavior. In the case of the mixed sample such behavior was expected as the sample is a mixture collected from the exhaust gases of different engines and operation conditions. In the case of samples B the lean conditions seemed to lead to the formation of a graphitic structure and a reactive surface layer, which was indicated by the larger amount of oxygen found in the composition analysis (Figure 29) and the highest reactivity of the filter samples up to 380°C.

In opposite to this behavior, there were samples like the Euro V and Euro 0 samples and graphite, which showed a steady increase of the rates and only a slight flattening in the presence of NO₂. These PM samples also contained only one carbon structure similar to the samples showing flattening of the curves. However, oxygen was able to form surface functional groups on the surface, which decompose earlier than those formed on samples showing flattening. The slight flattening of the C-oxidation rates of the Euro V and Euro 0 samples in the presence of NO₂ was again due to a NO₂ diffusion limitation.

4.5.2. Influence of water on the oxidation and the CO₂/CO ratios

It was already mentioned, that CO₂/CO ratios calculated from the CO₂ and CO concentrations (Figure 31) measured during the course of a TPO experiment with the FTIR spectrometer act as an indicator for changes in the reaction mechanism. In Figure 32 the CO₂/CO ratios of VW sample 2 are plotted over temperature showing that a change of the feed gas composition had a direct influence on the evolution of CO₂ and CO. In the presence of water the ratio increased significantly over the whole temperature range as exemplified by the experiments with O₂ and O₂ + H₂O as well as O₂ + NO₂ and O₂ + NO₂ + H₂O. This increase seemed to be caused by the water-gas shift reaction (WGS) occurring on the soot surface [39, 142, 160], which converted part of the primary produced CO to CO₂:



Furthermore, the CO₂/CO ratio was influenced by the presence of NO₂. In the temperature range up to 380°C the ratio increased due to an increased formation of carboxylic groups and lactones, which decompose to CO₂ and water [59], so that the CO₂/CO ratio of the O₂ + NO₂ experiment reached the same level as in the O₂ + H₂O experiment. At 380°C the CO₂/CO ratio decreased again for the experiments with NO₂ most probably again due to a diffusion limitation of NO₂. One can speculate that reaction (1.7) becomes the main reaction for the decomposition of oxygen surface complexes, when NO₂ is depleted on the sample surface, leading to an increase of CO evolution. When the temperature was further increased, the CO₂/CO ratio increased again due to the start of the soot oxidation by oxygen.

Moreover, the addition of water shifted the TG profiles (Figure 30) and the maxima of the oxidation rates (Figure 33) as well as the maximum concentrations of CO and CO₂ (Figure 31) to lower temperatures. Several feasible reaction mechanisms are proposed in the literature to explain this influence, but a final explanation has not been found yet. On the first view, the direct oxidation of soot by water does not seem to play an important role, since the oxidation with oxygen is 10⁴ times faster [161], but Ahlström et al. assumed that this reaction might be accelerated by the fast removal of strongly adsorbed hydrogen by oxygen, so that the next water molecule can attack the carbon surface [160]. Furthermore, it is assumed that water changes the structure of the soot surface, as known from the production of active carbon from carbonaceous materials by steam treatment [142, 160]. Neeft et al. proposed an influence of water on the stability of the oxygen surface functional groups [142], which could also explain the observed promoting effect of water. And finally, Jeguirim et al. speculated that HNO₃ and HONO are intermediates of the carbon-NO₂ reaction. In the presence of NO₂ and water these compounds are already present leading to increased C-oxidation rates [37].

4.5.3. Reaction network and mechanistic details of PM oxidation

In the chapter 1 a large part of the soot oxidation reactions reported in the literature was reviewed and discussed. However, a reaction network, which summarizes the mechanistic details during the soot oxidation with O₂ and NO₂ in dependence of the active sites, could not be found in the literature.

In order to close this gap, such a soot oxidation network was constructed with 1-Ethlynaphthalene as example for a PM structure. The scheme is based on elemental organic chemistry and the work of Jeguirim et al. [37], Setiabudi et al. [40] and Messerer et al. [39], who proposed the three reaction pathways for the parallel presence of O₂ and NO₂ were already discussed in the introduction. For this work, it was assumed that the three pathways occur in parallel and not isolated leading to many intersections. The shown reactions also include the reactions, which occur if either O₂ or NO₂ are present alone. Furthermore, the work of Muckenhuber et al. [59], Azambre et al. [53], Otsuka et al. [50], Brückner [51], Nikolaeva et al. [56] and He et al. [55] were considered.

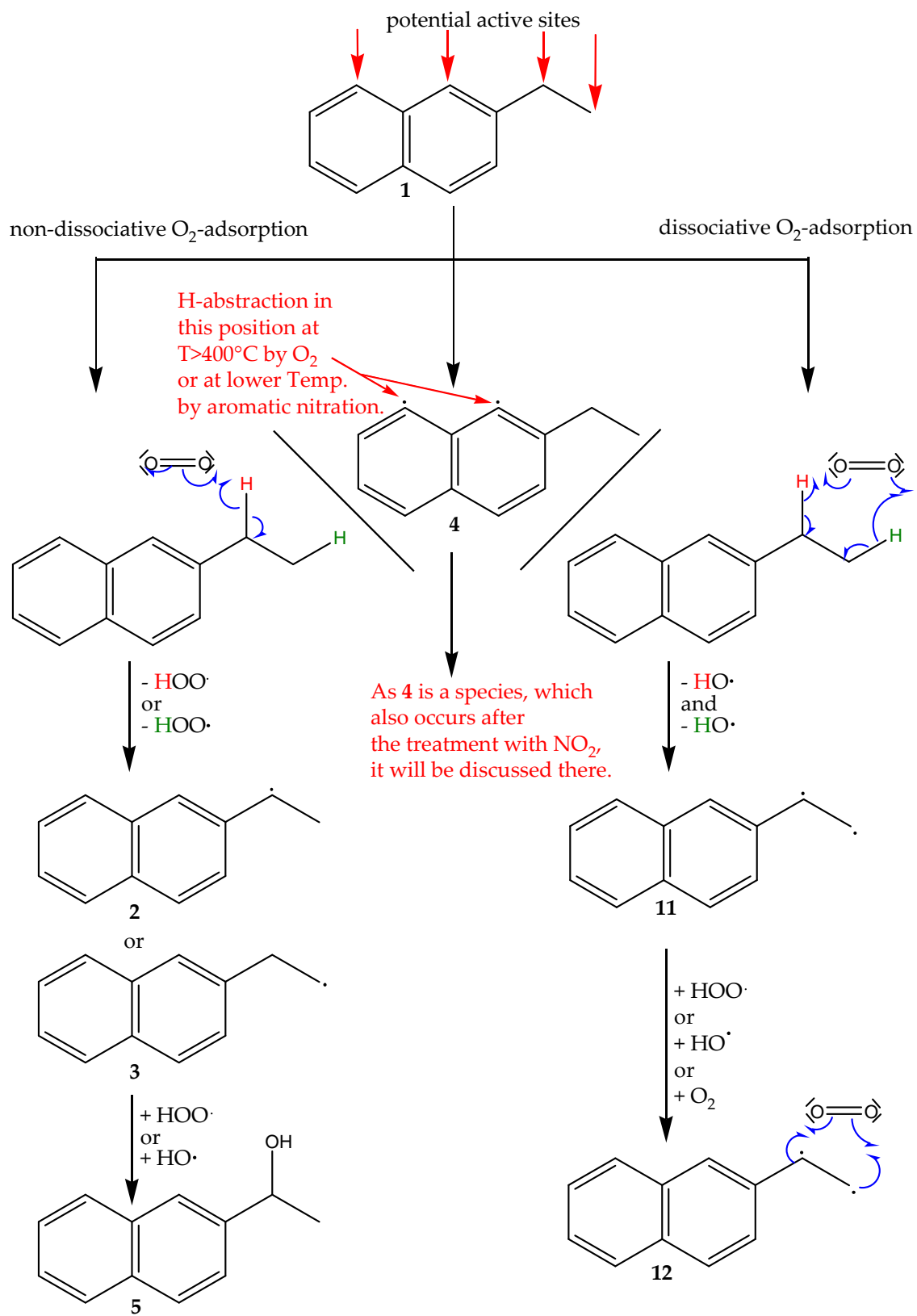
It should be kept in mind, that the reactivities of carbon atoms at edges of defective structures and those in the aromatic system are different. Since the variety of possibilities is too large for a complete discussion, only examples for the different steps are shown. The physisorption of the oxidant, which is the step prior to the reaction of oxidant and surface atoms, is not drawn.

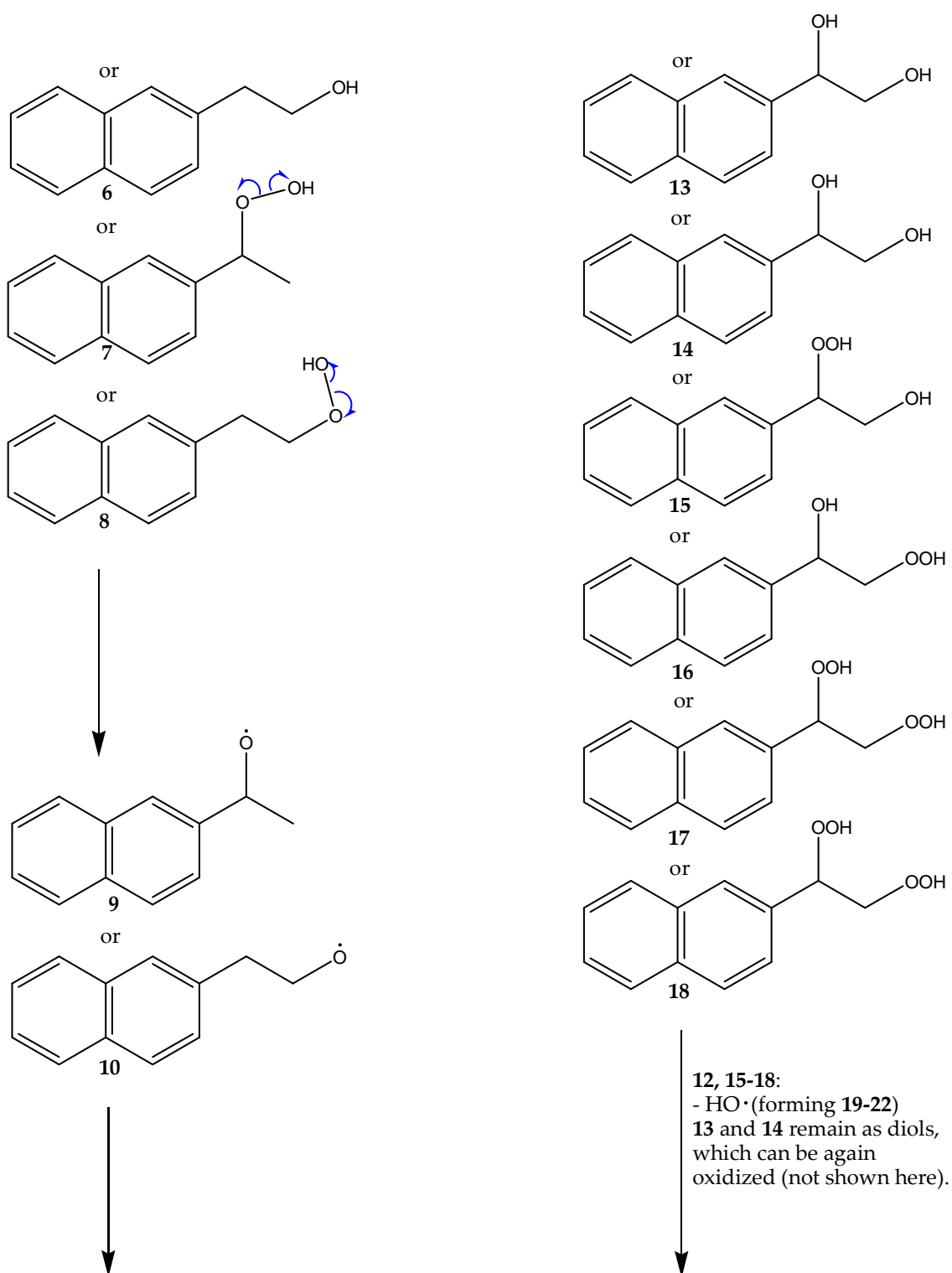
Regardless of the oxidant, the reaction stages are similar: first, hydrogen is abstracted (H-abstraction) by O₂ or NO₂ forming carbon radicals, HOO·, HO· and HONO. In a second step an O-atom is transferred to the surface. The resulting molecules most often also have a radicalic character, which undergo further oxidation reactions or rearrangements. In the end the formed surface functional groups decompose by decarboxylation or decarbonylation (Figure 3).

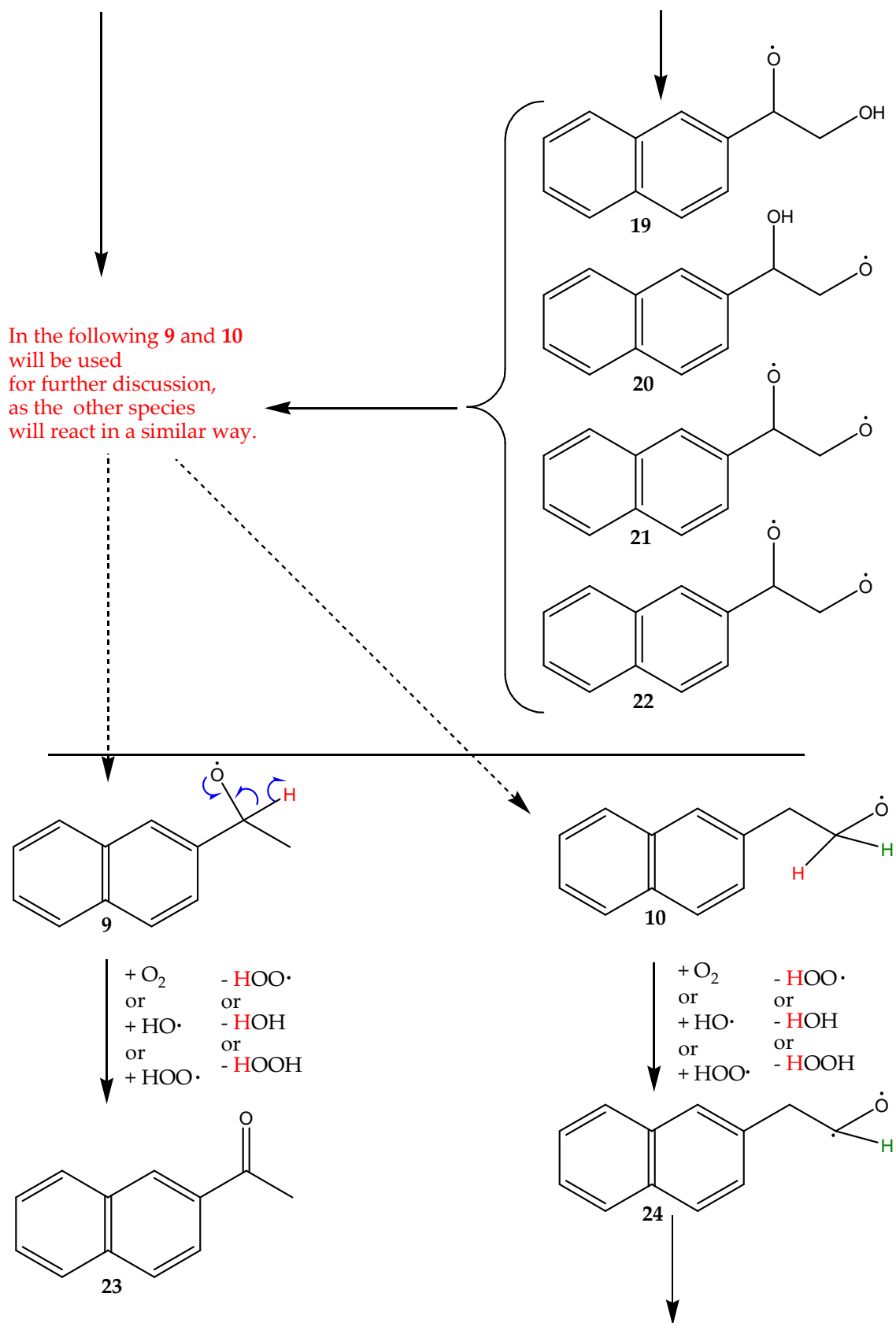
Beside O_2 and NO_2 also $HO\cdot$ and $HOO\cdot$ radicals are able to abstract hydrogen forming water and hydrogen peroxide, which decomposes again into 2 $HO\cdot$ on the soot surface.

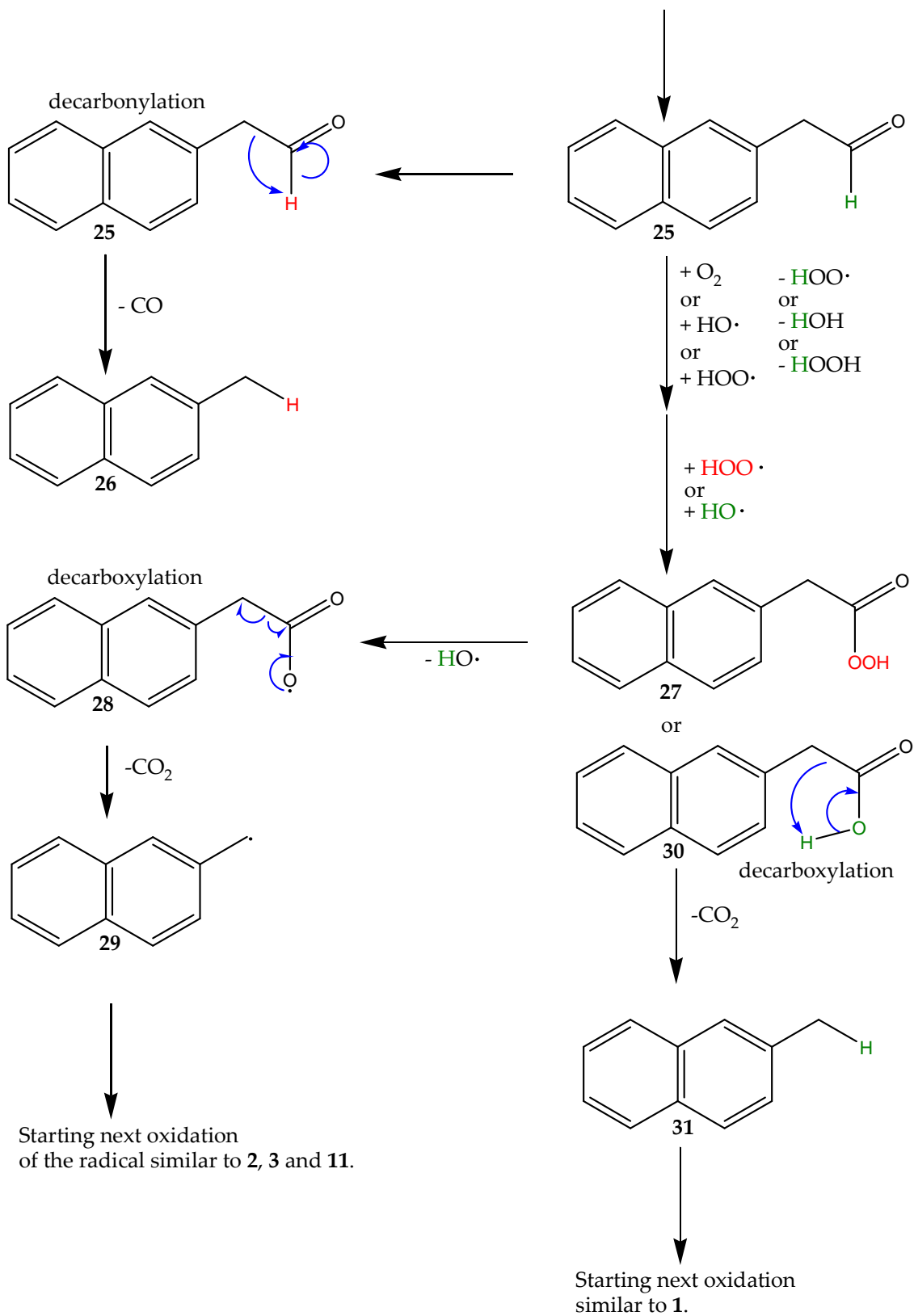
At the beginning of the scheme the O_2 carbon reactions are shown, followed by the reactions of carbon, NO_2 and O_2 . In the last part, specialities of the reactions of ketones and aldehydes are discussed. If a molecule can form several products this is indicated by "or".

Reactions with O₂

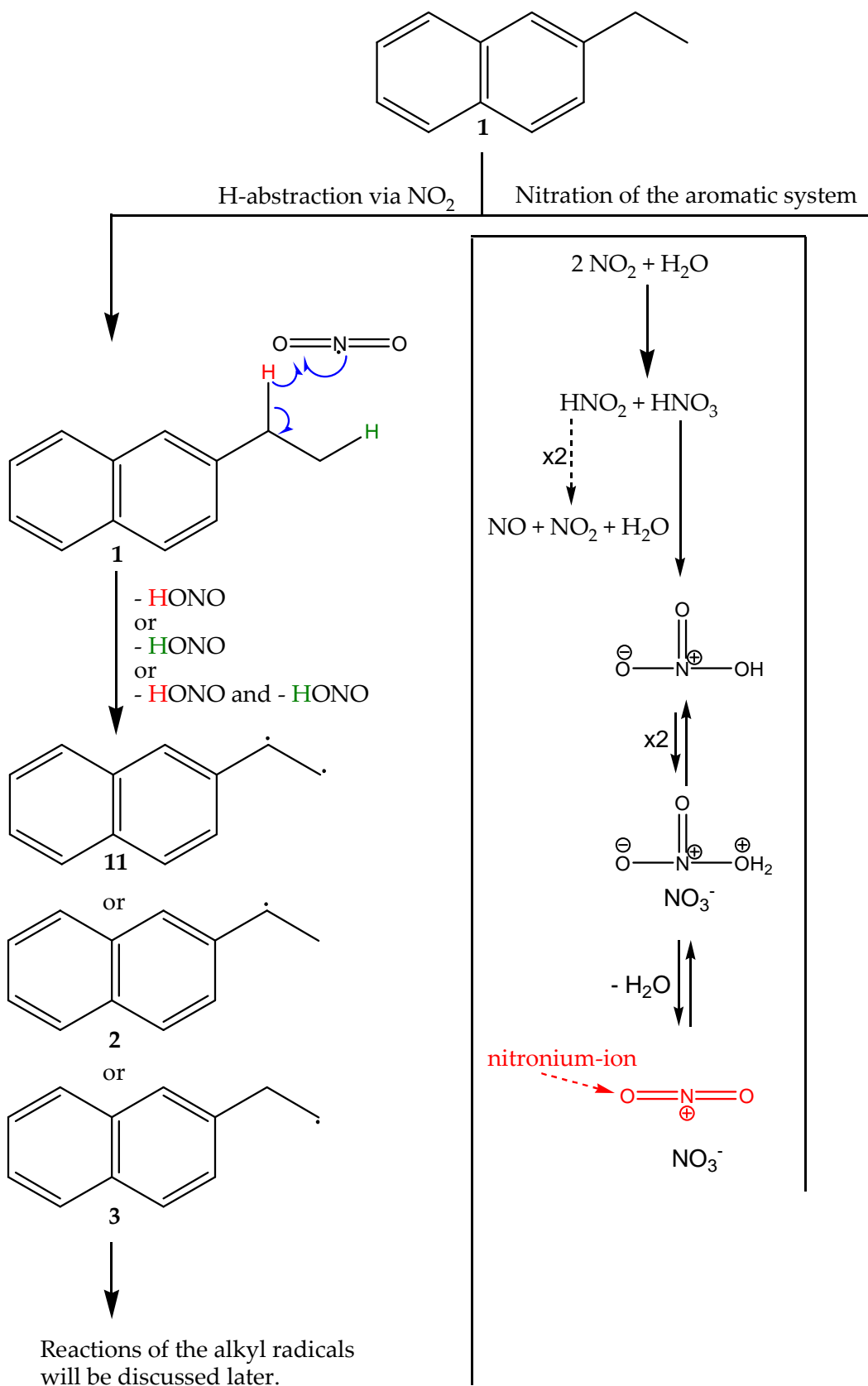


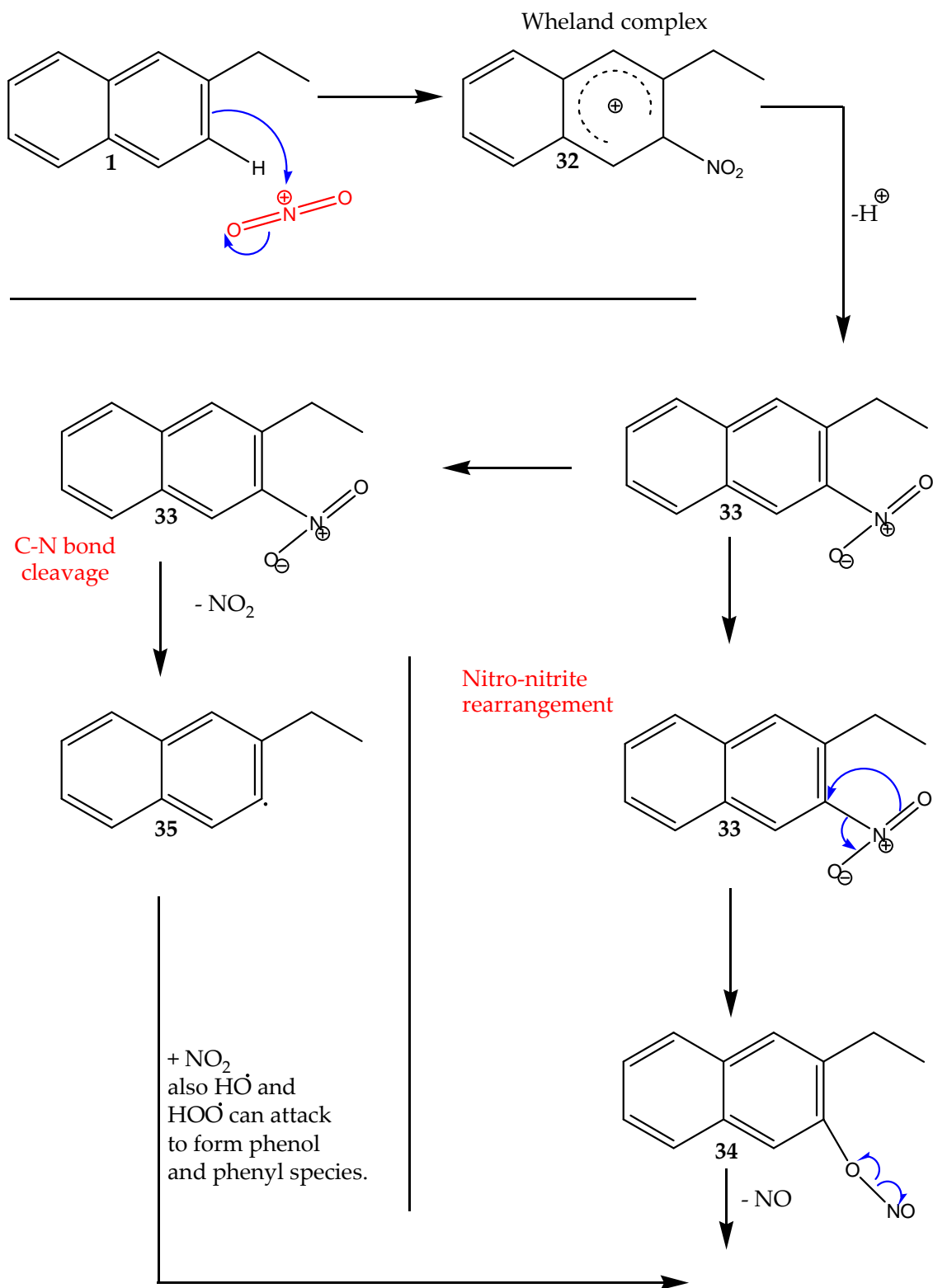


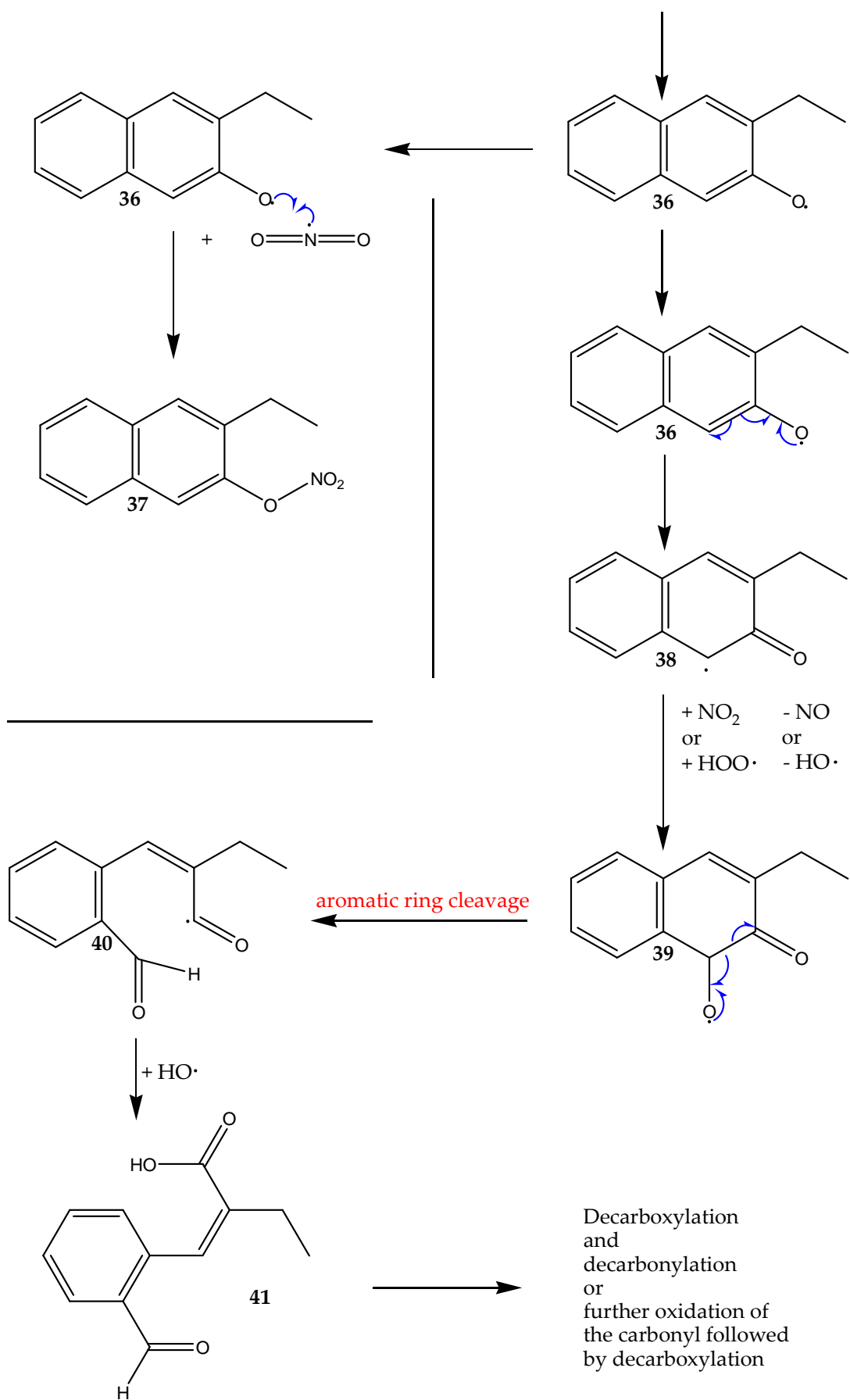




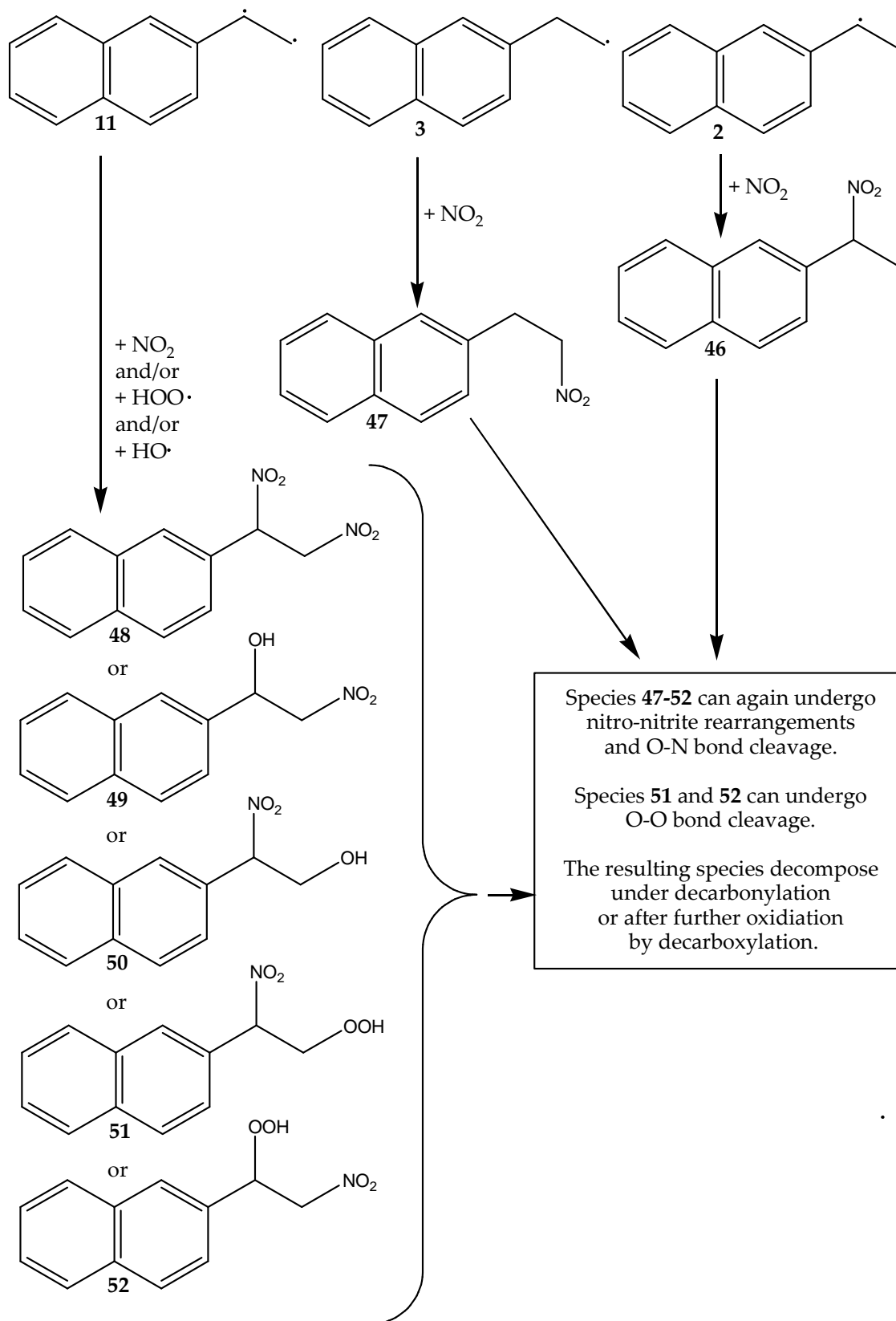
Reactions with NO₂ and O₂





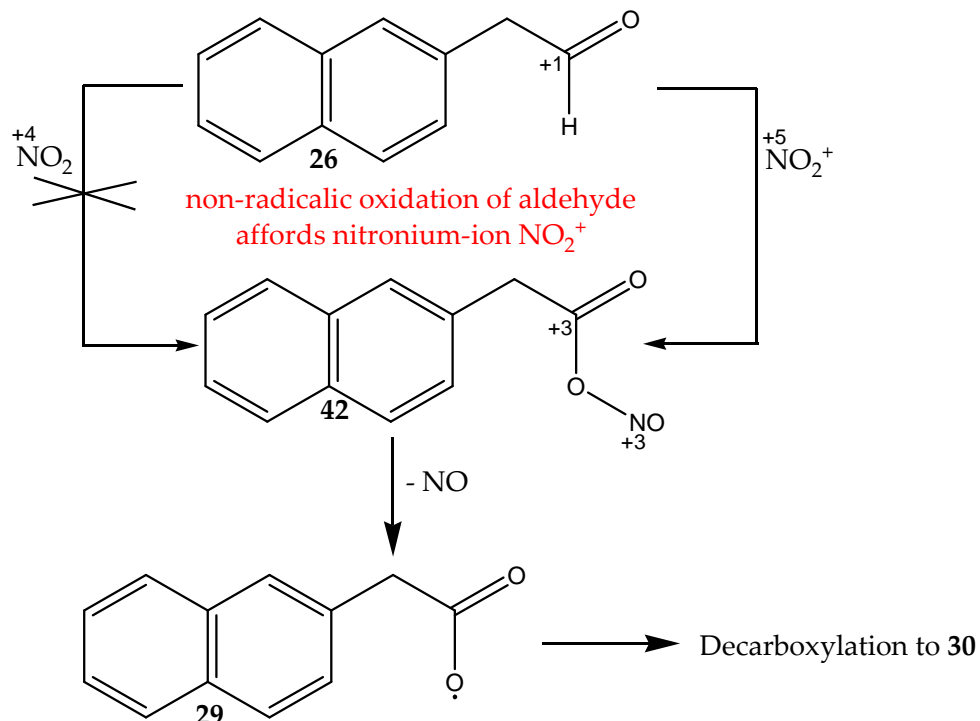


Reactions with NO₂ at the alkyl side chain

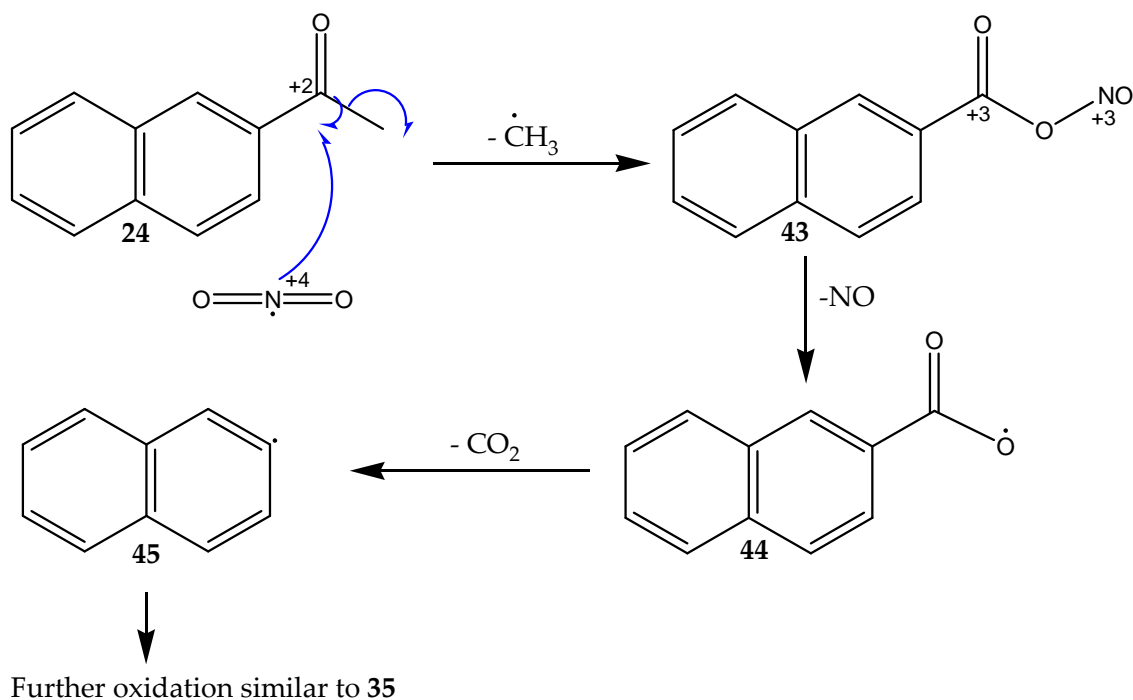


Reaction of aldehydes and ketones with NO₂

The active species for the oxidation of ketones and aldehydes in the presence of NO₂ are different.



oxidation of ketone works with NO₂ directly



4.6. Conclusions

A method for the detailed analysis of the composition of diesel PM samples was developed on a TG-FTIR system. This method yields a detailed analysis of diesel PM samples despite the change in their composition due to the decreased carbon content. The composition could be analyzed with high precision and the results were in good agreement with external analyses.

For reliable TPD/O measurements, the sample mass should not be below 300 μg , whereas measurement of the total carbon content is possible at a mass of only 10 μg . The system is unique in allowing quantitative analysis of carbon-bound hydrogen and oxygen, adsorbed sulfuric acid and water. In the case of powder samples, the ash content of a sample is estimated directly from the mass signal.

A significant advantage of this method is that only 3.5% of the initial weight of an elemental analysis are needed for a composition analysis of diesel PM. Under consideration of the fact, that the PM emissions of diesel engine will be further reduced, it will be still possible to perform meaningful PM composition analysis with this method.

The system also has a significant potential for realistic investigations of the oxidation behavior of PM samples with different condensable and corrosive reactive gas mixtures. The general reactivity order: $\text{O}_2 < \text{O}_2/\text{H}_2\text{O} \approx \text{O}_2/\text{NO}_2 < \text{O}_2/\text{H}_2\text{O}/\text{NO}_2$ for the oxidation of PM [22] was confirmed for the investigated powder soot samples and samples B collected on metal filters. However, for samples A collected on metal filters, the GfG soot and graphite no effect of water was observed. The results obtained with the TG-FTIR system agreed well with the results of external analyses of the same samples (graphite, GfG soot, PM samples on metal filters). Moreover, the ability

to dose condensable and corrosive reactive gases in parallel to mass loss and gas phase analysis exceeds the abilities of established reactivity analysis methods of PM. From the course of the C-oxidation rates conclusions on soot structures with different reactivities can be drawn.

Furthermore, the observed influence of water on the oxidation behavior emphasizes the importance of water dosage for realistic reactivity measurements, which is often not considered.

Beside the investigation of PM composition and reactivity, the system seems to have a large potential for the investigation of adsorption and desorption processes in parallel to surface reactions on catalysts. Exemplarily, this was shown in investigations of the NH_3 adsorption on catalysts for the hydrothermal gasification of biomass performed on the TG-FTIR system [162].

5. Influence of H_2SO_4 on the soot oxidation with NO_2

5.1. Introduction

During engine operation soot is accumulated on and in the walls of the DPF. As a consequence, the pressure drop over the DPF increases leading to an increase of fuel consumption. In order to avoid clogging of the DPF and keep fuel consumption on an acceptable level, the system has to be regenerated by oxidation of the accumulated soot with oxygen. However, the exhaust gas temperatures are often too low to ensure total oxidation of the soot and additional heat is required [30, 33]. In order to avoid additional heating, alternative soot oxidants were investigated. NO_2 , which is generated over the DOC, was found to oxidize soot at significantly lower temperatures than O_2 [35, 36, 40, 43, 82]. In addition, it was already shown in the last chapter that water, which is always present in the diesel engine exhaust gas, has a significant influence on soot oxidation. Beside water there might be additional gas components, which improve the DPF regeneration. Since fossil diesel fuel always contains sulfur, SO_3 and H_2SO_4 are potential candidates for that purpose. Although the sulfur content of modern diesel fuel is very low, always a small amount of SO_3 and H_2SO_4 is formed in the DOC from the conversion of SO_2 , and therefore, an influence on soot oxidation in the DPF cannot be excluded.

In fact, Oi-Uchisawa et al. and Obuchi et al. could show in laboratory experiments with model soots that traces of SO_2 further enhanced the oxidation of soot in the presence of a platinum-based oxidation catalyst, NO , O_2 and water [26, 163-165]. They concluded that over the platinum catalyst NO and SO_2 were oxidized to NO_2 and SO_3 , respectively, which was in equilibrium with H_2SO_4 in the presence of water. The NO_2 formed oxygen surface functional

groups, which decomposition was assumed to be catalyzed by H_2SO_4 [26, 163-165].

To exclude the influence of the catalyst soot interaction, the influence of H_2SO_4 on the soot oxidation was studied without catalyst in this work. Instead of dosing NO and SO_2 , NO_2 was dosed in the gas feed and H_2SO_4 was either dosed in the gas feed or impregnated on the soot prior to the soot oxidation experiment. Based on the results a new mechanism was developed, which explains the promoting effect of H_2SO_4 on the oxidation of diesel soot by NO_2 .

5.2. Experimental

For the investigations Printex U from Evonik was used as model substance for diesel soot since it was available in sufficient amounts, showed a reproducible composition and was well characterized in many studies [40, 62, 142]. About 60 mg of soot were loaded on cordierite monoliths (400 cpsi, $V = 15.5 \text{ mL}$, dimensions $26.5 \text{ mm} \times 26.5 \text{ mm} \times 22 \text{ mm}$; see Table 7) as sample carriers by dip coating into a dispersion of soot and isopropyl alcohol (IPA) as described in section 2.2.1. A part of the loaded monoliths were impregnated with 1 ($\pm 10\%$), 2 ($\pm 10\%$), 5 ($\pm 10\%$) and 10 ($\pm 10\%$) mg sulfuric acid (H_2SO_4) solution (see also section 2.2.1).

The experiments in the presence of NO_2 and $\text{SO}_3/\text{H}_2\text{SO}_4$ were performed in the heated tubular quartz reactor (Length: 650 mm; inner diameter: 49 mm) described in section 2.1.3. The total flow was $550 \text{ L}_\text{N}/\text{h}$ at STP resulting in a gas hourly space velocity (GHSV) of $35,000 \text{ h}^{-1}$. The basic feed gas consisted of 10% O_2 + 5% H_2O with nitrogen as balance. In the first part of the soot oxidation measurements 0, 200 and 1000 ppm NO_2 and 0, 1, 4 and 10 ppm H_2SO_4 were added to the basic feed gas. In the second part the H_2SO_4 -impregnated

monoliths were used and 0, 200 and 1000 ppm NO₂ were added to the basic feed gas. Additionally, the soot reactivity was also investigated with only 10% O₂ for comparison. The measurements were performed with a heating ramp of 10 K/min between 50°C and 700°C.

5.3. Results

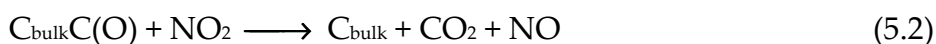
5.3.1. Introductory example for the impact of H₂SO₄ on the soot oxidation

Figure 42 shows the trends of the gas concentrations observed during a typical soot oxidation experiment performed in this study. The inlet gas concentrations for the chosen example were 200 ppm NO₂ + 10% O₂ + 5% H₂O + 18 ppm SO₂, with nitrogen as the balance.

The figure shows the outlet concentrations of CO, CO₂, NO, NO₂, SO₂, H₂SO₄ and HNO₃. At 170°C, the soot surface started to be oxidized by NO₂ leading to the formation of oxygen surface functional groups and gaseous NO, as shown in reaction (5.1) where C(O) represents a surface functional group and C_{bulk} the carbon backbone:



The slight increase of the CO₂ concentration at 180°C indicates that a part of the functional groups decomposed after a second attack by NO₂:



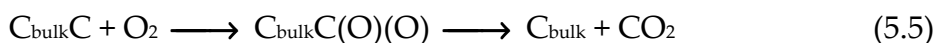
Since reaction (5.2) is a consecutive reaction of (5.1) it can be concluded that always more NO than CO₂ is produced. In fact, Figure 42 clearly shows that the slope of the NO concentration is more than two times steeper than the slope of the CO₂ concentration between 170-210°C.

At 10°C below the breakthrough of H₂SO₄, the NO₂ and NO concentrations reached a plateau due to limitation by the available amount of oxidizable carbon. Above 230°C, the NO and CO₂ concentrations increased again, while the NO₂ concentration decreased.

At 280°C, the NO₂ conversion exceeded 90%, and in parallel to reaction (5.2), the carbon was also oxidized to CO, as indicated by the increase in the CO concentration:



At 315°C, the H₂SO₄ desorption reached a maximum, and the NO₂ conversion reached 100% meaning that the CO and CO₂ concentration should also reach a plateau if only NO₂ accounts for soot oxidation. However, a rough balance showed that the amount of CO and CO₂ was too large to be produced only by the dosed NO₂. Therefore, it was concluded that all additional CO and CO₂ formed above this temperature must be due to the decomposition of previously formed surface functional groups according to reaction (5.1) or due to reactions (5.4) – (5.6) with oxygen:



With increasing temperature, the concentration of SO_2 , CO and CO_2 increase, while the sum of the NO and NO_2 concentration remained constant during the entire experiment. It is important to note that an influence of excess SO_2 on the reaction was not observed. SO_2 was added below 100°C , but H_2SO_4 did not break through until 210°C due to adsorption on the system walls and on the soot sample. NO_2 was added at 120°C . Later we will show that the amount of added H_2SO_4 was too small to influence the observed carbon oxidation significantly.

For the other NO_2 and H_2SO_4 concentrations specified in the experimental section the absolute concentrations of the products changed, but the general trends were similar.

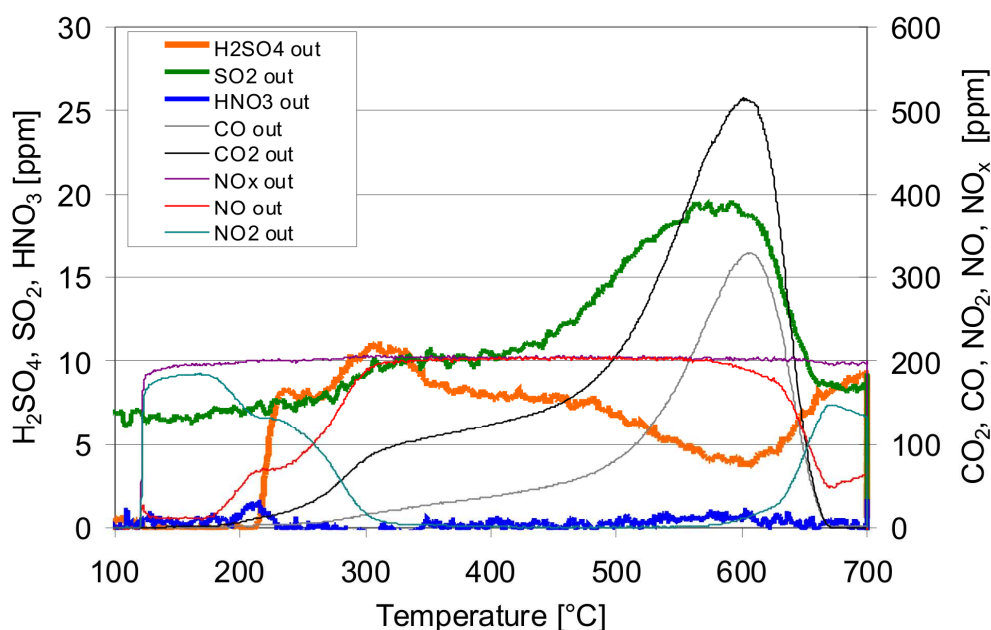


Figure 42: Outlet concentrations of CO , CO_2 , NO , NO_2 , NO_x , SO_2 , H_2SO_4 and HNO_3 in a soot oxidation experiment with 200 ppm NO_2 , 10% O_2 , 5% H_2O , SO_2 and 10 ppm H_2SO_4 in the feed gas.

5.3.2. NO₂ conversion and C-oxidation rates

The influence of H₂SO₄ on the soot oxidation with NO₂ was investigated systematically in the presence of different NO₂ and H₂SO₄ inlet concentrations by means of the NO₂ conversion and the C-oxidation rates. Figure 43 and Figure 44 show the NO₂ conversion during the soot oxidation with 200 and 1000 ppm NO₂ in the feed gas. Figure 43 depicts the results of the H₂SO₄ addition through the gas phase and Figure 44 presents the results of the H₂SO₄ addition by impregnation between 150°C and 450°C.

As a basis for comparison, the NO₂ conversion in the presence of 200 and 1000 ppm NO₂ without H₂SO₄ in the feed gas was included as reference in both figures. The increase of the NO₂ concentration from 200 ppm to 1000 ppm NO₂ led to an increase of the NO₂ conversion, however, the effect on the conversion was much less pronounced than that of the addition of H₂SO₄.

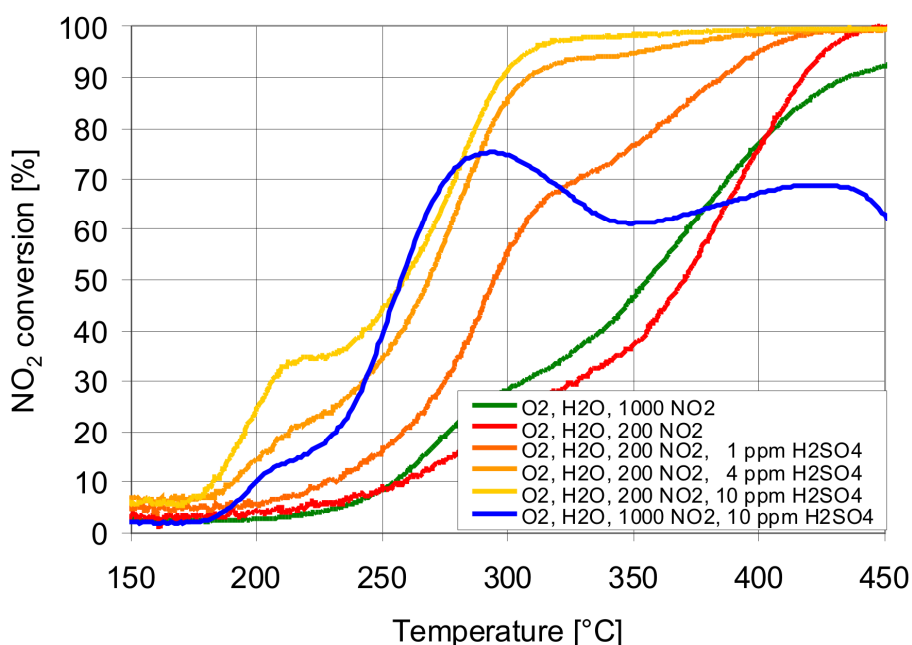


Figure 43: Increase of the NO₂ conversion rates of the soot oxidation experiments in the presence NO₂ and H₂SO₄ between 150°C and 450°C. Feed gas: 200 ppm NO₂ + 0, 1, 4, 10 ppm H₂SO₄ and 1000 ppm NO₂ + 0, 10 ppm H₂SO₄.

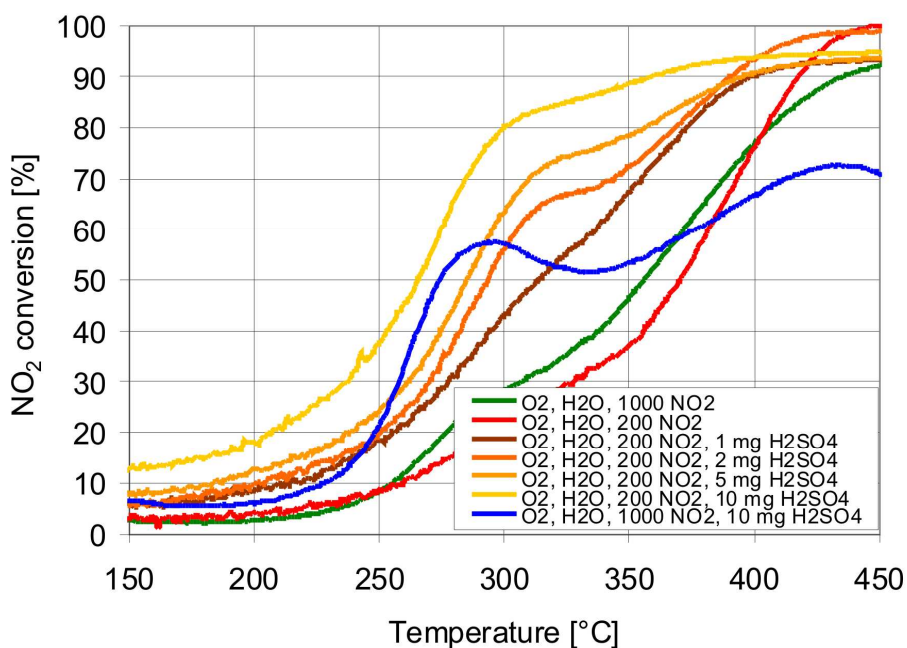


Figure 44: Increase of the NO_2 conversion rates of the soot oxidation experiments in the presence NO_2 and H_2SO_4 between 150°C and 450°C . Feed gas: $200 \text{ ppm NO}_2 + 0, 1, 5, 10 \text{ mg H}_2\text{SO}_4$ and $1000 \text{ ppm NO}_2 + 0, 10 \text{ mg H}_2\text{SO}_4$.

When 200 ppm NO_2 were added, soot oxidation was limited by the amount of available NO_2 above 450°C . Full NO_2 conversion was reached for all experiments with 200 ppm NO_2 and H_2SO_4 addition via the gas phase as well as for 200 ppm NO_2 and $1 \text{ mg H}_2\text{SO}_4$ added by impregnation. In the experiments with 1000 ppm NO_2 full conversion was not reached, since under these conditions the reaction was limited by the amount of oxidizable carbon in the corresponding temperature range, which was also the case for the impregnated samples with $2, 5$ and $10 \text{ mg H}_2\text{SO}_4$. This limitation could be also seen from the peaks in the NO_2 conversion with a maximum at 290°C .

In Figure 45 - Figure 48 the carbon oxidation (C-oxidation) rates of Printex U are shown for different reaction conditions. The C-oxidation rates of the experiments with $10\% \text{ O}_2 + 5\% \text{ H}_2\text{O} + \text{NO}_2$ were significantly higher than those

in the absence of NO₂. In Figure 45 for example the C-oxidation at 300°C in the absence of NO₂ was already reached at 200°C in the presence of 200 ppm NO₂. With an increase of the NO₂ concentration to 1000 ppm these differences were enhanced (Figure 47).

However, it was possible to further increase the level of carbon oxidation in the presence of NO₂ by the addition of small amounts of H₂SO₄. The addition of 1 ppm H₂SO₄ enhanced the C-oxidation at 300°C by 75% and the addition of 4 and 10 ppm by 120% (Figure 45). For 1000 ppm NO₂ the addition of 1 ppm H₂SO₄ at 300°C did not enhance the C-oxidation, but at levels of 4 and 10 ppm the rates were increased by a factor of 3 and 4, respectively (Figure 47).

For 200 ppm NO₂ (Figure 45) the trends of the C-oxidation rates approached each other above 410°C regardless of the reactive gas. For 1000 ppm NO₂ (Figure 47) the C-oxidation rates did not converge again and with 4 and 10 ppm H₂SO₄ in the reactive gas the soot sample was totally gasified 190°C lower compared to the experiments without NO₂ and H₂SO₄.

A similar picture was obtained for the oxidation of the soot samples, which were impregnated with H₂SO₄ before the measurement (Figure 46 and Figure 48): The carbon oxidation rate was enhanced when NO₂ was passed over the H₂SO₄-impregnated soot samples. In these graphs also the C-oxidation rates with 0 ppm NO₂ + 10% O₂ + 5% H₂O of a Printex U sample impregnated with 10 mg H₂SO₄ were added. These measurements did not show a significant difference between the other experiments without NO₂ up to 480°C. Above 480°C the C-oxidation rates increased slightly.

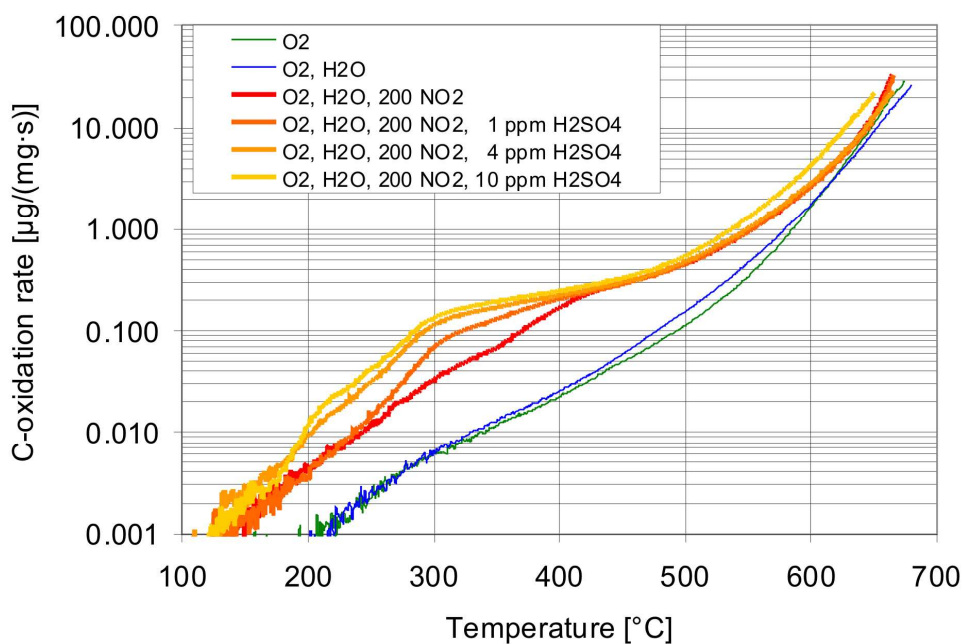


Figure 45: C-oxidation rates of the soot oxidation experiments in the presence of NO_2 and H_2SO_4 . Reactive gas compositions: 10% O_2 + 5% H_2O + 0 and 200 ppm NO_2 + 0, 1, 4 and 10 ppm H_2SO_4 . The C-oxidation rates are plotted until 99% carbon conversion.

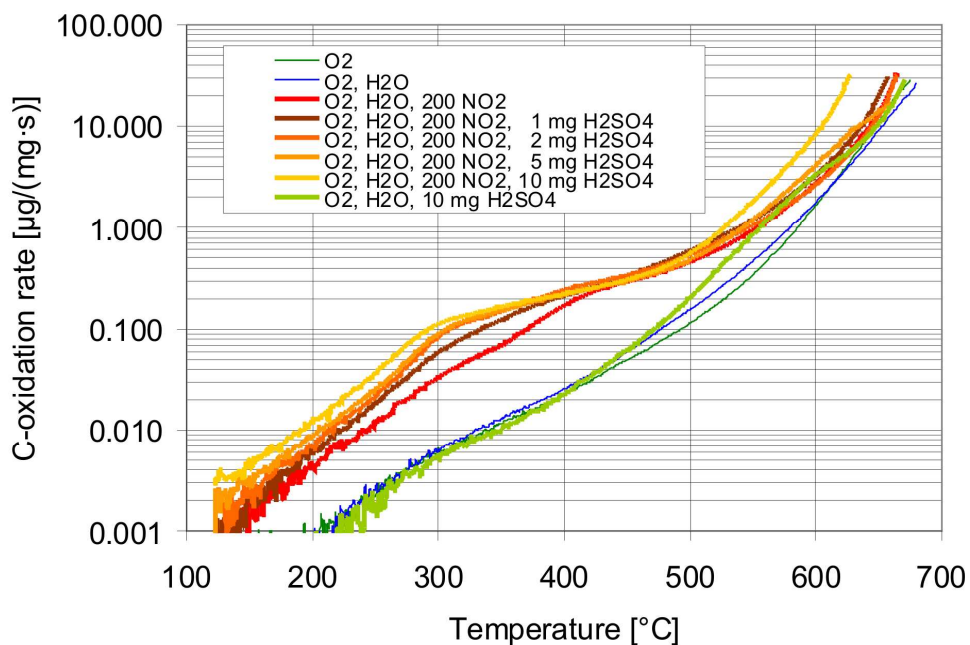


Figure 46: C-oxidation rates of the soot oxidation experiments in the presence of NO_2 and H_2SO_4 . Reactive gas compositions: 10% O_2 + 5% H_2O + 0 and 200 ppm NO_2 + 0, 1, 2, 5 and 10 mg H_2SO_4 . The C-oxidation rates are plotted up to 99% carbon conversion.

Influence of H_2SO_4 on the soot oxidation with NO_2

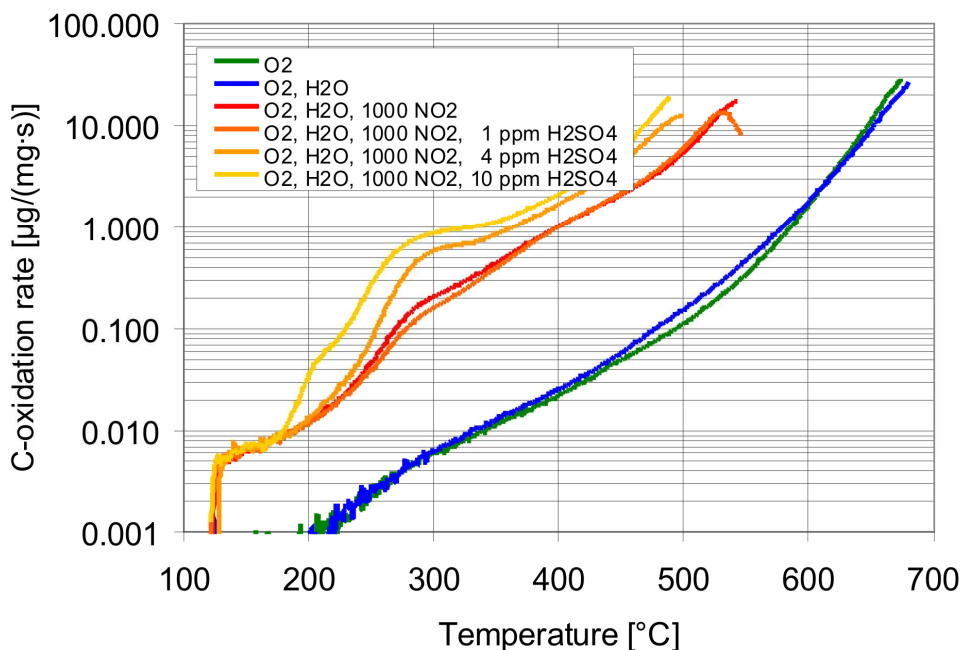


Figure 47: C-oxidation rates of the soot oxidation experiments in the presence of NO_2 and H_2SO_4 . Reactive gas compositions: $10\% \text{O}_2 + 5\% \text{H}_2\text{O} + 0$ and $1000 \text{ ppm NO}_2 + 0, 1, 4$ and $10 \text{ ppm H}_2\text{SO}_4$. The C-oxidation rates are plotted up to 99% carbon conversion.

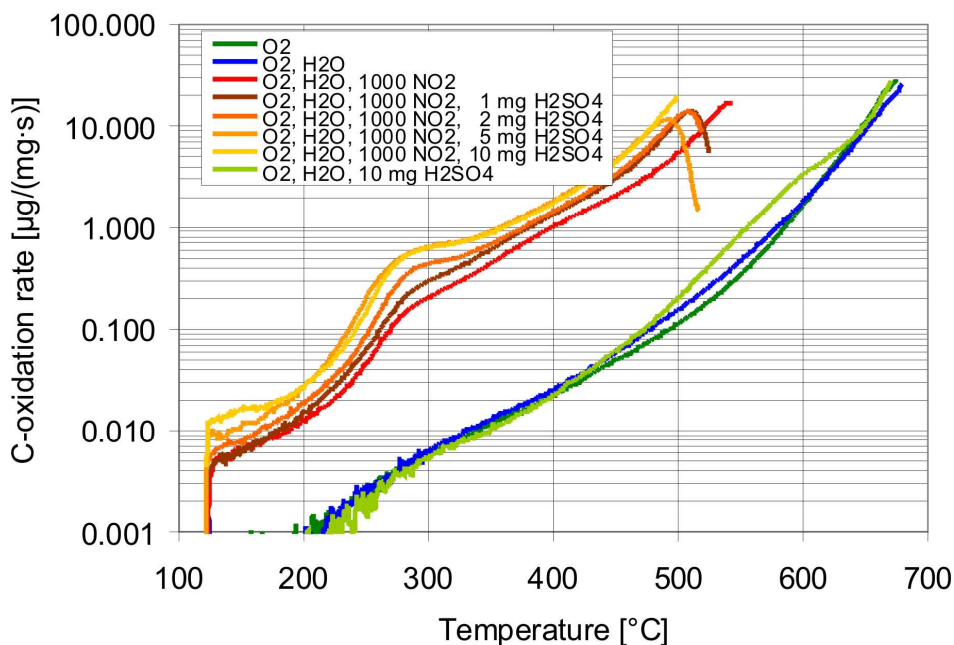
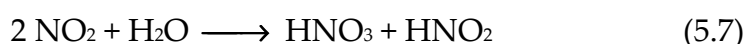


Figure 48: C-oxidation rates of the soot oxidation experiments in the presence of NO_2 and H_2SO_4 . Reactive gas compositions: $10\% \text{O}_2 + 5\% \text{H}_2\text{O} + 0$ and $1000 \text{ ppm NO}_2 + 0, 1, 2, 5, 10 \text{ mg H}_2\text{SO}_4$. The C-oxidation rates are plotted up to 99% carbon conversion.

5.3.3. HNO₃ evolution

In addition, also the trend of the HNO₃ concentration was investigated, since HNO₃ was assumed to be at least an intermediate of soot oxidation [37] and can be formed by a heterogeneous disproportionation reaction of NO₂ over soot (eq. 5.7) [166-168]:



In the example shown in Figure 42 only a maximum of 1 ppm HNO₃ was detected between 180°C and 220°C, but for higher NO₂ concentrations higher amounts of HNO₃ were detected as shown in Figure 49 and Figure 50.

In the experiment without H₂SO₄ in the feed gas, HNO₃ formation was below the detection limit when only 200 ppm NO₂ were dosed, but HNO₃ formation increased significantly when the NO₂ concentration was increased to 1000 ppm (Figure 49). The addition of 10 ppm H₂SO₄ to the reactive gas led to the formation of about 1 ppm HNO₃ at 210°C in the presence of 200 ppm NO₂. In the presence of 1000 ppm NO₂ the HNO₃ concentration between 120°C and 180°C was similar to the experiment without H₂SO₄ in the reactive gas, but between 180°C and 220°C a peak of 8 ppm HNO₃ could be observed.

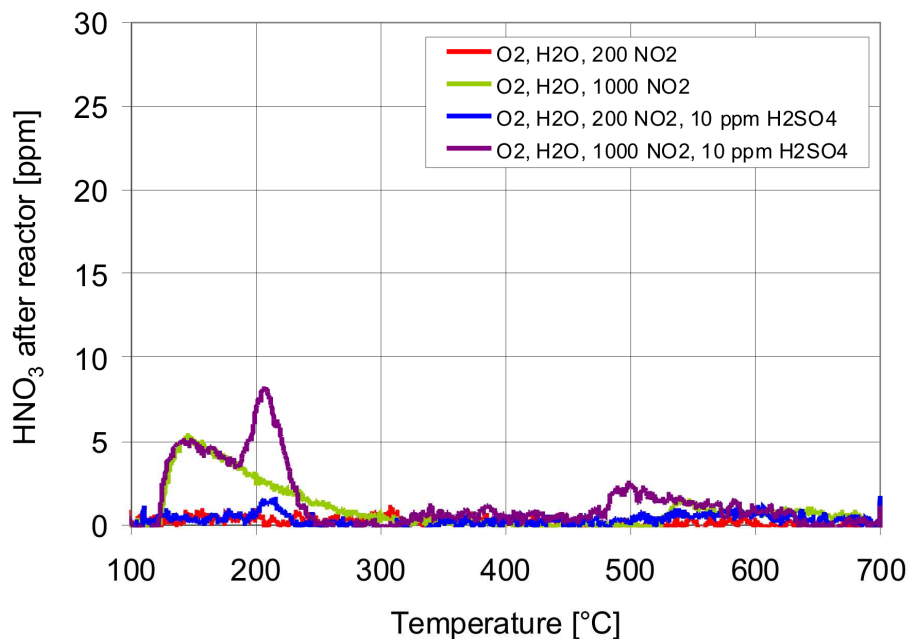


Figure 49: HNO_3 produced during soot oxidation in the presence of NO_2 and H_2SO_4 . Feed gas composition: 200 and 1000 ppm NO_2 + 0 and 10 ppm H_2SO_4 .

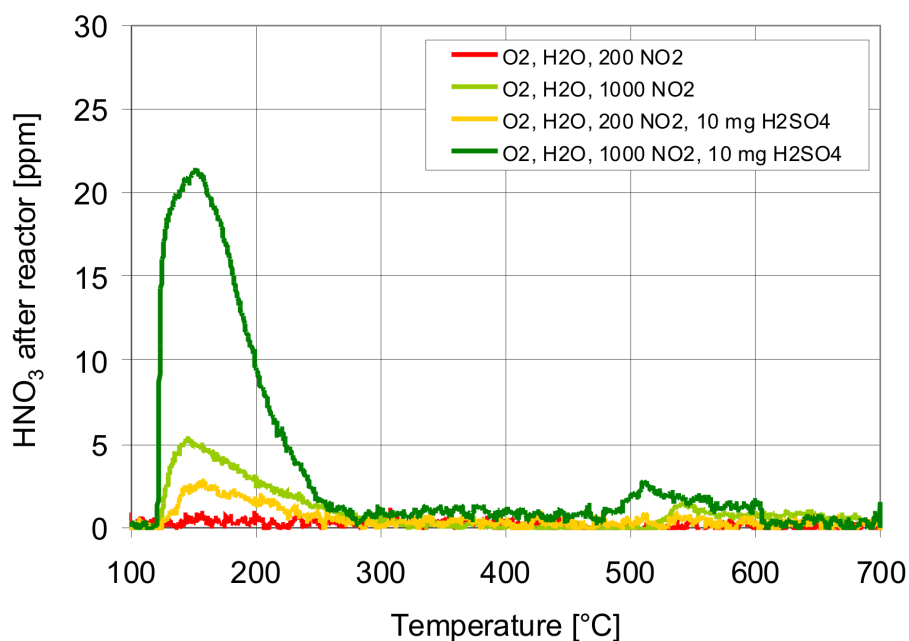


Figure 50: HNO_3 produced during soot oxidation in the presence of NO_2 and H_2SO_4 . Feed gas composition: 200 and 1000 ppm NO_2 + 0 and 10 mg H_2SO_4 .

The addition of H_2SO_4 by impregnation showed an even more pronounced effect (Figure 50): For both NO_2 inlet concentrations more HNO_3 was formed in comparison to the H_2SO_4 gas phase addition. Between 120°C and 280°C maximum HNO_3 concentrations of 2 and 22 ppm were obtained for 200 and 1000 ppm NO_2 , respectively.

In the final carbon gasification phase above 480°C up to 2.5 ppm HNO_3 were measured for the experiments with 1000 ppm NO_2 in the reactive gas. For 200 ppm NO_2 this increase was below 1 ppm, which was in the range of the measurement error.

It has to be mentioned, that the results obtained with the H_2SO_4 -impregnated samples could not be directly compared with the results of the experiments with H_2SO_4 in the feed gas. Whereas in the former case much H_2SO_4 was present at the start of the experiment, in the latter case the H_2SO_4 amount on the sample increased due to the SO_3 dosing through the gas phase.

5.4. Discussion

The presented data confirm again that the addition of NO_2 to the reactive gases containing O_2 and water resulted in an increase of the carbon oxidation rate over the whole temperature range, which was already described by several authors [34-43] and discussed in detail in section 4.5. In addition, it was observed that the C-oxidation rates could be further increased, when traces of H_2SO_4 were added to the reactive gas containing O_2 , H_2O and NO_2 (Figure 45). This was in accordance with the results of Oi-Uchisawa et al. and Obuchi et al., who also observed a significant increase of the C-oxidation rates in the presence of NO_2 , which could be further enhanced by the addition of small amounts of H_2SO_4 . However, in contrast to our experiments, Oi-Uchisawa et al. and Obuchi

et al. used a mixture of a commercially available carbon black and a Pt catalyst [26, 163-165] for their investigations. The catalyst was needed for the in situ generation of NO_2 and H_2SO_4 from NO and SO_2 . Beside NO and SO_2 their reactive gases contained also O_2 , H_2O and nitrogen as balance.

Based on their findings, they proposed a mechanism, which could explain this enhancement [165]. They suggested that first phenols and carboxylates were formed during the partial oxidation of the carbon surface with NO_2 . A further oxidation of these groups with NO_2 on the carbon surface would lead to their decomposition, but their electron-withdrawing character decreased the reactivity of neighboring carbon sites. The addition of H_2SO_4 could increase the C-oxidation rate, since the strong acidity was assumed to catalyze the decomposition of the surface functional groups formed by the first attack of NO_2 . Furthermore, they suggested that H_2SO_4 could hydrolyze esters and anhydrides, leading to the decarboxylation of the hydrolysis products. After the decomposition of the oxygenated surface species the carbon surface was "free" for a further oxidation cycle with NO_2 .

The explanation for the influence of H_2SO_4 on the carbon oxidation in the presence of NO_2 given in [165] seems to be plausible. The results of this work confirmed the assumption of Oi-Uchisawa et al. that a co-operative mechanism between H_2SO_4 and NO_2 existed, where H_2SO_4 behaved more like a catalyst than a stoichiometric reactant, i.e. even traces of H_2SO_4 had this promoting effect. The catalytic effect of H_2SO_4 on the oxidation capability of NO_2 was supported by our finding that below 480°C H_2SO_4 could not enhance the C-oxidation rates in the absence of NO_2 Figure 46 and Figure 48.

Although the explanation in [165] on the influence of H_2SO_4 on the carbon oxidation seems to be plausible, it is questionable, if the acceleration of the decarboxylation and of the hydrolysis of anhydrides and esters were the only

processes being responsible for the increased C-oxidation rates. We suggested that H_2SO_4 also influenced the carbon oxidation already at the nitration of the graphitic soot structure. The nitration of the carbon surface is considered as one of the major steps of the carbon oxidation process as shown in section 4.5.3. It is well known that the active species during the nitration of aromatics is not NO_2 or HNO_3 , but the more electrophilic NO_2^+ (nitronium-ion) [51, 169], which is formed in traces in conc. nitric acid.

HNO_3 formed according to eq. (5.7), was also found during the experiments of this work. HONO was not calibrated for these experiments, but its formation on Printex U was detected during the experiments for the investigation of the SCR effect over diesel soot (see chapter 6). While HONO decomposed quickly into NO , NO_2 and H_2O , HNO_3 probably formed small amounts of NO_2^+ according to route **B** in Figure 51.

Although we found HNO_3 only up to 250°C in larger amounts in the gas phase, it was most likely formed on the soot surface over the entire temperature range. This was confirmed by the HNO_3 traces measured above 500°C (Figure 49 and Figure 50), which occurred during the experiments with H_2SO_4 , when up to 95% of the carbon were already burned. There, the rate of desorption was again higher than the rate of reaction.

Furthermore, it is known, that also deactivated aromatics can be nitrified when nitrosulfuric acid – a mixture of conc. HNO_3 and conc. H_2SO_4 – is used, since the NO_2^+ concentration increases in the presence of a strong acid [51, 169]. We suggested that the addition of H_2SO_4 to the reactive gas containing NO_2 and H_2O also promoted these favorable conditions for the formation of NO_2^+ ions on the soot surface. The strong acidity of H_2SO_4 increased the NO_2^+ concentration by protonation of HNO_3 as shown in route **A** of Figure 51, compared to the self-protonation shown in route **B**.

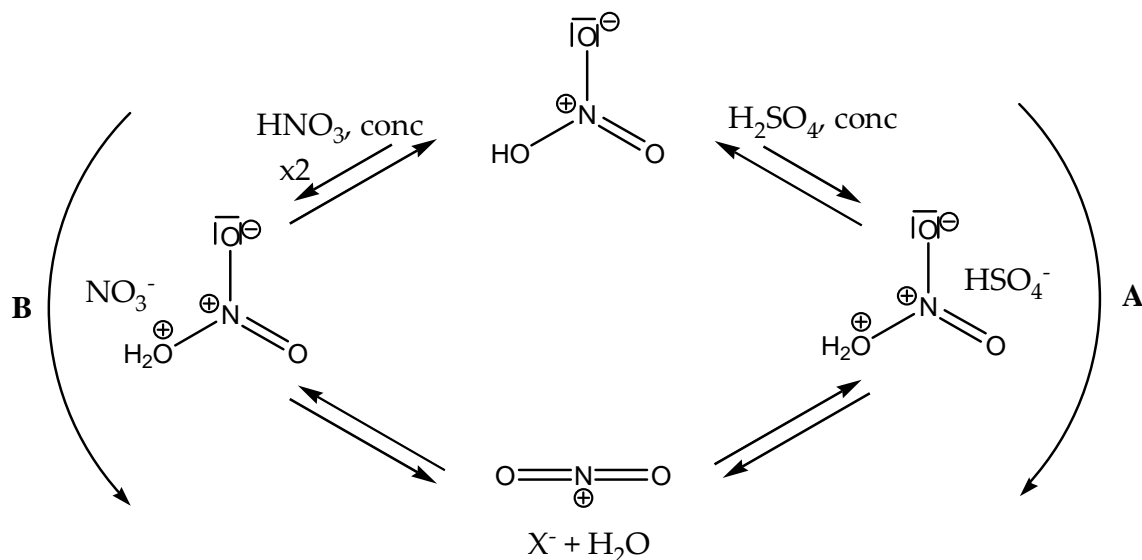


Figure 51: Mechanism of the NO_2^+ formation [51]. A: reaction route in nitrosulfuric acid; B: reaction route in conc. HNO_3 .

After the nitration the C- NO_2 bond was either homolytically cleaved resulting in an “aryl radical” and NO_2 or the nitro group rearranged to a nitrite as known for the decomposition of nitro aromatic compounds [54-58]. The nitrite decomposed homolytically in a “phenyl” radical and NO . Starting from these radical species a large number of reactions is thinkable, which are discussed in the soot oxidation network presented in section 4.5.3. Based on the analytical results and considerations it is reasonable to conclude that an increase of the nitration rate also enhanced the carbon oxidation. As already speculated, H_2SO_4 engaged the mechanism catalytically as proton donator, which could be regenerated after the nitration step.

Beside the enhanced formation of NO_2^+ , it was shown in Figure 49 and Figure 50 that H_2SO_4 also enhanced the HNO_3 formation. This can be explained by a closer look on the mechanism behind reaction (5.7) as shown in Figure 52. First, NO_2 dimerized to N_2O_4 (eq. (5.8)), which disproportionates into HNO_2 and HNO_3 (eq. (5.9)) in a second step in the presence of water. With increasing temperature

the equilibrium of the dimerization step is shifted to the NO_2 side. In the presence of H_2SO_4 , it was assumed that the HNO_3 concentration increased, because H_2SO_4 catalyzed the decomposition of N_2O_4 , as illustrated in reaction (5.6 - Figure 52) by protonation of N_2O_4 facilitating the attack of water. Therefore, H_2SO_4 catalyzed not only the formation of NO_2^+ , but also the formation of HNO_3 – the NO_2^+ precursor.

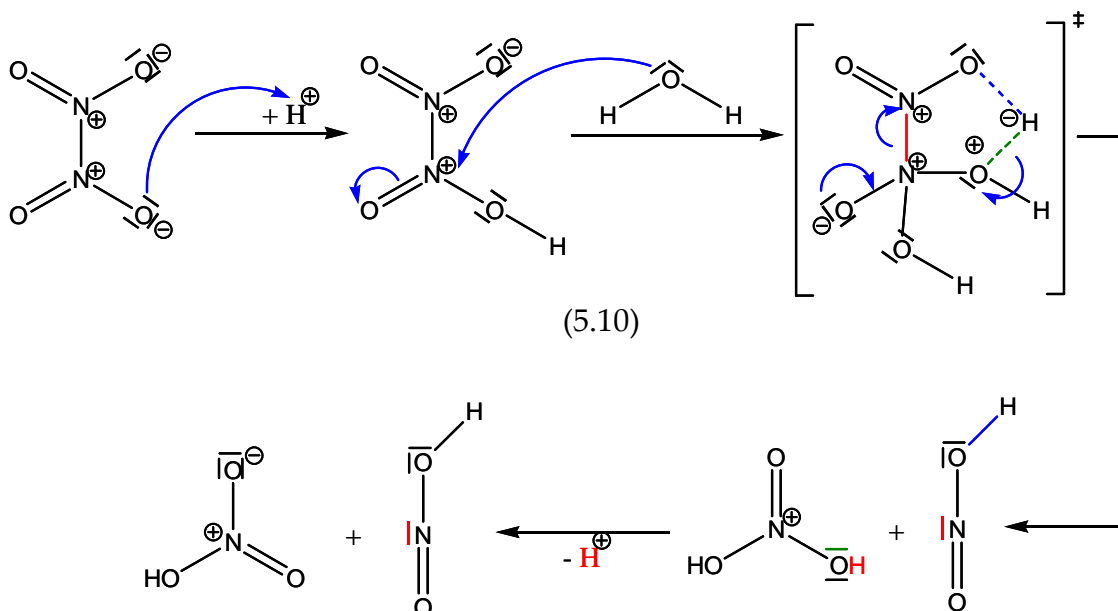
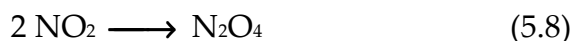


Figure 52: Mechanistic details of the HNO_3 formation over soot.

In the soot oxidation network, it was also shown, that beside the nitration of aromatics there are also other reactions of surface groups in the presence of NO_2 , which can only be explained with NO_2^+ as the active species. One example is the oxidation of aldehydes with NO_2 , which proceeds via an acylnitrite [62]. From the analysis of the oxidation states, it becomes clear, that an electrophilic,

non-radicalic attack under oxidation of the carbonyl carbon is only possible if the electrophile is NO_2^+ as shown in Figure 53.

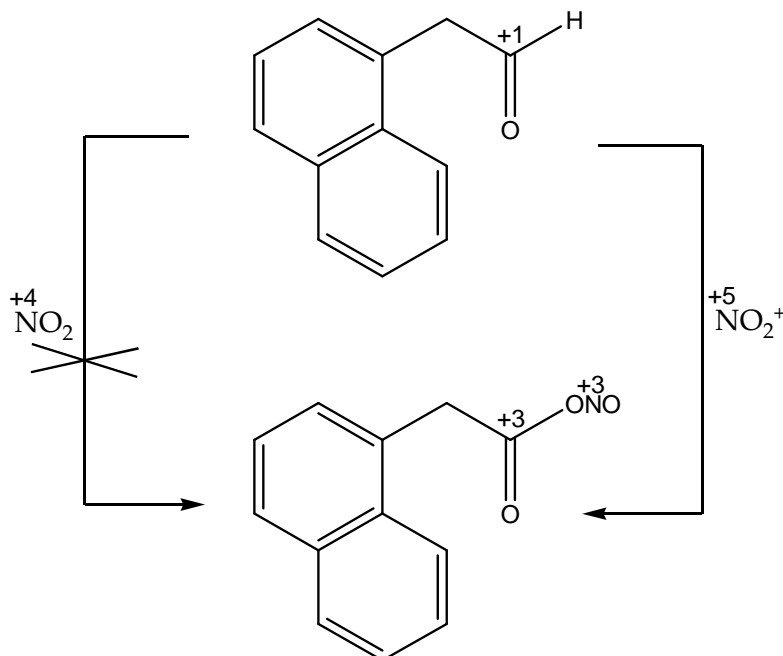


Figure 53: Example for reactions of surface groups with NO_2^+ : oxidation of aldehydes to nitrites, which further decompose in carboxylic acids.

A direct oxidation of soot by H_2SO_4 also had to be considered, since an increase of the SO_2 concentration with temperature in the product gas was observed, while the amount of SO_2 added to the SO_3 generator remained constant. However, the amounts of H_2SO_4 were too small to significantly contribute to the C-oxidation rates up to 450°C (Figure 46). Above 450°C a slight increase of the C-oxidation rate was observed (Figure 46 and Figure 48), which corresponds to the formation of SO_2 in Figure 42.

The results of the impregnated soot samples and those with H_2SO_4 addition by the gas phase showed that the differences were mainly driven by differences in the actual H_2SO_4 amounts. The impregnated samples were more active at 120°C , since the amount of H_2SO_4 was larger in this temperature range. During gas

phase addition adequate amounts of H_2SO_4 had to be accumulated before an increase of the C-oxidation rates could be observed.

5.5. Conclusions

Coming back to the question if the soot oxidation in diesel particulate filters by NO_2 is influenced by traces of H_2SO_4 formed by oxidation of fuel-sulfur in the combustion process over the diesel oxidation catalyst, it was clearly shown that it has a significant promoting effect on soot oxidation. Based on a detailed infrared gas phase analysis a new mechanism was suggested to explain the activation effect of H_2SO_4 , which acts most probably in parallel to the already published mechanisms. In our new mechanism H_2SO_4 acts as a catalyst at two stages. First, it enhances the formation of HNO_3 by catalyzing the disproportionation of N_2O_4 . And secondly, H_2SO_4 most likely increases the amount of NO_2^+ , which is the known active species for the nitration of aromatic structures. Once the aromatic system is nitrified, the C-N bond is either cleaved homolytically or the nitro group rearranges to a nitrite, which also decomposes homolytically to NO and a “phenyl radical”. These radical species are further oxidized leading to ring opening and decomposition of the aromatic system by decarboxylation and decarbonylation.

For applications with high-sulfur fuels, a significant influence of the soot oxidation by the sulfur has been expected. However, we could clearly show that even very small sulfur concentrations below 10 ppm, as found in modern low-sulfur diesel fuels, have a strong catalytic effect on the soot oxidation activity. Moreover, the situation is aggravated by the fact that the $\text{SO}_3/\text{H}_2\text{SO}_4$ is accumulated in the DOC under low load conditions and can be released quickly in high concentrations, when the exhaust temperature increases [170].

6. Selective catalytic reduction of NO_x with NH₃ on soot

6.1. Introduction

In section 1.3.1, the selective catalytic reduction with NH₃ was introduced as one of the state-of-the-art technologies for the reduction of NO_x emissions in lean exhaust gases [89, 171, 172]. There are three overall reactions equations which describe the stoichiometries observed under different conditions and with different catalysts [88, 171]:



So far, it was possible to reach the legal emission limits by applying either a SCR system or a DPF and adapting the combustion conditions accordingly. But the tighter future limits necessitate the application of both particulate filter and SCR system in the same vehicle. Although the emission limits are achieved, this combination results in a disadvantageous weight and cost increase. Therefore, ideas of combining both functions in one aftertreatment device are forwarded. According to this concept, DPF and SCR catalyst could be placed in the same housing or even the coating of filter structures with SCR catalysts is thinkable. Consequently, the reducing agent has to be dosed upstream of the DPF leading to the presence of nitrogen oxides (NO_x), reducing agent and diesel soot in one reaction compartment, where they may react with each other. This comprises known reactions, which were not relevant up to now, because reactants such as soot and urea have not been in contact, and probably also new reactions, which

have not been considered at all. It is obvious that thorough studies of the chemistry in such combined DPF-SCR systems are required for a proper reaction design and before such systems can be brought to the market.

In fact, similar reaction systems are known from literature. In the 1980's it was found that NO may be reduced over highly activated carbons in the presence of NH_3 and that this effect can be exploited for the SCR of NO_x from industrial exhaust gases [105-107, 115]. The oxidation of NO to NO_2 was recognized as prerequisite step for the occurrence of the SCR reaction. Although NO oxidation seems to proceed relatively efficient over activated carbons at low temperatures, which is discernible from their higher ability to reduce NO_x in this temperature region compared to typical metal oxide-based catalysts, the general NO_x reduction over carbon is still rather low. Therefore, the applied space velocities were most often below 2000 h^{-1} [100, 103, 127, 129].

This raised the question if in a combined DPF-SCR systems soot might also react as catalyst for NO_x reduction although space velocities are more than ten times higher in mobile applications. Therefore, a laboratory study was performed to investigate the influence of different diesel exhaust gas components, i.e. NO_2 , NO, NH_3 and H_2SO_4 , and temperature on the SCR reaction of NO_x over diesel and model soot. Furthermore, the influence of different space velocities and the relation between soot oxidation and SCR process on soot, which occur in parallel, were examined.

It was planned to perform the experiments in the TG-FTIR system described in chapter 3 because it should allow the investigation of adsorption and desorption processes in parallel to the analysis of the evolved gases. However, the problem rose, that the measured activity in this instrument was strongly dependent on mass transport limitations on one hand. On the other hand, the investigation of adsorption and desorption processes of gas components and

reaction products by following the trend of the TG mass signal was not reproducible, because the mass changes could not be allocated to the certain compounds. Therefore, the plan was changed and the main parts of the measurements were performed in a tubular quartz reactor equipped with FTIR gas analysis. The project was financially supported by the Swiss National Fond (Project: 200021_125257).

6.2. Experimental

6.2.1. Samples and their characterization

For the study Printex U, the Euro V, Euro 0 and the mixed soot sample were used, which were already discussed in terms of composition and reactivity in chapter 4. In addition, the surface areas of the samples were measured by BET measurements and the ash was characterized by ICP-OES measurements. The measured surface areas did not differ significantly and were comparatively small in comparison to activated carbons. For Printex U $103 \text{ m}^2/\text{g}$, for the Euro V soot sample $110 \text{ m}^2/\text{g}$, for the Euro 0 soot sample $132 \text{ m}^2/\text{g}$ and for the mixed soot sample $145 \text{ m}^2/\text{g}$ were obtained. The ash composition is shown in Table 15 for the Euro V, Euro 0 and the mixed soot sample. Printex U did not contain metals above the detection limits of the ICP-OES analysis.

In addition to the BET analysis, Printex U and the Euro V sample were also investigated with TEM in order to search for structural differences because the largest part of the experiments were performed with Printex U instead of real diesel soot sample. The use of Printex U had the advantage, that it was available in sufficient amounts and it is a well characterized model substance for diesel soot [40, 62, 142]. The diesel soot samples were available only in small amounts and therefore the study was restricted to selected experiments, which were

mainly used to confirm the transferability of the Printex U results to real systems.

The TEM measurements showed hardly any difference in size and structure of the primary particles (Figure 54 – “100 nm” pictures) between the two samples. From the “10 nm” and “5 nm” pictures it seemed that the Euro V sample was little more amorphous in comparison to Printex U.

Table 15: Metal concentrations in the Euro 0, Euro V soot sample and the mixed soot sample

	Euro 0	mixed soot	Euro V
	[wt%]	[wt%]	[wt%]
Ag	-	0.0078	-
Al	0.0914	0.0684	0.0234
B	-	0.0141	-
Ba	0.0017	0.0024	-
Ca	1.5199	0.4235	0.9185
Ce	-	0.0082	-
Cr	0.1077	0.0157	0.2204
Cu	0.0413	0.0318	0.0566
Fe	0.9640	0.6804	0.9867
K	0.0248	0.0211	0.0156
Mg	0.0476	0.0755	0.0355
Mn	0.0226	0.0118	0.0216
Mo	-	0.0065	-
Na	0.3447	0.2584	0.0312
Ni	0.0392	0.0159	0.1073
P	0.4353	0.1855	0.1560
Pb	-	-	0.0098
S	0.6926	4.0632	0.1950
Si	0.4807	0.1478	-
Sr	0.0010	0.0013	-
Ti	0.0050	0.0046	0.0018
Zn	0.4640	0.2393	0.0839
Zr	-	0.0016	-

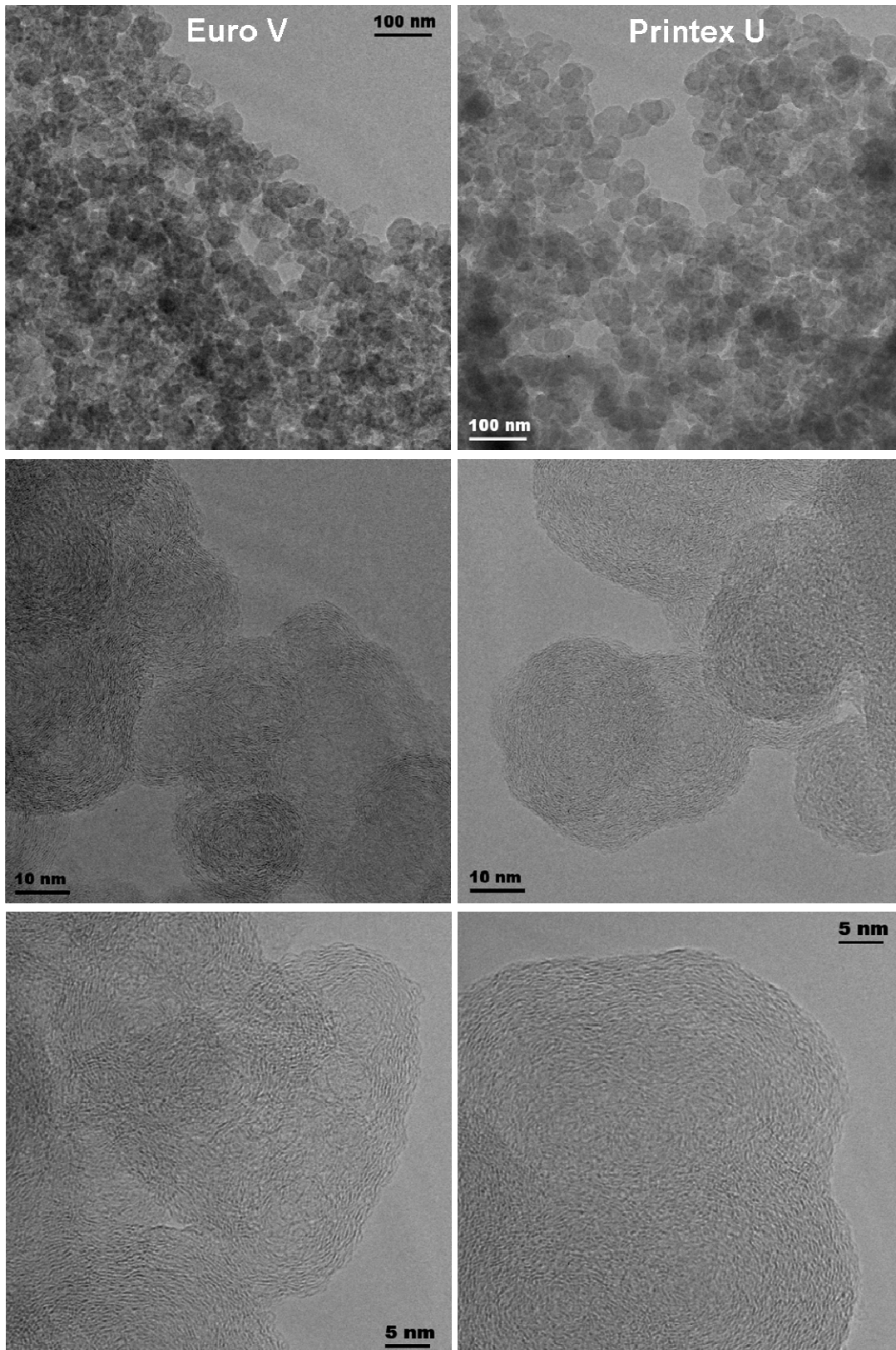


Figure 54: TEM pictures of the Euro V soot sample (left side) and Printex U (right side) at increasing magnification.

6.2.2. Activity measurements in the tubular quartz reactor

The SCR reaction over soot was mainly investigated in the heated tubular quartz reactor described in section 2.1.3. The soot samples were brought into the tubular quartz reactor coated on the cordierite monoliths (400 cps) presented in Table 7, which had different sizes to allow space velocity variations independently of the variation of the total flow. The applied gas hourly space velocities (GHSV) were 3000 h⁻¹, 9000 h⁻¹, 17,000 h⁻¹, 35,000 h⁻¹ and 70,000 h⁻¹. Since 35,000 h⁻¹ is a realistic space velocity for mobile application it was defined as the standard GHSV for this study and used in the experiments if not mentioned differently. The total flows were 275 L/h or 550 L/h at STP depending on the desired space velocity. The base feed gas, which was used for all experiments, consisted of 10% O₂ + 5% H₂O with nitrogen as balance.

To investigate the influence of H₂SO₄ on the NO_x reduction over soot, some of the soot-loaded monoliths were impregnated with 5 mg H₂SO₄ in a second step, instead of dosing SO_x over a Pt catalyst in presence of 10% O₂.

The first measurements in the tubular reactor were carried out as temperature-programmed reaction (TPR) experiments with Printex U. In these experiments Printex U was heated up from 50°C to 700°C with a heating rate of 10 K/min. Between 50°C and 150°C the reactive gas consisted of 10% O₂ + 5% H₂O with nitrogen as balance, to which 250 ppm NO₂ + 250 ppm NH₃ were added above 150°C. However, the reproducibility of these experiments was rather poor. Therefore, Printex U was exposed to 10% O₂ + 5% H₂O + 250 ppm NO₂ + 250 ppm NH₃ up to five hours in long-term isothermal experiments at 200°C, 250°C, 300°C and 350°C in order to check the reasons for the poor reproducibility. The observed NO_x reductions are summarized in Figure 55.

At 300°C and 350°C pronounced activation phases could be observed, which led to maximum NO_x reduction of 28% and 31%, respectively. But due to soot

oxidation with NO_2 , which reached high rates at these temperatures, the NO_x reduction decreased again directly after the maximum. After 2.5 h and 3.8 h the experiments were terminated. In the experiment at 250°C a distinct activation paired with moderate C-oxidation rates was detected. After 3 h a slight decrease of the NO_x reduction rate was observed and after 4.3 h the experiment was terminated. At 200°C the soot surface could hardly be activated for the SCR reaction.

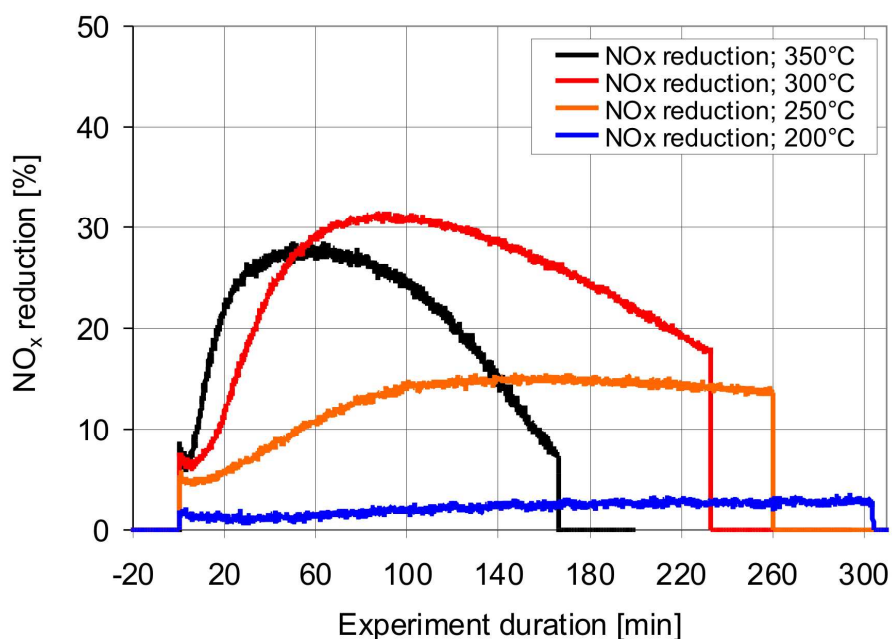


Figure 55: NO_x reduction during activation experiments of Printex U under SCR conditions (10% O_2 , 5% H_2O , 250 ppm NO_2 , 250 ppm NH_3) at 200°C , 250°C , 300°C and 350°C .

These experiments showed clearly, that the soot went through a significant activation phase at temperatures above 250°C . This activation phase was also the reason for the bad reproducibility of the TPR experiments because the pre-activation states of the samples at the beginning of the measurements could not be kept constant. Therefore, only isothermal experiments were conducted in the following, in which the activation phase was awaited before the actual measurements started.

During the activation phase the samples were treated for 25 min with 10% O₂ + 5% H₂O + 250 ppm NO₂ + 250 ppm NH₃ in the feed gas. After that the NH₃, NO and NO₂ concentrations were varied in concentration series (series 1-3) according to Table 16 consecutively. NO without NO₂ was not taken into consideration in the series experiments since no NO_x reduction was observed in the absence of NO₂ as discussed later. For each temperature one soot-coated monolith was used.

Table 16: Variation procedure of the NO₂, NO and NH₃ concentrations for the isothermal investigation of the SCR effect on soot. Between each series the sample was flushed with 10% O₂ + 5% H₂O with nitrogen as balance for 10 min.

Series	Period [min]	NO ₂ [ppm]	NH ₃ [ppm]	NO [ppm]
1	0	250	0	0
	5	250	100	0
	5	250	250	0
	5	250	500	0
	5	250	0	0
	5	0	0	0
	10	0	0	0
2	0	250	0	0
	5	250	250	0
	5	250	250	100
	5	250	250	250
	5	250	250	500
	5	250	250	0
	5	250	0	0
	5	0	0	0
3	0	100	0	0
	5	100	100	0
	5	100	250	0
	5	100	0	0
	5	250	0	0
	5	250	250	0
	5	250	0	0
	5	500	0	0
	5	500	250	0
	5	500	500	0
	5	500	0	0
	5	0	0	0

All series were repeated three to five times, since NO_x reduction still went through a maximum, but it was much less pronounced than in the TPR experiments at least. When the carbon consumption on the monoliths exceeded 50-60%, the measurements were terminated to exclude influences due to soot limitation. Then the samples were heated up to 700°C with 10% O₂ in the feed gas in order to estimate the total carbon amount.

For the data analysis the series showing the highest NO_x reduction values were taken, since it was assumed that in real systems no activation phase exists. In real systems NO_x reduction better equilibrated because soot is continuously trapped, activated and oxidized leading to constant conversion rates close to the maximum, which was found in the model experiments.

6.2.3. Activity measurements in the TG-FTIR system

The investigations of the SCR reaction over soot in the TG-FTIR system were first also carried out as TPR experiments, showing again poor reproducibility. Therefore, it was switched to isothermal experiments similar to those in the tubular reactor. However, the time for each step had to be extended up to 10 min due to the small flow of 150 mL/min through the TG apparatus.

In the first experiments, the soot was added to the system as powder on the quartz disk already used for the investigation of soot composition and reactivity, but again the reproducibility was rather poor. Therefore, also soot-coated cordierites were prepared, which fitted exactly in the furnace of the TG apparatus (Figure 56). The cordierite was coated with 7-8 mg soot. The resulting GHSV was 3200 h⁻¹ – one order of magnitude lower than the standard GHSV in the quartz reactor.

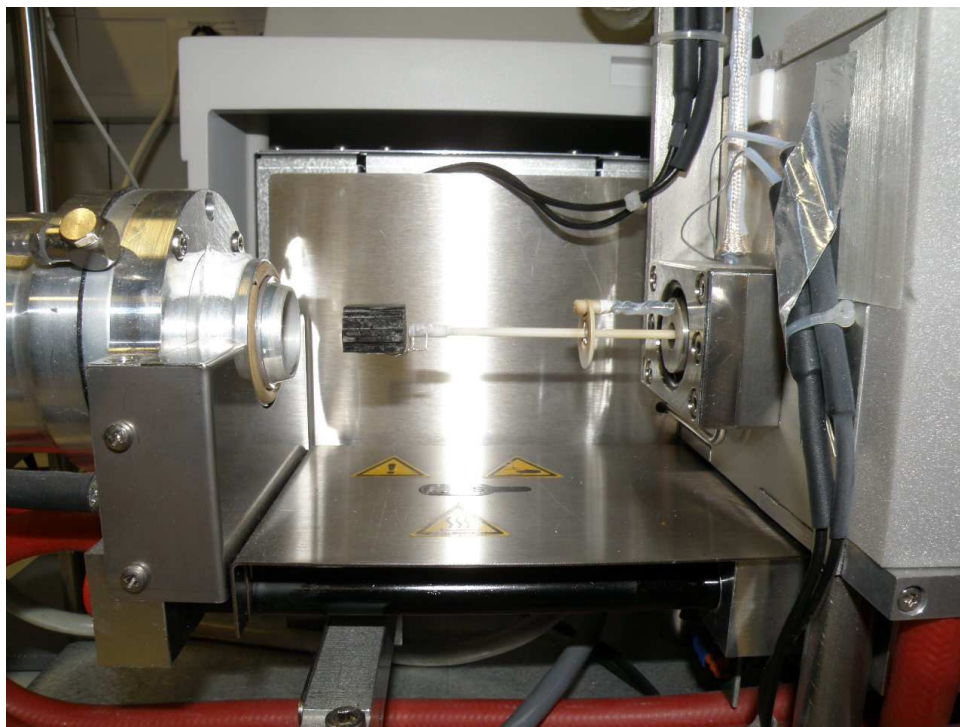


Figure 56: TG furnace in open position with soot-loaded cordierite on the sample holder.

6.2.4. DRIFTS investigations of Printex U

Printex U was used for DRIFTS measurements in order to investigate the formation of surface functional groups in the presence of NO_2 , NH_3 and water. The PM samples were diluted 1:100 with CaF_2 as recommended for investigations with carbon black in [173]. The use of CaF_2 is important, since KBr supports the formation of nitrates [174] and therefore would falsify the results. About 25 mg of this mixture were placed in the DRIFTS cell. After that the sample was heated to 400°C in inert atmosphere before the measurements, which were performed at 300°C . Each spectrum was averaged over 1000 scans at a resolution of 4 cm^{-1} .

6.3. Results and Discussion

6.3.1. SCR reaction of Printex U in the presence of NO and NH₃

Before the results of the isothermal experiments with NO₂ and NO₂ + NO will be presented and discussed, a closer look is taken at the NO_x reduction over Printex U in the presence of only NO + NH₃. These measurements were included for comparison because in the literature only reports about the SCR effect over carbon materials with NO and NH₃ in the feed gas could be found.

In the present work, the lowest possible space velocity of 3000 h⁻¹ was applied, since it was assumed that the prerequisite for the occurrence of a SCR effect is the oxidation of NO to NO₂ [103] and the activity of soot for this oxidation step was expected to be rather low. The experiments were carried out with Printex U, coated on monolith 1 of Table 7, in TPR experiments between 200°C and 450°C with 10% O₂ + 5% H₂O + 0 and 250 ppm NO + 250 ppm NH₃ at a heating rate of 5 K/min. In Figure 57 the NO_x reduction (for explanation see section 2.4.2), the NH₃ conversion U_{NH_3} , the NO, NO₂, NO_x, NH₃ concentrations and the sum of the nitrogen components in the presence of NO are plotted over temperature. The NH₃ concentration remained constant up to 280°C. At higher temperatures it decreased together with the sum of the nitrogen components, while the NO concentration increased slightly leading to a negative NO_x reduction. However, the NH₃ conversion increased faster than the NO concentration. NO₂ was not observed during the course of the measurement. From these results it was concluded that Printex U is not active for NO oxidation and NO_x reduction under these conditions, but is able to oxidize NH₃ selectively to nitrogen.

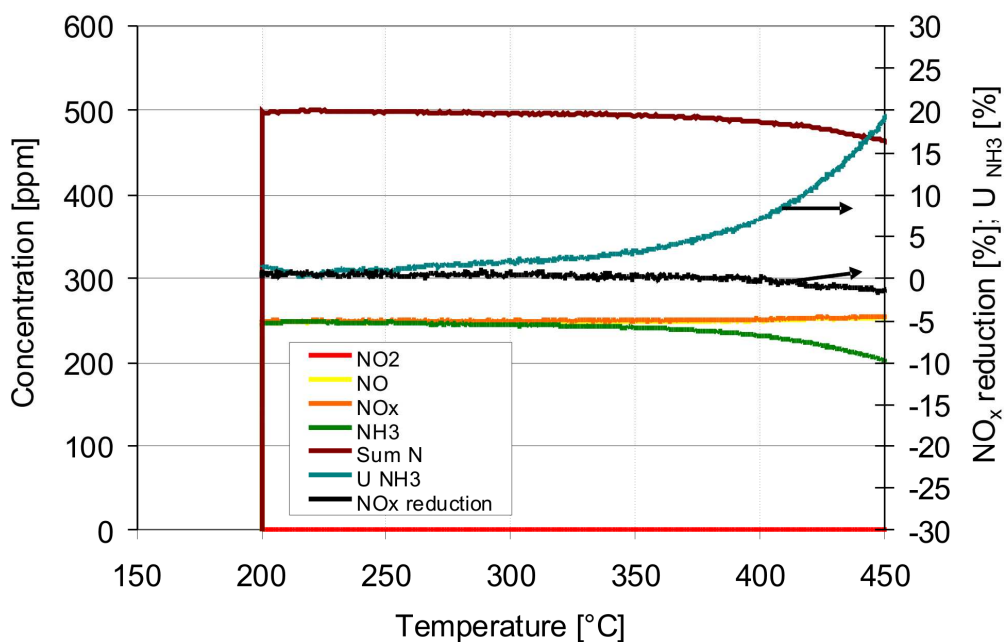


Figure 57: NO_x reduction, NH₃ conversion and concentrations of NO, NO₂, NO_x and NH₃ on Printex U at a space velocity of 3000 h⁻¹ during a TPR investigation with 250 ppm NO + 250 ppm NH₃ from 200°C to 450°C. Additionally, the sum of the nitrogen-containing components is shown.

To confirm the NH₃ oxidation capability, it was checked how NH₃ and Printex U interact under similar conditions in the absence of NO. In Figure 58 the NH₃ conversion and the development of the concentrations of NO, NO₂, NO_x, NH₃ and the sum of the nitrogen components of this experiments are shown. Between 200°C and 280°C all curves remained constant. Above 280°C a decrease of the NH₃ and the sum curve could be observed, while the NO concentration and the NH₃ conversion increased. The evolved NO was due to NH₃ oxidation, but the amount was too small to explain the significant NH₃ decrease. This means that the largest part of NH₃ must have been selectively oxidized to nitrogen (selective catalytic oxidation = SCO) [124], which could not be detected by FTIR spectroscopy. The higher NH₃ conversion observed in this experiment compared to the NH₃ conversion in the presence of NO was most

probably due to missing competitive adsorption of NH_3 and NO on the soot surface.

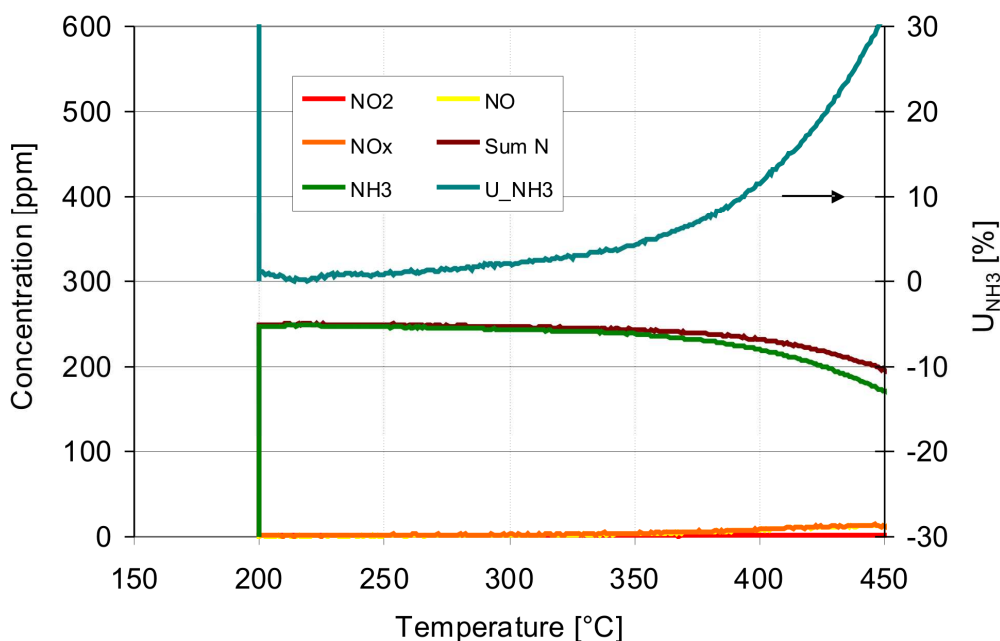


Figure 58: NH_3 conversion and concentrations of NO , NO_2 , NO_x and NH_3 on Printex U at a space velocity of 3000 h^{-1} during a TPR investigation with $0 \text{ ppm NO} + 250 \text{ ppm NH}_3$ from 200°C to 450°C . Additionally, the sum of the nitrogen-containing components is shown.

6.3.2. SCR reaction over Printex U in the presence of NO_2 , NO and NH_3

Although no NO_x reduction was observed in the TPR experiments with NO and NH_3 in the feed gas, it was shown in the experimental section that in the presence of NO_2 Printex U was SCR active. Therefore, NO_2 was always added to the following isothermal experiments, in which the NO_x reduction over soot was investigated in dependence of the NO_2 , NH_3 and NO concentration at different temperatures and space velocities in isothermal experiments.

In Figure 59 - Figure 62 the NO_x reduction rates over Printex U at temperatures between 200°C and 350°C for different concentrations of NO_2 , NO and NH_3 (Table 16) are shown. Beside the NO_x reduction, the stoichiometric ratio is

plotted on the secondary y-axis (for explanation see section 2.4.4). Higher temperatures were not considered in the figures since the rate of carbon oxidation and the rate of NH_3 oxidation to N_2 became too large to measure reproducible NO_x reduction rates. On the other hand, below 200°C the NO_x reduction activity was too small and was mainly driven by ammonium nitrate formation on the soot surface.

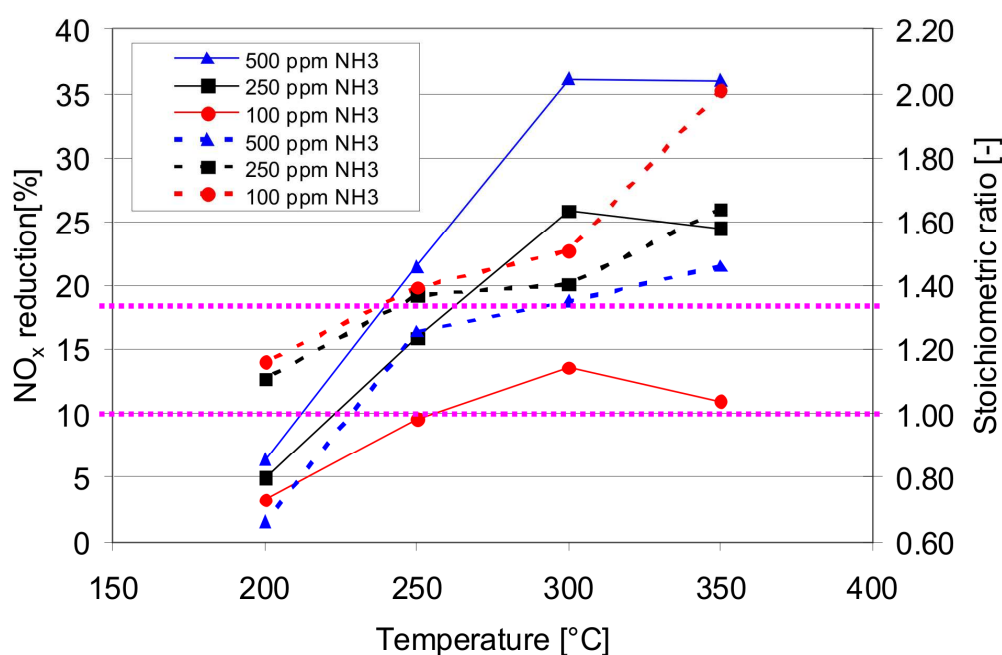


Figure 59: NO_x reduction and measured stoichiometric ratios over Printex U in dependence of the NH_3 concentration between 200°C and 350°C at a GHSV of $35,000 \text{ h}^{-1}$. Concentrations in the base feed gas: 250 ppm NO_2 + variable NH_3 concentrations. Solid lines: NO_x reduction [%]; dotted lines: measured stoichiometric ratios; purple dotted lines: stoichiometry of the *fast SCR* and *NO_2 SCR* reaction.

The data in Figure 59 showed that an increase of the NH_3 concentration resulted in an increase of the NO_x reduction up to 36% for 500 ppm NH_3 and in a decrease of the measured stoichiometry. At $250\text{-}300^\circ\text{C}$ stoichiometric ratios of 1.25-1.50 were found in dependence of the NH_3 concentration indicating the NO_2 SCR reaction with a theoretical stoichiometry of 1.33 (eq. (6.3)). At 200°C

the NO_x reduction rates were smaller and also the stoichiometric ratio decreased to 0.7-1.2. However, at this low temperature the measurement error of the stoichiometric ratio was higher due to the small conversion rates. Above 300°C , the NO_x reduction remained constant within the experimental error due to a limitation of NO_2 and the stoichiometric factors increased for all NH_3 concentrations, since the unselective NH_3 oxidation increased.

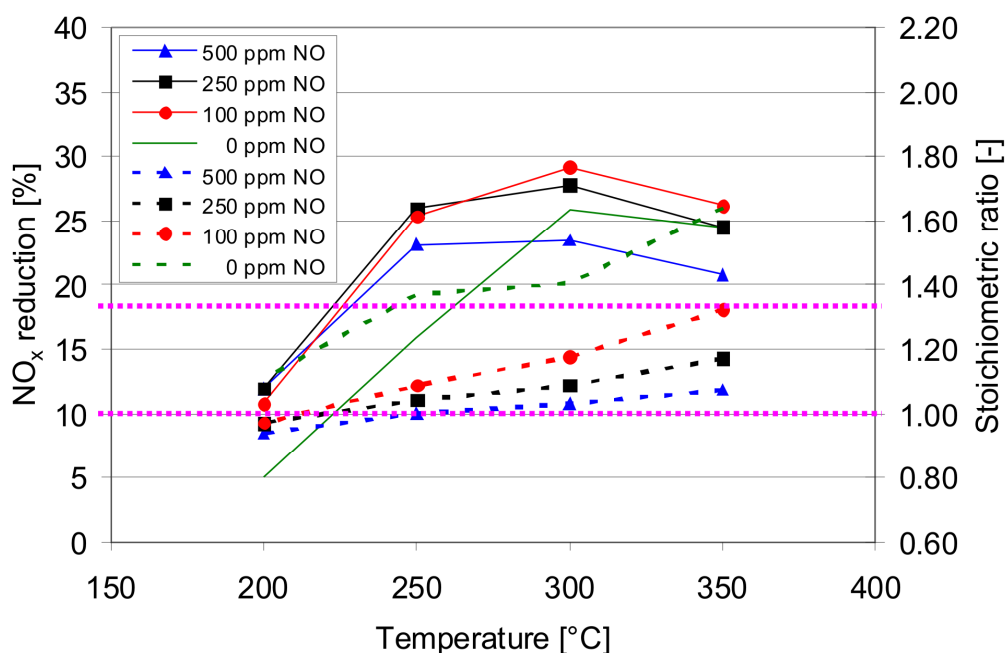


Figure 60: NO_x reduction and measured stoichiometric ratios over Printex U in dependence of the NO concentration between 200°C and 350°C at a GHSV of $35,000\text{ h}^{-1}$. Concentrations in the base feed gas: $250\text{ ppm NO}_2 + 250\text{ ppm NH}_3 + \text{variable NO concentrations}$. Solid lines: NO_x reduction [%]; dotted lines: measured stoichiometric ratios; purple dotted lines: stoichiometry of the *fast SCR* and *$\text{NO}_2\text{ SCR}$* reaction.

The comparison of the experiments with 0, 100, 250 and 500 ppm NO in Figure 60 showed that the presence of NO led to an increase of the NO_x reduction rate up to 10% at $200\text{-}250^\circ\text{C}$. At 300°C , the rates were higher for 100 ppm and 250 ppm NO, but smaller for 500 ppm NO. At 350°C , only the rate with 100 ppm NO was higher than the experiment without NO. In comparison to the experiment with 0 ppm NO the measured stoichiometric ratios decreased with

increasing NO concentration. For 250 ppm and 500 ppm NO values around 1 were reached indicating the *fast SCR* reaction. For 100 ppm NO the measured stoichiometry was slightly higher, most probably due to the occurrence of the *fast SCR* and NO_2 SCR reaction in parallel. The further increase of the measured stoichiometry at higher temperatures was due to unselective NH_3 oxidation.

Although the stoichiometric ratios indicated the occurrence of the *fast SCR* reaction in the presence of 500 ppm NO, the NO_x reduction activity of Printex U seemed to be higher in the absence of NO above 300°C. However, it has to be pointed out that the NO_x reduction is a relative parameter, which compares the amount of converted NO_x with the amount of NO_x in the feed gas (eq. 2.2)). Therefore, the NO_2 and NH_3 conversion should be considered in order to clarify the reasons for the observed trend. In Figure 61, the total NO_2 conversion due to SCR reaction and soot oxidation is plotted together with the NH_3 conversion.

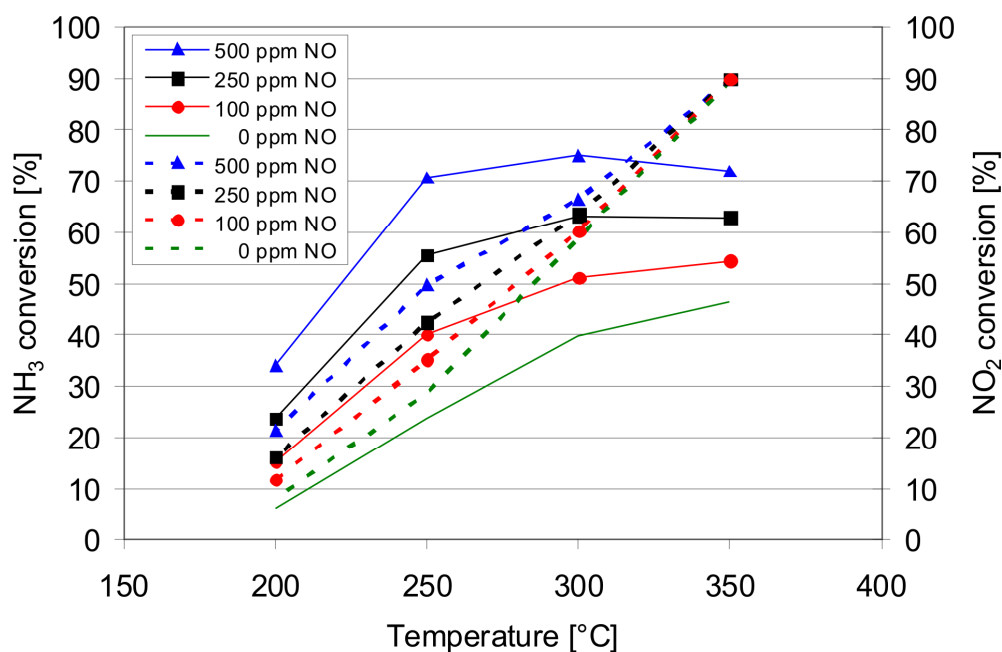


Figure 61: NH_3 and NO_2 conversion over Printex U in dependence of the NO concentration between 200°C and 350°C at a GHSV of 35,000 h^{-1} . Concentrations in the base feed gas: 250 ppm NO_2 + 250 ppm NH_3 + variable NO concentrations. Solid lines: NH_3 conversion [%]; dotted lines: NO_2 conversion due to SCR and soot oxidation.

The curves show clearly that the NO₂ conversion was enhanced with increasing NO concentration between 200°C and 300°C. Around 300°C, the NO₂ conversion rates approached each other independent of the NO concentration. At 350°C the NO₂ conversion reached 90% for all feed gas compositions indicating that the NO₂ concentration became the rate limiting parameter. In parallel, the NH₃ conversion also increased with the NO concentration. Above 250°C the NH₃ conversion rates flattened out, but kept their relative distances among each other.

Since all experiments were performed on the same soot sample for a given temperature, the NO₂ conversion due to soot oxidation remained constant in that temperature range. Therefore, the increase of the NO₂ conversion in Figure 61 for a given temperature must have been due to the concentration-dependent participation of NO in the SCR process. This conclusion was supported by the increase of the corresponding NH₃ conversion with increasing NO concentration and the smaller stoichiometric ratios measured for higher NO inlet concentrations. Therefore, the smaller NO_x reduction observed for 500 ppm above 300°C (Figure 60) in comparison to the series without NO was not due to the smaller activity of Printex U in that temperature range. The reason was the NO₂ limitation and the fact, that NO could not be reduced by NH₃ in a *standard* SCR reaction in the absence of NO₂ (as shown in Figure 57). In other words, an increase of the NO inlet concentration led to a decrease of the NO_x reduction for 500 ppm at 350°C in comparison to the series with 0 ppm NO, because the NO_x inlet concentration was increased, while the amount of reduced NO_x remained constant due to the NO₂-limitation of the SCR reaction.

The variation of the NO₂ concentration (Figure 62) showed decreasing NO_x reduction rates with increasing NO₂ concentrations at constant NH₃

concentration. This was due to the fact, that NO_2 could not be completely reduced to nitrogen because of an understoichiometric dosage of NH_3 compared to NO_2 . The measured stoichiometric ratios were between 1.30-1.40 at 250-300°C for 500 ppm and 250 ppm NO_2 , but increased at 100 ppm due to unselective NH_3 oxidation reactions. At 350°C the factor increased in consequence of unselective NH_3 oxidation for all concentrations. From these results it is concluded that again the NO_2 SCR reaction prevailed.

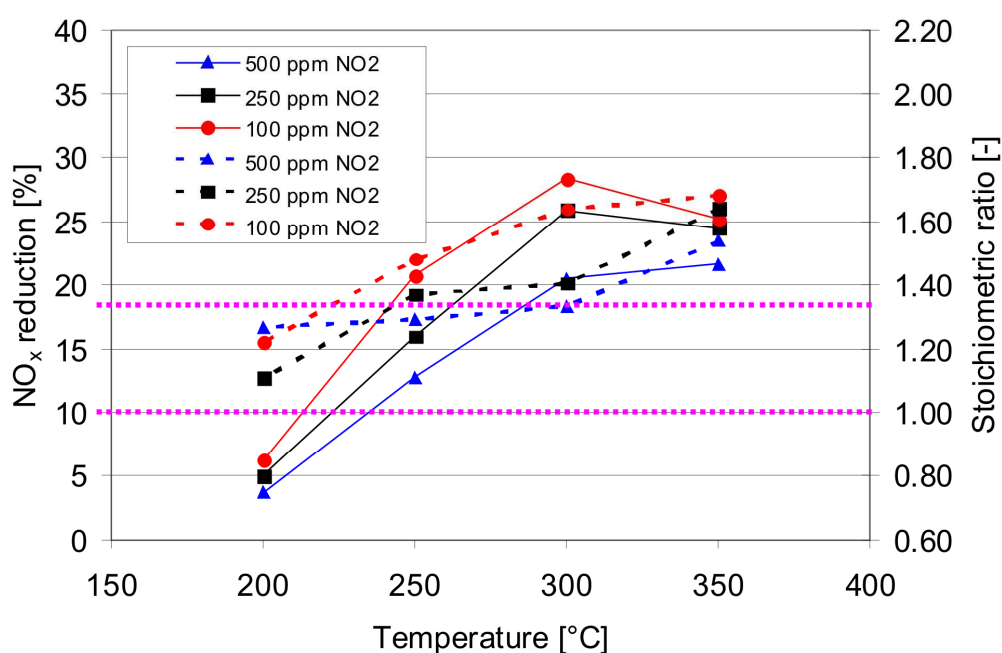


Figure 62: NO_x reduction and measured stoichiometric ratios over Printex U in dependence of the NO_2 concentration between 200°C and 350°C at a GHSV of $35,000 \text{ h}^{-1}$. Concentrations in the base feed gas: 250 ppm NH_3 + variable NO_2 concentrations. Solid lines: NO_x reduction [%]; dotted lines: measured stoichiometric ratios; purple dotted lines: stoichiometry of the *fast SCR* and NO_2 SCR reaction.

6.3.3. C-oxidation rates of Printex U in the presence of NO_2 , NO and NH_3

Since the SCR reaction on soot is of interest for combined SCR and DPF systems [31], it is important to investigate not only the NO_x reduction activity of soot,

but also the influence of different SCR conditions on the parallel occurring C-oxidation.

In Figure 63 - Figure 65 the C-oxidation rates (for explanation see section 2.4.1) at different NH_3 , NO_2 and NO concentrations between 200-350°C are plotted beside the NO_x reduction. The comparison of the C-oxidation rates at 0 ppm NH_3 with those at 100 ppm, 250 ppm and 500 ppm NH_3 did not show a distinct difference between 200°C and 250°C (Figure 63).

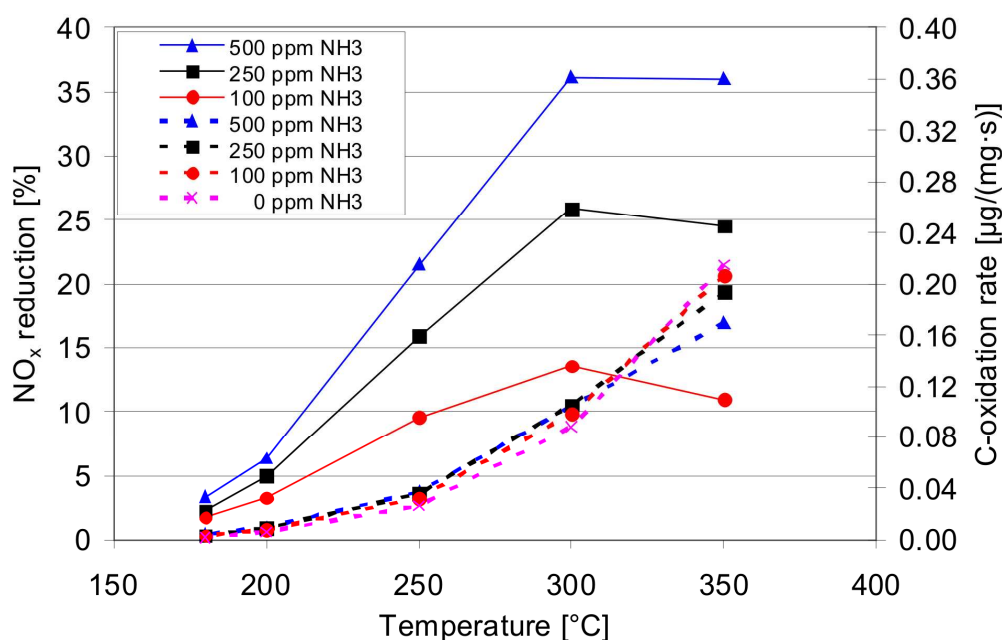


Figure 63: NO_x reduction and C-oxidation rates of Printex U during the SCR measurements in dependence of the NH_3 concentration between 200°C and 350°C at a GHSV of $35,000 \text{ h}^{-1}$. Concentrations in the base feed gas: 250 ppm NO_2 + variable NH_3 concentrations. Solid lines: NO_x reduction [%]; dotted lines: C-oxidation rates.

However, at temperatures from 250°C to 300°C the rates at 0 ppm and 100 ppm NH_3 were slightly lower than those at 250 ppm and 500 ppm NH_3 . This difference can be explained by the decomposition of nitrile and amide species, which are formed from the reaction of NH_3 with carboxylic functional groups as reported in [124]. The decomposition products of these functional groups are

HCN and HNCO, respectively. (In section 6.3.4 the formation and decomposition of these groups will be shown in detail.) Above 300°C the inverse situation was observed; the C-oxidation rates in absence of NH₃ were highest and decreased with increasing NH₃ concentration since soot oxidation became more active in this temperature range and the fraction of NO₂, which was consumed in the SCR reaction SCR was not available for soot oxidation.

Varying the NO concentration from 100 ppm to 250 ppm and 500 ppm NO did not change much the C-oxidation rates between 200°C and 350°C (Figure 64).

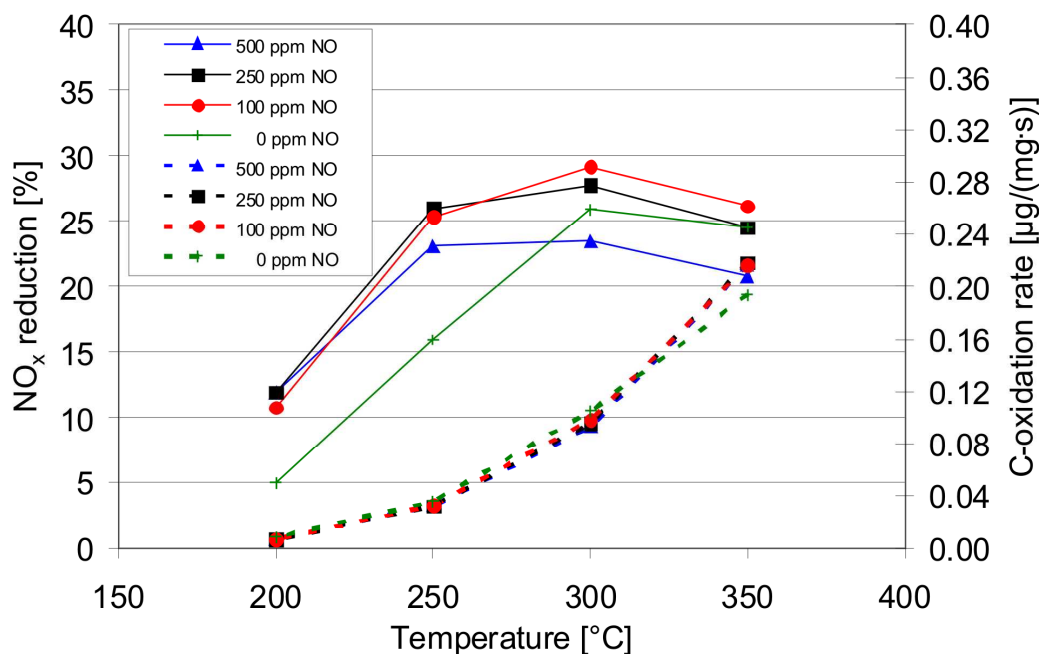


Figure 64: NO_x reduction and C-oxidation rates of Printex U during the SCR measurements in dependence of the NO concentration between 200°C and 350°C at a GHSV of 35,000 h⁻¹. Concentrations in the base feed gas: 250 ppm NO₂ + 250 ppm NH₃ + variable NO concentrations. Solid lines: NO_x reduction [%]; dotted lines: C-oxidation rates.

The C-oxidation rates without NO in the feed were also almost the same as those with NO in the feed at 200-250°C, but slightly exceeded the values of the

experiments with NO between 250 °C and 300 °C. This was due to the increased NO₂ consumption by SCR in the presence of NO and therefore decreasing NO₂ amounts, which could account for the soot oxidation. Above 300°C, the C-oxidation rates without NO were below those with NO in the reactive gas. It seemed that in the presence of NO a smaller amount of the carbon sample was oxidized between 250°C and 300°C, which could account for the C-oxidation rates at higher temperatures.

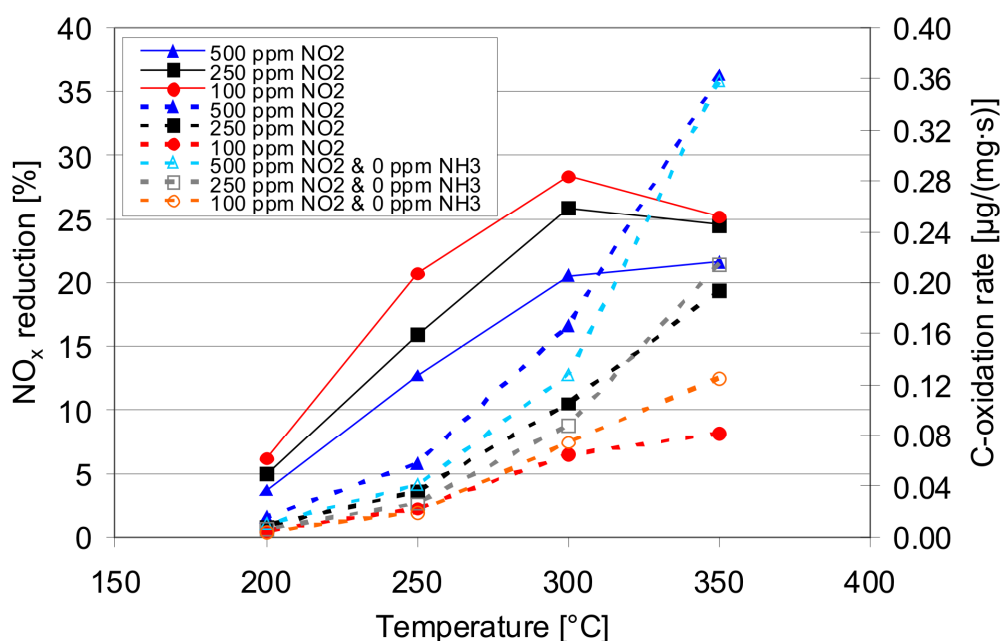


Figure 65: NO_x reduction and C-oxidation rates of Printex U during the SCR measurements in dependence of the NO₂ concentration between 200°C and 350°C at a GHSV of 35,000 h⁻¹. Concentrations in the base feed gas: 250 ppm NH₃ + variable NO₂ concentrations. Solid lines: NO_x reduction [%]; dotted lines: C-oxidation rates.

In Figure 65 the C-oxidation rates are shown for different NO₂ feed gas concentrations. An increase of the NO₂ concentration led to an expected increase of the C-oxidation, but it was interesting to note that for 250 ppm and 500 ppm the C-oxidation rates were higher in the presence NH₃. This effect

might again be explained by the formation of amide species and nitriles, which decompose into HNCO and HCN.

The measurements of the C-oxidation rates with different NH_3 , NO and NO_2 concentrations showed only a minor influence of the SCR conditions on the soot oxidation. This suggested, that nitrogen species involved in the SCR process did not affect the decomposition of surface functional groups responsible for the soot oxidation, no matter if they are chemisorbed or physisorbed.

6.3.4. Byproducts generated in the presence of NO_2 , NO and NH_3 over Printex U

During the investigation of the NO_x reduction over Printex U also the concentrations of HCN, HNCO, N_2O , HNO_3 and HONO were measured, which were reaction intermediates of the SCR reaction and the soot oxidation or products of unselective side reactions.

In Figure 66 - Figure 68 the concentrations of HCN, HNCO, N_2O and HNO_3 during the SCR measurements presented in Figure 59 - Figure 65 are shown. HONO was not included in the graphs since it showed a distinct cross-sensitivity with NH_3 in the FTIR analysis and a background shift over the duration of the experiment. However, it is important to note, that at the beginning of the measurements after the addition of 250 ppm NO_2 , but before the NH_3 dosage, up to 5 ppm HONO were evolved. Therefore, it is reasonable to assume that HONO was also formed in the presence of NH_3 , although it could not be measured. The HNO_3 concentrations have to be interpreted carefully since they also were slightly cross-sensitive with NH_3 .

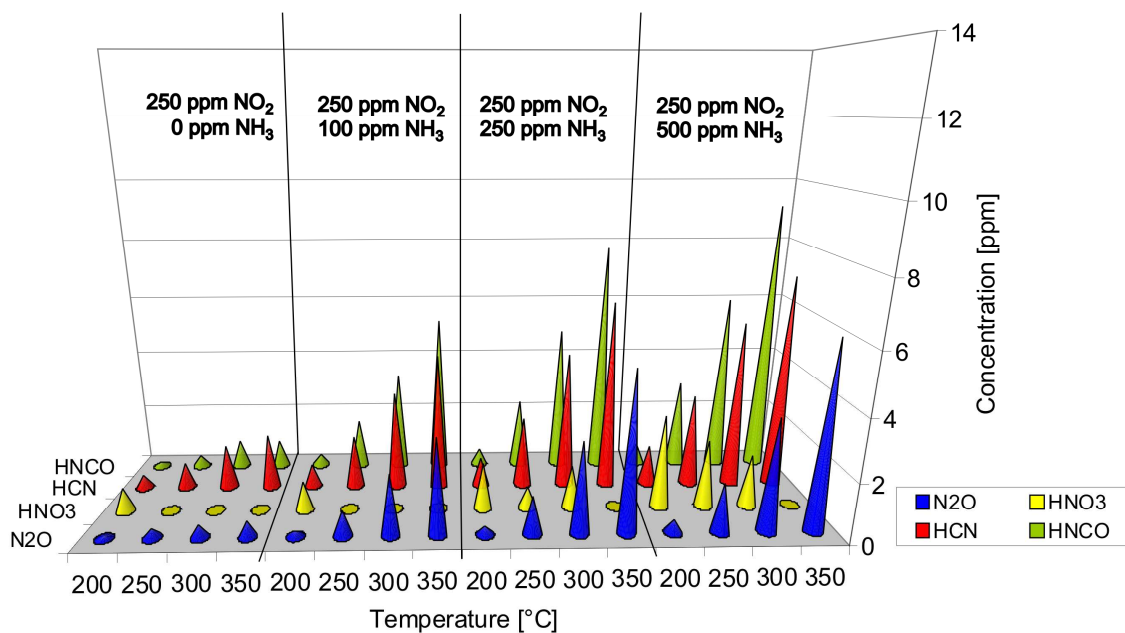


Figure 66: Byproducts of the SCR reaction on Printex U in dependence of the NH₃ concentration between 200°C and 350°C at a GHSV of 35,000 h⁻¹.

In Figure 66 the side products are shown in dependence of the NH₃ concentration. In the absence of NH₃ small amounts of HCN and HNCO were found at 200°C, while N₂O and HNO₃ did not exceed their detection limits.

With the addition of 100 ppm NH₃, side product formation was observable over the whole temperature range. HCN and HNCO showed a significant concentration gain with temperature similar to N₂O. This trend was further pronounced upon the addition of 250 ppm and 500 ppm NH₃. HNO₃ was detected at 200°C for all NH₃ concentrations, but then the concentration decreased again below the detection limit. With increasing NH₃ amount dosed, also detectable amounts of HNO₃ were observed at higher temperatures; however, this was most probably due to the cross-sensitivity with NH₃. At 350°C hardly any HNO₃ was found, because the rate of reaction was larger than the rate of desorption.

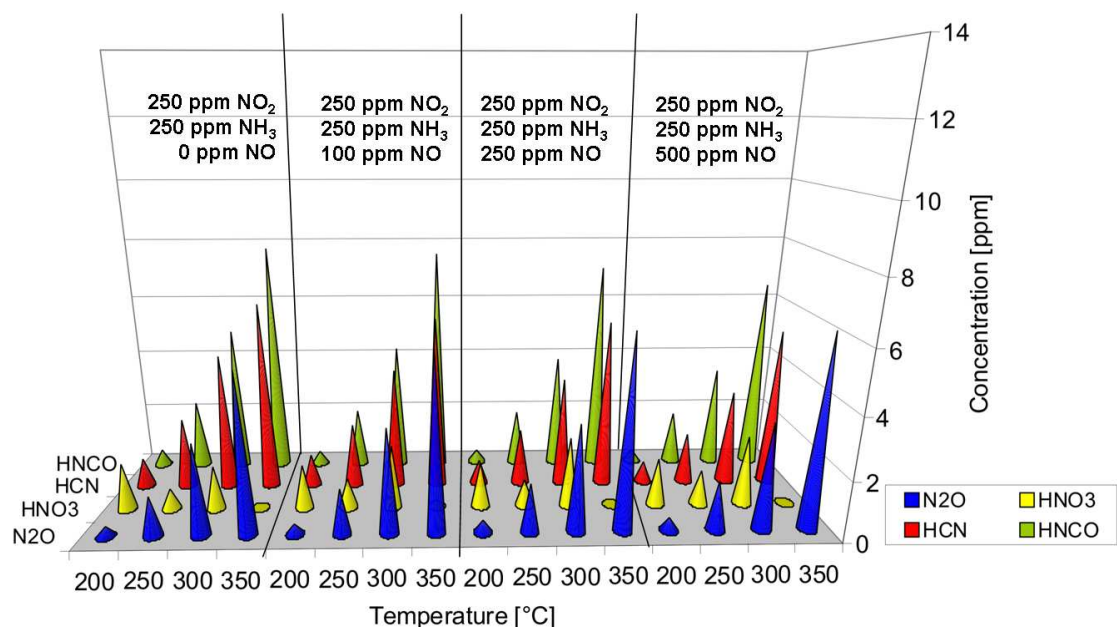


Figure 67: Byproducts of the SCR reaction on Printex U in dependence of the NO concentration between 200°C and 350°C at a GHSV of 35,000 h⁻¹.

In Figure 67 the results for HCN, HNCO, N₂O and HNO₃ at different concentrations of NO are shown. The NO₂ and NH₃ concentration were kept constant at 250 ppm. Between 200°C and 300°C small amounts of HNO₃ were emitted in the presence of NH₃ close to the detection limit, but it seemed as if they were not influenced by the NO variation. The N₂O concentration showed an increase with temperature, but decreased only very little with increasing NO concentration. The HCN and HNCO concentration increased with temperature, but more interesting to note was that HCN and even more pronounced HNCO decreased with increasing NO concentration. This decrease was caused by the acceleration of the SCR reaction by adding more NO, which limited the NH₃ concentration - the main source for HCN and HNCO formation as will be shown later.

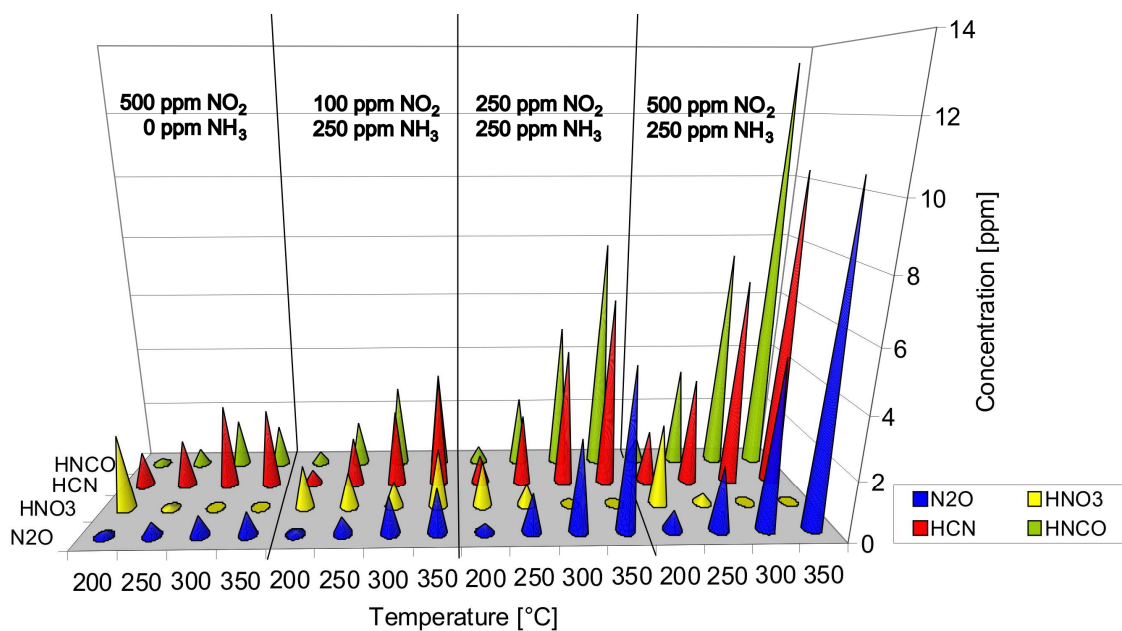
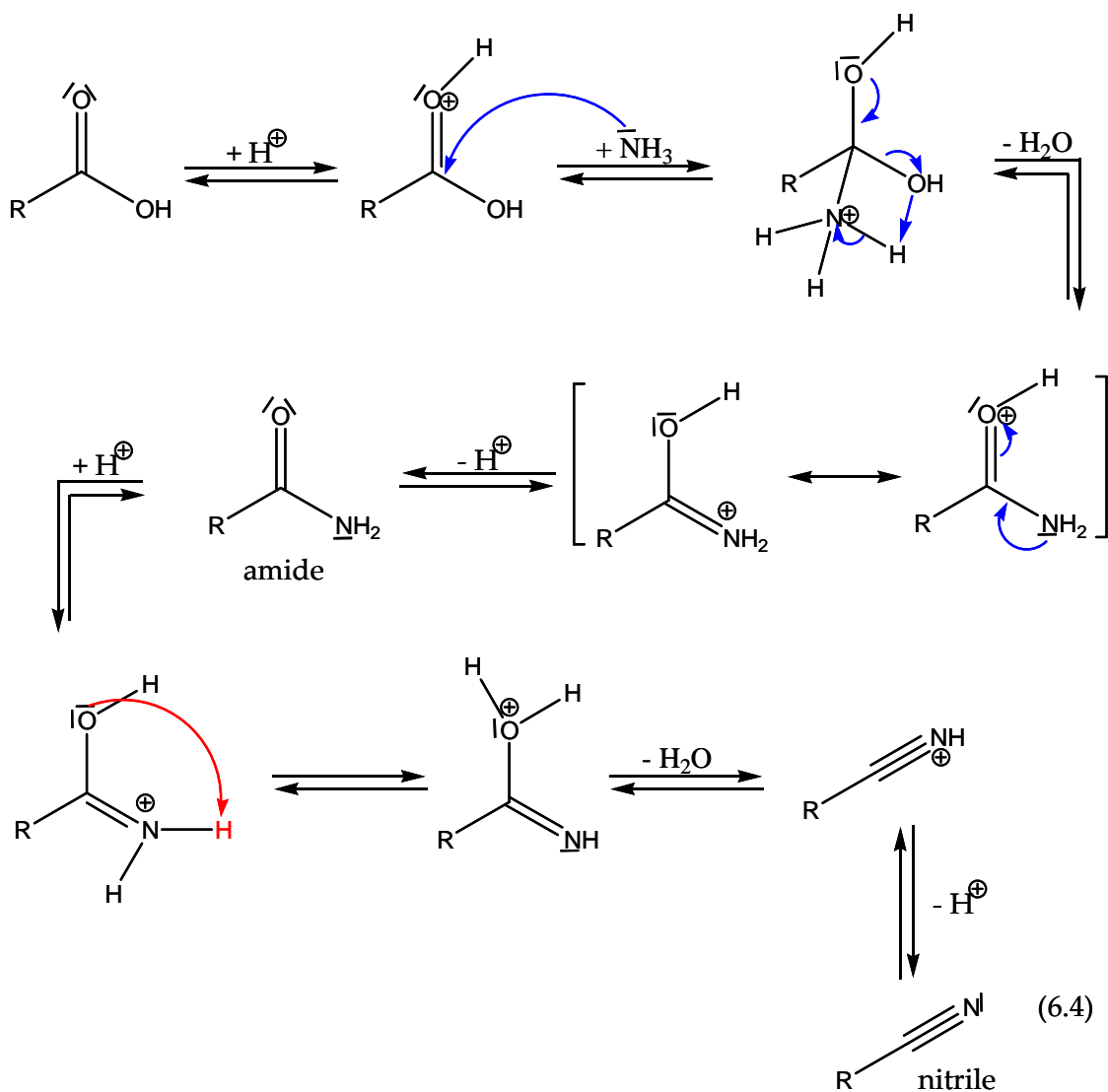


Figure 68: Byproducts of the SCR reaction on Printex U in dependence of the NO₂ concentration between 200°C and 350°C at a GHSV of 35,000 h⁻¹.

Figure 68 presents the results of the HCN, HNCO and N₂O measurements at different NO₂ concentrations. In comparison to the results presented in Figure 66, the data of the experiments with 500 ppm NO₂ and 0 ppm NH₃ show that the presence of NH₃ led to increased concentrations of HCN, HNCO and N₂O with increasing NO₂ concentration. The HNO₃ concentration exceeded its detection limit only at 200°C. The addition of 100 ppm NO₂ and 250 ppm NH₃ led to an enhanced formation of HNCO, HCN and N₂O, as already discussed for Figure 67. An increase of the NO₂ concentration and temperature enhanced the HCN, HNCO and N₂O concentrations. With 500 ppm NO₂ and 250 ppm NH₃ concentrations up to 10 ppm HCN, 14 ppm HNCO and 10 ppm N₂O were reached at 350°C.

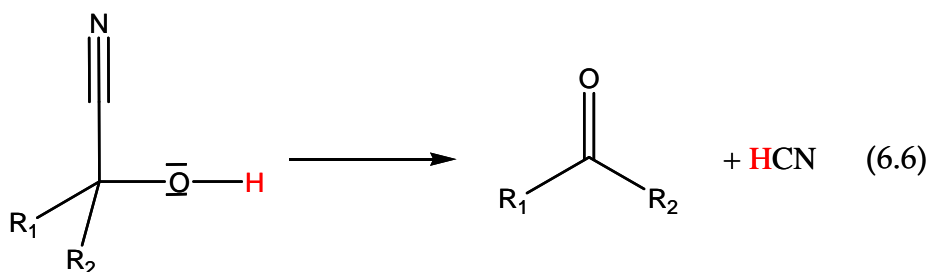
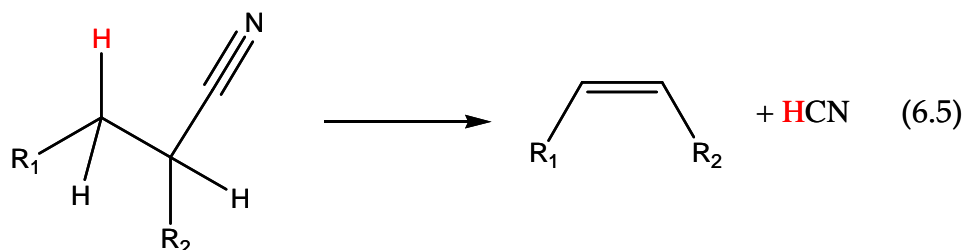
As already mentioned in the previous section, HCN was most probably formed by the decomposition of surface nitriles. The nitrile groups, which were

indicated by C=N vibrations found during DRIFTS measurements of this work (see section 6.3.9) and the study of Zawadzki et al. [124], were most probably formed from the reaction of NH_3 with carboxylic acids, leading to amides first, which decompose similar to the back reaction of the nitrile hydrolysis, as shown in reaction (6.4) [175]. Here, the acid catalyzed nitrile formation is described, however, it can also be base catalyzed [175]:



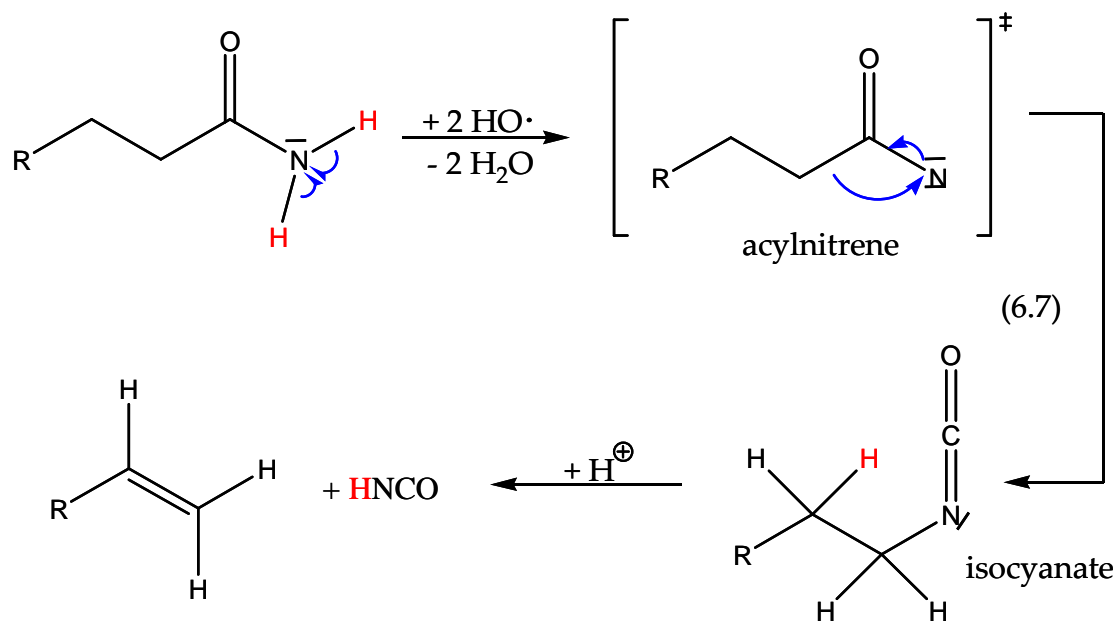
For the decomposition of the nitriles under evolution of HCN two reactions are thinkable: First, reaction (6.5), which leads to the formation of an alkene and

HCN similar to the back reaction of the so-called hydrocyanation [176, 177]. And second, reaction (6.6), which occurs in the case of hydroxyl nitrile species leading to the formation of an aldehyde or ketone in dependence of R_1 and R_2 [51]:



It was assumed that, HNCO was most probably formed by the decomposition of surface isocyanates, which were confirmed during the DRIFTS measurements of this work (see section 6.3.9) and the study of Zawadzki et al. [124]. It was suggested that the isocyanates were formed during the rearrangement of surface amides (eq. (6.7)), which might proceed via intermediates similar to those assumed for the *Hofmann*-rearrangement [51, 175]. Since the hypobromite, which is normally used for the Hofmann rearrangement, is missing over soot, $\text{OH}\cdot$ resulting from the soot oxidation (see section 4.5.3) was suggested to take the role of the base to form the acylnitrene species. The acylnitrene has only an electron sextet, which stabilizes by the rearrangement to a isocyanate. In the last step, the isocyanate was assumed to

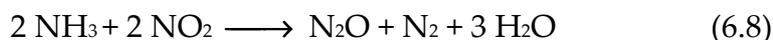
decompose under formation of HNCO and an alkene in a reaction similar to reaction (6.5):



The occurrence of reactions (6.4)-(6.7) was indicated by the increase of the HCN and HNCO concentration with increasing NH_3 concentration observed during the NH_3 variation (Figure 66). Moreover, these reactions also explain the strongly raised HCN and HNCO concentrations observed in Figure 68, which occurred only in the presence for 500 ppm NO_2 + 250 ppm NH_3 . Most probably the increased HNCO and HCN formation was due to the enhanced formation of derivatives of carboxylic acids in the presence of high amounts of NO_2 [62], which reacted with NH_3 to NCO and nitriles species.

Since N_2O resulted from a comproportionation reaction during NO_x reduction (eq. (6.8)) and from the oxidation of NH_3 (eq. (6.9)) [89], it was expected to increase with the NO_x reduction, i.e. with the NH_3 and NO_2 concentration as well as with temperature, which was confirmed by the trends presented in

Figure 66 - Figure 68, and explains especially the significant N₂O gain during the NO₂ variation depicted in Figure 68.



HNO₃ and HONO were formed in presence of water on the soot surface by a disproportionation of NO₂, as already shown in chapter 5 (eq. (5.3)) [166-168], which was supported by the detection of HNO₃ and HONO during the experiments without NH₃ in the feed gas (Figure 68):



Furthermore, HONO could be generated via hydrogen abstraction from the soot surface by NO₂ as shown in [42] and as it is known from partial oxidation of light organic molecules in the gas phase [50] (see soot oxidation network in section 4.5.3).

6.3.5. Influence of the space velocity on the SCR reaction over Printex U

Figure 69 - Figure 71 show NO_x reduction and NO₂ conversion during the variation of the space velocity between 70,000 and 3000 h⁻¹ in the tubular reactor at 250°C for different concentrations of NH₃, NO and NO₂. As stated in Table 7 the GHSV 17,000 h⁻¹ was realized with two differently dimensioned monoliths. The same results have been obtained in both experiments, which only differed in the range of the measurement error. Therefore, only the results of monolith 3 have been included.

The data showed clearly that a decrease of the space velocity led to a large increase of the NO_x reduction and NO_2 conversion for all reactive gas compositions due to an increase of the residence time in the reactor. Again, the trend that an increase of the NH_3 concentration ended up in an increased NO_x reduction rate was confirmed (Figure 69). The steeper ascent of the NO_x reduction curves for 250 ppm and 500 ppm NH_3 at low space velocities in comparison to the curve for 100 ppm NH_3 was caused by the limited amount of NH_3 compared to the 250 ppm of NO_2 dosed. This could be also seen from the NO_2 conversion, which was about 15% lower than those at higher NH_3 concentrations.

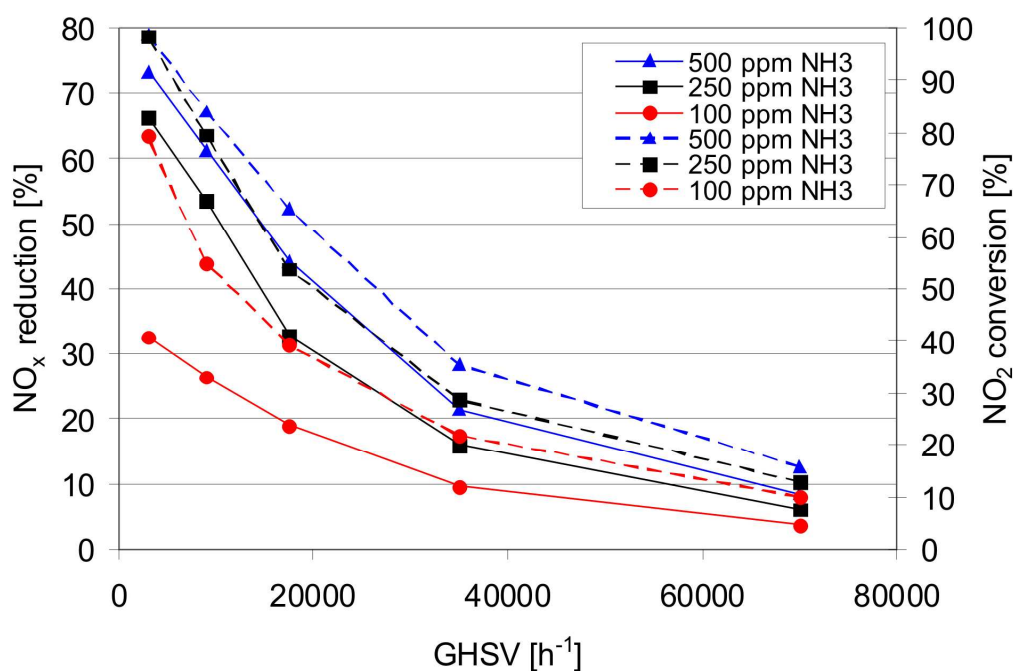


Figure 69: NO_x reduction and NO_2 conversion over Printex U at different space velocities (3000 h^{-1} , 9000 h^{-1} , 17,000 h^{-1} , 35,000 h^{-1} and 70,000 h^{-1}) in dependence of the NH_3 concentration at 250°C. Concentrations in the basic feed gas: 250 ppm NO_2 + variable NH_3 concentrations. Solid lines: NO_x reduction [%]; dotted lines: NO_2 conversion. The y-axis was scaled up to 80% in opposite to the Figure 59 - Figure 65.

An increase of the NO concentration in Figure 70 led to an enhanced NO_x reduction at space velocities above 30,000 h^{-1} similar to the results in Figure 60.

But at space velocities lower than $30,000 \text{ h}^{-1}$ the NO_x reduction showed a steeper ascent in the absence of NO than with 100 ppm, 250 ppm and 500 ppm NO in the feed gas. This was due to the fact, that in the presence of NO the reaction was limited by the NH_3 quantity and excess NO_x could not be removed as observable from the difference in the NO_2 conversions with 500 ppm NO and without NO.

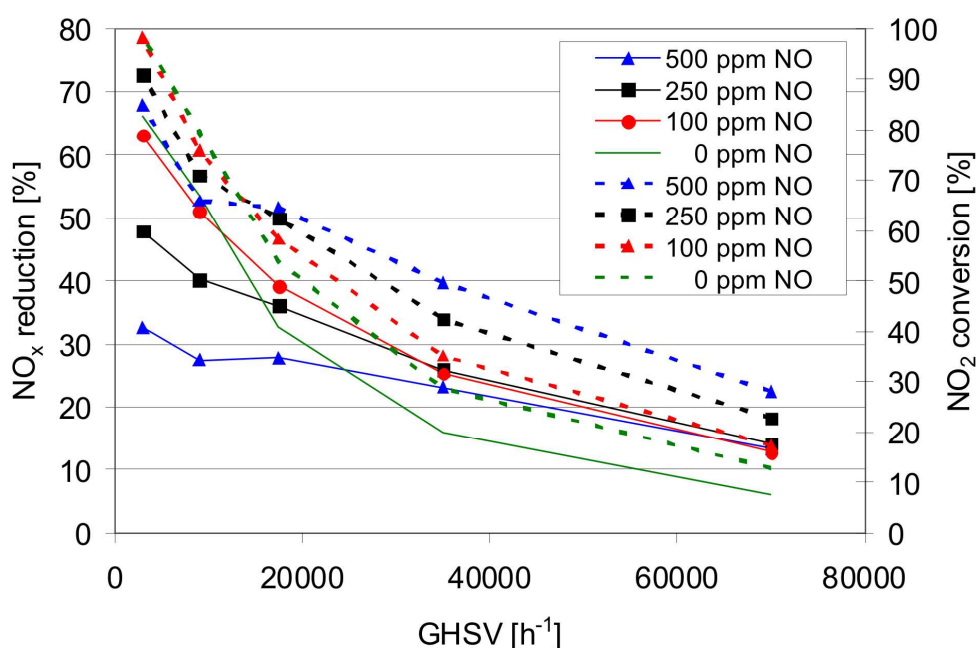


Figure 70: NO_x reduction and NO_2 conversion over Printex U at different space velocities (3000 h^{-1} , 9000 h^{-1} , $17,000 \text{ h}^{-1}$, $35,000 \text{ h}^{-1}$ and $70,000 \text{ h}^{-1}$) in dependence of the NO concentration at 250°C . Concentrations in the basic feed gas: 250 ppm NO_2 + 250 ppm NH_3 + variable NO concentrations. Solid lines: NO_x reduction [%]; dotted lines: NO_2 conversion. The y-axis was scaled up to 80% in opposite to the Figure 59 - Figure 65.

Figure 71 presents the results of the NO_2 variation. On the first view it might be irritating that the NO_x reduction rate at 3000 h^{-1} and 100 ppm NO_2 reached only 60%, while it reached 66% at 250 ppm NO_2 although the NO_2 was totally converted in both cases. This could be explained with the soot oxidation, which is accompanied by a reduction of a constant amount of NO_2 to NO, independent of the NO_2 concentration. At high space velocities this did not affect the NO_x

reduction rate, because the NO_2 conversion rates were much lower, but at lower space velocities total NO_2 conversion was reached limiting the NO_x reduction rates.

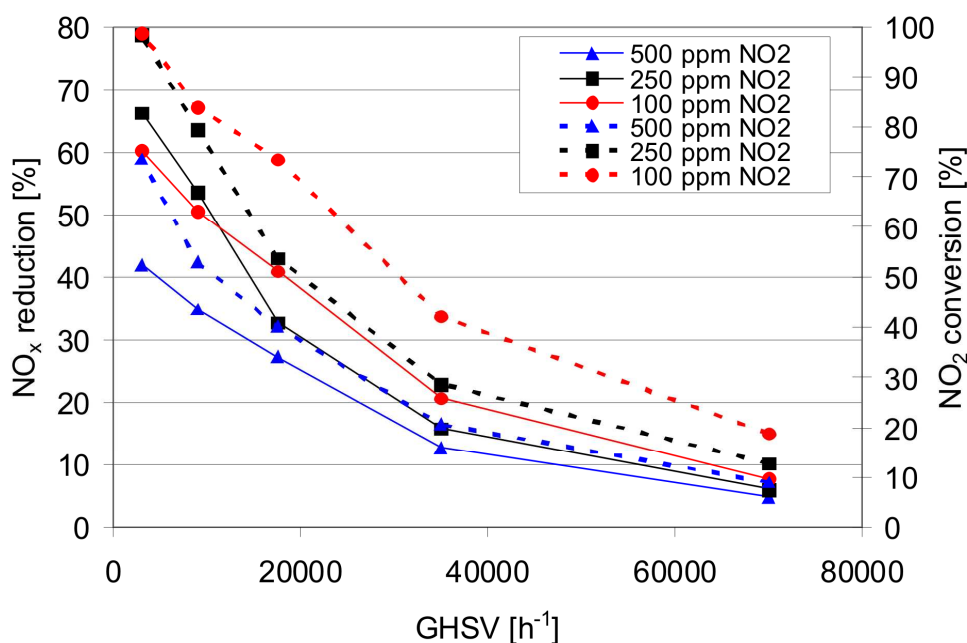


Figure 71: NO_x reduction and NO_2 conversion over Printex U at different space velocities (3000 h^{-1} , 9000 h^{-1} , $17,000 \text{ h}^{-1}$, $35,000 \text{ h}^{-1}$ and $70,000 \text{ h}^{-1}$) in dependence of the NO_2 concentration at 250°C . Concentrations in the basic feed gas: 250 ppm NH_3 + variable NO_2 concentrations. Solid lines: NO_x reduction [%]; dotted lines: NO_2 conversion. The y-axis was scaled up to 80% in opposite to the Figure 59 - Figure 65.

One may speculate that part of the NO formed from NO_2 during soot oxidation has participated in the SCR reaction at low space velocities in opposite to the results at $35,000 \text{ h}^{-1}$ presented in Figure 59 - Figure 61, where the influence of NO could be excluded. This view is supported by the observed stoichiometric ratios in Figure 72 in the presence and the absence of NO at different space velocities. The measured stoichiometric ratios in the presence of NO reached values of 1-1.10 and were almost constant under the applied conditions. This ratio is characteristic for the occurrence of the *fast SCR* reaction. On the other hand the measured stoichiometric ratios in the absence of NO were 1.29 and

1.37 for space velocities of 70,000 h⁻¹ and 35,000 h⁻¹, respectively, indicating the NO₂ SCR reaction. At lower space velocities the measured stoichiometric ratios decreased to 1.20 at 3000 h⁻¹ indicating the parallel running of the *fast SCR* and NO₂ SCR reaction. It cannot be excluded that a small amount of NO formed during soot oxidation from NO₂ could also participate in the SCR process.

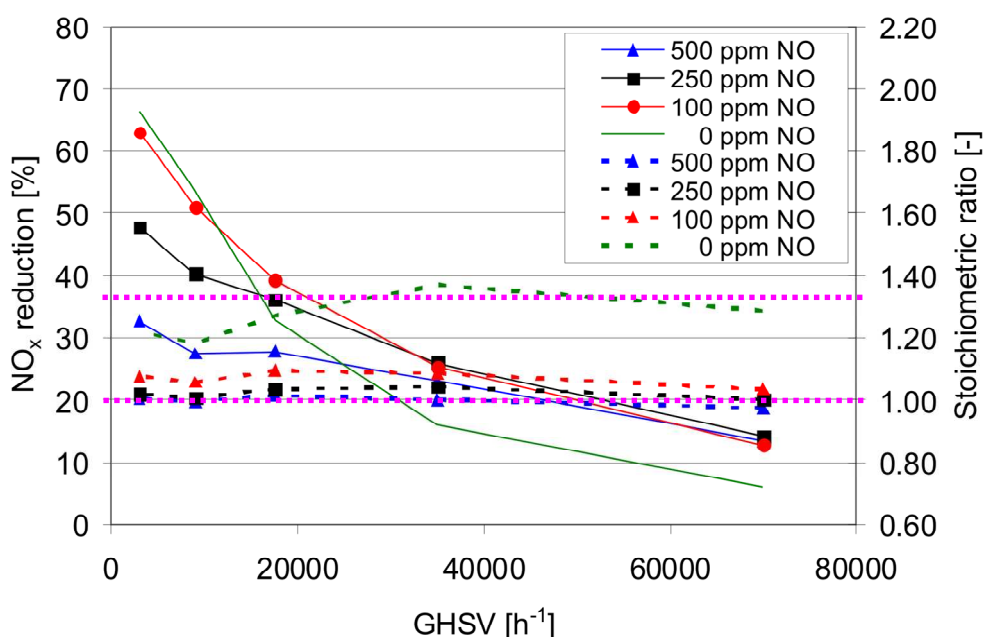


Figure 72: NO_x reduction and measured stoichiometric ratios over Printex U at different space velocities (3000 h⁻¹, 9000 h⁻¹, 17,000 h⁻¹, 35,000 h⁻¹ and 70,000 h⁻¹) in dependence of the NO concentration at 250°C. Concentrations in the feed gas: 250 ppm NO₂ + 250 ppm NH₃ + variable NO concentrations. Solid lines: NO_x reduction rate [%]; dotted lines: measured stoichiometric ratios; purple dotted lines: stoichiometry of the *fast SCR* (=1) and NO₂ SCR (=1.33) reaction. The y-axis was scaled up to 80% in opposite to the Figure 59 - Figure 65.

6.3.6. SCR reaction over diesel soot in comparison to Printex U

After the NO_x reduction over Printex U was investigated in dependence of the NO₂, NO and NH₃ concentration, temperature and the GHSV, selected

experiments were performed with the real diesel soot (Euro V, Euro 0, mixed soot) samples. Their ability to reduce NO_x was tested at 250°C and 300°C in dependence of the NO , NO_2 and NH_3 concentration. In Figure 73 and Figure 74 the NO_x reduction and measured stoichiometric ratios in the presence of 250 ppm NO_2 and 250 ppm NH_3 are plotted over the NO concentration, which was varied between 0 ppm and 500 ppm. The results for Printex U were added for comparison. These experiments were chosen since they most clearly show the similarities and differences of model and real soot samples.

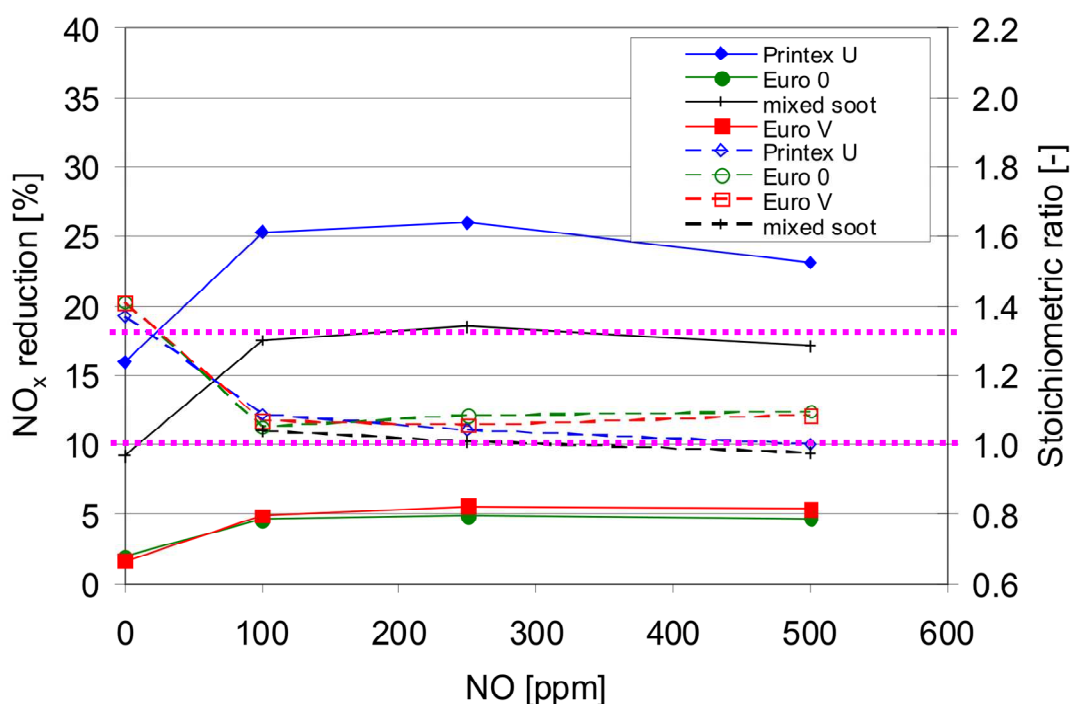


Figure 73: NO_x reduction and measured stoichiometric ratios over Printex U, Euro 0, Euro V soot and the mixed soot sample in dependence of the NO at 250°C. GHSV: $35,000 \text{ h}^{-1}$. Concentrations in the basic feed gas: 250 ppm NO_2 + 250 ppm NH_3 + variable NO concentrations; Solid lines: NO_x reduction [%]; dashed lines: measured stoichiometric ratios; purple dotted lines: stoichiometry of the *fast SCR* (=1) and *NO_2 SCR* (=1.33) reaction.

At 250°C (Figure 73) the mixed soot sample showed a NO_x reduction of about 9% - two third of Printex U. With a rate of less than 3%, the Euro 0 and Euro V

soot were hardly active for NO_x reduction at 0 ppm NO. The addition of 100 ppm NO enhanced the rates for all samples. Higher amounts of NO led to decreasing NO_x reduction for the mixed soot sample since excess NO could not be removed, as already discussed for Printex U in Figure 60 and Figure 61. Apparently, the rates of Euro 0 and Euro V remained constant at about 5% in the range of the experimental error even after the addition of 250 ppm and 500 ppm NO. But due to the low overall conversion small changes in the NO_x reduction rates in presence of excess NO might not be resolved. The measured stoichiometric ratios with the diesel soot samples were around 1 in the presence of NO and, hence, indicated the *fast SCR* reaction just like for Printex U. Without NO in the feed gas the stoichiometric ratios increased up to 1.4 for all samples indicating the NO_2 SCR reaction.

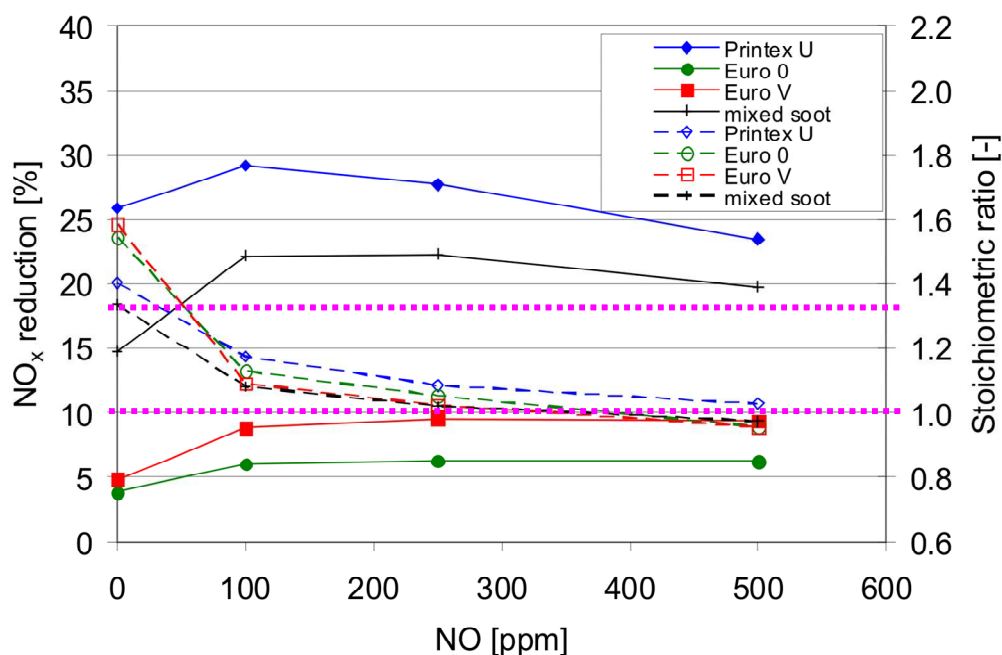


Figure 74: NO_x reduction and measured stoichiometric ratios over Printex U, Euro 0 soot, Euro V soot and the mixed soot sample in dependence of the NO at 300°C. GHSV: $35,000 \text{ h}^{-1}$. Concentrations in the basic feed gas: 250 ppm NO_2 + 250 ppm NH_3 + variable NO concentrations; Solid lines: NO_x reduction [%]; dashed lines: measured stoichiometric ratios; purple dotted lines: stoichiometry of the *fast SCR* (=1) and NO_2 SCR (=1.33) reaction.

At 300°C (Figure 74) NO_x reduction showed the same trend as at 250°C, but reached higher absolute levels. The only distinct difference can be seen between NO_x reduction over the Euro V and Euro 0 samples.

The trends observed for the variation of the NO_2 and NH_3 concentration at 250°C and 300°C for the real diesel soot samples were similar to those obtained for Printex U (Figure 59 and Figure 62): with increasing NH_3 concentration the NO_x reduction also increased, while the NO_x reduction decreased with increasing NO_2 concentration. In addition, the order of the NO_x reduction curves observed for the NO variation were the same independent of the NO_2 and NH_3 concentration: Printex U was most active, followed by the mixed soot sample, while the Euro V and Euro 0 showed the lowest activity in the series.

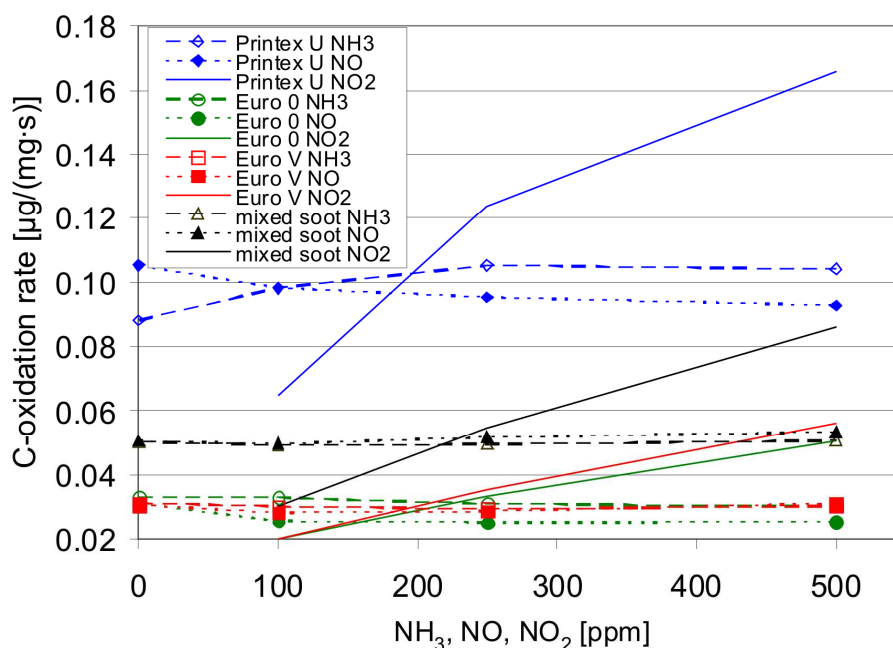


Figure 75: C-oxidation rates over Printex U, Euro 0 soot, Euro V soot and the mixed soot sample in dependence of the NH_3 , NO and NO_2 concentration at 300°C. GHSV: 35,000 h^{-1} . Dashed lines with open symbols: C-oxidation rates of NH_3 variation; dotted lines with filled symbols: C-oxidation rates of NO ; solid lines without symbols: C-oxidation rates of NO_2 .

The comparison of the C-oxidation rates of the different soot samples during NH_3 , NO and NO_2 variation showed interesting results. The C-oxidation rates of the mixed soot sample were hardly influenced by the changing gas composition. The C-oxidation rates of the Euro V and Euro 0 samples were not influenced by the variation of the NH_3 concentration, but the variation of NO led to a small decrease of the C-oxidation since more NO_2 was consumed in the SCR process (see stoichiometric ratios in Figure 72 and Figure 73). And as expected, the oxidation rates were increased by the increase of the NO_2 concentration. However, the C-oxidation rates of the real diesel soot samples were much smaller in comparison to those over Printex U at 250°C and this difference was even more pronounced at 300°C (Figure 75). This was in apparent contrast to the fact, that Printex U was less reactive under transient conditions.

In Figure 76 the byproducts generated during the SCR measurements with 250 ppm NO_2 and 250 ppm NH_3 of the three diesel soot samples are shown in comparison to Printex U at 250°C and 300°C . The data clearly demonstrate, that the more SCR active Printex U evolved more N_2O , HCN and HNCO, while from the diesel soot samples evolved more HNO_3 . The trends among the diesel soot samples were similar to the comparison with Printex U: The more SCR active mixed soot sample, showed higher concentrations of N_2O , HCN and HNCO in the gas phase, while the Euro 0 and Euro V sample evolved higher amounts of HNO_3 .

The observed relative trends between the four soot samples were the same for other concentrations of NO_2 , NH_3 as well as in the presence of NO.

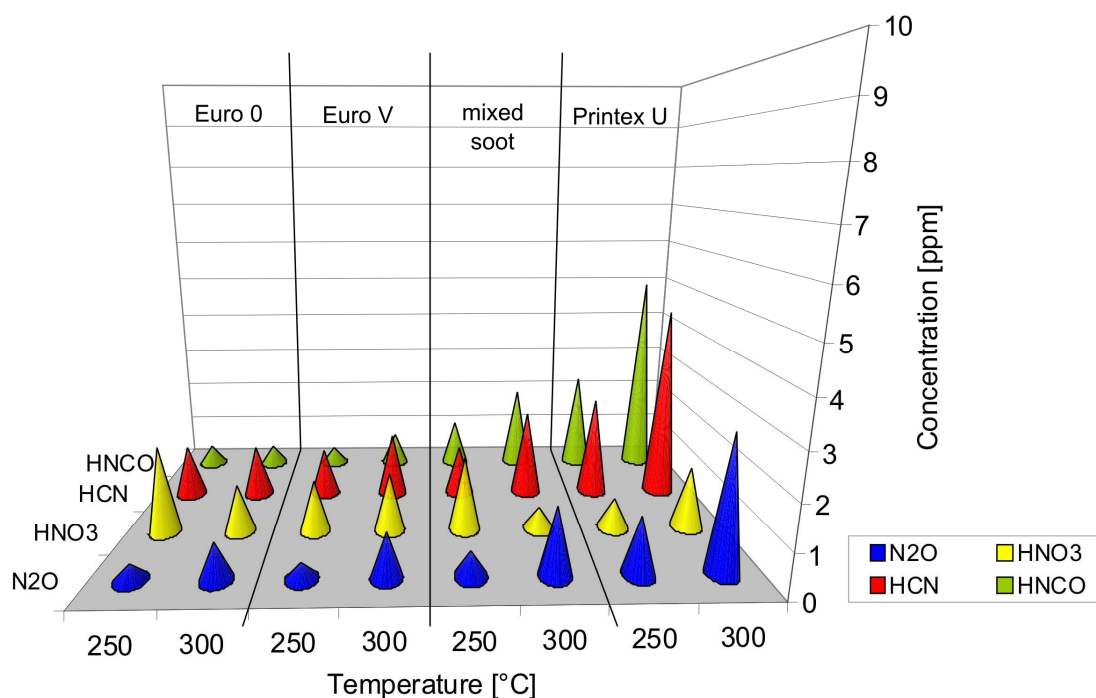


Figure 76: Byproducts of the SCR reaction on Printex U, Euro 0 soot, Euro V soot and the mixed soot sample in dependence of the NH_3 concentration at 250°C and 300°C at a GHSV of $35,000 \text{ h}^{-1}$. Concentrations in the basic feed gas: 250 ppm NO_2 + 250 ppm NH_3 .

From the findings that Printex U showed a higher NO_x reduction and also higher C-oxidation rates in isothermal experiments the question raised, how these differences are originated. In the literature different activated carbon materials with different activities for NO_x removal were described [105, 106, 109, 114, 118, 119, 127, 129, 178-180], but the reasons for their activity could be not completely clarified. At least the occurrence of acidic surface functional groups for NH_3 adsorption (see eq. (1.44)) was identified as an important property of an SCR active carbon material [108, 120, 129, 181, 182]. The authors reported that measures, which increased the number of acidic groups, resulted also in an increase of the NO_x reduction. From investigations of the soot oxidation in the presence of NO_2 it was concluded that NO_2 promotes the formation of carboxylic acids and lactones differently on model and diesel soot

samples [62], but the mechanisms and structural prerequisites did not become clear.

Based on the reports in the last paragraph [62, 108, 120, 129, 181, 182], it was suggested that one reason for the highest NO_x reduction over Printex U in the series was its high activity to form acidic surface functional groups on the carbon surface. Since the OC content of this soot was less than 1% the EC structure was most likely responsible for the formation of acidic surface functional groups. The assumption of more acidic groups for NH_3 adsorption in Printex U was supported by the observed evolution of higher amounts of HCN and HNCO formed (Figure 76), which result almost completely from the decomposition of acidic groups in this temperature range and the increased C-oxidation rates. In addition, the higher amounts of HNO_3 evolved by the real diesel soot samples in comparison to Printex U indicated that the disproportionation step of NO_2 according to eq. (6.6), which is a prerequisite for the occurrence of the SCR reaction (as will be shown later), was most probably not the limiting reaction step. This was also counted as a hint, that the adsorption properties for NH_3 were the critical factor for the SCR reaction over soot.

However, the higher activity to form acidic groups under isothermal conditions was in contrast to the lower reactivity of Printex U under transient conditions, as these groups are known to have low decomposition temperatures in comparison to other functional groups [59]. Therefore, it was assumed that also equilibrium effects were responsible for these observations. This assumption was confirmed by a comparison of the envelope of the NO_x reduction over a complete course of an isothermal experiment. In Figure 77 the NO_x reduction (raw data) of the four soot samples measured at 250°C are plotted over time.

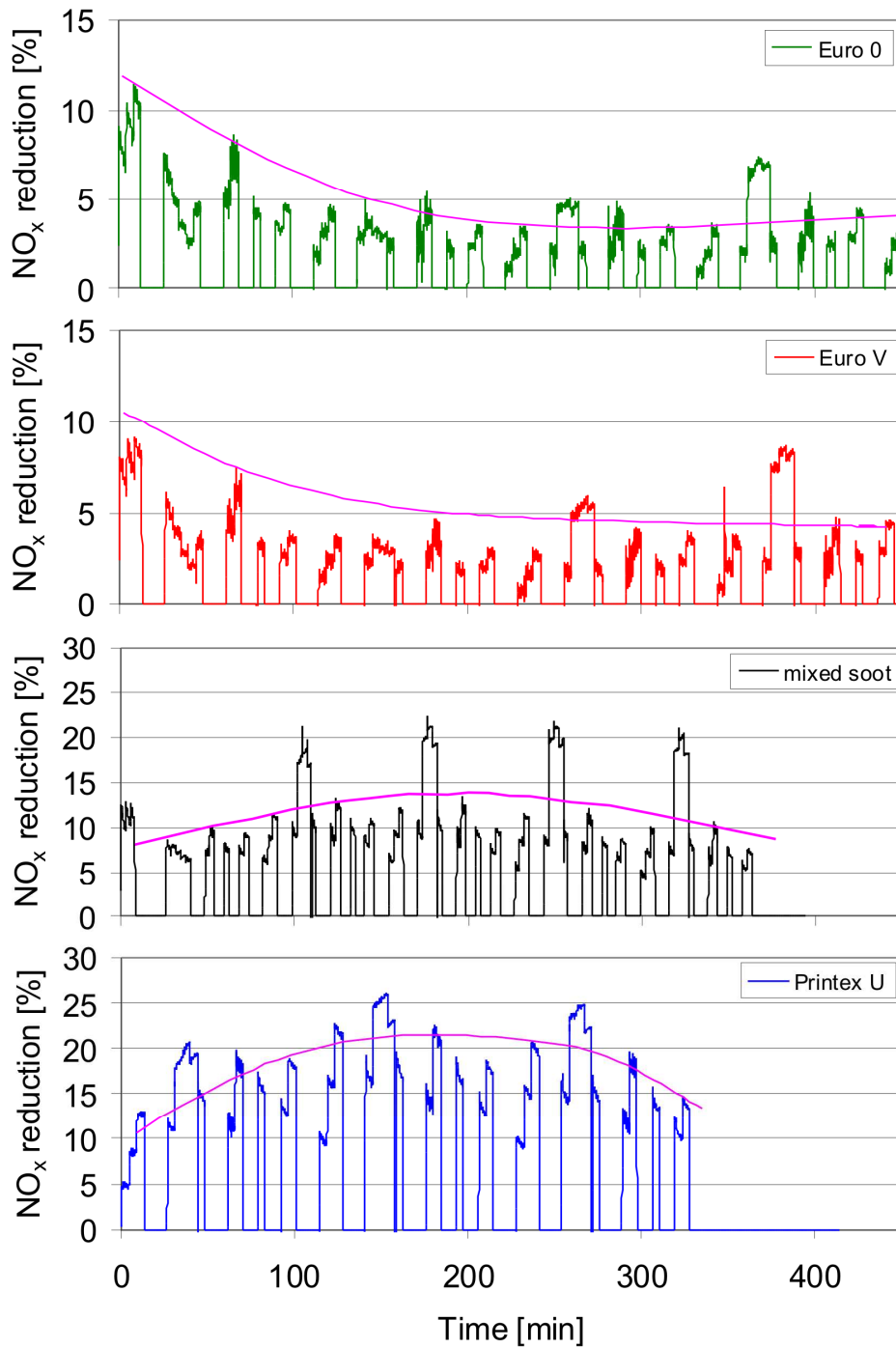


Figure 77: NO_x reduction (raw data) and their envelope of Printex U, mixed soot, Euro V soot and Euro 0 soot over a complete isothermal experiment with repeated series of the blocks 1-3 (Table 16). It should be noted, that the y-axis is scaled to 30% for Printex U and the mixed soot, but only to 15% for the Euro 0 and Euro V sample.

To facilitate the comparison of the NO_x reduction trends the envelope is plotted for each sample. Since the C-oxidation rates of the real diesel soot samples were smaller, the experimental series could be repeated up to five times, while for Printex U the measurements were terminated after three repetitions. But this was already enough to indicate the clear difference between the envelope of Printex U and those of the Euro 0 and Euro V soot.

At the beginning of the measurement the NO_x reduction was almost similar for all samples. But the NO_x reduction increased with time in the repeated series for Printex U, while it decreased for the Euro 0 and Euro V soot sample. After three repetitions the NO_x reduction activity of Printex U decreased due to the loss of carbon by oxidation. The envelope of the NO_x reduction activity of the mixed soot sample showed a similar trend as the curve of Printex U, but less pronounced.

From these results it was concluded, that in the transient soot oxidation experiments equilibrium conditions could not be reached for Printex U, but in the isothermal experiments the equilibrium conditions were reached leading to higher C-oxidation by NO_2 and also a higher NO_x reduction activity. The real diesel soot samples showed higher reactivity during the transient experiments because the equilibrium was reached faster, but the lower C-oxidation rates in the isothermal experiments showed that the solid carbon/gas phase carbon (CO_2 , CO , HCN , HNCO) equilibrium was more on the side of the solid carbon than for Printex U. The mixed soot took a position between Printex U and the other diesel soot samples.

Beside the equilibrium effects, it can be speculated that the alkali metals in the ashes of the diesel soot samples (Table 15), might also contribute to the lower NO_x reduction in comparison to Printex U. These metals are strongly basic and

Ahmed et al. reported about their inhibiting influence on the NO_x reduction over activated carbons for NO_x removal [130]. However, this hypothesis was not investigated in more detail in the present work.

As already reported by other authors [130, 181] the BET surface area did not seem to influence the NO_x reduction since Printex U showed the highest activity, but had the lowest surface area.

6.3.7. SCR effect over diesel soot in the presence of H₂SO₄

The higher NO_x reduction activity of the mixed soot sample in comparison to the Euro V and Euro 0 soot sample was explained with equilibrium effects. However, the presence of H₂SO₄ (2.3wt% - Figure 28), which was found during the composition analysis of the mixed soot sample as SO₂, might also contribute to the higher activity. In the literature it was described, that the activity of carbon materials for NO_x reduction could be increased by impregnation with H₂SO₄ followed by calcination [127]. Again this enhancement was explained with the increase of the acidic surface groups due to the oxidative nature of H₂SO₄. In the mixed soot sample a similar mechanism is conceivable, as the H₂SO₄ might have oxidized the surface during heating to the reaction temperature.

However, a direct influence of H₂SO₄ on the NO_x reduction seemed to be also possible. In order to investigate this hypothesis isothermal NO_x reduction experiments were performed at 200°C and 250°C with Printex U-coated monoliths, which were impregnated with H₂SO₄. The NO₂, NO and NH₃ concentrations were varied according to Table 16. In Figure 78 the results of the NH₃ variation are shown. Independent of the NH₃ concentration and temperature the NO_x reduction was significantly increased in the presence of

H₂SO₄. This was also observed for the NO and NO₂ variation. The concentration of the measured byproducts was similar to the experiments without H₂SO₄. The results supported the hypothesis of a direct influence of H₂SO₄ on the NO_x reduction activity, which was most probably not due to the formation of more acidic surface functional groups as the discussion of the mechanistic details in section 6.4 will show.

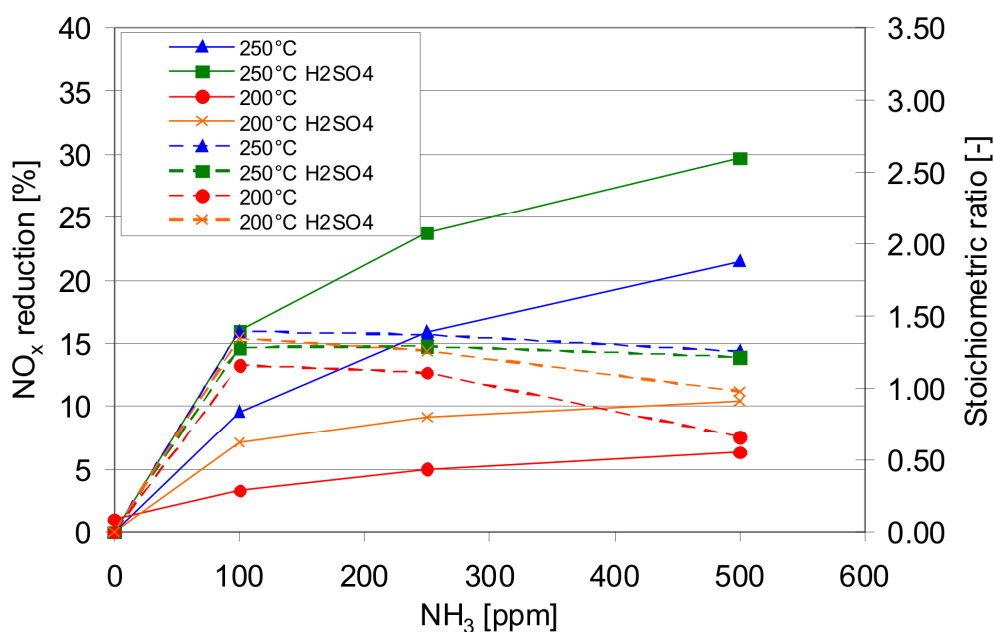


Figure 78: NO_x reduction and stoichiometric ratios over Printex U impregnated with 5 mg sulfuric acid at 200°C and 250°C in dependence of the NH₃ concentration. The results for Printex U without impregnation were added for comparison. Concentrations in the basic feed gas: 250 ppm NO₂ and variable NH₃ concentrations. Solid lines: NO_x reduction [%]; dashed lines: stoichiometric ratio. The curves obtained with H₂SO₄ are indicated with “H₂SO₄” in the legend.

6.3.8. Investigation of the SCR effect over diesel soot in the TG-FTIR system

Originally it was planned to perform the investigation of the SCR effect over soot in the TG-FTIR system described in chapter 3. The first experiments were performed in the TPR mode with Printex U; however, the reproducibility was rather poor. For improvement, the measurements were performed isothermally and the soot samples were coated on cordierite monoliths. Moreover, the investigations in the tubular quartz reactor described in the previous sections were started in parallel for comparison and classification of the TG-FTIR results. In the beginning, a comparison of the results obtained in the TG-FTIR system indicated higher NO_x reduction ability than the experiments in the tubular reactor. However, the space velocities of the base experiments in the tubular reactor were a factor of 10 higher than in the TG-FTIR system, which worked at a space velocity of 3200 h⁻¹. The reduction of the space velocity in the tubular reactor from 35,000 h⁻¹ to 3000 h⁻¹, however, showed a higher NO_x reduction activity of Printex U than measured in the TG-FTIR system, e.g. at 250°C the NO_x reduction was 66% in the presence of 250 ppm NH₃ and 250 ppm NO₂, while the NO_x reduction reached only 37% in the TG-FTIR system under the same conditions. The analysis of the NH₃ conversion in both setups showed, that it was 86% in the tubular reactor, but only 45% in the TG-FTIR system. Therefore, it was concluded, that the SCR reaction in the TG-FTIR system was NH₃ limited due to mass transport limitations, which resulted from the design-caused bypass of the gas flow. Subsequent test experiments with a vanadium-based classical SCR catalyst in the TG-FTIR system showed that the bypass was about 50% of the total flow. In addition to the mass transport limitations in the system, it was observed that the mass signal could hardly be analyzed and interpreted. This was due to the large number of different feed gas compounds,

which adsorbed and desorbed on the soot sample, and the parallel soot oxidation, which also contributed to the mass loss. Therefore it could not be distinguished between the reactions and effects, which were responsible for a mass increase or decrease.

Based on these results it was decided to stop the investigation of the SCR effect over diesel soot in the TG-FTIR system and continue the study exclusively in the tubular quartz reactor, because the space velocities were more realistic and the reactions were not limited by mass transport limitations.

6.3.9. DRIFTS measurements with Printex U

In order to investigate the functional groups, which are formed under SCR conditions on Printex U, several DRIFTS experiments were performed with wet and dry feed gases. For the experiments under wet conditions, the feed gas for the background collection always contained 10% O₂ + 5% H₂O in nitrogen, while it contained only 10% O₂ for the experiments under dry conditions. Then, 1000 ppm NO₂ were added to the feed gases. After 20 min a spectrum was collected in situ. The in situ collection had the disadvantage that also gas phase components contribute to the spectrum. However, this procedure allowed the investigation under reaction conditions similar to those in the tubular reactor. After the spectrum collection, 1000 ppm NH₃ were dosed to the gas flow containing 1000 ppm NO₂ + 10% O₂ + 5% H₂O for the experiments with wet feed gas. Again a spectrum was collected after 20 min. Then the system was purged for 20 min with 10% O₂ + 5% H₂O in nitrogen in order to collect a final spectrum containing only absorption bands of the chemisorbed species. With a second fresh soot sample also the NH₃-soot interaction in the absence of NO₂ was investigated with a similar procedure.

During the measurements the problem raised that the gas inlet tube was quickly clogged by deposits of ammonium nitrate (NH_4NO_3), since the cell could not be heated sufficiently, which led to fluctuating inlet flows. Insufficient heating was also the reason for the deposition of nitrates on the windows of the DRIFTS cell, which falsified the results since the deposited amount could not kept constant. Both processes strongly reduced the reproducibility of the measurements. However, the reproducibility was even further reduced due to carbon consumption by oxidation. Due to the poor reproducibility the analysis of the DRIFTS measurements was only performed qualitatively and the absorbance had to be given in arbitrary units.

In Figure 79 the DRIFTS spectra of the experiments with dry feed gas are shown. In the presence of 10% O_2 + 1000 ppm NO_2 (labeled as (a)) absorption bands occurred at 3840-3000 cm^{-1} , 2966-2856 cm^{-1} , 2420-2305 cm^{-1} , 1900-1700 cm^{-1} , a double peak with maxima at 1631 cm^{-1} and 1604 cm^{-1} in the region at 1700-1500 cm^{-1} and 1310-1100 cm^{-1} . The large absorption at 3840-3000 cm^{-1} was due to vibrations of the O-H bond of acidic surface functional groups [124, 125] and traces of H_2O in the system. The peaks at 2966-2856 cm^{-1} , the maxima at 1631 cm^{-1} and at 1602 cm^{-1} were due to absorptions of gaseous NO_2 as a comparison with a NO_2 gas phase spectrum collected with the Nexus 600 FTIR spectrometer showed. Since a part of the soot was oxidized to CO_2 in the presence of O_2 and NO_2 absorption bands of gaseous CO_2 occurred at 2420-2305 cm^{-1} , which was also confirmed with a gas phase spectrum of CO_2 . In the region at 1900-1700 cm^{-1} absorption bands of C=O vibrations of carboxylic acids, esters and carboxylic anhydrides were observed. The absorptions in the regions of 1310-1100 cm^{-1} were due to C-O vibrations of acidic functional groups [71], C-O vibrations in surface nitrites [61, 62, 183] and C- NO_2 vibrations [61, 62, 183].

In the presence of 10% O₂ + 1000 ppm NH₃ (b) a strong band occurred around 3334 cm⁻¹, which can be allocated to N-H vibrations of NH₃ adsorbed via hydrogen atoms [124]. Gaseous NH₃ might also contribute to the absorption bands in this region. However, the observed absorption is too large to result only from gaseous NH₃, as a comparison of the relative peak height of the peak at 1627 cm⁻¹, which was surely due to gas phase NH₃, and a real gas phase spectrum of NH₃ showed. In the region at 2420-2305 cm⁻¹ negative absorption bands of CO₂ were observed, which were due to a background shift of CO₂. The negative absorption in the region of 1540-1400 cm⁻¹ might be due to a background shift of C=C and C-H absorptions. The peak at 1355 cm⁻¹ was most probably due to symmetric vibrations of COO⁻ according to Zawadzki et al., who observed a band at 1366 cm⁻¹ in their adsorption experiments with NH₃ on soot.

When 10% O₂ + 1000 ppm NO₂ + 1000 ppm NH₃ (c) were dosed in parallel, most of the absorption bands observed in the presence of only NO₂ or NH₃ in the previous experiments were confirmed. However, the shape of the region between 3840-3000 cm⁻¹ changed, as the bands of the N-H and O-H vibrations overlapped.

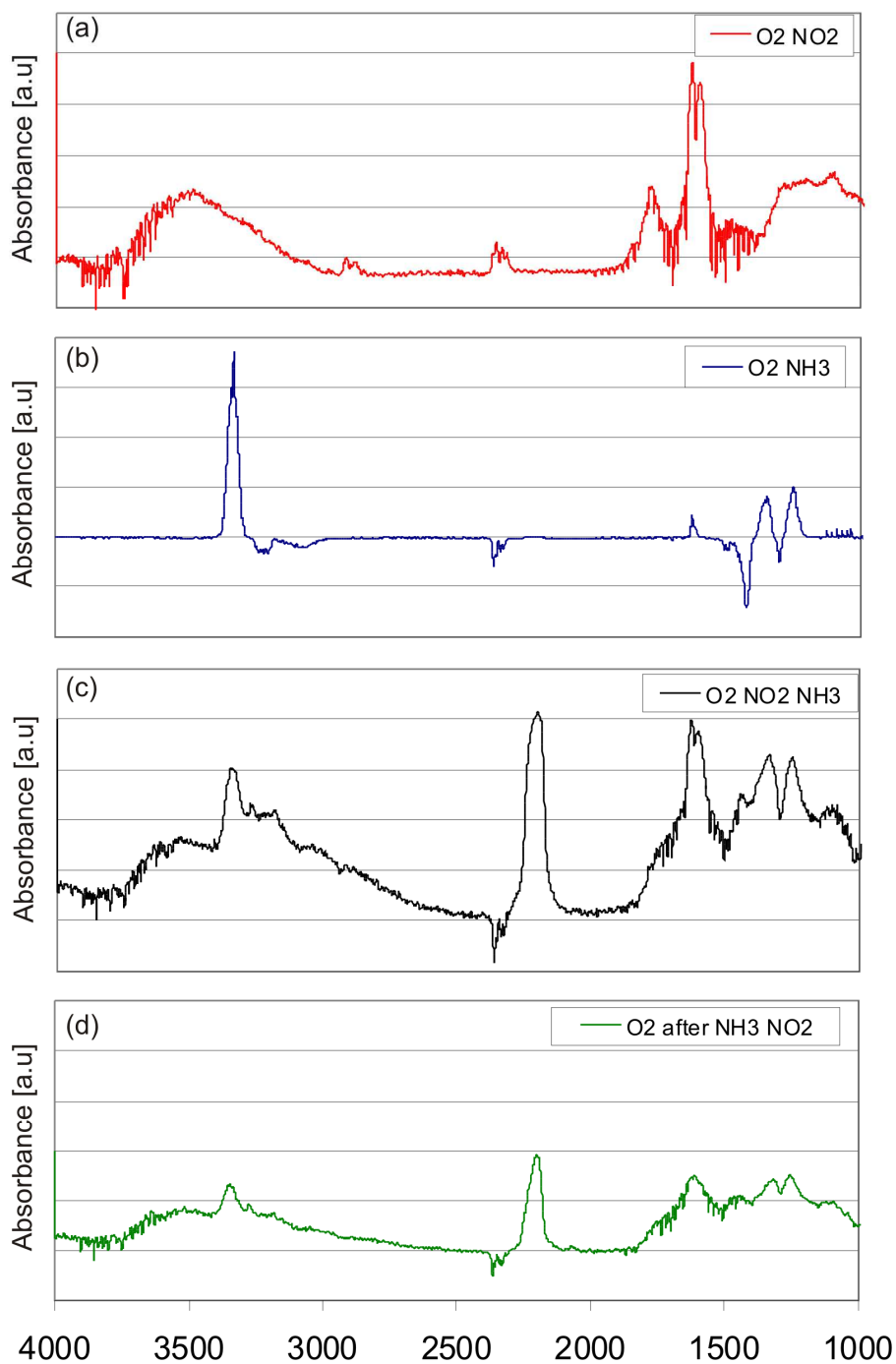


Figure 79: DRIFTS spectra of Printex U treated with different dry feed gases compositions. (a) O₂ + NO₂, (b) O₂ + NH₃, (c) O₂ + NH₃ + NO₂, (d) O₂ after NH₃ + NO₂.

At 3353 cm⁻¹ a larger peak was observed. Long and Yang, who performed DRIFTS measurements of NH₃ adsorbed on Fe-ZSM-5, attributed this peak to

adsorbed NH_4^+ [184]. Since no other interpretation of this peak was found in literature, it was assumed that the peak had the same origin in the experiments on soot. The peak with a maximum at 2208 cm^{-1} was allocated to isocyanate species [124, 185], which are formed from the reaction with NH_3 and carboxylic derivatives. As this peak was not found in the experiment with $\text{O}_2 + \text{NH}_3$ (b), its appearance was taken as confirmation for the results of Muckenhuber et al., who reported that NO_2 forms more acidic surface functional groups in comparison to O_2 [59]. Gaseous N_2O , which is also infrared-active in this region, might contribute to this peak, however, the peak shape of gaseous N_2O is different. This, and the fact that after purging the absorption band was still obtained, were taken as confirmation of the presence of isocyanate species. Apart from this, the spectrum collected after purging (d) showed mostly all absorption bands, which were also obtained in the *situ* spectrum, except those of gaseous NO_2 . However, the intensities of the absorption bands were reduced in comparison to the *in situ* spectrum. The absence of NO_2 in the feed gas showed that the absorption band of gaseous NO_2 overlapped with absorption bands at $1700\text{-}1500\text{ cm}^{-1}$ having a maximum at 1631 cm^{-1} , which were most probably due to C- NO_2 , C=O and N=O [62] vibrations as well as vibrations of C=N [186].

In Figure 80 the spectra of the experiments with wet feed gas are shown. In the presence of $10\% \text{ O}_2 + 5\% \text{ H}_2\text{O} + 1000\text{ ppm NO}_2$ (e) the same absorption bands were measured as observed with dry feed gas. However, an additional absorption band occurred with a maximum at 1342 cm^{-1} , which was due to vibrations of NO_2 in nitro groups on the surface [62]. With dry feed gas this peak most probably did not occur since in the absence of water less NO_2^+ is

formed, which is the active species in the nitration of aromatic structures as shown in Figure 52.

In the spectrum of the soot sample treated with 10% O₂ + 5% H₂O + 1000 ppm NH₃ (f) the absorption bands observed with dry feed gas were missing. This was most probably due to the fact that large amounts condensed on the system walls in the presence of H₂O or that NH₃ had to compete for adsorption sites with H₂O. Only a band at 3900-3260 cm⁻¹ was observed, but this was most likely due to O-H vibrations on the surface. The absorption band at 2420-2305 cm⁻¹ was due to a background shift of CO₂ and in the region at 1950-1300 cm⁻¹ the bands were due to a H₂O background shift.

When 10% O₂ + 5% H₂O + 1000 ppm NO₂ + 1000 ppm NH₃ (g) were dosed in parallel, again N-H and O-H vibrations were observed above 3000 cm⁻¹ similar to the experiments with dry feed gas. Under these conditions also the absorption band of isocyanates could be confirmed again, however, its maximum was shifted to 2221 cm⁻¹. The peaks below 1800 cm⁻¹ were already observed in the presence of 10% O₂ + 1000 ppm NO₂ + 5% H₂O (e). After purging the system again (h) the overlapping of the absorption bands of gaseous NO₂ with absorptions bands in the region at 1700-1500 cm⁻¹, due to C-NO₂, C=O and N=O vibrations [62] as well as C=N vibrations [186] became visible.

In general, the measurements showed that for more detailed investigations of adsorbed species and surface processes, the used DRIFTS cell should be exchanged by a cell, which is optimized for investigations with condensable gas mixtures. However, the obtained results presented a useful qualitative overview of the formed surface functional groups.

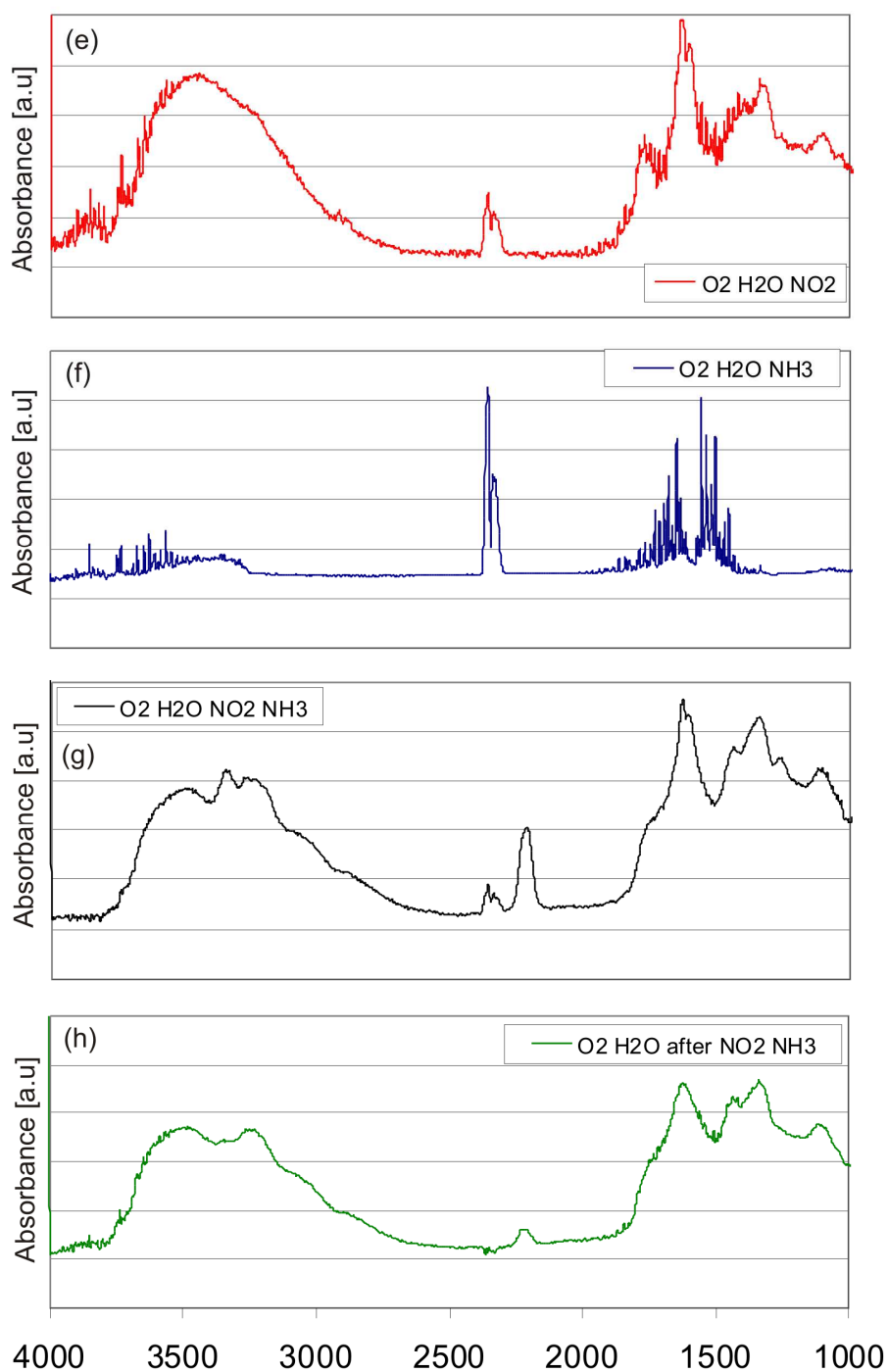


Figure 80: DRIFTS spectra of Printex U with treated with different wet feed gas compositions. (e) O₂ + H₂O + NO₂, (f) O₂ + H₂O + NH₃, (g) O₂ + H₂O + NH₃ + NO₂, (h) O₂ + H₂O after NH₃ + NO₂.

6.4. Mechanism

On the basis of two general observations and the assumption that the SCR reaction steps on soot are similar to the SCR process on inorganic catalysts a mechanism for the NO_x removal on diesel soot in the presence of NO_2 , NO and NH_3 was developed:

Firstly, hardly any coupling of the C-oxidation rates and the SCR reaction was observed. Therefore, it was concluded that the NO_x involved in the SCR reaction on soot did not form strong bonds with the soot (e.g. surface nitrates and nitrites) and had a more physisorbed nature. This conclusion was kept, although the DRIFTS measurements showed that surface functional groups with C-N and C-O bonds were formed [41, 53, 60, 61], since these groups most probably were only involved in the soot oxidation.

The adsorption of NH_3 on the other hand is most probably supported by the presence of acidic surface functional groups due to acid-base-interaction (eq. (1.44)) [117-120, 129, 131], which was confirmed by the DRIFTS measurements as absorption bands of adsorbed NH_3 were only obtained in the presence of NO_2 . The so-formed ammonium ions (NH_4^+) as counter parts of the acidic surface functional groups does not seem to influence the decarboxylation of these groups during the soot oxidation.

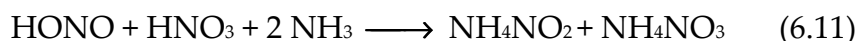
Secondly, stoichiometries were measured, which imply the NO_2 SCR (eq. 6.3)) reaction in the absence of NO and in the presence of NO the *fast* SCR reaction (eq. 6.2)). The *standard* SCR reaction (eq. 6.1)) was excluded due to the SCR inactivity of soot in the absence of NO_2 .

Following these observations, the first step of the SCR process after the adsorption of the reactants should be the heterogeneous disproportionation of two NO_2 molecules to HONO and HNO_3 (eq. 6.9). This step is not only

discussed for the NO_2 SCR and *fast SCR* reaction on inorganic catalysts in the presence of H_2O [86], but was also observed on other surfaces (e.g. soot and SiO_2 particles) at RT during investigations concerning atmospheric chemistry [167, 168, 187] and was confirmed by the evolution of HONO and HNO_3 during the measurements in this study:



HONO and HNO_3 are assumed to remain physisorbed on the surface, where they form ammonium nitrate (NH_4NO_3) and ammonium nitrite (NH_4NO_2) in the presence of NH_3 [86]:



At this point, it has to be mentioned, that NH_4NO_2 and NH_4NO_3 in eq. (6.11) should be considered as isolated molecules or ionic species at the soot surface and not as bulk material. It is important to note that the occurring chemistry is described formally and therefore, also an ionic formulation is thinkable.

After the formation of the nitrite, it decomposes immediately in nitrogen and water forming the first nitrogen molecule [172], because NH_4NO_2 is unstable above 60-70°C:



The remaining NH_4NO_3 decomposes again into HNO_3 and NH_3 [95]:

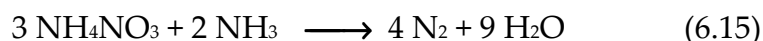


In the *fast SCR* mechanism, which occurred in the presence of NO as confirmed by the stoichiometric ratios (Figure 60), the HNO₃ is reduced by NO in a subsequent step [94]:



The formed HONO reacts again with NH₃ to NH₄NO₂ according to reaction (6.11) and then decomposes to nitrogen and water (eq. (6.12)). Summarizing reaction (6.10) and (6.11)-(6.14) leads to the overall equation for the *fast SCR* reaction (6.2).

During the measurements in the absence of NO in the feed gas the stoichiometry of the NO₂ SCR mechanism was observed (Figure 59 and Figure 62). In this mechanism, the reactions are similar to the *fast SCR* mechanism up to reaction (6.13), but reaction (6.14) does not occur since NO is missing as reducing agent. According to the observed stoichiometric ratio, NH₃ takes the part of the reducing agent for NH₄NO₃ in case of the NO₂ SCR reaction [95]:



Combination of eq. (6.10), (6.11)-(6.13) and (6.15) leads to the known overall NO₂ SCR reaction (6.3).

The consumption of HNO₃ according to the reactions (6.14) and (6.15) during the SCR process on soot was supported by the comparison of the diesel soot samples and Printex U: The diesel soot samples showing lower NO_x reduction evolved higher amounts of HNO₃, because they were not consumed in the

further SCR process. Therefore, a mechanism without inclusion of NH_4NO_3 as proposed by Richter et al. and Jüntgen et al. [103, 115] (see section 1.3.2) can be most probably excluded for the soot samples used in the present study. Furthermore, this observed HNO_3 emissions led to the conclusion, that the disproportionation step does not limit the SCR reaction and that most probably the presence of adsorption sites for NH_3 is the limiting factor.

For the sake of completeness the byproducts, which occurred during the SCR investigations beside HONO and HNO_3 have to be mentioned, although, they were already discussed in section 6.3.4. N_2O was formed according to reaction (6.16) from the decomposition of NH_4NO_3 at temperatures above 200°C [95], which is a part of reaction (6.8):



Another pathway for the formation of N_2O is the oxidation of NH_3 with NO_2 according to reaction (6.9) [86]. Although, HCN and HNCO were formed from the reaction of carboxylic functional groups with NH_3 , which was indicated by the DRIFTS investigations, both species did not contribute to the NO_x reduction.

Before the reactions of the *fast* and NO_2 SCR processes over diesel soot will be summarized in Figure 81 to close this chapter, the influence of H_2SO_4 on the SCR reaction over diesel soot has to be discussed shortly. The results of the H_2SO_4 impregnated monoliths presented in section 6.3.7 showed clearly the enhancement of the NO_x reduction in the presence of H_2SO_4 , which might also explain a part of the higher reactivity of the mixed soot sample in comparison to the other diesel soot samples. The mechanism of this enhancement is most probably similar to the mechanism of the enhanced HNO_3 formation observed

during the investigations of the H_2SO_4 influence on the soot oxidation (chapter 5). There it was shown, that H_2SO_4 most probably accelerates the disproportionation of N_2O_4 (Figure 52). Since this is also the initial reaction step of the SCR process (reaction (6.10)) it was concluded that the impact of H_2SO_4 on this reaction step is the same under SCR condition. An increase of the HNO_3 concentration was not observed under SCR conditions, since it was directly consumed leading to an increased NO_x reduction.

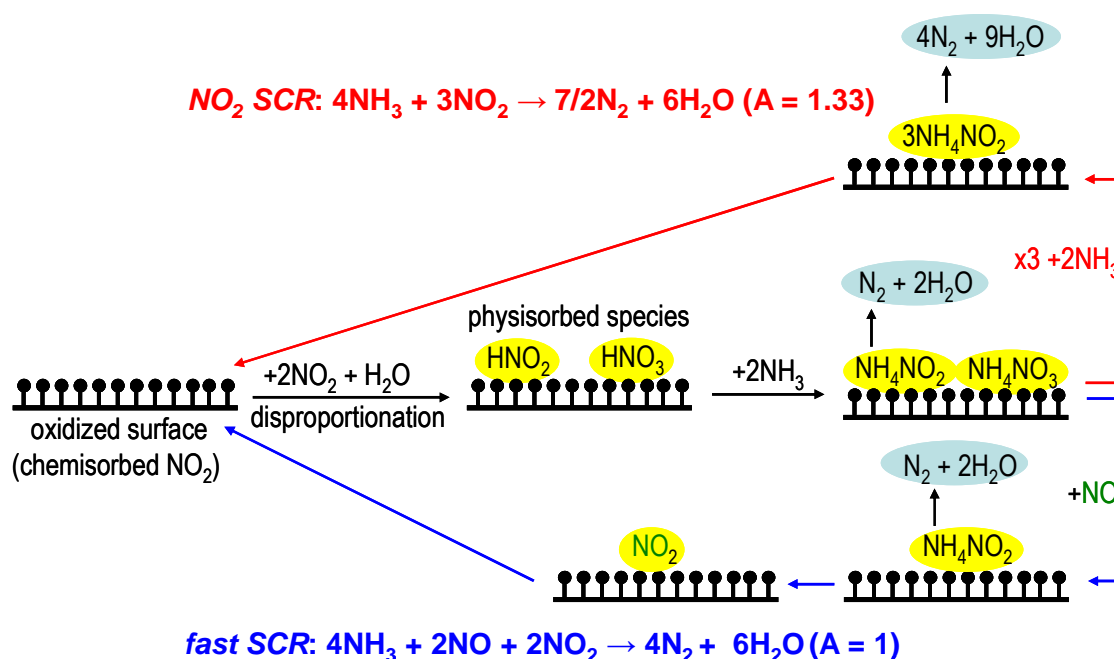


Figure 81: Suggested mechanism for the selective catalytic reduction of NO_x on diesel soot.

6.5. Conclusions

The investigations of the NO_x reduction by SCR with NH_3 showed that model and diesel soot samples were able to remove NO_x in model exhaust gases up to 25% at $35,000 \text{ h}^{-1}$. A reduction of the space velocities led to an increase of the

NO_x reduction up to a factor of 3. The disproportionation of NO₂ is the initial step of the SCR process on soot. Therefore, the presence of NO₂ in the feed gas was a prerequisite, since the oxidation of NO was kinetically inhibited due to the high space velocities.

However, if both, NO and NO₂, were present in the feed gas, the NO_x reduction was higher than in the absence of NO, since the *fast SCR* reaction could proceed. Without NO in the feed gas the *NO₂ SCR* reaction pathway was followed. The presence of alkali metals or their oxides might inhibit the NO_x reduction.

The parallel processes soot oxidation and SCR of NO_x influenced each other only very little. Therefore, it was concluded, that the NO_x do not have to form strong bonds like nitrates and nitrites on the soot surface for the occurrence of the SCR process and have a more physisorbed nature. NH₃ adsorbs most probably on the surface by acid-base interaction with acidic surface functional groups. Reaction products of NH₃ and carboxyl derivatives, responsible for the emission of HCN and HNCO, most probably do not take part in the SCR process.

The NO_x reduction of activated carbons showed that at space velocities around 2000 h⁻¹ up to 80% of NO can be removed from the exhaust gases of industrial processes. Although the study in the present work showed that with a space velocity of 35,000 h⁻¹ only up to 20% of NO_x can be removed over diesel soot in laboratory experiments, the found SCR effect on diesel soot can be exploited to improve future diesel exhaust aftertreatment systems.

In these systems both a DPF and a SCR device, will be anyway necessary in series to reach the emission limits. Therefore, it would be an advantage to place the devices in one housing in order to reduce the system size and weight. NO₂ is also present from NO oxidation in the DOC upstream of the combined DPF-SCR device, since it is needed for the continuous regeneration of the DPF. And

as the filter regeneration is not influenced by the SCR conditions, it would be reasonable for a further reduction of the SCR catalyst to dose urea upstream of the DPF and reduce NO_x already partially over soot.

Acknowledgement

At this point I would like to acknowledge F. Krumeich (ETHZ) for the taking TEM pictures and S. Köchli (PSI) for the ICP-OES measurements.

7. Summary and Outlook

This work consisted of four parts: First, the development and setup of the TG-FTIR instrument for investigations with condensable and corrosive feed gases. Second, the investigation of the composition and reactivity of diesel soot in the TG-FTIR system. Third, the investigation of the influence of the H_2SO_4 on the soot oxidation with NO_2 in a tubular quartz reactor. And fourth, the investigation of the selective catalytic reduction of NO_x with NH_3 over soot.

The results of the composition and reactivity analysis of diesel soot in the TG-FTIR system showed that the instrument is suitable for these kinds of investigations delivering important information already with small sample amounts ($\approx 300 \mu\text{g}$). Although, a large number of soot samples was already investigated during this work, it would be interesting to test the instrument for routine soot analysis with samples generated under defined engine load conditions. This would allow examining the relations between soot composition and reactivity on one side and the load conditions as well as parameters like different diesel fuels and lubrication oils on the other.

Although, the TG-FTIR system reached its limit during the investigation of the NO_x reduction with NH_3 over diesel soot, the possibility to work with condensable and corrosive gases seems to be very helpful for investigations of other materials. Measurements with an inorganic SCR catalyst and a catalyst for the hydrothermal gasification of biomass of other PSI projects gave already promising results.

In this work it was shown, that oxidation with NO_2 can be significantly enhanced with traces of H_2SO_4 dosed to the feed gas. In a future work, it should be investigated how this effect influences the regeneration of real DPF systems. And moreover, the question should be answered if small amounts of SO_2 and

H₂SO₄, which are always present in the exhaust gas of diesel engines, can be used directed to improve the DPF regeneration (e.g. storage materials).

Furthermore, it could be shown that beside the different soot oxidation reactions also the reduction of NO_x occurs in parallel on diesel soot, when NH₃ is added to a model diesel exhaust gas. This NO_x reduction activity of model and diesel soot was analyzed in detail during this work. The results showed, that the activity differs significantly between the investigated samples, which was most probably due to structural differences. However, the responsible structure-reactivity relations could not be discovered conclusively. Therefore, it would be interesting to investigate the NO_x reduction activity of diesel soot samples generated and collected under defined conditions. The results of these experiments would also facilitate the application of NO_x reduction activity of diesel soot in combined SCR-DPF systems. For the further investigations detailed DRIFTS investigations seem to be suitable beside the measurements in the tubular reactor. However, the DRIFTS cell has to be adapted to avoid condensation of the dosed feed gases.

8. Bibliography

- [1] J. Bünger, J. Krahl, K. Baum, O. Schröder, M. Müller, G. Westphal, P. Ruhнау, T. G. Schulz and E. Hallier, *Arch Toxicol* 74, **2000**, 490-498.
- [2] I. M. Kennedy, *Proc. Combust. Inst.* 31, **2007**, 2757-2770.
- [3] J. Lewtas, *Mutat Res-Rev Mutat* 636, **2007**, 95-133.
- [4] D. L. Mauzerall, B. Sultan, N. Kim and D. F. Bradford, *Atmos. Environ.* 39, **2005**, 2851-2866.
- [5] Amtsblatt der Europäischen Union, EU regulation No. 715/2007.
- [6] R. van Basshuysen and F. Schäfer (eds.), *Handbuch Verbrennungsmotoren*, 2. edition, Vieweg and Teubner, Braunschweig, Wiesbaden, **2002**.
- [7] H. Tschoeke, A. Graf, J. Stein, M. Krüger, J. Schaller, N. Breuer, K. Engeljehring and W. Schindler, *Diesel engine exhaust emissions*, in *Handbook of diesel engines*, K. Mollenhauer and H. Tschoeke (eds.), Springer, Berlin, Heidelberg, **2010**, p. 417-485.
- [8] H. Schulz, G. Bandeira De Melo and F. Ousmanov, *Combust. Flame* 118, **1999**, 179-190.
- [9] H. Richter and J. B. Howard, *Prog. Energ. Combust.* 26, **2000**, 565-608.
- [10] S. Pischinger, *Filterregeneration durch reaktiven Russ*, FVV-Forschungsantrag, internal report, **2008**.
- [11] M. S. Skjøth-Rasmussen, P. Glarborg, M. Østberg, J. T. Johannessen, H. Livbjerg, A. D. Jensen and T. S. Christensen, *Combust. Flame* 136, **2004**, 91-128.
- [12] B. S. Haynes and H. G. Wagner, *Prog. Energ. Combust.* 7, **1981**, 229-273.
- [13] H. Muckenhuber, *Dieselmotoren und seine Modelle - spektroskopische Untersuchungen zur Reaktion mit NO₂*, dissertation, Technical University Wien, **2005**.

- [14] J. O. Müller, *Investigations on Environmental Carbons*, dissertation, Technical University Berlin, **2005**.
- [15] M. E. Schuster, M. Hävecker, R. Arrigo, R. Blume, M. Knauer, N. P. Ivleva, D. S. Su, R. Niessner and R. Schlögl, *J. Phys. Chem. A* **115**, **2011**, 2568-2580.
- [16] D. S. Su, et al., *Catal. Today* **90**, **2004**, 127-132.
- [17] B. Bougie, L. C. Ganippa, A. P. Van Vliet, W. L. Meerts, N. J. Dam and J. J. Ter Meulen, *Proc. Combust. Inst.* **31**, **2007**, 685-691.
- [18] M. Lapuerta, F. J. Martos and J. M. Herreros, *J. Aerosol Sci.* **38**, **2007**, 455-466.
- [19] A. K. K. Virtanen, J. M. Ristimäki, K. M. Vaaraslahti and J. Keskinen, *Environ. Sci. Technol.* **38**, **2004**, 2551-2556.
- [20] M. Lapuerta, O. Armas, J. J. Hernández and A. Tsolakis, *Fuel* **89**, **2010**, 3106-3113.
- [21] J. O. Müller, D. S. Su, R. E. Jentoft, J. Kröhnert, F. C. Jentoft and R. Schlögl, *Catal. Today* **102-103**, **2005**, 259-265.
- [22] B. R. Stanmore, J. F. Brilhac and P. Gilot, *Carbon* **39**, **2001**, 2247-2268.
- [23] S. H. Cadle, P. Mulawa, P. Groblicki, C. Laroo, R. A. Ragazzi, K. Nelson, G. Gallagher and B. Zielinska, *Environ. Sci. Technol.* **35**, **2000**, 26-32.
- [24] A. D. H. Clague, J. B. Donnet, T. K. Wang and J. C. M. Peng, *Carbon* **37**, **1999**, 1553-1565.
- [25] R. Barbella, A. Ciajolo, A. D'anna and C. Bertoli, *Combust. Flame* **77**, **1989**, 267-277.
- [26] A. Obuchi, A. Ohi, H. Aoyama and H. Ohuchi, *Combust. Flame* **70**, **1987**, 215-224.
- [27] R. J. Farrauto and K. E. Voss, *Appl. Catal. B-Environ* **10**, **1996**, 29-51.

- [28] M. Zinbo, L. M. Skewes, C. E. Hunter and D. Schuetzle, *Thermochim. Acta* **166**, **1990**, 267-275.
- [29] M. Mehring, O. Kröcher and M. Elsener, *Dieseldruck II - Differenzierte Mikroanalytik von Particulate Matter (PM)*, final report of FVV project No. 1006, Frankfurt/Main, **2010**.
- [30] M. V. Twigg, *Appl. Catal. B-Environ.* **70**, **2007**, 2-15.
- [31] E. Jacob, R. Müller, A. Scheeder and P. Treiber, *Baumaschine.de* **2008**,
- [32] B. Van Eickels, H. P. Dummann, L. Pace and A. Reck, *SAE 2007-32-0054*, **2007**.
- [33] J. P. A. Neeft, M. Makkee and J. A. Moulijn, *Fuel Process. Technol.* **47**, **1996**, 1-69.
- [34] A. R. Chughtai, S. A. Gordon and D. M. Smith, *Carbon* **32**, **1994**, 405-416.
- [35] P. Ehrburger, J. F. Brillhac, Y. Drouillot, V. Logie and P. Gilot, *SAE 2002-01-1683*, **2002**.
- [36] F. Jacquot, V. Logie, J. F. Brillhac and P. Gilot, *Carbon* **40**, **2002**, 335-343.
- [37] M. Jeguirim, V. Tschamber, J. F. Brillhac and P. Ehrburger, *Fuel* **84**, **2005**, 1949-1956.
- [38] B. A. Lur'e and A. V. Mikhno, *Kinet. Catal.* **38**, **1995**, 535-540.
- [39] A. Messerer, R. Niessner and U. Poschl, *Carbon* **44**, **2006**, 307-324.
- [40] A. Setiabudi, M. Makkee and J. A. Moulijn, *Appl. Catal. B-Environ.* **50**, **2004**, 185-194.
- [41] N. Shirahama, S. H. Moon, K. H. Choi, T. Enjoji, S. Kawano, Y. Korai, M. Tanoura and I. Mochida, *Carbon* **40**, **2002**, 2605-2611.
- [42] D. Stadler and M. J. Rossi, *Phys. Chem. Chem. Phys.* **2**, **2000**, 5420-5429.
- [43] B. R. Stanmore, V. Tschamber and J. F. Brillhac, *Fuel* **87**, **2008**, 131-146.
- [44] P. Ciambelli, V. Palma, P. Russo and S. Vaccaro, *Catal. Today* **60**, **2000**, 43-49.

- [45] G. Saracco, C. Badini, N. Russo and V. Specchia, *Appl. Catal. B-Environ.* **21**, **1999**, 233-242.
- [46] H. Marsh and K. Kuo, *Kinetics and catalysis of carbon gasification in Introduction to carbon science*, H. Marsh (ed.), Butterworths, London, **1989**, p. 107.
- [47] S. G. Chen, R. T. Yang, F. Kapteijn and J. A. Moulijn, *Ind. Eng. Chem. Res.* **32**, **1993**, 2835-2840.
- [48] A. N. Hayhurst and M. S. Parmar, *Chem. Eng. Sci.* **53**, **1998**, 427-438.
- [49] J. A. Moulijn and F. Kapteijn, *Carbon* **33**, **1995**, 1155-1165.
- [50] K. Otsuka, R. Takahashi, K. Amakawa and I. Yamanaka, *Catal. Today* **45**, **1998**, 23-28.
- [51] R. Brückner, *Reaktionsmechanismen*, 2. edition, Springer, Heidelberg, Berlin, **2003**.
- [52] M. Jeguirim, V. Tschamber, J. F. Brilhac and P. Ehrburger, *J. Anal. Appl. Pyrol.* **72**, **2004**, 171-181.
- [53] B. Azambre, S. Collura, J. M. Trichard and J. V. Weber, *Appl. Surf. Sci.* **253**, **2006**, 2296-2303.
- [54] W. J. Pitz and C. K. Westbrook, *Proc. Combust. Inst.* **31**, **2007**, 2343-2351.
- [55] Y. Z. He, J. P. Cui, W. G. Mallard and W. Tsang, *J. Am. Chem. Soc.* **110**, **1988**, 3754-3759.
- [56] E. V. Nikolaeva, A. G. Shamov, D. V. Chackov, D. A. Gordeev and G. M. Khraphovsky, *Butlerov Communications* **3**, **2001**, 15-23.
- [57] C. Poon and P. M. Mayer, *Int. J. Mass Spectrom.* **255-256**, **2006**, 93-101.
- [58] W. Tsang, D. Robaugh and W. G. Mallard, *J. Phys. Chem.* **90**, **1986**, 5968-5973.
- [59] H. Muckenhuber and H. Grothe, *Carbon* **44**, **2006**, 546-559.

- [60] X. Gao, S. Liu, Y. Zhang, Z. Luo, M. Ni and K. Cen, *Fuel Process. Technol.* **92**, **2011**, 139-146.
- [61] U. Kirchner, V. Scheer and R. Vogt, *J. Phys. Chem. A* **104**, **2000**, 8908-8915.
- [62] H. Muckenhuber and H. Grothe, *Carbon* **45**, **2007**, 321-329.
- [63] M. Matti Maricq, *J. Aerosol Sci.* **38**, **2007**, 1079-1118.
- [64] S. Collura, N. Chaoui, B. Azambre, G. Finqueneisel, O. Heintz, A. Krzton, A. Koch and J. V. Weber, *Carbon* **43**, **2005**, 605-613.
- [65] K. J. Rockne, G. L. Taghon and D. S. Kosson, *Chemosphere* **41**, **2000**, 1125-1135.
- [66] M. Knauer, M. Carrara, D. Rothe, R. Niessner and N. P. Ivleva, *Aerosol Sci. Tech.* **43**, **2008**, 1-8.
- [67] M. Knauer, M. E. Schuster, D. Su, R. Schlögl, R. Niessner and N. P. Ivleva, *J. Phys. Chem. A* **113**, **2009**, 13871-13880.
- [68] A. Braun, A. Kubatova, S. Wirick and S. B. Mun, *J. Electron Spectrosc.* **170**, **2007**, 42-48.
- [69] A. Braun, F. E. Huggins, N. Shah, Y. Chen, S. Wirick, S. B. Mun, C. Jacobsen and G. P. Huffman, *Carbon* **43**, **2005**, 117-124.
- [70] P. Burg, P. Fydrych, D. Cagniant, G. Nanse, J. Bimer and A. Jankowska, *Carbon* **40**, **2002**, 1521-1531.
- [71] A. Dandekar, R. T. K. Baker and M. A. Vannice, *Carbon* **36**, **1998**, 1821-1831.
- [72] G. W. Israel, K. Mollenhauer, E. K. Ulrich, R. Bollmann-Weiss, G. Lilge and D. Moser, *MTZ* **56**, **1995**, 568-577.
- [73] *Verfahren zur Bestimmung von organischen Stoffen im Feinstaub, anwendbar für partikelförmige Dieselmotoremissionen*, BGI 505-44, Carl Heymanns Verlag KG, Köln, June **1995**.

- [74] *Messen von Ruß (Immission): Chemisch-analytische Bestimmung des elementaren Kohlenstoffs nach Extraktion und Thermodesorption des organischen Kohlenstoffs*, VDI/DIN Handbuch Reinhaltung der Luft, Band 4, VDI Richtlinie 2465 Blatt 1, Beuth- Verlag, Berlin Dezember **1996**.
- [75] *Messen von Ruß (Immission) : Thermographische Bestimmung des elementaren Kohlenstoffes nach Thermodesorption des organischen Kohlenstoffes*, VDI/DIN Handbuch Reinhaltung der Luft, Band 4, VDI Richtlinie 2465 Blatt 2, Beuth- Verlag, Berlin, Mai **1999**.
- [76] *Manual of Analytical Methods, 4th Edition, Diesel Particulate (as Elemental Carbon)*, 4th Edition NIOSH Manual of Analytical Methods Issue 3, National Institute for Occupational Safety and Health, Cincinnati, Ohio, march **2003**.
- [77] H.H. Fricke, Untersuchung von Filterproben von Motorenprüfständen, final report of FVV-project No. 926, Frankfurt/Main, **2008**.
- [78] M. Lapuerta, R. Ballesteros and J. Rodríguez-Fernández, *Meas. Sci. and Technol.* **18**, **2007**, 650-658.
- [79] G. A. Stratakis and A. M. Stamatelos, *Combust. Flame* **132**, **2003**, 157-169.
- [80] J. A. Macphee, L. Giroux, J. P. Charland, J. F. Gransden and J. T. Price, *Fuel* **83**, **2004**, 1855-1860.
- [81] K. Tikhomirov, O. Krocher, M. Elsener and A. Wokaun, *Appl. Catal. B- Environ.* **64**, **2006**, 72-78.
- [82] H. Muckenhuber and H. Grothe, *Top. Catal.* **30-31**, **2004**, 287-291.
- [83] J. Ofner and H. Grothe, *Asian Chem. Lett.* **11**, **2007**.
- [84] G. Busca, M. A. Larrubia, L. Arrighi and G. Ramis, *Catal. Today* **107-108**, **2005**, 139-148.
- [85] G. Busca, L. Lietti, G. Ramis and F. Berti, *Appl. Catal. B-Environ.* **18**, **1998**, 1-36.

- [86] M. Devadas, O. Krocher, M. Elsener, A. Wokaun, N. Soger, M. Pfeifer, Y. Demel and L. Mussmann, *Appl. Catal. B-Environ.* **67**, **2006**, 187-196.
- [87] O. Kröcher, *Stud. Surf. Sci. Catal.* **171**, **2007**, 261-289
- [88] M. Koebel, M. Elsener and G. Madia, SAE 2001-01-3625, **2001**.
- [89] O. Kroeher, M. Devadas, M. Elsener, A. Wokaun, N. Soger, M. Pfeifer, Y. Demel and L. Mussmann, *Appl. Catal. B-Environ.* **66**, **2006**, 208-216.
- [90] M. Koebel, G. Madia and M. Elsener, *Catal.Today* **73**, **2002**, 239-247.
- [91] M. Koebel, G. Madia, F. Raimondi and A. Wokaun, *J. Catal.* **209**, **2002**, 159-165.
- [92] G. Ramis, G. Busca, F. Bregani and P. Forzatti, *Appl. Catal.* **64**, **1990**, 259-278.
- [93] M. Kantcheva, V. Bushev and D. Klissurski, *J. Catal.* **145**, **1994**, 96-106.
- [94] I. Nova, C. Ciardelli, E. Tronconi, D. Chatterjee and B. Bandl-Konrad, *Catal. Today* **114**, **2006**, 3-12.
- [95] A. Grossale, I. Nova and E. Tronconi, *Catal. Lett.* **130**, **2009**, 525-531.
- [96] G. Madia, M. Koebel, M. Elsener and A. Wokaun, *Ind. Eng. Chem. Res.* **41**, **2002**, 3512-3517.
- [97] H. Andersen, W. Green and D. Steele, *Ind. Eng. Chem.* **53**, **1961**, 199-204.
- [98] H. Andersen and C. Keith, *Method of Purifying Gases Containing Oxygen and Oxides fo Nitrogen*, US Patent Office, *US 3008796*, **1958**.
- [99] R. M. Heck, *Catal. Today* **53**, **1999**, 519-523.
- [100] H. Jüntgen, E. Richter and H. Kuhl, *Fuel* **67**, **1988**, 775-780.
- [101] S. Gruhl, W. Pusch, S. Humburger and G.-G. Börger, *Katalysatoren, Verfahren zu seiner Herstellung und dessen Verwendung*, Espacenet, *DE 3727642*, **1989**.

- [102] H.-H. Heins, P. Danz, M. Ullrich, H. Henkel, K. Holzer, E. Zirngiebel and S. Gruhl, *Catalyst for the reduction of nitrogen oxides from waste gases and process for the preparation thereof*, Freepatentsonline, EP 0480255, **1993**.
- [103] H. Jüntgen, Erd. Koh. Erd. Petr. V. 39, **1986**, 546-551.
- [104] H. Jüntgen, J. Degel and K. Knoblauch, *Verwendung eines Formkokeses für die gleichzeitige Entfernung von Schwefeloxiden und Stickoxiden aus Abgasen*, Espacenet, DE 3036531, **1982**.
- [105] H. Jüntgen, K. Knoblauch, E. Richter, H.-J. Schmidt and M. Folz, *Verfahren zur Entfernung von Schwefeloxiden und Stickoxiden aus Abgasen*, Espacenet, DE 2911712, **1980**.
- [106] H. Jüntgen, E. Richter, K. Knoblauch and T. Hoang-Phu, Chem. Eng. Sci. **43**, **1988**, 419-428.
- [107] K. Knoblauch, E. Richter and H. Jüntgen, Fuel **60**, **1981**, 832-838.
- [108] Y. Komatsubara, S. Ida, H. Fujitsu and I. Mochida, Fuel **63**, **1984**, 1738-1742.
- [109] H. Kuhl, H. Baumann, H. Jüntgen, P. Ehrburger, J. Dentzer and J. Lahaye, Fuel **68**, **1989**, 129-130.
- [110] K. Kusakabe, M. Kashima, S. Morooka and Y. Kato, Fuel **67**, **1988**, 714-718.
- [111] I. Mochida, M. Ogaki, H. Fujitsu, Y. Komatsubara and S. Ida, Fuel **62**, **1983**, 867-868.
- [112] I. Mochida, M. Ogaki, H. Fujitsu, Y. Komatsubara and S. Ida, Fuel **64**, **1985**, 1054-1057.
- [113] Ninomiya, et al., *Verfahren zur Entfernung von Stickoxyden aus Abgasen*, Europäisches Patentamt, DE 2433076, **1975**.
- [114] E. Richter, R. Kleinschmidt, E. Pilarczyk, K. Knoblauch and H. Jüntgen, Thermochi. Acta **85**, **1985**, 315-318.

- [115] E. Richter, K. Knoblauch and H. Jüntgen, *Gas Sep. Purif.* **1**, **1987**, 35-43.
- [116] E. Richter, H.-J. Schmidt, H. Jüntgen and K. Knoblauch, *Katalysatoren zur Stickoxidentfernung aus Abgasen*, Espacenet, *DE 3512169 A1*, **1986**.
- [117] G. S. Szymanski, T. Grzybek and H. Papp, *Catal. Today* **90**, **2004**, 51-59.
- [118] L. Singoredjo, F. Kapteijn, J. A. Moulijn, J.-M. Martin-Martinez and H.-P. Boehm, *Carbon* **31**, **1993**, 213-222.
- [119] J. M. Martin-Martinez, L. Singoredjo, M. Mittelmeijer-Hazeleger, F. Kapteijn and J. A. Moulijn, *Carbon* **32**, **1994**, 897-904.
- [120] S. N. Ahmed, R. Baldwin, F. Derbyshire, B. Mcenaney and J. Stencel, *Fuel* **72**, **1993**, 287-292.
- [121] J. Muniz, G. Marban and A. B. Fuertes, *Appl. Catal. B-Environ.* **23**, **1999**, 25-35.
- [122] J. Muniz, G. Marban and A. B. Fuertes, *Appl. Catal. B-Environ.* **27**, **2000**, 27-36.
- [123] N. Shirahama, I. Mochida, Y. Korai, K. H. Choi, T. Enjoji, T. Shimohara and A. Yasutake, *Appl. Catal. B-Environ.* **52**, **2004**, 173-179.
- [124] J. Zawadzki and M. Wisniewski, *Carbon* **41**, **2003**, 2257-2267.
- [125] J. Zawadzki, M. Wisniewski and K. Skowronska, *Carbon* **41**, **2003**, 235-246.
- [126] H. Teng and E. M. Suuberg, *J. Phys. Chem.* **97**, **1993**, 478-483.
- [127] M. T. Izquierdo, B. Rubio, A. M. De Yuso and D. Ballester, *Fuel Processing Technology* **92**, **2011**, 1362-1367.
- [128] H. Teng, Y.-F. Hsu and Y.-T. Tu, *Appl. Catal. B-Environ.* **20**, **1999**, 145-154.
- [129] B. J. Ku, J. K. Lee, D. Park and H.-K. Rhee, *Ind. Eng. Chem. Res.* **33**, **1994**, 2868-2874.

- [130] S. N. Ahmed, J. M. Stencel, F. J. Derbyshire and R. M. Baldwin, *Fuel Process. Technol.* **34**, **1993**, 123-136.
- [131] J. K. Lee, T. J. Park, D. Park and S. Park, *Ind. Eng. Chem. Res.* **32**, **1993**, 1882-1887.
- [132] T. Grzybek, J. Klinik, B. Samojeden, V. Suprun and H. Papp, *Catal. Today* **137**, **2008**, 228-234
- [133] J. Kee Lee, D. Jin Suh, S. Park and D. Park, *Fuel* **72**, **1993**, 935-939.
- [134] H. Jüntgen, *Erd. Koh. Erd. Petr. V.* **39**, **1986**, 546-550.
- [135] N. Shirahama, I. Mochida, Y. Korai, K. H. Choi, T. Enjoji, T. Shimohara and A. Yasutake, *Appl. Catal. B-Environ.* **57**, **2005**, 237-245.
- [136] E. Richter, *Catal. Today* **7**, **1990**, 93-112.
- [137] A. R. Chughtai, M. M. O. Atteya, J. Kim, B. K. Konowalchuk and D. M. Smith, *Carbon* **36**, **1998**, 1573-1589.
- [138] C. Dene and R. Himes, *Continuous Measurement Technologies for SO₃ and H₂SO₄ in Coal-Fired Power Plants*, EPRI, 1009812, Palo Alto, California, **2004**.
- [139] M. Koebel and M. Elsener, *Gefahrst. Reinhalt. L.* **57**, **1997**, 193-199.
- [140] *Messen der Schwefeltrioxi-Konzentration, Wasserstoffperoxid-Verfahren, Titrimetrische Bestimmungen*, VDI 2462 Bl. 2, Beuth-Verlag, Berlin, **1974**.
- [141] *Messen der Schwefeltrioxi-Konzentration, 2-Propanol-Verfahren*, VDI 2462 Bl. 7, Beuth-Verlag, Berlin, **1985**.
- [142] J. P. A. Neeft, T. X. Nijhuis, E. Smakman, M. Makkee and J. A. Moulijn, *Fuel* **76**, **1997**, 1129-1136.
- [143] J. Madarász, S. Kaneko, M. Okuya and G. Pokol, *Thermochim. Acta* **489**, **2009**, 37-44.
- [144] J. Madarász, P. P. Varga and G. Pokol, *J. Anal. Appl. Pyrol.* **79**, **2007**, 475-478.

- [145] H. Qu, W. Wu, H. Wu, J. Xie and J. Xu, *J. Therm. Anal. Calorim.* **2010**, DOI 10.1007/s10973-010-1103-3.
- [146] D. Wyrzykowski, E. Hebanowska, G. Nowak-Wiczak, M. Makowski and L. Chmurzyński, *J. Therm. Anal. Calorim.* **2010**, DOI 10.1007/s10973-010-1015-2.
- [147] S. Etienne, C. Becker, D. Ruch, A. Germain and C. Calberg, *J. Therm. Anal. Calorim.* **100**, **2010**, 667-677.
- [148] A. Mocanu, L. Odochian, N. Apostolescu and C. Moldoveanu, *J. Therm. Anal. Calorim.* **100**, **2010**, 615-622.
- [149] A. F. Plante, J. M. Fernández and J. Leifeld, *Geoderma* **153**, **2009**, 1-10.
- [150] B. Souza, A. Moreira and A. Teixeira, *J. Therm. Anal. Calorim.* **97**, **2009**, 637-642.
- [151] L. Tao, G.-B. Zhao, J. Qian and Y.-K. Qin, *J. Hazard. Mater.* **175**, **2010**, 754-761.
- [152] T. Xu and X. Huang, *J. Anal. Appl. Pyrol.* **87**, **2010**, 217-223.
- [153] P. Gilot, A. Brillard and B. R. Stanmore, *Combust. Flame* **102**, **1995**, 471-480.
- [154] J. P. A. Neeft, F. Hoornaert, M. Makkee and J. A. Moulijn, *Thermochim. Acta* **287**, **1996**, 261-278.
- [155] T. P. Herbell, *Thermochim. Acta* **4**, **1972**, 295-307.
- [156] C. G. R. Nair and K. N. Ninan, *Thermochim. Acta* **23**, **1978**, 161-169.
- [157] A. E. Lear, T. C. Brown and B. S. Haynes, *Symposium (International) on Combustion* **23**, **1991**, 1191-1197.
- [158] S. Pischinger, R. Niessner and M. Aigner, *Filterregeneration durch reaktiven Russ*, final report of FVV-project No. 954, Frankfurt/Main, **2008**,
- [159] R. Niessner, *personal communication*, **2010**.

- [160] A. F. Ahlström and C. U. I. Odenbrand, *Carbon* 27, **1989**, 475-483.
- [161] K. Matsui, H. Tsuji and A. Makino, *Carbon* 21, **1983**, 320-321.
- [162] PSI internal measurements, **2011**.
- [163] J. Oi Uchisawa, A. Obuchi, Z. Zhao and S. Kushiyama, *Appl. Catal. B-Environ.* 18, **1998**, L183-L187.
- [164] J. Oi-Uchisawa, A. Obuchi, R. Enomoto, A. Ogata and S. Kushiyama, *Chem. Commun.* **1998**, 2255-2256.
- [165] J. Oi-Uchisawa, A. Obuchi, A. Ogata, R. Enomoto and S. Kushiyama, *Appl. Catal. B-Environ* 21, **1999**, 9-17.
- [166] H. Akimoto, H. Bandow, F. Sakamaki, G. Inoue, M. Hoshino and M. Okuda, *Environ. Sci. Technol.* 14, **1980**, 172-179.
- [167] J. Kleffmann, K. H. Becker and P. Wiesen, *Atmos. Environ.* 32, **1998**, 2721-2729.
- [168] F. Sakamaki, H. Shiro and H. Akimoto, *Int. J. Chem. Kinet.* 15, **1980**, 1013-1029.
- [169] M. B. Smith and J. March, *March's Advanced Organic Chemistry*, 5.th edition, Wiley, New York, **2001**.
- [170] O. Kröcher, M. Widmer, M. Elsener and D. Rothe, *Ind. Eng. Chem. Res.* 48, **2009**, 9847-9857.
- [171] M. Koebel, M. Elsener and M. Kleemann, *Catal. Today* 59, **2000**, 335-345.
- [172] Y. H. Yeom, J. Henao, M. J. Li, W. M. H. Sachtler and E. Weitz, *J. Catal.* 231, **2005**, 181-193.
- [173] J. J. Venter and M. A. Vannice, *Carbon* 26, **1988**, 889-902.
- [174] M. Elsener, personal communication, **2011**.
- [175] K. Vollhardt and N. Schore, *Organische Chemie*, 3. edition, Wiley VCH, Weinheim, **2000**.
- [176] W. Keim, A. Behr, H. O. Lühr and J. Weisser, *J. Catal.* 78, **1982**, 209-216.

- [177] E. Puentes, A. F. Noels, R. Warin, A. J. Hubert, P. Teyssié and D. Y. Waddan, *J. Mol. Catal.* **31**, **1985**, 183-190.
- [178] I. Aarna and E. M. Suuberg, *Fuel* **76**, **1997**, 475-491.
- [179] M. T. Izquierdo, B. Rubio, C. Mayoral and J. M. Andrés, *Fuel* **82**, **2003**, 147-151.
- [180] I. Mochida, M. Kishino, S. Kawano, K. Sakanishi, Y. Korai, A. Yasutake and M. Yoshikawa, *Fuel* **77**, **1998**, 1741-1746.
- [181] M. T. Izquierdo, B. Rubio, C. Mayoral and J. M. Andrés, *Appl. Catal. B-Environ.* **33**, **2001**, 315-324.
- [182] I. Mochida and S. Kawano, *Ind. Eng. Chem. Res.* **30**, **1991**, 2322-2327.
- [183] M. S. Akhter, A. R. Chughtai and D. M. Smith, *J. Phys. Chem.* **88**, **1984**, 5334-5342.
- [184] R. Q. Long and R. T. Yang, *J. Catal.* **194**, **2000**, 80-90.
- [185] V. A. Matyshak and O. V. Krylov, *Catal.Today* **25**, **1995**, 1-87.
- [186] C. N. Banwell and E. M. Mccash, *Molekülspektroskopie*, Oldenbourg Verlag, München, Wien, **1999**.
- [187] V. H. Grassian, *J. Phys. Chem. A* **106**, **2002**, 860-877.

List of publications

The following list summarizes the journal articles, posters and talks, which were prepared during this work. Chapters 2-6 formed the basis for these publications.

Journal Articles

1. Max Mehring, Oliver Kröcher and Martin Elsener
Development of a TG-FTIR system for investigations with condensable and corrosive gases, Journal of Thermal Analysis and Calorimetry, **2011**, DOI 10.1007/s10973-010-1178-x.
2. M. Mehring, M. Elsener and O. Kröcher
Mikroanalytik und Reaktivität von Dieselpartikeln, Motorentechnische Zeitschrift (MTZ), 72, **2011**, 690-696.
Also published as:
Micro-analytics and reactivity of diesel particulate matter, MTZ worldwide edition **09/2011**.

Posters

1. M. Mehring, O. Kröcher, M. Elsener and A. Wokaun
Development of a TGA-FTIR system as R&D tool in exhaust gas aftertreatment,
12th ETH-Conference Combustion Generated Nanoparticles, Zurich,
Switzerland, June 23 - 25 (2008).
2. M. Mehring, O. Kröcher and M. Elsener
*Development of a TGA-FTIR system for research in the field of exhaust gas
aftertreatment,*
CAPoC8: 8th International Congress on Catalysis and Automotive Pollution
Control, Brussels, Belgium, April 15-17 (2009).
3. M. Mehring, O. Kröcher and M. Elsener
*Investigation of diesel soot reactivity with a new TG-FTIR system for research with
condensable and corrosive gases,*
13th ETH-Conference Combustion Generated Nanoparticles, Zurich,
Switzerland, June 22 - 24 (2009).
4. M. Mehring, M. Elsener, O. Kröcher, M. Schubnell, U. Jörimann, A. Möps
and D. Hohler
*Investigation of diesel soot reactivity with a new TG-FTIR system for research with
condensable and corrosive gases,*
NATAS 2009: 37th Annual Conference of the North American Thermal
Analysis Society, Lubbock/USA, September 20-23 (2009).

Talks

1. M. Mehring, M. Elsener and O. Kröcher
FTIR-Spektroskopie kombiniert mit Thermoanalyse zur Untersuchung von Materialien mit reaktiven und kondensierbaren Gasen,
User Meeting Thermo Scientific, Seligenstadt, Germany, March 22-23 (2009).
2. M. Mehring, M. Elsener and O. Kröcher
Investigation of diesel soot reactivities with condensable and corrosive gases in a new TG-FTIR system,
14th Conference on Combustion Generated Nanoparticles, Zurich, Switzerland, August 2-4 (2010).
3. M. Mehring, M. Elsener and O. Kröcher
A new TG-FTIR system for investigations with condensable and corrosive gases,
10th European Symposium on Thermal Analysis and Calorimetry, Rotterdam, The Netherlands, August 23-27 (2010).
4. M. Mehring, M. Elsener and O. Kröcher
Detailed diesel soot analysis by TG-FTIR,
Anakon 2011, Zurich, Switzerland, March 22-25 (2011).

Curriculum vitae

Name: Max Mehring
Date of Birth: October 11th, 1980
Place of birth: Offenbach/Main, Germany
Nationality: German

Education

Since 10/2007 PhD student in the Catalysis for Energy Group under the supervision of Prof. Dr. A. Wokaun (ETH Zürich) at the Paul Scherrer Institute, Villigen, Switzerland.

03/2007 – 08/2007 Diploma-thesis (Master equivalent) at the Eduard-Zintl-Institute under the supervision of Prof. Dr. R. Schäfer, Technical University of Darmstadt, Germany.
Subject: *Electrical molecular beam experiments at the example of small neutral barium clusters*

4/2002 – 08/2007 Chemistry studies at the Technical University of Darmstadt, Germany.

10/2001 – 03/2002 Chemical Engineer studies at the Technical University of Karlsruhe, Germany.